ISSN: 0067-3064

Ministry of Higher Education and of Scientific Research
Blida 1 University
Sciences Faculty, Physics Department

2nd International Conference on Computational & Applied Physics
ICCAP' 2023
Blida (Algeria) 08 -10 October 2023

Book Of Abstracts

Editors : Dr. Bouamra Faiza

Head of Physical Chemical Laboratory of Inorganic Materials and their Applications - LPCMIA-.
University of Blida1- Faculty of Sciences - Physics Department
BP270 Route de Soumaa - Blida
Phone: +213 (0) 6 66 72 60 41

Dr. Guittoum Abderrahim

Senior Researcher, Maître de Recherche A /HDR
Mössbauer & Positron Laboratories

Materials Physics Department, Division of Physics,

Nuclear Research Centre of Algiers,

2 Bd Frantz Fanon, Bp 399, Alger-Gare, Algiers, Algeria.
Tel: 213 (0) 21 43 44 44 Poste: 440/441
Fax: 213 (0) 21 43 42 80
Mobile: 213 (0) 656 00 61 36

Organized by : *Laboratory of Physical-Chemical Inorganics Materials and their applications*

Blida 1 University

ISSN: 0067-3064

About the conference:

The 2nd International Conference on Computational & Applied Physics (ICCAP'2023) was held from October 8th to 10th, 2023. This conference was organized by the Laboratory of Physical-Chemical Inorganic Materials and their Applications (LPCMIA) at Blida1 University, within the Faculty of Sciences, Physics Department, in Algeria.

The event gathered academics, researchers, and scientists from various fields of physics, making it a significant platform for knowledge exchange and scientific discourse. Participants had the opportunity to attend a range of activities, including plenary lectures, oral sessions, and poster presentations. The primary objective of ICCAP'2023 was to unite Algerian and international scientists and researchers to share information, enhance their understanding of different research areas, and discuss the latest advancements in computational and applied physics. The conference also actively involved graduate students, underlining the importance of materials physics and its diverse applications.

This year's edition introduced several new and pivotal topics such as "Data Science and Artificial Intelligence (AI) for Physical and Chemical Materials," "Micro and Nanophysics (MEMS, NEMS, BIOMEMS, RFMEMS, Sensors, and Actuators) and Metamaterials: Modeling, Simulation, and Experimental Characterization," and "Medical Image Processing Methods and Their Applications." These additions aimed to provide a comprehensive overview of these cutting-edge fields and their significant impact on physics research.

The topics presented at the conference included:

- **TOPIC 01**: Data Science and Artificial Intelligence (AI) for Physical and Chemical Materials.
- **TOPIC 02**: Synthesis and Characterization of Optical and Magnetic Materials and Their Applications.
- **TOPIC 03**: Quantum Simulation and First-Principles Modeling of Physical Properties of Low-Dimensional and Periodic Systems.
- **TOPIC 04**: Medical Image Processing Methods and Their Applications.
- **TOPIC 05**: Micro and Nanophysics (MEMS, NEMS, BIOMEMS, RFMEMS, Sensors, and Actuators) and Metamaterials: Modeling, Simulation, and Experimental Characterization.

ICCAP'2023 successfully created an engaging environment for researchers and students alike to delve into the latest research trends, discuss innovative ideas, and establish collaborations that could drive future scientific endeavors.

ISSN: 0067-3064

Scientific Committee:

Prof. RNDr. Jana Kalbacova Vejpravova, Czech Republic.
Prof. Martin Kalbáč**,** Czech Republic
PROF. ZERHOUNI NOUREDDINE, FRANCE.
PROF. LOUNIS SAMIR, GERMANY.
PROF. BENAMARA OMAR, FRANCE
PROF. MICHEL RÉRAT, FRANCE.
PROF. BAADJI NADJIB, ALGERIA.
PROF. MOHAMED EL SAYED, EGYPT.
PROF. TERRISSA LABIB SADEK, ALGERIA.
PROF. RUDOLF SCHAEFER, GERMANY.
PROF. KHELIF ABDELKRIM, FRANCE.
PROF. NICOLAS BODIN, FRANCE.
PROF. SALIM MOURAD CHÉRIF, FRANCE.
PROF.FERROUKHI OUASSILA, ALGERIA
PROF. JEAN MARC GRENECHE, FRANCE.
PROF. LEBBOU KHEIREDDINE, FRANCE.
PROF. BENAMAR MOHAMED EL AMINE, ALGERIA.
PROF. KHERFI FAYÇAL, ALGERIA.
PROF. DERBAL MOURAD, ALGERIA.
PROF. BENBRAHIM NASSIMA, ALGERIA
PROF. SALHI NASSIMA, ALGERIA.
PROF. ROUDANE MOHAMED, ALGERIA.
PROF. TAOUTI MOHAMED BENABDALLAH, ALGERIA.
PROF. TABLAOUI MEFTAH, ALGERIA.
PROF. CHERFA YAZID, ALGERIA.
PROF. CHERFA ASSIA, ALGERIA.
PROF. KASMI SOUAD, ALGERIA.
PROF. REKIK BRAHIM, ALGERIA

HONORARY PRESIDENT OF THE CONFERENCE:
Pr. BEZZINA MOHAMED
CHAIRMAN :
DR. BOUAMRA FAIZA
VICE-CHAIRMAN:
DR. GUITTOUM ABDERAHIM.
LOCAL ORGANIZING COMMITTEE CHAIRMAN :
PR. SAADI LEILA

Members of local organizing committee:

MRS. OUITIS SARAH CHAHINEZ, ALGERIA
MR. BOUMESHED SOFIANE, ALGERIA
MRS. OUDJER HAYET.ALGERIA
MRS. ALI MESSAOUD ANISSA, ALGERIA
MR. BOUTAHRAOUI BELKACEM, ALGERIA

ISSN: 0067-3064

MR. BELGROUNE NADIR, ALGERIA
MRS. M'HAMEDI KAWTHER, ALGERIA
MR. HASSEIN-BEY ABDELKADER, ALGERIA
MRS. OULD ARAB HALIMA, , ALGERIA
MR. NAIT MOHANED MUSTAPHA, ALGERIA
MR. LATARCHA NASSIM, ALGERIA
MR. HACHAMA MOHAMED, ALGERIA
MR. CHEKNANE BENAMAR, ALGERIA
MR. AHMED LOUAZANI, ALGERIA
MRS. OUIR SOUAD, ALGERIA
MRS. BOURAYOU DALEL, ALGERIA

Acknowledgement
First,
The organizers would like to thank all participants to the ICCAP'2023 and invited speakers for agreeing to take part in this conference;

- Prof. **Jana Kalbacova Vejpravova**, Czech Republic.
- Prof. Martin Kalbáč, Czech Republic.
- Prof. Lounis Samir, Germany.
- Prof. Benamara Omar, France
- Prof. Baadji Nadjib, Algeria.
- Prof. Michel Rérat, France.
- Prof. Khelif Abdelkrim, France.
- Prof. Jean Marc Greneche, France.
- Prof. Zerhouni Noureddine, France.
- Prof. Silvia Maria Casassa, Italy

Secondly,

We would like to thank sponsors:
As Diamand sponsors we have:

- **Sosemie*/*** *Société Semoulerie Minoterie L'Etoile***.**
- **EURL Adichim.**
- **ITCMD*/*** *EURL IT CLASSROOM & DIDACTICS IMPORT.*

As platinum sponsors :

- **ESST /Ecole Supérieure de Science et Technologie.**
- **SARL Sinal**

ISSN: 0067-3064

ISSN: 0067-3064

Van der Waals heterostructures tunable with chiral light and magnetic field
PL 01

Jana K. Vejpravova

Charles University, Faculty of Mathematics and Physics, Department of Condensed Matter Physics
Ke Karlovu 5, Praha 2, 121 16, Czech Republic
Phone: +420-951-552-735 E-mail: jana.vejpravova@matfyz.cuni.cz Web: vejpravova.eu

Abstract: VdW materials and their heterostructures feature significant optical properties tunable via external physical fields (photonic, magnetic, electric, and strain) [1-3] or proximity effects with other materials or molecules [4-5], which made them superior constituents for designing advanced devices.In my talk, I will first summarize the state of the art in the field and the most important theoretical concepts. Next, I will present our recent experimental and theoretical results on hybrid layered architectures based on transition metal dichalcogenides (TMDs), layered magnets, and magnetic molecules, including their rational design, fabrication, and performance under chiral light and magnetic field down to helium temperatures.
First, we developed a new strategy to obtain close to atomically thin lasing devices based on TMDs separated by a few layers of hBN [6]. The collective oscillation of the optically pumped excitonic dipoles stimulates robust phase synchronization and provides the so-called superradiant emission (SRE).
Another fundamental property of the TMDs is the valley-selective optoelectronic response, which can be conveniently studied using circularly polarized light and implemented in various valleytronic (pseudo-spintronic) concepts. In this vein, the corresponding TMD component(s) must provide a sufficient valley contrast (polarization and coherence), which is usually smeared out due to inter-valley scattering events [7]. We developed a general strategy to boost room-temperature chiral light emission suitable for applications in opto-valleytronic devices, employing mixed dimensional heterostructures of TMDs and magnetic molecules.
Finally, I will introduce prospects of proximity effects in 2D magnet–TMD heterostructures.

References:
[1] J. M. Allen, T. C. Vincent, K. B. Richard, Chem. Rev. 110 (2010) 132.
[2] M. Xu, T. Liang, M. Shi, H. Chen, Chem. Rev. 113 (2013) 3766.
[3] G. Fiori, F. Bonaccorso, G. Iannaccone, T. Palacios, D. Neumaier, A. Seabaugh, S. K. Banerjee, L. Colombo, Nat. Nanotechnol. 9 (2014) 768.

ISSN: 0067-3064

[4]M. R. Habib, H. Li, Y. Kong, T. Liang, S. M. Obaidulla, S. Xie, S. Wang, X. Ma, H. Su, M. Xu, Nanoscale 10 (2018) 16107.
[5] P. Choudhury, L. Ravavarapu, R. Dekle, S. Chowdhury, J. Phys. Chem. C 121 (2017) 2959.
[6] G. Haider, K. Sampathkumar, T. Verhagen, L. Nádvorník, F.J. Sonia, V. Valeš, J. Sýkora, P. Kapusta, P. Němec, M. Hof, O. Frank, Y.-F. Chen, J. Vejpravová, M. Kalbáč, Adv. Funct. Mater. 31 (2021) 2102196.
[7] G. Wang, A. Chernikov, M. M. Glazov, T. F. Heinz, X. Marie, T. Amand, B. Urbaszek, Rev. Mod. Phys. 90 (2018) 21001.
[8] V. Varade, G. Holam, A. Slobodeniuk, R. Korytar, T. Novotny, V. Holy, J. Plsek, M. Zacek, M. Basova, J. Sykora, M. Hoff, J. Miksatko, M. Kalbac, J. Vejpravova, submitted, ACS Nano 17 (2023) 2170.

ISSN: 0067-3064

Novel approaches to preparation of 2D materials, their modifications and application in devices
PL 02

Martin Kalbac

J. Heyrovsky Institute of Physical Chemistry of the Czech Academy of Sciences, Dolejškova 2155/3, 182 23 Prague, Czech Republic, *kalbac@jh-inst.cas.cz*

Abstract:
Two dimensional materials are strongly affected by the environment. This can be exploited in many applications. On the other hand this feature also means a challenge, when the properties of the two dimensional materials need to be precisely controlled. I will present our approach for their preparation in ultraclean conditions, which allows to limit effects of the environment. Furthermore, I will show possible approaches for their further chemical modifications by introducing functional groups including a control of the functionalization process in terms of localization of the functional groups. Mastering of these processes pave the way to precisely control electronic structure of two dimensional materials and thus enable their more advanced applications. Finally, I willshow how tailored chemical functionalization can be exploited to optimize function of supercapacitor in graphene /PANI composite and to realize fast, ultrasensitive and broadband 2D detector.

[1] L. Assies, Ch. Fu, P. Kovaricek Z. Bastl, K. A. Drogowska, J. Lang, V. L. P. Guerra,P.Samorı, E. Orgiu, D. F. Perepichka and M. Kalbac, J. Mat. Chem. C, 7 12240 (2019).
[2] L.Valenta, P. Kovaricek, V. Vales, Z. Bastl, K. A. Drogowska,T. A. Verhagen, R. Cibulka, and M. Kalbac, Angew. Chem. Int. Ed.58, 1324-1328 (2019).
[3] M.Bláha, M. Bouša, V. Valeš, O. Frank, M. Kalbáč, ACS Applied Materials & Interface, 13, 34686-34695, (2021).
[4] M. Thakur, G.Haider, F. J. Sonia, J.Plšek, A. Rodriguez, V. Mishra, J. Panda, O. Gedeon, M. Mergl, O. Volochanskyi,V. Valeš, O. Frank, J. Vejpravova, and M. Kalbáč : Small, 2205575 (2023).

ISSN: 0067-3064

Emergence of intrinsic antiferromagnetic topological solitons in thin films
PL 03

Samir Lounis

Peter Grünberg Institut and Institute for Advanced Simulations, Forschungszentrum Jülich& JARA, 52425 Jülich, Germany, Faculty of Physics, University of Duisburg-Essen and CENIDE, 47053 Duisburg, Germany

Abstract: Antiferromagnetic (AFM) skyrmions are envisioned as ideal localized topological magnetic bits in future information technologies. In contrast to ferromagnetic (FM) skyrmions, they are immune to the skyrmion Hall effect, might offer potential terahertz dynamics while being insensitive to external magnetic fields and dipolar interactions. Although observed in synthetic AFM structures and as complex textures in intrinsic AFM bulk materials, their realization in non-synthetic AFM films, of crucial importance in racetrack concepts, has been elusive. We made recently progress in predicting from first-principles and in discussing realistic combination of materials that can host intrinsic (non-synthetic) topological AFM solitons, which can have intriguing properties. For instance, we unveiled the presence of single and strikingly interpenetrating chains of AFM skyrmions with non-trivial dynamics in a row-wise AFM Cr film deposited on PdFe bilayer grown on fccIr(111) surface [1,2]. Substituting Cr with various combination of Mn and Pd-based filmsyields to novel chiral particles within the realm of AFM topological magnetism: frustrated AFM multimeronic spin-textures residing in a Néel magnetic state [3]. These structures carry distinct topological charges and can combine in various multimeronic sequences with increased stability against external magnetic fields. Similar states have been identified in artificial adatom nanostructures, where atoms are not positioned as nearest neighbors [4], which then impacts topological superconductivity, and in 2D van der Waals heterostructures [5]. These textures can be identified with all-electrical means using conventional current perpendicular-to-plane sensing devices thanks to the recently proposed chiral and anisotropic spin-mixing magnetoresistance, which enables a readout of the chirality and helicity [6]. These findings open up exciting avenues for engineering and detecting intrinsic AFM chiral entities in the same films. This development holds great promise for information technology devices utilizing non-synthetic AFM quantum materials.

References:

[1] Aldarawsheh, et al. “Emergence of zero-field non-synthetic single and interchained antiferromagnetic skyrmions in thin films”,
Nature Commun. 13, 7369 (2022)

ISSN: 0067-3064

[2] Aldarawsheh et al. “A spin model for intrinsic antiferromagnetic skyrmions on a triangular lattice”, Frontiers in Physics 11, 335 (2023)
[3] Aldrawsheh et al. “Intrinsic antiferromagnetic multimeronicNéel spin-textures in ultrathin films”, arXiv:2306.04720 (2023); accepted in Journal of Physical Chemistry Letters
[4] Soldini et al. “Two-dimensional Shiba lattices as a possible platform for crystalline topological superconductivity”, Nature Phys. (2023)
[5] Abuawwad et al. “CrTe2 as a two-dimensional material for topological magnetism in complex heterobilayers”, PRB 108, 094409 (2023)
[6] Fernandes et al. “Spin-orbit enabled all-electrical readout of chiral spin-textures”, Nature Commun. 13, 1576 (2022)

ISSN: 0067-3064

Interplay between electron correlation, spin-orbit coupling and crystalline structure in ferroelectric metal $LiOsO_3$

PL 04

Nadjib Baadji

Département de Physique, Faculté des Sciences,& Laboratoire de Physique des Matériaux et ses applications, Université Mohamed Boudiaf, M'sila, 28000, Algeria

Abstract: Ferroelectric metal is a concept, initially proposed by Blount and Anderson [1], and identified recently, by Shi et al. [2]. Experimentally, The metallic bulk $LiOsO_3$ undergo a ferroelectric-like phase transition from a high-temperature centro-symmetric structure R-3C (non-polarized paraelectric state) to non-centro-symmetric phase R3C (a low-temperature "FE" polarized state). This distinctive characteristic offers a unique opportunity to investigate the interaction between free electrons and electric dipoles. However, the bad conductivity and enhancements from the electron contribution to the specific heat and the paramagnetic susceptibility indicate a strong electron correlation in $LiOsO_3$[3] whereas it expected to be small in 5d transition metal. In addition, the strong spin-orbit coupling in 5d may explain the puzzling experimental fact is its paramagnetic state down to very low temperature with negligible magnetic moment [4]. Consequently, the electron correlation, spin-orbit coupling and crystal field splitting should all be treated of the same footing, as they are all on the scale of an electron volt. Here we show, using density functional theory that in presence of SOC and within the right crystalline structure we could explain most of the observed properties of the polar metal $LiOsO_3$ without resort to the electron correlations and that free electron model cannot be used to describe the physical properties of the ferroelectric metal $LiOsO_3$.

References :

[1] P. W. Anderson,& E. I. Blount, "Symmetry considerations on martensitic transformations:
Ferroelectric metals?", Phys. Rev. Lett. 14, 217219 (1965).
[2] Y. Shi, et al. "A ferroelectric-like structural transition in a metal", Nature Materials 12, 1024 (2013)
[3] J.-S. Zhou, et al."Strongly correlated electrons in the ferroelectric metal LiOsO3", Phys. Rev. B 104, 115130 (2021).
[4] Yu Zhang et al. "Possible Origin of the Absence of Magnetic Order in LiOsO3: Spin–Orbit Coupling Controlled Ground State", physica status solidi (RRL), 12 1800396 (2018)

ISSN: 0067-3064

Sound opacity, in the light of acoustic metamaterials
PL 05

Prof. Abdelkrim Khelif

CNRS-International-NTU-Thales Research Alliance (CINTRA), Singapore
Email: abdelkrim.khelif@gmail.com

Abstract: For more than twenty years now, Acoustic Metamaterials are experiencing growing success due to exotic phenomena and their wide variety of applications. Recently, various studies involving resonators have shown how to create acoustic black holes through absorption phenomena. This talk aims to highlight acoustic mechanisms underlying acoustic opacity that can enable the emergence of concrete applications such as sound shields. In the first part, we present an experimental demonstration of sound absorption tailorability, using acoustic metamaterials made of resonant cavities that do not rely on any dissipative material, but rather take advantage of the inherent visco-thermal characteristics of air. As confirmed by numerical calculation, we particularly show that using quarter-wave-like resonators made of deep subwavelength slits allows a high confinement of the acoustic energy of an incident wave. This leads to enhance the dissipation in the cavities and, consequently, generates strong sound absorption, even over a wide frequency band. We finally demonstrate experimentally the key role of the filling ratio in tailoring such an absorption, using a metamaterial constituted of space-coiled cavities embedded in a polystyrene matrix. This paves the way for tremendous opportunities in soundproofing because of its low density, low volume, broadband and tailorable capabilities.
In the second part, we report on the omnidirectional sound screening of an acoustic metamaterials based on local resonances. We investigate both experimentally and theoretically how the coupling between two resonators, with different quality factors, can generate asymmetric lineshapes of the transmission, leading to the opaque counter-part of the low frequency Enhanced Acoustic Transmission. Moreover, we study the angular dependence of its transmission properties, and demonstrate that such an opacity band, due to deep subwavelength features of cavities, avoids diffraction that have been proved to be the main limitation of omnidirectional capabilities of locally resonant perforated plates.

ISSN: 0067-3064

Eutectic oxides ceramic for industrial applications
PL 06

Omar BENAMARA[1], Kheirreddine LEBBOU[2]

[1] Zadient Technologies SAS, 354 Voie Magellan73800 Sainte-Hélène-du-Lac, France.
[2]Institut Lumière Matière, UMR5306 Université Lyon1-CNRS, Université de Lyon, Lyon 69622, Villeurbanne Cedex, France. e-mail: Omar.Benamara@zadient.tech

Abstract: Unidirectionally solidified eutectic ceramic have a few properties which make them of interest as potential engineering materials. In addition to their utilization in gas turbine engines, they can be used for ships and eventually in aircraft such turbine design. The use of these materials in aeronautic will depend not only on superior engineering design but more importantly on the availability of the eutectic ceramic with a significant advantage in high temperature morphology and microstructure over presently available metals and alloys. The great advantage of the unidirectionally solidified eutectic for high temperature applications is their performed properties: High melting temperature, good resistance to corrosion by liquids and gases and high temperature potential strength. These performed properties allow to use them to solve the materials engineering problem in the highest temperature applications. A large portion of the efforts in eutectic ceramic oxides research have dealt with developing process technology. To elaborate homogeneous morphology under flat solid-liquid interface during solidification at microscopic and macroscopic level it is necessary to control the thermal gradients along the solidification direction [1-4]. It has been clearly shown in several eutectic system that the knowledge of the relationship between microstructures and properties is a key factor to control the system performance. The functional properties of the eutectic oxide's materials are strongly dependent on characteristics of the microstructure (morphology, phase geometry and size) which dependent on the solidification process. In this presentation, the microstructure morphology, crystallography, and residual stresses evolution as function of the solidification rate of the Al2O3-YAG-ZrO2 ternary eutectic oxide grown by micro pulling down with different forms will be discussed. The effect of the residual stress on the crystallographic orientations and physical properties of the Al2O3-YAG-ZrO2 ternary eutectic will be also discussed.

References:

[1] O. Benamara et al, Journal of the European Ceramic Society 41(11), (2021).
[2] O. Benamara et al, Royal Society of Chemistry RSC Adv ,11,13602 (2021).
[3] O. Benamara et al, Journal of Crystal Growth, vol. 449, p. 67-74 (2016).
[4] O. Benamara et al, Journal of Crystal Growth, vol. 429, p. 27-34 (2015).

ISSN: 0067-3064

The Behavior of double Tungstate in the presence of rare earths on its structural, optical, and vibrational properties
PL 07

Pr. Brahim REKIK

LPCMIA Laboratory, Department of Physics, Faculty of Sciences, Saad Dahleb Blida 1 University, Blida, BP 270 Soumaa Road Blida, Algeria.

Abstract: Spectroscopic, vibrational and luminescent properties of the double Tungstate with the general formula $AB(WO_4)_2$ (A = monovalent ion; Li, Na, K, ad B = trivalent ion; rare earth or Bi) which form a wide range of inorganic compounds with monoclinic and tetragonal symmetries, offer high performance and attract greater research interest in structural , phosphorescent and laser applications, due to their structural diversity and high absorption cross section [1].
In this presentation, consideration will be given to the area of structural, polymorphic and optical change based mainly on rare earth ions (Yetterbium Yb^{3+}, Erbium Er^{3+}, thuliumTm^{3+} and Europium Eu^{3+}) for some double tungstates ($LiB(WO_4)_2$ with B= Gd, Lu and Bi prepared by solid state reaction from Na_2CO_3, Li_2CO_3, Gd_2O_3, Lu_2O_3, Yb_2O_3 , Er_2O_3 ,Eu_2O_3 ,Tm_2O_3 Bi_2O_3 and WO_3), through XRD, Raman and spectroscopy analysis, taking into account a many effects on these compounds properties like that ; crystal Growth technical, synthesis temperature, ionic radius of element and wavelengths excitation [2].

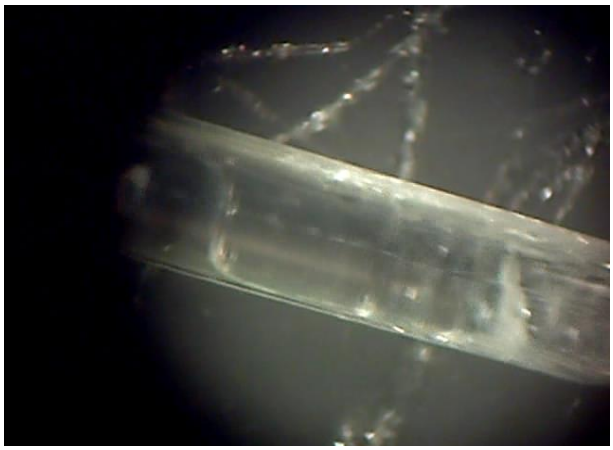

Fig 1. Fiber Crystal of $LiGd(WO_4)_2$ doped ytterbium

The influence of the synthesis temperature and elaboration method, in particular crystal growth, on the structural, optical and vibrational properties of materials based on

ISSN: 0067-3064

double tungstates. During this work, three tungstate oxide systems doped with rare earth ions, were developed and studied: $LiGd(WO_4)_2$, $LiLu(WO_4)_2$, and $LiBi(WO_4)_2$.

Keywords: Double tungstate (DT); Crystal Growth; Spectroscopy; structural change; Raman.

ISSN: 0067-3064

Artificial Intelligence for CT-Images Auto-segmentation in Radiation Therapy
PL 08

Fayçal Kharfi[1,2]

Laboratory of Dosing, Analysis and Characterisation with high resolution, Ferhat Abbas-Sétif 1 University, Setif, Algeria
Department of Physics, Faculty of Sciences, Ferhat Abbas-Setif 1 University, Setif, Algeria

Abstract: Nowadays, Artificial Intelligence (AI) is involved in different domains,in place of humans,for carrying out several tasks requiring high attention, speed and accuracy.An important issue in current medical and healthcare research is that of precision and how getting accurate data from patient in order to offer him the most appropriate and personalized treatment. In radiation therapy (RT), computed tomography (CT) images are primordial for the treatment planning and dose calculation. In this work, the use of CT-images in radiation therapy will be highlighted with a special focus on the importance of the image-segmentation process. The main objective of this work is the presentation of the application of AI in radiation therapy for image auto-segmentation. The workflow and the most important tools used for the implementation of such technology in RT for such purpose will be described. Moreover, the application of AI, particularly Deep learning (DL), for image auto-segmentation in RT will be presented through an example of an open source DL notebook that builds a convolution neuron network (CNN) based on the convolutional networks for biomedical image segmentation “U-Net”. A literature comparison between different conventional and AI-DL CT-images auto-segmentation will be also provided. Finally, the advantages and threats behind the implementation of AI in radiation therapy and medicine will be discussed.

Keywords: Artificial Intelligence; Deep Learning; Radiation Therapy; Treatment Planning; CT-imagesauto-segmentation.

ISSN: 0067-3064

Raman spectrum of adsorbed water molecules on MgO surfaces
PL 09

Michel Rérat

Université de Pau et des Pays de l'Adour, E2S, IPREM, UMR 5254, Pau, France
Email: michel.rerat@univ-pau.fr

Abstract: This work has been recently published in Crystals / MDPI (2023) by M. Dekermenjian, A. Merlen, A. Ruediger and M. Rérat. [1]. I will present the theoretical part of the work. A typical experimental Raman spectrum of MgO nanoparticles in the OH stretching region is reported in Figure (a) and compared to the Raman spectrum of liquid water in the same spectral range (b).The optimized energy of one or two molecules per unit cell of water adsorbed on the stable MgO(001) surface and one molecule per unit cell on the less stable but more reactive MgO(011) and MgO(112) surfaces has been obtained using the B3LYP+D3 hamiltonian and a double zeta plus polarization and d atomic orbital basis set. It leads to the following geometries for 2 H2O on MgO(001) and 1 H2O on MgO(112):

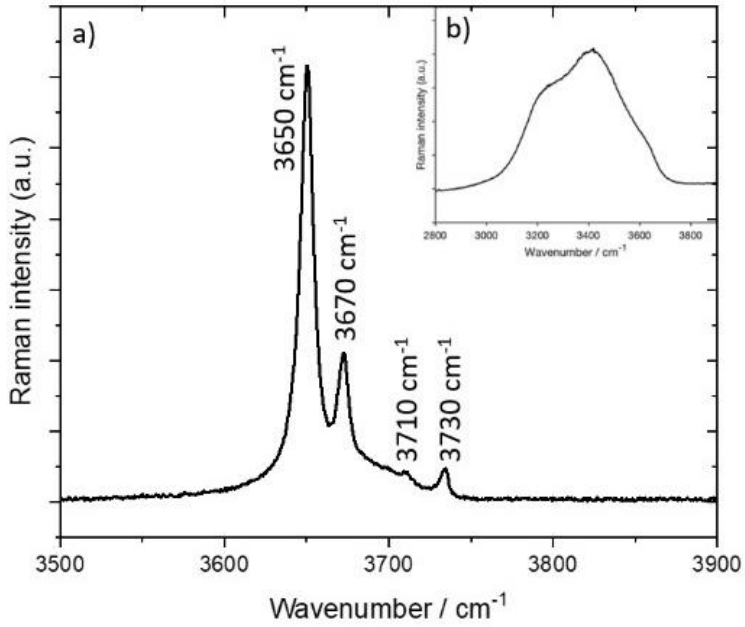

The first case is a physisorption with distance between H of H2O and O of MgO equal to 1.8 Å, while the second case is a chemisorption with the dissociation of H2O on MgO in MgOH and OH.

ISSN: 0067-3064

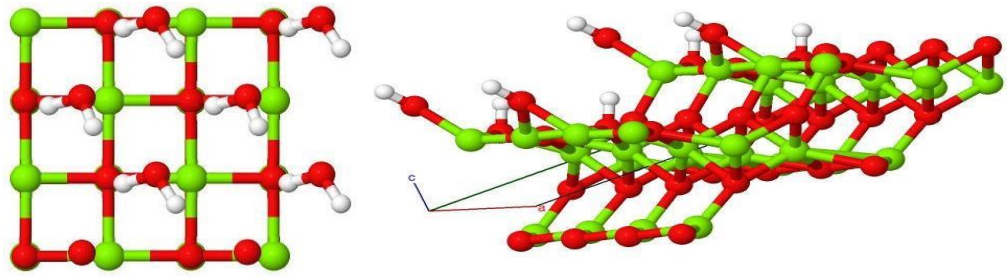

Then, a vibration interaction of configuration (VCI) method [2] implemented in the Crystal code (www.crystal.unito.it,) [3] has been used to obtain the anharmonic mode frequencies of the optimized configurations, while the Raman intensities were calculated analytically by a self-consistent coupled- perturbed (SC-CP) method [4]. Results are reported in the following table with the water and brucite Raman spectra, and a comparison is done with harmonic values. For all the configurations, frequencies are red-shifted by 100-200 cm^{-1} with the anharmonic correction while the Raman intensities remain practically constant.

Configuration	**Frequencies / Intensities**	
	Harmonic	**Anharmonic**
H2O	3846 / 30 , 3731 / 86	3684 / 31 , 3603 / 86
1 H2O / MgO(001)	3768 / 103 , 3321 / 67	3672 / 108 , 3182 / 67
2 H2O / MgO(001)	3753 / 104 , 3618 / 245 3378 / 242 , 3126 / 122	3654 / 106 , 3481 / 270 3182 / 228 , 2947 / 138
H2O-MgO(011)	3805 / 102 , 3584 / 114	3701 / 106 , 3397 / 112
H2O-MgO(112)	3816 / 125 , 3696 / 68	3724 / 130 , 3603 / 70
Mg(OH)2, brucite	3805 / 459	3676 / 455

Table: Raman frequencies (in cm^{-1}) /intensities (in Å4 amu^{-1}) of water, brucite and H2O on MgO

In the following figure, the calculated Raman spectra corresponding to the dissociation of H2O on the reactive MgO surfaces (in red) and of brucite (black square) fitted to the experimental largest intensity of Figure (a) seem to be in a relative good agreement (except H2O/MgO(011) at ~ 3400 cm-1) with experiment. It shows that intermediate species resulting from the dissociation of adsorbed water on MgO appear before formation of brucite.

ISSN: 0067-3064

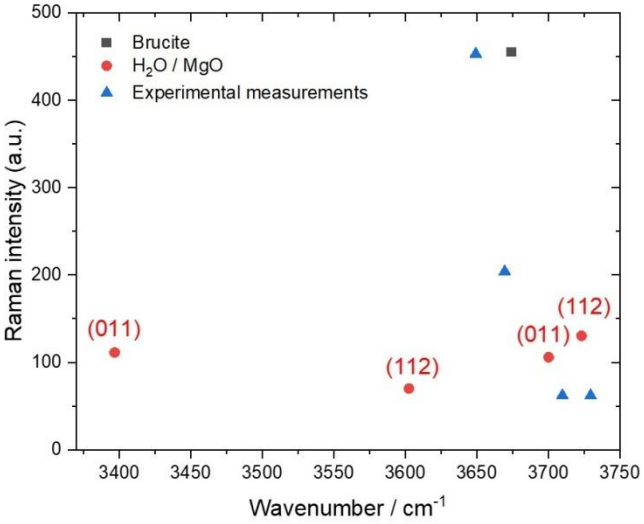

References:

[1] Crystals 2023, 13, 1153. 10.3390/cryst13081153
[2] Journal of Chemical Theory and Computation 2020 16 (5), 3343-3351, 10.1021/acs.jctc.9b01061
[3] J. Chem. Phys. 152, 204111 (2020); 10.1063/5.0004892
[4] J. Chem. Phys. 139, 164101 (2013); 10.1063/1.4824442 and 164102 (2013); 10.1063/1.4824443

ISSN: 0067-3064

Crystal23: a modern tool for ab initio solid state chemistry & physics
PL10

Silvia Casassa silvia.casassa@unito.it;

www.crystal.unito.it Chemistry Department, University of Turin, Italy

Abstract: The new release of the CRYSTAL ab initio package for solid state chemistry and physics is presented. First, the theoretical background is shortly recovered to allow for a better understanding of the limitations and peculiarity of the code [1]. Then, some features are discussed with reference to some applications of both fundamental and technological interest. In particular:

- the massive parallel implementation of the code that allows for the modeling of realistic systems [2];
- the possibility to compute some electron transport properties and derive the thermo-electric performance of several materials (InGaN and Half-Heusler alloys, nanotubes, etc..) [3];
- the new extension of the topological analysis of the charge density to f− and g−type basis functions which opens the way to the study of lanthanide and ac-tinide compounds [4];
- the new visual tool which allows to easily classified the chemical interactions and to design migration paths inside materials [5];
- the incoming Born-Oppenheimer molecular dynamics algorithms[6].

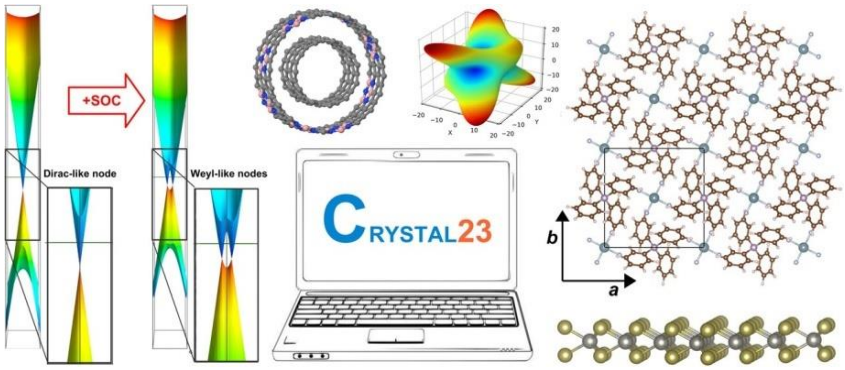

ISSN: 0067-3064

References :

[1] A. Erba, J. K. Desmarais, S. Casassa, B. Civalleri, L. Don, I. J. Bush, B. Searle, L. Maschio, L.-E. Daga, A. Cossard, C. Ribaldone, E. Ascrizzi, N. L. Marana, J.-P. Flament, B. Kirtman. J. Chem. Theory Comput., (2023), https://doi.org/10.1021/acs.jctc.2c00958

[2] S. Casassa, A. Erba, J. Baima, R. Orlando, J. Comp. Chem. 36, 1940 (2015).

[3] H. C. Aroussi, N. L. Marana, F. Hamdache, R. Houaria, S. Bahlouli and S. Casassa, J. Phys. Chem. Solids 154, 110047 (2021).

[4] A. Cossard, J.K. Desmarais, S. Casassa, C. Gatti and A. Erba, J. Phys. Chem. Lett. 12, 1862 (2021).

[5] J. F. Silva, G. S. L. Fabris, J. R. Sambrano, A. R. Albuquerque, A. S. Maya, J. Chem. Inf. Model. 63, 1999 (2023).

[6] C. Ribaldone and S. Casassa, J. Chem. Theory Comput., submitted.

ISSN: 0067-3064

Structural and magnetic properties of nanostructures
PL 11

J.M. Greneche

Institut des Molécules et Matériaux du Mans, UMR CNRS 6283, Le Mans Université
72085 Le Mans Cedex, France
jean-marc.greneche@univ-lemans.fr

Abstract:
Over the last four decades, a great deal of effort has been devoted to developing and studying of the physical properties of nanostructures. The first important stage involves synthesis in order to obtain well-controlled and reproducible systems, including nanoparticles, multilayers, and nanostructured materials, with the aim of controlling their chemical characteristics, i.e. size, morphology and chemical composition of crystalline grains, the thickness of the grain boundaries and the quality of interfaces, respectively. The second step focuses on their structural and physical properties that requirein-depth characterizations using experimental approaches based on different techniques.
This fundamental approach is necessary to better understand the relationship between the morphology of nanostructures and their physical properties.
We give some examples to illustrate this strategy using results obtained by Mössbauer spectrometry, a local probe technique well suited to the study of these complex materials.

ISSN: 0067-3064

ORAL

ISSN: 0067-3064

Magnetic properties of the site-diluted spin-1 Blume Capel multiyer system: A Monte Carlo simulation study
OL 01

Amel Benmansour[1,2], Smaine Bekhechi[2] , Nabil Badr-Eddine Brahmi[2]

[1]Department of physics, Faculty of Sciences, Laboratory of Automatics, University of Tlemcen, BP119, Algeria
[2]Department of physics, Faculty of Sciences, Laboratory of Theoretical Physics, University of Tlemcen, BP119, Algeria.

Abstract: We used standard Monte Carlo simulations to investigate the magnetic properties of a spin-1 Ising multilayer system composed of two non-equivalent planes A and B, where B being site-diluted. Antiferromagnetic interlayer and ferromagnetic intralayer spin couplings have been considered. Our calculations indicated the occurrence of a compensation phenomenon where the magnetization vanishes before the critical temperature. The effects of various model parameters on the system magnetic properties have been examined in detail and presented in the form of phase diagrams. The results bore some resemblance with those reported in some previous works on systems with or without site-dilution. Depending on values of the spin concentration parameter P the model displayed first- and second-order phase boundaries with the existence of a tricritical point.

ISSN: 0067-3064

Monitoring the microstructural changes during quenching of X70 steel using magnetic Barkhausen noise method OL02

Hocine NEBAIR[1,2], Sami ZIDELMEL[3], Bachir HELIFA[1], Samir BENSAID[4], Ibn Khaldoun LEFKAIER[1]

[1]Laboratoire de Physique des Matériaux, Université de Laghouat, B.P. 37G route de Ghardaia 03000 Laghouat, Algeria
helifa@yahoo.fr; lefkaierk@gmail.com
[2]Ecole Normale Supérieure de Laghouat, BP 4033, Laghouat, Algeria
h.nebair@ens-lagh.dz
[3]Laboratoire de Génie des Procèdes, Laghouat, Algeria
s.zidelmel@lagh-univ.dz
[4]Laboratoire des Matériaux et du Développement Durable, Université de Bouira , Bouira, Algeria
s.bensaid@univ-bouira.dz

Abstract: This research aims to follow the microstructural changes during the quenching of X70 steel by magnetic Barkhausen noise (MBN). In order to monitor the relationship between mechanical properties and micromagnetic parameters, a direct quench (DQ) treatment is used at the inter-critical annealing (IAT) temperature ranges applied to the samples from 740°C to 820°C. MBNs were performed using the MikroMach instrument. Hardness measurements and microstructure examinations were carried out using a durometer and optical microscopy. The experimental results show that the DQ treatment revealed a hard martensite distributed in a ductile ferrite matrix. Martensite volume fraction (MVF) and hardness increase with increasing IAT. These treatments make it possible to obtain the highest hardness in DQ treatment at higher temperature. Indeed, the MBN method proved to be very sensitive to changes in microstructure and MVF morphologies.

Keywords: Heat treatment; Microstructure Morphology; Barkhausen magnetic noise; Hardness measurement.

ISSN: 0067-3064

Synthesis and Characterization of Magnetic Phosphides Powders Using an Anisotropic Reitveld Model Accounting OL 03

Samira Berrebib[1], Wassila Tebib[1], Sihem Benaissa1, Meriem Kettache[1], Douniazed Lamrous[2,3]

[1] Materials Physico-Chemistry Laboratory, Science and Technology Faculty, Chadli Bendjedid - El Tarf University, P.B. 73, El Tarf 36000, Algeria.
[2] Université Chadli Bendjeddid, Faculté des Sciences et de la Technologie, Département de Physique, El tarf.
[3] Laboratoire LM2S, Université Badji Mokhtar, Faculté des Sciences, Département de Physique, Annaba.

Abstract: Solid state reactions path have been studied in a phosphides powders mixture milled for 1 h in a planetary Retsch PM400 mill. The characterization of the obtained powders was carried out by X ray diffraction (XRD) in a Brucker D8 diffractometer and a surface probe using SEM-EDX FEI Quanta 250. The structural, microstructural and mechanical properties of the product studies, using an anisotropic Rietveld model accounting, reveal the formation of nanometric (20 nm) phosphides phases (75 %) in addition to 25 % of iron solid solution with 51 nm and Poisson coefficient equal to 0.15. SEM study exhibits different morphologies to a size distribution of the nodules with a large quantity (48-58 %) of fine nodules below 2 µm. The average size of nodules varies between 2 and 2.6 µm.

Keywords: Phosphides, SEM, XRD, Rietveld, MAUD.

ISSN: 0067-3064

Theoretical study of Cr substitution on tetragonal $BaTiO_3$ electrical and magnetic properties
OL 04

B. BELMABROUK[1]* and N. ILES[1]
[1] Laboratoire de physique des couches minces et matériaux pour l'électronique (LPCMME), Université Oran 1 Ahmed Ben Bella, Oran, Algérie
* mail adress : bouchrabelmabrouk1996@gmail.com

Abstract:
The latest research are focusing on materials that exhibit ferroelectric and ferromagnetic behavior simultaneously. These materials, known as magnetoelectrics or multiferroics are promising materials for data storage[1]. Barium titanate, $BaTiO_3$, was the first ferroelectric and piezoelectric ceramic well studied among the wide range of ABO_3 [2]. Other properties can be induced in $BaTiO_3$ by doping with a transition metal. Among the doping elements, chromium stood out as a promising transition metal for improving the properties of barium titanate for many applications [3]. In view of the information gathered from previous articles and various works that were carried out on the substitution of the Ti site by a transition metal, we decided in this study to focus on the impact of Cr introduction on the electrical and magnetic properties of BTO. We demonstrate the introduction of 0.5 of Cr in BTO.The density functional theory (DFT) as implanted in ABINIT and WIEN2K code is employed to compute structural, electronic and magnetic properties of $BaCrO_3$, $BaTiO_3$ and $BaTi_{0.5}Cr_{0.5}O_3$. The spin-polarized generalized gradient approximations (GGA) as well as the Hubbard corrective term (GGA+U) were used. The structural parameters of tetragonal (P4mm) $BaTiO_3$ labeled BTO and cubic ($Pm\bar{3}m$) $BaCrO_3$ labeled BCO bulk structures have been optimized to be close to the experimental values. The forces were relaxed until a criterion of convergence of 10^{-4} eV/Å was reached. The calculations were performed using a 10x10x10 Monkhorst-Pack mesh and cut-off energy of 35 Ha. The obtained lattice parameter for P4mm $BaTiO_3$ was then used to construct a 2x2x2 supercell that contains 40 atoms with 4 Cr atoms substituted. The forces were also relaxed until a convergence criterion of 10^{-4} eV/Å. A 4x4x4 Monkhorst-Pack mesh was used to perform the calculations on the supercell. The Hubbard term used for supercell were U= 4eV with J = 0.4eV (10%). Berry Phase approach was used to calculate the spontaneous polarization of our systems.The tetragonal $BaTiO_3$ calculated lattice parameter is equal to the experimental result[4]. The bulk modulus is overestimated by 7% compared to the experimental value reported in ref. [4]. The calculated spontenous polarization is about 2% inferiour to the experimental value. In $BaCrO_3$ case, the resuts were obtained for cubic BCO in FM phase. The calculated structural parameters are compared with other theoretical results. The comparison with experimlental study remains weak due to the lack of bibliographical references and experimental work

ISSN: 0067-3064

carried out on $BaCrO_3$. The optimized lattice parameter is 1.3% higher than the calculated value mentionned in ref.[5]. However, the bulk modulus is 28% lower than the other theoretical study. For the other structural parameters, the values are approximately the same. For the $BaTi_{0.5}Cr_{0.5}O_3$ supercell, we found that the lattice parameters and the bulk modulus remained relatively close to the initial parameters.
The Total and Partial Density of State of BTO exhibited a dielectric behavior with a band gap of 1.9 eV. The valence band was constructed with oxygen p states especially near Fermi level. On the other hand, Titanium d states occupied the conduction band. Hybridization between the p-states of oxygen and the d-states of titanium was weak and took place in an energy range -6 eV to Fermi level.The total density of state and the partial density of states of BCO showed that for the spin-up channel has a metallic character. Though, spin-down channel exhibited a semi-conducting behavior with a band gap of 2.79 eV. Consequently, our compound was considered half-metallic ferromagnetic. The total density of state and partial density of state of FM $BaTi_{0.5}Cr_{0.5}O_3$ compound had an insulating character with a distinguished band gap. There was an occupied localized state in the band gap that was attributed to d states of Chromium. [3]Chromium and Titanium d states composed majorly the conduction band in the large energy range from 2 eV to 7 eV. The calculated spin moment per Cr atom is 1.93 μ_B.
In conclusion, by using the GGA+ U PBE, we predict the perovskite $BaTiO_3$, $BaCrO_3$ and $BaTi_{0.5}Cr_{0.5}O_3$ crystal may be a candidate for spintronics applications due to its half-metallic ferromagnetic character. This is a significant result from a technological point for polycrystalline single phase multiferroic room temperature materials.

Keywords: Barium Titanate, Substitution, Perovskite, First Principle Calculation, Multiferroics.

References:

[1] H. Liu et X. Yang, « A brief review on perovskite multiferroics », *Ferroelectrics*, vol. 507, n° 1, p. 69-85, janv. 2017, doi: 10.1080/00150193.2017.1283171.
[2] V. Buscaglia, M. T. Buscaglia, et G. Canu, « BaTiO3-Based Ceramics: Fundamentals, Properties and Applications », in *Encyclopedia of Materials: Technical Ceramics and Glasses*, Elsevier, 2021, p. 311-344. doi: 10.1016/B978-0-12-803581-8.12132-0.
[3] D. Issam, M. Achehboune, I. Boukhoubza, R. Hatel, Z. El Adnani, A. Rezzouk, « Investigation of the crystal structure, electronic and optical properties of Cr-doped BaTiO3 on the Ti site using first principles calculations», Journal of Physics and Chemistry of Solids 175 (2023), 111209.
[4] S. Aoyagi, Y. Kuroiwa, A. Sawada, I. Yamashita, et T. Atake, « Composite Structure of BaTiO 3 Nanoparticle Investigated by SR X-Ray Diffraction », *J. Phys. Soc. Jpn.*, vol. 71, n° 5, p. 1218-1221, mai 2002, doi: 10.1143/JPSJ.71.1218.[5] N. A. Noor, M. B. Saddique, B. Ul Haq, A. Laref, et M. Rashid, « Investigations of half-metallic ferromagnetism and thermoelectric properties of cubic XCrO3 (X = Ca,Sr,Ba)

ISSN: 0067-3064

compounds via first-principles approaches », *Phys. Lett. A*, vol. 382, nº 42-43, p. 3095-3102, oct. 2018, doi: 10.1016/j.physleta.2018.07.045.

ISSN: 0067-3064

Study of the magnetic properties of Ni-Zn-Cu ferrite materials for energy storage
OL 05

Zahi Souilah[1*] and Amina Sidi Moussa[2]

1 Centre for Development of Advanced Technologies (CDTA), City 20-08-56, Baba Hassen, Algiers, Algeria.
2 Ecole Nationale Polytechnique, 10 Rue des Frères Oudek, El Harrach, Alegria.
* Corresponding author. E-mail address: souilahzahi@gmail.com

Abstract: Homogeneous Ni-Zn-Cu ferrite particles with well-controlled electromagnetic properties can be obtained by several chemical methods. In this study, uniform Ni-Zn-Cu ferrite particles were prepared and fabricated by sol-gel method at low temperatures. Scanning electron microscope (SEM) image analyzes were used to identify the formation of Ni–Zn–Cu spinel ferrite. The results obtained by X-ray diffraction (XRD) showed that a certain amount of single-phase spinel ferrite components can be formed at temperatures below 1000°C. The microstructure of the sintered ferrite core had fine, uniform grains containing spinel ferrite magnetic domains. The initial magnetic permeability of the sintered ferrite cores at 1200 °C showed that the inductance of the fabricated ferrite cores has a greatest value, and the corresponding losses were small. Therefore, at the end, a new design was reported to improve the efficiency of solar panels for storing electrical energy.

Keywords: Soft ferrite, characteristics, microstructure, magnetic properties, energy storage.

ISSN: 0067-3064

MODELING, OPTIMIZATION AND SIMULATION OF PYROELECTRIC INFRARED DETECTOR BASED ON P(VDF-TrFE) COPOLYMER. OL 06

Mohamed BEHLOUL [1]*, Nour Eddine DERGUINI [2], Djamel KENDIL [3], Essaid BOUSBIAT [4]

[1]* Department of Physics, University of Boumerdes, Algeria
Laboratory of sensor-based integrated systems (LSIC) ENS kouba, Algiers, Algeria
Email [1] - m.behloul@univ-boumerdes.dz
Email [2] - noureddine.derguini@g.ens-kouba.dz
Email [3] - djamel.kendil@g.ens-kouba.dz
Email [4] - essaid.bousbiat@g.ens-kouba.dz

Abstract: This article presents a thermal model of the pyroelectric detector based on copolymer P(VDF TrFE). A one-dimensional of the heat equation was solved for the simulation of the response of the pyroelectric detector based on P (VDF-Tr FE). We studied the temperature, current and voltage response of the pyroelectric detector in different possible structures and arrangements and their influence either by the nature or by the thickness of the layers, these studies allowed to find an optimal response in the structure (Copo/ porous silicon) without addition of thermal insulation. Keyword: Pyroelectric, P (VDF -TrFE), Thermal model, Detector.

1. Heat Transfer Equation:
1.1. Mathematical model.
1.2. Pyroelectric detector model.
2. Simulation and optimization of pyroelectric detector:
2.1. Influence of the nature of heat insulation.
2.2. Influence of the thickness of substrate.
2.3. Influence of the nature of substrate.

References

[1] H. Zhang, W. Wang, S. Zhang, et Z. Zhao, « Semi-analytic solution of three-dimensional temperature response functions », Int. J. Heat Mass Transf., vol. 118, p. 208-222, mars 2018.
[2] A. Mahrane, M. Djafari-Rouhani, A. Najmi, et D. Esteve, « Effects of the Substrate on the Response of P (VDF-TrFE) Pyroelectric Detector », MRS Proc., vol. 299, p. 297, 1994.
[3] Derguini Noureddine, thèse de Magister « Modélisation et simulation d'un capteur infrarouge carte d'acquisition à base d'un CPLD », ENS Kouba-Algérie, Page (58-60), 2007.

ISSN: 0067-3064

Tunable electric polarization in ultrathin half-metallic [BaFeO3]m/[BaTiO3]n superlattices : an ab initio study OL 07

N. Iles[1], A. Bezzalla[2]

[1] Laboratoire de Physique des Couches Minces et Matériaux pour l'Electronique, Université Oran 1 Ahmed Ben Bella, Oran, Algérie.
[2] Laboratoire de Physique des Matériaux et des Fluides, Faculté de Physique, Université des Sciences et de la Technologie d'Oran, USTO-MB, Oran, BP1505 Oran El Mnaouer, Algérie. Email : n_ilesdz@yahoo.fr

Abstract: The most challenging feature in the progress of material science nowadays is controlling physical properties with respect to material size. The technology of electronic devices is based on the integration of multifunctional materials at a nanoscopic level. Because most ABO3 perovskites offer a large spectrum of physical properties such as electric polarization and magnetization (ferroelectricity and ferromagnetism), these ternary oxides are potential candidates as multifunctional materials for new miniaturized devices. Particular examples include, ferroelectric memories, transducers and new storage devices based on spintronics [1-3]. In this theoretical study, a fundamental analysis from ab initio calculations is performed to understand the competition between ferroelectricity and ferromagnetism ultrathin [BaFeO3]m/[BaTiO3]n superlattices with varying periodicities m/n from 1 to 4. According to our finding, the electronic structure analysis revealed a half-metallic character in all m/n systems. A clear dependence between the minority gap and m/n periodicities was observed in the DOS plots. Two categories of superlattices were distinguished from the electric polarization calculations. The first includes 1/1, 2/3, 3/2, and 4/1 with a polarization comparable to the bulk value of BaTiO3. The second category includes the 2/1, 1/2, 1/3, 3/1, and 1/4 systems with polarization amplitudes of 30% larger than the BaTiO3 bulk value. All m/n superlattices remained ferromagnetic this behavior is in accordance of experiment [4]. These findings paved the way to new promising applications of those ultrathin superlattices with tunable electronic properties. KEY WORDS Superlattices, [BaFeO3]m/[BaTiO3]n, electric polarization, half-metallic.

References

[1] Ortega N, Kumar A, Scott J F and Katiyar R S 2015 J. Phys.: Condens. Matter 27 504002
[2] Wu H, Xia W, Xue P and Zhu X 2017 Ferroelectrics 518 127
[3] Sun B, Zhou G, Sun L, Zhao H, Chen Y, Yang F, Zhao Y and Song Q 2021 Nanoscale Horiz. 6 939

ISSN: 0067-3064

[4] Fukatani R, Yokota H, Ogura S, Uesu Y, Bartasyte A, Fukunaga M, Noda Y 2012 Jpn. J Appl. Phys. 51 09LB01

ISSN: 0067-3064

Transverse photons Dispersion laws at Next-to-Leading Order in Hot SQED
OL 08

Karima Bouakaz[1]*, Amel Youcefi[1] and Abdessamad Abada[2]

[1]Department of Physics, Laboratoire de Physique des Particules et de Physique Statistique, Ecole Normale Supérieure, BP 92 Vieux-Kouba, Algiers
[2] Department of Physics, United Arab Emirates University, P. O. B. 17551, Al Ain, United Arab Emirates
E-mail : karima.bouakaz@g.ens-kouba.dz

Abstract: The difficulties encontred in the infrared sector within the gluon and quark damping rates calculated using imaginary time formalism [1, 2, 3, 4, 5, 6, 7]. A similar observation has been done in the context of scalar electrodynamics [8]. To look further into the infrared behavior, we propose to calculate the next-to-leading order dispersion relations for slow-moving Transverse Photons at high temperature scalar quantum electrodynamics (Scalar QED), using the real time formalism (RTF) in physical representation. We derive the analytic expressions of hard thermal loop (HTL) contributions to propagators and vertices to determine the expressions of the effective propagators and vertices in RTF that contribute to the complete next-to leading order contribution of retarded transverse photons self-energy. The real part and the opposite of the imaginary part of the retarded transverse photons self-energy are related to the next-to-leading order contributions of energy and damping rate respectively.

Keywords: Hard thermal loop, Hot Scalar QED, NLO Computations, Soft Transverse photons energy, damping rate.

References

[1]. A. Abada, O. Azi and K. Benchallal, Phys. Lett.B425, 158-164 (1998).
[2]. A. Abada, O. Azi, Phys. Lett.B463, 117-125 (1999).
[3]. A. Abada, K. Bouakaz and O. Azi, Phys. Scr. 74, 77 103 (2006).
[4]. A. Abada, K. Bouakaz and N. Daira-Aifa, Eur. Phys. J.C18, 765-777 (2001).
[5]. A. Abada, N. Daira Aifa and K. Bouakaz, Int.J.Mod.Phys.A21, 5317-5332 (2006).
[6]. K. Bouakaz, A. Abada, AIP Conf.Proc.1006:150-153, (2008).
[7]. A. Abada, K. Bouakaz and D. Deghiche, Mod.Phys.Lett.A22, 903-914 (2007).
[8]. A. Abada and K. Bouakaz, JHEP01, 161-187 (2006).

ISSN: 0067-3064

Electron Transport Analysis For GaSb MOSFET n+nn+ Channel
OL 09

Y.LAIDOUNI [a*], C. SAYAH [a], B. BOUAZZA[b], S. FEROUANI [c]

[a]Smart Structures Laboratory (SSL), Department of Electronic and Telecommunications, University Belhadj BOUCHAIB of Ain Témouchent.
Po Box 284, 46000, Algeria.
Authors[a] E-mail: *yousfia.laidouni@univ-temouchent.edu.dz*
chou28dz@gmail.com

Abstract: Velocity is a crucial factor in defining the electrical properties and performance of MOSFETs. The shrinking of transistor size from submicron to nanometer domain makes the calculation and measurement of this physical quantity increasingly problematic. Through this study, we try to determine how the velocity evolves with temperature. We conducted electron transport calculations on a 45-110-45 nm MOSFET n+-n-n+ GaSb channel structure using a three-valley model. Our analysis employed a bipolar Monte Carlo simulator coupled with the Poisson solver, including ionized impurity, polar, non-polar optical phonon, and acoustic deformation potential. We present carrier transport phenomena for a two-dimensional submicron structure and discuss the effect of temperature on the dispersion rate for strong values ranging from 77 K to 600 K. Our results showed that increasing temperature leads to a higher dispersion rate, causing a decrease in carrier velocity and the maximum drift velocity is reduced.

Keywords : Ensemble Monte Carlo, III-V compounds, Poisson equation, particle dynamics.

Introduction: We employed a 2D self-consistent Monte Carlo transport model to simulate a temperature dependencies on electron transport in an n+-n-n+ device with a symmetric profile. The central region of the device has a width of 0.11 μm, maintaining a uniform hosting concentration of $4x10^{23}$ cm^{-3}. Both the emitter and collector regions feature symmetrical rectangular shapes, each measuring 45 nm in width, and possess uniform doping with a specific concentration of 2×10^{21} cm^{-3}.

Self-Consistent Monte-Carlo Model: The Monte Carlo method has found extensive application across diverse scientific domains, underscoring its robustness and reliability. Nevertheless, it is imperative to acknowledge that the efficacy of this method is contingent upon the inherent particle nature of electrons within submicron devices[1].

ISSN: 0067-3064

In our study, we explore the effects of temperature variation upon the electron transport within an n+-n-n+ structure comprised of GaSb. To achieve this investigation, we employed an Ensemble Monte Carlo (EMC) technique, operating in conjunction with the Poisson equation, represented as:

$$\nabla^2 \varphi = \frac{\rho}{\varepsilon} \qquad (1)$$

The EMC method computes particle dynamics within brief time intervals, followed by the solution of the Poisson equation at the end of each interval to ascertain the potential distribution [2].

The methodology involves generating random free-flight times for individual particles by specifying the type of diffusion occurring at the end of each flight, adjusting the particle's energy and momentum post-diffusion, and subsequently iterating the process for the next free flight. Monitoring particle trajectories at various points in the simulation enables the statistical estimation of crucial physical parameters. Illustrative instances encompass the determination of the average drift velocity under an applied electric field and the computation of the average energy of particles, thereby offering valuable insights into the dynamic behavior of the system [3].

In the implementation phase, a three-valley model is utilized for the conduction band, integrating ionized impurity, polar and non-polar optical phonon, and acoustic deformation potential [4]. Boundary conditions, especially crucial in submicron devices, are meticulously defined due to the substantial impact of contact properties on the overall behavior of the device.

Conclusion: Our study focused on the energy and velocity of electrons with increasing bias voltage and lattice temperature. Results indicate pronounced electron accumulation near the anode in the active region. Elevating the temperature to 600 K reduces the maximum drift velocity.

Electrons injected from the cathode exhibit quasi-ballistic travel initially, but significant transfer to upper satellite valleys occurs near the anode, leading to reduced average electron velocity in that region. At low temperatures and high bias voltages, backscattering effects become prominent, causing electron accumulation near the anode.

References :

[1] J. M. Sellier, J. E. Fonseca, et G. Klimeck, « Archimedes, the free Monte Carlo simulator: A GNU package for submicron semiconductor devices on nanoHUB », in *2012 15th International Workshop on Computational Electronics*, Madison, WI, USA: IEEE, mai 2012, p. 1-4. doi: 10.1109/IWCE.2012.6242861.

[2] C. SAYAH « Thése de doctorat_Etudes-des-Effets-du-Champ-Electromagnétique-sur-les-Propriétés-des-Composés-III-V-par-la-Méthode-de-Monte-Carlo-et-l'Equation-de-Poisson-Couplée.pdf» .

[3] A. Guen-Bouazza, C. Sayah, B. Bouazza, et N. E. Chabane-Sari, « Steady-State and Transient Electron Transport within Bulk InAs, InP and GaAs: An Updated

ISSN: 0067-3064

Semiclassical Three-Valley Monte Carlo Simulation Analysis », *JMP*, vol. 04, n° 05, p. 616-621, 2013, doi: 10.4236/jmp.2013.45089.
[4] C. Sayah, B. Bouazza, A. Guen-Bouazza, et N. E. Chabane-Sari, « Simulation of Electron Transport in GaN Based MESFET Using Monte Carlo Method », *World Applied Programming*.

ISSN: 0067-3064

Mixed convection heat transfer by nanofluid enhancement [ZnO-water] in a cavity with partial sides heating OL 10

M. BOUNIB [1], A. BOUHEZZA[2], A. KHELIFA [3], H. MEZAACHE[4]

[1]Department of Physics, Sciences Faculty, 20th August 1955-Skikda University, Skikda, 21000, Algeria
2Department of Technology, Technology Faculty, 20th August 1955-Skikda University, Skikda 21000, Algeria.
3Unité de Recherche Appliquée en Energies Renouvelables, URAER, Centre Développement des Energies Renouvelables, CDER, 47133, Ghardaïa, Alegria.
4 Laboratory of Soil and Hydraulic, Department of Hydraulic, Faculty of Technology, Badji Mokhtar Annaba University, Annaba, Algeria.

Abstract: In This paper presents the results of a two-dimensional numerical study on the flow of nanofluids in a square cavity under mixed convection conditions. The cavity is heated by two heat sources located on the sidewalls, while the other walls are kept at a moderate temperature. The nanofluid used in the study is an incompressible Newtonian fluid with stable thermo physical properties, and Boussinesq's assumption was adopted. The governing equation for this phenomenon has been solved using Fluent, which is based on the finite volume method. The study investigates the hydrodynamic aspects of flow with respect to the concentration and diameter of nanoparticles, considering various parameters such as nanoparticle concentration ($0 \leq \Phi \leq 0.06$), Richardson number (Ri = 1), and nanoparticle diameter (29 nm, 49 nm, and 69 nm).

Introduction: Heat transfer is a fundamental engineering topic in many industrial fields, where heat plays a primary role as a critical process in industry and technology. Although it appears in the forms of radiation, conduction and convection, the latter is more targeted in some special areas: cooling of processors, electronic components, radiators, heat exchangers, and so on. In recent decades, researchers have been drawn to numerical simulations to gain a better understanding of the heat transfer process. Suriya Uma Devi et al. [1] numerically investigated the natural convection of the nanofluid. Their results show that the presence of an external magnetic field, the heat transfer rate of the hybrid nanofluid (Cu-Al2O3/water) is faster than that of the nanofluid (Copper / water). Sherani et al. [2] reported on a numerical investigation of the transient mixed convection of a nanofluid in a square cavity with several cylinders rotating in harmonic motion. They Notice that the rotation of the cylinders with harmonic motion has an effect near the moving wall. Mahmoodi et al. [3] numerically studied the natural convection in C-shaped packages. The authors concluded that raising the rate of heat transfer requires increased Rayleigh numbers and particle size

ISSN: 0067-3064

ratio, in addition to narrow box dimensions. Suresh et al. [4] conducted an experimental study, where their results showed that the thermal conductivity and viscosity of the prepared hybrid nanofluid increased with the volumetric concentration of nanoparticles

References

[1] S. Suriya Uma Devi and S.P. Anjali Devi, "Numerical investigation of three-dimensional hybrid Cu–Al2O3/water nanofluid flow over a stretching sheet with effecting Lorentz force subject to Newtonian heating", Canadian Journal of Physics 94 (2016) 490–496. Doi: https://doi.org/10.1139/cjp-2015-0799.

[2] N. Shirani, D. Toghraie, M. Zarringhalam and M. Afrand, "Numerical simulation of transient mixed convection of water–Cu nanofluid in a square cavity with multiple rotating cylinders. Journal of Thermal Analysis and Calorimetry. Doi: https://doi.org/10.1007/s10973-020-09379-3.International Journal of Heat and Mass Transfer 119 (2018) 939-961. Doi: https://doi.org/10.1016/j.ijheatmasstransfer. 2017.11.136.

[3] M. Mahmoodi, S. M. Hashemi, "Numerical 10.1016/j.ijthermalsci.2012.01.002. study of natural convection of a nanofluid in C-shaped enclosures", International Journal of Thermal Sciences. Doi: 10.1016/j.ijthermalsci. 2012.01.002.

[4] A.S. Suresh, K.P. Venkitaraj, P. Selvakumar, M. Chandrasekar, "Synthesis of Al2O3–Cu/water hybrid nanofluids using two step method and its thermo physical properties», Colloids and Surfaces A: Physicochem. Eng. Aspects 388 (2011) 41–48. Doi : 10.1016/j.colsurfa.2011.08.005.

[5] Soufi E., H., (2013). Application des Nanofluide pour le réfroidissement : étude d'un cas d'une géométrie simple, Thèse de Master en Génie Chimique, Université Kasdi Merbahd'Ougla.

[6] [A. Baïri and N. Laraqi, "Natural convective heat transfer in a hemispherical cavity filled with ZnO H2O nanofluid saturated porous medium", International Journal of Modern Physics 29 (2018). Doi: https://doi.org/10.1142/S0129183118500973

ISSN: 0067-3064

A comparative study of LiH, O2 and GaCl energies under a three-dimensional hyperbolic potential
OL 11

A. Haddouche [a,b*], and R. Yekkenb [b]

[a] Ecole Nationale Supérieure des Travaux Publics, BP 32 Rue Sidi Garidi, 16006, Kouba, Alger, Algeria.
[b] Laboratoire de Physique Théorique et de didactique, Faculté de Physique, USTHB. BP 32, Al-Alia, 16111, Bab Ezzouar, Alger, Algeria.
a.haddouche@enstp.edu.dz

Abstract: In this study, we provide a solution of Schrödinger equation with the three-dimensional hyperbolic Pöschl-Teller potential [1]. To this end, we considered three methods: Quantum supersymmetry, Nikiforov-Uvarov and numerical method. On the one hand, we compared energies that are obtained, taking the numerical method's results as a reference; on the other hand, we extended the study by inserting linear energy dependence into the potential to see how this dependence affects the results and the methods themselves.

Theoretical overview:

1. Quantum supersymmetry: This method [2] is based on the factorization of the Hamiltonian, the latter provides us two scaling operators and whose successive application allows us to determine the energy spectrum and the eigenfunctions thanks to the shape invariance property. We recall that, the introduction of energy dependence [3] induces some theoretical modifications on the method as well as to the usual rules of quantum mechanics [4] (scalar product and so on…).

2. Nikiforov-Uvarov (NU) method: It constitutes a polynomial method developed by Nikiforov and Uvarov [5]. The first step of this method is the transformation of the Schrödinger stationary equation to a generalized hypergeometric one. This method is based on soluting second order linear differential equations with the help of special orthogonal functions. The solution of Schrödinger equation with energy dependent potential by this method is, as we will see, straightforward.

3. Numerical method: our numerical solution [6] is based on the fourth order Runge-Kutta method. It has been extended to encompass energy-dependent wave equations.

Results and discussion: Wave functions and energy spectra of diatomic molecules are derived by using the three mentioned methods. Application is done to LiH, O2 and GaCl molecules. These latter diatomic molecules have different reduced masses. The results show the effects of mass difference on the exactness and the effect of energy dependence.

ISSN: 0067-3064

Conclusion:

a- Both SQM and NU methods give satisfyingly exact and analytic results.
b- Energy-dependence affects the wave functions as well as the energy eigenvalues.
c- Lower reduced-mass molecules are in better approximation in their results.

References

[1] G. Pöschl, E. Teller, Z. Phys. 83, 143 (1933).
[2] F. Cooper, A. Khare, U. Sukhatme, Phys. Rep. 251, 267 (1995).
[3] R. J. Lombard, J. Mareš, and C. Volpe. Journal of Physics G : Nuclear and Particle Physics,34(9) :1879 (2007)
[4] R. Yekken, M. Lassaut, and R. J. Lombard, Annals of Physics, 338 :195 – 206, (2013).
[5] A. F. Nikiforov, V. B. Uvarov, Birkh a ¨ user, Basel (1988).
[6] W. Lucha, F.F. Schöberl, Int. J. Mod. Phys. C, 10, 607 (1999).

ISSN: 0067-3064

KMC simulation of nano PSi formation from p-type Si(100) using electrochemical etching in HF acid solution: initial stages of etching studies
OL 12

S. Bouchendouka(a), Y. Belaroussi(b), A. Ali Messaoud(a), A. Boumeddiene (a), D. Maafri(b), B. Zatout(b), F. Bouamra(a)

(a) LPCMIA, Sciences Faculty, Saad Dahlab University - Blida 1
(b)Centre de Développement des Technologies Avancées, Baba Hassen Alger

Abstract: This paper presents kinetic Monte-Carlo simulation (KMCS) of porous silicon structures formation from p-type Si(100), using electrochemical anodization in HF acid solution, with respect to the experimental conditions. The basic principle of a KMC simulation is to generate a Poisson process of stochastic events with a hierarchy of rate constants, in such a way that, events with higher rates are more probable to occur than slower ones. In our applying KMCS to electrochemical system, the fundamental challenges is the treatment of charge transfer arising from the formation of Si-F bonds in contact to pure silicon at the interface HF/ p-type Si(100), which affect the initial stage of formation of porous surface. The results obtained is consistent with available experimental data [1-2].

Keywords: nanoporous silicon (nano PSi), electrochemical etching , KMC simulation, hydrofluoric acid etching.

References

[1] Y. Belaroussi , M. Rack , A.A. Saadi , G. Scheenc, M.T. Belaroussi, M. Trabelsi, J.-P. Raskin , High quality silicon-based substrates for microwave and millimeter wave passive circuits, Solid-State Electronics 135 (2017) 78–84.
[2] Y.Belaroussi, M. T. Belaroussi, G. Scheen 2, K, K. Ben Ali, J., J.-P. Raskin , Porous Si substrate: a high-quality and cheap substrate for advanced RF applications, Nano Studies, 2013, 8, 45-52.
[3] V. M. Donnelly, Review Article: Reactions of fluorine atoms with silicon, revisited, again, Journal of Vacuum Science & Technology A 35, 05C202 (2017).

ISSN: 0067-3064

Synthesis and characterization of LaAl0.9Fe0.1O3 perovskite: Application to oxygen photo-production OL 13

Hamza MEDJADJI[a]*, Ali BOULAHOUACHE [a, b], Khaled DERKAOUI[c], Mohamed TRARI[d], Nassima SALHI [a,b]

[a] Laboratoire LCPMM, Faculté des Sciences, Université BLIDA1, B.P 270, Route de Soumaa, BLIDA, Algérie.
[b] Laboratoire de Chimie du Gaz Naturel, Faculté de Chimie, USTHB, BP32, El-Alia, 16111 Bab Ezzouar, Alger, Algérie.
[c] Research Center On Semiconductors Technology for Energetic, CRTSE-TESE - 02, Bd. Dr. Frantz Fanon, 7 Merveilles, Box 140, 16038 Algiers, Algeria.
[d] Laboratoire de Stockage et valorization de l'énergie renouvelable, Faculté de Chimie, USTHB, BP32, El-Alia, 16111 Bab Ezzouar, Alger, Algérie.
hamzamedjadji1990@gmail.com

Abstract: Perovskite materials with the general formula ABO3, where A and B represent cations of different sizes, have attracted significant attention in pollution reduction and environmental remediation processes. These materials possess unique properties, including ion exchange, absorption, catalytic potential, high surface-to-volume ratio, porosity, good thermal stability, and redox properties [2,3]. Notably, the presence of lanthanum in position A within the perovskite structure leads to a decrease in the electro affinity and an increase in the band bending at the solid/electrolyte interface, resulting in a complete separation of electron/hole (e-/h+) pairs [4]. In the present work, LaAl0.9Fe0.1O3 perovskite photocatalyst where iron partially substitutes aluminum, was synthesized using the sol-gel method, where nitrate precursor salts were used as raw materials and propionic acid acted as a complexing agent. Various techniques, including thermal analysis (TG-ATD), X-ray Diffraction (XRD), Fourier Transform Infrared Spectroscopy (FT-IR), UV visible Spectrophotometry, Scanning Electron Microscopy (SEM-EDX), X-ray photoelectron spectroscopy (XPS) with C1s as a reference and electrochemical analyses were employed for the characterization. The XRD pattern confirmed the formation of LaAl0.9Fe0.1O3 with a Rhombohedral structure with R-3c space group and an average crystallite size of 36 nm, making this perovskite a nanomaterial. SEM analysis showed a heterogeneous surface distribution with agglomerated particles of different sizes. SEM-EDX analysis further validated the presence of La, Al, Fe, and O elements without any impurities, indicating phase purity. The XPS spectra of LaAl0.9Fe0.1O3 revealed the presence of La 3+, Al 3+ and the lower binding energy indicated the presence of Fe2+ Additionally, the presence of two O 1s photolines corresponds to two different oxygen species. The direct optical band gap Eg (2.28 eV) was determined from the diffuse reflectance. Furthermore, X-ray Photoelectron Spectroscopy (XPS)

ISSN: 0067-3064

analysis indicated a valence band energy of 3.25 eV. The FT-IR analysis revealed characteristic bands of LaAl0.9Fe0.1O3 at 652 cm-1 and 420 cm-1, attributed to Fe-O bending and deformation modes, respectively. Mott-Schottky (C-2-E) measurements confirmed n-type behavior, with a flat-band potential of 0.38 VSCE. The perovskite LaAl0.9Fe0.1O3 was tested for oxygen production under visible light irradiation. An evolution rate of 91.59 µmol of O2 is obtained in NaOH solution (0.1 M).

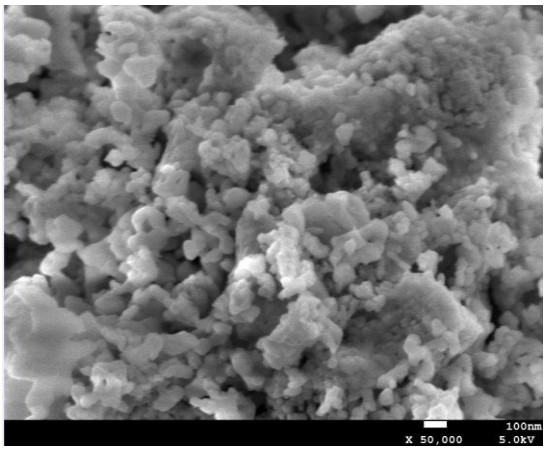

Fig. : SEM micrographs of LaAl0.9Fe0.1O3

Keywords: Perovskite, Sol-gel, visible light irradiation, Photocatalyst

References

[1] Liu, Haiying, et al. "Screening stable and metastable ABO3 perovskites using machine learning and the materials project." Computational Materials Science 177 (2020): 109614.
[2] Bradha, M., et al. "Synthesis of photocatalytic La (1–x) AxTiO3. 5–δ (A= Ba, Sr, Ca) nano perovskites and their application for photocatalytic oxidation of congo red dye in aqueous solution." Journal of Rare Earths 33.2 (2015): 160-167.
[3] Shandilya, Pooja, et al. "Properties, optimized morphologies, and advanced strategies for photocatalytic applications of WO3 based photocatalysts." Journal of Hazardous Materials (2022): 128218.
[4] Boumaza, S., et al. "Synthesis by citrates sol-gel method and characterization of the perovskite LaFeO3: applicatio

ISSN: 0067-3064

NLMS an Enhanced Variant of the LMS for the Active Noise Cancellation
OL 14

[a] A. Chiheb and [a, b] H. Khelladi

[a] Faculty of Electrical Engineering, BP 32 El Alia, Bab-Ezzouar, 16111, Algeria
[b] Material Physics Laboratory, Faculty of Physics, BP 32 El Alia, Bab-Ezzouar, 16111, Algeria

Abstract: In this study, one of the least mean squares (LMS) algorithm variants is examined the so- called normalized least mean squares algorithm (NLMS). Indeed, LMS algorithm has some drawbacks mostly related to the slow convergence rate. For that purpose, many modifications have been applied to it and the normalized least mean squares algorithm (NLMS) is a modified LMS algorithm allowing the increase of the convergence rate. In order to evaluate the potential of the two proposed adaptive algorithms, the simulations are achieved by using several recordings. From this numerical study, the NLMS algorithm shows a good performance enhancement in term of convergence speed compared to LMS algorithm.

Keywords: Adaptive algorithms, LMS algorithm, NLMS algorithm.

Normalized Least Mean Square algorithm: In the standard LMS algorithm, when the convergence factor is large, the algorithm is confronted by a gradient noise amplification problem. This difficulty is overcome by creating the variant NLMS algorithm **[1-3]**, which takes into account the variation of the signal levels at the filter input **[4]**.

1. Least Mean Square algorithm: The LMS algorithm updates its coefficients to obtain an optimal solution based on the gradient-descent method. LMS requires a simple implementation and less computation complexity, it is widely used, and many variants are developed in order to improve its practical performances [**5-6]**.

2. Theory of the NLMS algorithm: NLMS algorithm is an extension of the traditional LMS, and the only difference is that the NLMS algorithm exploits a variable convergence rate that aims the minimization of the instantaneous output error **[1]**. The adaptation of the weight vector is normalized with respect to the squared Euclidian norm of the input vector **[7]**.

Simulation experiments:

The LMS and NLMS algorithms are implemented on different noise recordings to observe the performance of each one.

1. LMS algorithm implementation: In order to examine the performance of this algorithm, some noise sources are applied to the LMS algorithm. The noise cancellation is observed by plotting the noise source and the noise attenuation on the

ISSN: 0067-3064

same figure and this for each source. A gradual attenuation of the input signal with the generation of the anti-noise is observed.

2. NLMS algorithm implementation: The same process is applied with NLMS algorithm. After displaying the figures of the obtained results, a high convergence speed in noise cancellation is noticed.

3. Comparison of the LMS and NLMS: In this section, an overall comparison between the two algorithms is done by displaying on the same figure the attenuated noise by using each algorithm, for the same noise source. A great enhancement is reached with the NLMS variant.

Conclusion: After implementing the two above-mentioned algorithms on the several types of noise, the NLMS algorithm attests a fast converging adaptation.

References

[1] Paulo S. R. Diniz, "Adaptive Filtering Algorithms and Practical Implementation", Fifth Edition, Springer, 2020.

[2] L.V.Rajani Kumari, Asha jyothi sabavat, Y.Padma Sai, "Performance Evaluation of Adaptive Filtering Algorithms for Denoising the ECG Signal", Second International Conference on Electronics and Sustainable Communication Systems (ICESC), IEEE 2021.

[3] Atar Mon, Thiri Thandar Aung, Chit Htay Lwin, "Active Noise Cancellation in Audio Signal
Processing", International Research Journal of Engineering and Technology (IRJET), 2016.

[4] Behrouz Farhang-Boroujeny, "Adaptive Filters Theory and Applications", second edition, John Wiley & Sons, 2013.

[5] Colin Hansen, Scott Snyder, Xiaojun Qiu, Laura Brooks, Danielle Moreau, "Active Control of Noise and Vibration", second edition,CRC Press, 2012.

[6] Huang Quanzhen, Gao Zhiyuan, Gao Shouwei, Shao Yong, Zhu Xiaojin, "Comparison of LMS and RLS Algorithm for Active Vibration Control of Smart Structures", Third International Conference on Measuring Technology and Mechatronics Automation, IEEE 2011.

[7] Khan Imran, Moazzam Muhammad, Rabbani Muhammad Shoaib, Johansson Sven and Hakansson Lars, "Performance Evaluation of Control Algorithms Implemented on a Remotely Controlled Active Noise Control Laboratory", 20th International Congress on Sound and Vibration 2013 (ICSV 20), Curran Associates, Inc., 2013.

ISSN: 0067-3064

A Smart GRU-Based Estimator for SnO2 Thin films Characteristics⋆ OL 15

Faiza Bouamra[1], Mohamed Sayah[2], Labib Seddik Terrissa[3], and Noureddine Zerhouni[4]

[1] LPCMIA Laboratory, University of Blida1, Sciences Faculty, Physics Department, BP270 route de Soumaa, Algeria
[2] LITIO laboratory, University of Oran1, Department of Computer Science, BP1524, El Mnaouer, Es-senia, Oran, Algeria
[3] LINFI Laboratory, Department of Computer Science, University of Biskra, BP145 RP 07000, Algeria
[4] FEMTO-ST, Franche-Comt´ e Electronique M´ ecanique Thermique et Optique Sciences et Technologies, France

Abstract: In material physics, characterization techniques are foremost crucial for obtaining the materials data regarding the physical proper-ties as well as structural, electronics, magnetic, optic, dielectric, and spectroscopic characteristics [1]. However, for many materials, ensuring availability and safe accessibility is not always easy and fully warranted. Moreover, the use of modeling and simulation techniques [2] need a lot of theoretical knowledge, in addition of being associated to costly com-putation time and a great complexity deal. Thus, analyzing materials with different techniques for multiple samples simultaneously, still be very challenging [3] for engineers and researchers. It is worth noting that although of being very risky, X-ray diffraction is the well known and widely used characterization technique which gathers data from struc tural properties of crystalline 1d, 2d or 3d materials [4]. Currently, new data-driven methods are considered to estimate or even to forecast physical properties of materials. These well known artificial in-telligence (AI) techniques are widely adopted in various domains such as machinery, chemistry, physics, and PHM (Prognostics and Health Man-agement) [5][6][7][8][9]. We propose in this paper, a GRU for Gated Re-current Unit model [10] to estimate structural characteristics or proper-ties of thin films of tin oxide SnO2(110). Indeed, thin films samples are elaborated experimentally by the technique Sol-Gel Deep-Coating in the context of some defined conditions such as catalysis, velocity of deep, time of deep, number of deep. The obtained samples are characterized with X-ray diffraction technique and then analyzed with HighScore tool, to have the structural parameters a, b and D. ⋆ LPCMIA, LITIO, LINFI, and FEMTO-ST. Our proposed GRU neural network estimator of the structural proper-ties, is generated after a learning and testing processes over the collected data samples dictionary from the real experiences. And, the elaborated experiments show benefits of the AI-based GRU approach use for mate-rial characterization and prove the relevance

ISSN: 0067-3064

and insights of implement- ing data-driven models for material properties estimation. Nevertheless, the use of more robust and complex AI models should certainly boost the material characterization domain and this will cover a wide range of materials in future.

Keywords: Crystalline · Characterization · X-ray diffraction · Estima-tion · GRU.

ISSN: 0067-3064

Smart Prediction of Global Solar Radiation for the City of Batna Using Fuzzy Logic
OL 16

Samah Yahiaoui,Ouarda Assas
Electronic Departement, University of Batna 2 Algeria.
Advanced Electronics Laboratory.
E-mail addresses: sa.yahiaoui@univ-batna2.dz
ou.assas@univ-batna2.dz

Abstract: Algeria, like any other country, has a limited number of solar radiation measuring devices due to their price. This is why there is a huge lack in the data that is used in solar systems. Thus, the objective of this article is the estimation of daily solar radiation on a horizontal surface for the city of BATNA Algeria using the climatic parameters (temperature, humidity, pressure, wind speed and finally the rain) and the fuzzy logic that is a very powerful means of human reasoning. In what follows, we will present the fifteen systems dedicated to this. For the validation and evaluation of the accuracy and estimation capacity, several error criteria were used, which are (RMSE, nRMSE, MAE, MSE, MBE ,nMBE and R^2). The results provided by the adopted system allows us to conclude that despite the simplicity of the system developed, it was possible to estimate the values of solar radiation with an accuracy of RMSE=6.059, nRMSE=0.355, MAE=5.268, MSE=36.70, MBE=5.261,nMBE and R^2 =0.961.

Keywords: Prediction, Fuzzy logic, Solar radiation, Modeling.

ISSN: 0067-3064

A new piezoresistive flow sensor design and fabrication based on soft lithography technique for Microfluidic Systems Using PDMS and Conductive PDMS
OL 17

Abdelkader Hassein-Bey [(1)], Nadir Belgroune[(1)], Asma Leila Hassein-Bey[(1)], Burhanuddin Yeop Majlis[(2)] and Rafik Serhane[(3)]

[(1)] Physical Chemical Laboratory of Inorganics Materials and their Applications (LPCMIA), University of Blida1 Blida 09000, Algeria.
[(2)] Institute of Microengineering and Nanoelectronics (IMEN) Universiti Kebangsaan Malaysia UKM Bangi, Selangor, Malaysia.
[(3)] Centre for Development of Advanced Technologies. 20 Août 1956 City, Baba Hassen, P.O. Box 17, DZ-16303 Algiers, Algeria

Abstract: Over the last two decades, microfluidics has emerged as a significant driver for the development of various applications. The increasing interest in this technology can be attributed to the diverse range of microfluidic devices used in labs-on-chip (LOC) and micro Total Analysis Systems (µTAS) applications [1]. These devices incorporate components for fluid control, trapping, separation of biological cells, and data acquisition, enabling the manipulation and analysis of small fluid samples. Accurate control of fluid volume is essential, and this is achieved using flow rate sensors. Various flow sensor designs are available in the literature, based on sensing principles such as thermal phenomena, pressure phenomena, and mechanical bending measured by optical microscopy, laser interferometry, or piezoresistivity, especially in the case of airflow [2]. Polydimethylsiloxane (PDMS) is the commonly used material for fabricating this kind of microfluidic system [2]. PDMS exhibits new and interesting electric properties that transform it from an insulating polymer to a conductive one by adding conducting carbon black (CB) nanoparticles [3]. Additionally, conductive Polydimethylsiloxane (CPDMS) demonstrates piezoresistive behavior [3]. A prevalent approach for PDMS-based device fabrication involves the use of a thin multilayer, based on soft-lithography technique, is used to develop a microfluidic flow sensor.
The proposed fluid flow sensor consists of a piezoresistive microbridge made of CPDM integrated directly within a PDMS microchannel. The fluid is injected to the microchannel through the inlet and leaving the microchannel through the outlet. The sensing element is a CPDMS microbridge placed in the middle of the microchannel. The fluid flow motion in microchannel causes a mechanical deflection of the piezoresistive microbridge. The transduction mechanism based on the piezoresistivity property of CPDMS composite converts the mechanical deflection of microbridge to an electrical resistance variation. Thus, the structure is composed of three PDMS layers that form the CPDMS sensing element integrated within a microchannel. Sensors based

ISSN: 0067-3064

on PDMS bring several advantages such as low toxicity, thermal stability and low permeability with biocompatibility characteristics. This process involves casting liquid PDMS onto a rigid SU-8 mold crafted through cost-effective conventional photolithography, completing fabrication in under 24 hours [2, 3]. Initially, two separate SU-8 molds are fashioned using Micro Chem Corp.'s negative photoresist on silicon wafers, employing standard photolithography. The mold preparation for top, middle, and bottom layers is outlined. In the subsequent step, PDMS layers are formed by pouring a 10:1 ratio mixture of PDMS prepolymer and curing agent onto the SU-8 molds for replication. Plastic film prevents bubble introduction during curing. After curing, layers are peeled off. The third step involves Corona treatment on the top layer for PDMS surface oxidation, enhancing interlayer adhesion. The bottom and middle layers are then bonded. Following this, the plastic layer is removed, and the top layer is sealed. Crucially, the alignment of the three PDMS layers requires microscope precision, ensuring accurate layer overlay and design precision.

In this paper, we present the design and fabrication of a piezoresistive flow sensor utilizing PDMS and CPDMS materials. The sensor's working principle is based on the deflection of a CPDMS microbridge due to fluid motion within a PDMS microchannel. Finite Element Method (FEM) simulations, as previously reported, were conducted to optimize the sensor design using COMSOL Multiphysics software [4]. We showcase the fabrication of the flow sensor using the soft lithography technique and present the results of experimental performance testing. This flow sensor was swiftly prototyped at a low cost. The measured sensitivity of 0.361% ml^{-1}.min aligns with the predicted value of 0.234% ml^{-1}.min obtained from simulations. Furthermore, the sensor can effectively measure the flow rate of biological fluids with a wide range of properties. Consequently, the sensor's electrical response opens a new horizon for various applications in microfluidic systems and BioMEMS.

Keywords: Microfluidic - Flow Sensor - Conductive PDMS - Piezoresistivity - Soft Lithography.

References

[1] Culbertson C. T., Mickleburgh T. G., ‘Stewart-James S. A., Sellens K. A., Pressnall M.: ‘Micro Total Analysis Systems: Fundamental Advances and Biological Applications’, Anal. Chem., 2014, 86, pp. 95−118

[2] Chen P., Zhao Y., Tian B., Li Y.: ‘Design and fluid–structure interaction analysis of a micromachined cantilever-based differential pressure flow sensor’, Micro & Nano Letters, 2014, 9 (10), pp. 650–654

[3] Luheng W., Tianhuai D., Peng W.: ‘Influence of carbon black concentration on piezoresistivity’ , Carbon, 2009, 47, pp. 3151–3157

[4] Belgroune N., Hassein-Bey A., Hassein-Bey A.S.L., Tahraoui A., Majlis B.Y. , Benamar M. E. A., Serhane R.: ‘Design and FEM simulation study of a microflow sensor based on piezoresistive PDMS composite for microfluidic systems’, Microsystem Technologies, 2016, DOI :10.1007/s00542-016-2891-6

ISSN: 0067-3064

Natural Radioactivity in Swimming Pools: a case study from Algeria
OL 18

BELLIL Wafa [1, 2], BOUKHENFOUF Wassila[1], MEZAGHCHA Younes, MAIRECHE Yacine

[1] DAC Laboratory, Physics Department, Faculty of Sciences, Ferhat ABBAS University, Sétif 1 Algeria
[2] LPTHIRM, FS, BP : 270 Route de soumaa Blida (Algeria)
bellil.wafa@gmail.com

Abstract: Thermal water is known for its content of a part of natural radioactivity. The present work studies the dosage of radon in two closed swimming pools filled with thermal water in Hammam Soukhna. The LULDUM detector is used to assess the dose of gamma and beta radiation in these swimming pools. An evaluation of the radioactivity health risks for visitors and workers has been established and compared with experimental data published in the literature. All results obtained were below the values recommended by the International Atomic Energy Agency. 1. Introduction: There are on the Algerian territory more than 200 thermal springs according to the studies carried out in this subject. Most of these hot springs are located in the East with varying temperatures from 19°C to 98°C. These springs are visited by tourists for traditional thermal baths, or are requested by patients for medical reasons because these waters are endowed with scientifically proven therapeutic properties. Their qualities come from underground journey they make in the bowels of the earth, which charges them with virtues additional. These waters are rich in various radioelements; in particular Radon (222Rn) which is one of the main causes of lung cancer. Its concentration is increased in closed environments such as homes and workplaces. It is conceded that spas are the model example of a closed place where the risk of Rn due to thermal waters accumulates at the risk of radioactivity of building materials of spas. For this, a study is made on the evaluation of doses and the health risks of this radioactivity on visitors and workers in thermal stations. 2. Results and discussion 2.1. Assessment of radiological risk indices: Several radiological parameters are calculated such as the natural radioactivity level, Radium equivalent activity, the absorbed dose, the external and internal risk and finally, the excess cancer risk index (ELCR). The table below gives the values of ELCR

	M.G.H.U. spa	Belmihoub Arab spa
ELCR (10-3)	**0.033**	**0,037**

Table 1 : values of ELCR

ISSN: 0067-3064

Conclusion: This study has been carried out for two swimming pools filled by thermal water in order to assess the risks caused by estimating several radiological parameters. The doses received by workers and visitors are calculated from the specific relation illustrated by United Nations Scientific Committee on the Effects of Atomic Radiation. The values found for these parameters do not exceed the admissible values.

References

[1] UNSCEAR, Sources, Effects and Risks of Ionizing Radiation. Report to the General Assembly, New York, 2000.
[2] Bahtijari et al., Radon activity assessment of thermal water in Spas of Kosovo by using different methods, International Journal of Radiation Research, 20.1 (2022):229-233.
[3] Labidi, S., Darwish Al-Azmi, and R. Ben Salah. "Indoor radon in Tunisian spas." Radioprotection 47.3 (2012): 361-373

ISSN: 0067-3064

Development and Characterization of an Anisotropic Wet Release Process for Micro-Cantilever Fabrication on Silicon Substrate
OL 19

Nadir Belgroune [(1)], Abdelkader Hassein-Bey [(1)] and Burhanuddin Yeop Majlis[(2)]

[(1)] Physical Chemical Laboratory of Inorganics Materials and their Applications (LPCMIA), University of Blida1 Blida 09000, Algeria.
[(2)] Institute of Microengineering and Nanoelectronics (IMEN) Universiti Kebangsaan Malaysia UKM Bangi, Selangor, Malaysia.

Abstract: Silicon processing technology has matured over the past four decades, evolving into a cornerstone of modern industry. In the last fifteen years, these processing techniques, initially perfected for large-scale integrated circuit fabrication, have been ingeniously adapted and refined to give birth to microelectromechanical systems (MEMS). MEMS devices is characterized by their miniaturized components and extraordinary versatility, have been incorporated into countless sectors and revolutionizing industries as diverse as healthcare, automotive, aerospace, and consumer electronics including pressure sensors, accelerometers, and ink jet print heads [1-2]. The main useful MEMS microstructure used in these devices are the membrane, micro-cantilever, and micro-bridge. One of the largest used is micro-cantilever structure, a single-clamped beam, it has recently attracted considerable interests in the development of a wide range of novel physical, chemical, and biological sensors [3-4].

This paper reports on the development and characterization of an anisotropic wet release process tailored for the precision fabrication of micro-cantilevers on silicon substrates. The process is implemented using a series of meticulously designed masks and processing steps, featuring double-sided potassium hydroxide (KOH) etching on silicon wafers coated with nitride [5]. The key aspect under investigation is the optimization of the etching solution, a critical determinant of controlled silicon substrate etching. This process adheres to standard integrated circuit manufacturing, using the bulk micromachining technology [5-6].

The Scanning Electron Microscope (SEM) analysis of the fabricated structures reveals compelling insights into their morphological characteristics. Firstly, the initial membranes produced by our process have a depth of 250 µm following a precise KOH etching process, although their surface roughness requires amelioration. Notably, the introduction of a 10% isopropyl alcohol (IPA) solution mitigates this issue. The subsequent fabrication of micro-cantilevers showcases their triangular morphology, a testament to the anisotropic etching attributes of KOH. These micro-cantilevers exhibit dimensions of 1200 µm in length, 500 µm in width, and 200 µm in thickness, promising

ISSN: 0067-3064

to serve as critical components in a wide array of MEMS applications. This analysis has played a pivotal role in characterizing the morphological structure, aiding in the optimizing of the process and enhancing surface smoothness. These insights open avenues for further research and underscore the pivotal role of controlled etching in MEMS technology.

References

[1] Shaeffer, D.K. MEMS inertial sensors: A tutorial overview. IEEE Commun. Mag. 2013, 51, 100–109.
[2] Nazir, S. and Kwon O. S. 'Micro-Electromechanical Systems-based Sensors and Their Applications' Applied Science and Convergence Technology 2022; 31(2): 40-45.
[3] Qing ZHU, 'Microcantilever Sensors in Biological and Chemical Detections' Sensors & Transducers Journal, Vol. 125, Issue 2, February 2011, pp. 1-21
[4] Putrino, G.; Keating, A.; Martyniuk, M.; Faraone, L.; Dell, J. 'Chemical and biological sensors based on microelectromechanical systems.' In Nanomaterials: Science and Applications; Pan Stanford Publishing Pte Ltd.: Singapore, 2016; pp. 107–145.
[5] Zubel, I. 'Anisotropic etching of Si.' J Micromech Microeng, 2019, 29(9):93002
[6] Pal, P. and Sato, K. 'Silicon wet bulk micromachining for MEMS.' Pan Stanford Publishing, Singapore, 2017, p 412.

ISSN: 0067-3064

Analysis of the environmental impact of hot-dip galvanization on the environment OL 20

O. Kebour [a], B.Amrouche[b]

[a] Université de Saad Dahlab, Route de Soumaa, BP 270 BLIDA Ouled Yaich 09200, Algérie. Tél : Email : Kebour.omar50@gmail.com
[b] Université de Saad Dahlab, Route de Soumaa, BP 270 BLIDA Ouled Yaich 09200, Algérie. Tél : Email : amrouche_badia@yahoo.fr

Abstract
Hot-dip galvanizing processes require the use of hazardous chemicals, metals such as zinc and aluminum, and a high temperature of around 450°C to keep the zinc in a liquid state 24 hours a day, all year round in the galvanizing bath. These conditions pose a particular threat to the environment. The objective of this paper is to highlight this threat through an analysis of the environmental impact of the hot-dip galvanizing process of an industrial unit with a production capacity of 40,000 tons/year, located in the Rouiba industrial zone in Algiers, with the identification and evaluation of the environmental aspects as well as the aspects requiring special monitoring.
The results obtained, give us the environmental risks and their level of acceptability in this industry in relation to the inputs of the galvanization process (raw material (Zinc), electricity, gas, acid,...etc), and the outputs (steel and Zinc scraps, emission of gases such as nitrogen dioxide, generating air pollution, acid rain and soil acidification
This developed evaluation method can be applied and generalized for all the economic operators who operate in the same field of activity wishing to control and minimize the harmful effects of the galvanization by immersion on the environment.

Keywords: Zinc; Hot dip galvanizing; Environmental aspects and impacts; Environmental risks.

ISSN: 0067-3064

X ray diffraction analysis of Fe-Cu-Zn-Sn powders mixture via Rietveld method
OL 21

Soumia SMILI[1], Chaffia DJEBBARI[1,2], Douniazed LAMROUS [3,4], Saida BOUKEFFA[1]

[1] Materials Physico-Chemistry Laboratory (LPCM),Physics Department, Science and Technology Faculty, Eltarf University, P.B. 73, Eltarf 36000, Algeria
[2] Technology Department, Technology Faculty, University 20 August 1955-Skikda, Algeria.
[3] Physics Department, Science and Technology Faculty, Eltarf University, P.B. 73, Eltarf 36000, Algeria.
[4] LM2S Laboratory, Physics Department, Science Faculty, University Badji Mokhtar, Annaba, Algeria.
Email address: s.smili@univ-eltarf.dz

Abstract: The mechanical alloying process has been used to prepare Fe-Cu-Zn-Sn intermetallic compound from elemental Fe powders, brass (Cu-30Zn) and bronze (Cu-10Sn) alloys in planetary ball mill type Retsch PM400. The obtained product after 1h of milling has been characterized by X-ray diffraction (XRD).The structural and microstructural parameters (lattice parameters, crystallites size, microstrains, dislocations density, and phase fraction) were determined from the XRD patterns by means of a full-pattern fitting program (MAUD) based on the Rietveld method [1, 2]. The procedure consists in modeling the diffraction peak profiles by analytical functions. The Rietveld refinement of the X-ray diffraction patterns detected the formation of binary intermetallic phases: ɣ-brass Cu5Zn8, Cu10Sn3, and Cu41Sn11 in addition to alfa-Fe. The microstructural study reveals the formation of nanoscale grains for all the phases.

Keywords: brass alloy, bronze alloy, X-ray diffraction, Reitveld, Maud, ball milling.

References

[1] Lutterotti, L.: MAUD CPD, Newsletter (IUCr) 24 (2000). [2] Rietveld H.M, Appl J. Cryst. 2 65 (1969).

ISSN: 0067-3064

Confinement Effects by Structured Side Walls on Swift Granular Flows
OL 22

Hafsa Sebbah [(1)] and Sidi Mohammed Khefif [(2)]

[(1):] Université Abou bekr Belkaid de Tlemcen, Algeria
[(2):] Ecole Supérieure en Sciences Appliquées de Tlemcen, Algeria

Abstract :

Introduction

- **Confined swift granular flows:** Granular dense flows down inclined channel are very common in industry and geophysical processes as cereal grain processing and rock avalanche [2]. These flows present a challenge for both theoretical and experimental studies because the complexity of the grain-grain and grain-wall interactions [2].
- **Influence of the structure of the walls:** For a better understanding of the impact of the walls on the flow structure, we carried out numerical simulations of four (4) different systems, flat substrate, and side walls [1,2,3], structured substrate and walls built by gluing spheres on the boundaries of the system, flat substrate and structured side walls and finally smooth side walls and structured substrate. These systems are filled with grains at different heights and inclined at different angles, then we observe the gravity induced flows.

Methodology

- **Numerical Simulations:** Using a discrete element method DEM algorithm, we analyzed these numerical simulations in depth by looking into flow velocity profiles, volume fraction and the granular temperature.
- **Results:** Through our numerical experiments, we show that the nature of the substrate has no impact on the nature of the flow, however, it's clear that the bumpy lateral walls obstruct the f low by decreasing its velocity and also they make it less dense.

Conclusion: We conclude that the nature of the base of the channel has no influence on the dynamics of the flow unlike the sidewalls.

References

[1] N. Brodu, P. Richard, R. Delannay, Shallow granular flows down flat frictional channels: Steady flows and longitudinal vortices, PHYSICAL REVIEW E 87, 022202 (2013).

[2] N. Brodu, R. Delannay, A. Valance, P. Richard, New patterns in high-speed granular flows, Cambridge University Press, vol. 769, pp. 218–228 (16 March 2015)

ISSN: 0067-3064

[3] V. J. Ralaiarisoa, A. Valance, N. Brodu, R Delannay, High speed confined granular flows down inclined: numerical simulations, EPJ Web of Conferences 140 , 03081 (2017)

ISSN: 0067-3064

Spin Gapless Semiconductor FeMnGa-Based Interface Characterization of Current-Perpendicular-to-Plane Spin Valves
OL 23

Y. Bensaidane*[,1], B. Helifa [1], I. Lefkaier [1] and N. Baadj [2]

[1] Laboratory: LPM, University of Laghouat - BP 37G - Laghouat, Algeria
[2] Laboratory: LMPA, Physics department university of Mohamed Boudiaf-M'sila, Algeria
* y.bensaidane@lagh-univ.dz

Abstract: Spin gapless semiconductors, also known a special class of half-metallic magnets, have received more and more attention in spintronic applications due to the complete spin polarization and the electrical conductivity between half-metals and semiconductors, To explore the potential spintronic applications of the Heusler alloy FeMnGa (FMG), and interface properties. employing the first-principles calculations within density functional theory (DFT) combined with the nonequilibrium Green's function.we investigated the interfacial electronic, magnetic, and spin transport properties of FMG /Pd/ FMG Due to the interface rehybridization, the magnetic moment of the interface atom gets enhanced .further analysis on electronic structures reveals that owing to the interface states, the interface spin polarization is decreased. The transmission curves of FMG /Pd/ FMG reveal that the transmission coefficient at the Fermi level in the majority spin channel is much higher than that in the minority spin channel. Therefore, FMG /Pd/ FMG CPP-SV with an (Ga;Mn) -terminated interface structure has a better application in a spintronics device.

Introduction: Since the first theoretical prediction of the half metallicity of Heusler alloys, there has been explosive interest in manipulating the electron spin in a Heusler-alloy-based spintronic device [1]. As one of the most important spintronics devices, a current-perpendicular-to-plane (CPP) spin valve (SV) based on the giant magnetoresistive (GMR) effect consists of a nonmagnetic metal as a spacer that is sandwiched between two ferromagnetic materials. It can produce two distinct states: a low-resistance state, when two electrodes are in parallel magnetization configuration, and a high-resistance state, when they are in antiparallel magnetization configuration. Half-metallic Heusler alloys (HMHAs) are regarded as one of the most promising candidates for electrode materials in CPP-SV owing to their high Curie temperature. Moreover, the majority spin bands of HMHA across the Fermi level show typical metallicity, while minority spin bands possess an energy gap around the Fermi level. Such a novel band structure results in a theoretical 100% spin polarization. we investigate remarkable candidate for CPP-SV by studying the interface magnetism,

ISSN: 0067-3064

electrical structure, and spin transport features of FMG /Pd/ FMG CPP-SV since the MR ratio of spin valves based on a Heusler alloy greatly depends on its interface properties.

References

[1] de Groot, R. A.; Mueller, F. M.; Engen, P. G. v.; Buschow, K. H. J. Phys. Rev. Lett. 1983, 50, 2024 2027. doi:10.1103/physrevlett.50.2024

[2] Rungger, I., Sanvito, S.: Algorithm for the construction of self-energies for electronic transport calculations based on singularity elimination and singular value decomposition. Physical Review B 78(3), 035407 (2008)

ISSN: 0067-3064

Synthesis and physical, optical and electrochemical properties of LaMnO3 semiconductor perovskite oxide OL 24

Ali BOULAHOUACHE [a, b],*, Nassima SALHI [a,b], Hamza MEDJADJI[a], Maroua Benlembarek[a] , Khaled DERKAOUI[c], Cherifa Rabia[a], Mohamed TRARI[d],

[a] Laboratoire LCPMM, Faculté des Sciences, Université BLIDA1, B.P 270, Route de Soumaa, BLIDA, Algérie.
[b] Laboratoire de Chimie du Gaz Naturel, Faculté de Chimie, USTHB, BP32, El-Alia, 16111 Bab Ezzouar, Alger, Algérie.
[c] Research Center On Semiconductors Technology for Energetic, CRTSE-TESE- 02, Bd. Dr. Frantz Fanon, 7 Merveilles, Box 140, 16038 Algiers, Algeria.
[d] Laboratoire de Stockage et valorization de l'énergie renouvelable, Faculté de Chimie, USTHB, BP32, El-Alia, 16111 Bab Ezzouar, Alger, Algérie.
*boulahouache@yahoo.com

Abstract: In this study, a mixed oxide LaMnO3 perovskite-type material with defined structure was prepared with a high purity via sol-gel method using nitrates precursor salts as raw materials and propionic acid as solvent, followed by a calcination at 850°C. The sample underwent comprehensive characterization, with a particular focus on structural and textural, optic and electrochemical analyses using: (TG-TDA), X-ray Diffraction (XRD), XRF, BET, Fourier Transform Infrared Spectroscopy (FT-IR), Scanning Electron Microscopy (SEM-EDX), X-ray photoelectron spectroscopy (XPS) and UV-visible Spectrophotometry. Additionally, electrochemical characterization of LaMnO3 allowed to draw up an energy diagram for this photocatalyst, serving as a preliminary step towards its application in photocatalysis fields. Thermogravimetric analysis revealed the formation of metal oxide above 550°C. XRD analysis showed a pure and single phase LaMnO3 with cubic symmetry, Pm3m spatial group and a crystallite size of 17 nm. LaMnO3 can be classified as a nanomaterial. A low specific area 10 m2.g-1 was obtained but sufficient for photocatalytic application. The XRF analysis revealed La/Mn molar ratio close to the unity indicating the single structure phase. The various vibrational bands observed by FT-IR spectroscopy in the 400-1000 cm-1 range are attributed to metal-oxygen, La-O, Mn-O and La-O-Mn bonds. The SEM micrograph shows the presence of large blocks and a surface with several holes, resulting of nitrate removal during the solvent evaporation stage and calcination. The flat band (EFB), the gap energy (Eg), the valence and conduction band potentials are-0.18 V, 1.89, 3.4 and 1.51 eV respectively. The LaMnO3 semi-conductor has n-type behavior with electrons as majority carriers.

Keywords: Perovskite, Sol-gel, Elechtrochemical analysis, Semi-conductor, n-Type behavior

ISSN: 0067-3064

A Hybrid Approach for Diabetic Retinopathy Detection using Deep Learning and SVM
OL 25

Sofiane Boumeshed[1], Noureddin Belkhamessa[1], Yazid Cherfa1, Assia Cherfa[1]

[1] Department of Electronics, Faculty of Technology, University of Blida 1, Blida, Algeria

Abstract: Diabetic retinopathy (DR) is a critical and potentially blinding complication of diabetes mellitus, affecting millions of individuals worldwide [1]. Early detection and timely intervention are paramount for effective management [2]. In this study, we propose a novel approach that combines the power of deep learning, represented by the Residual Neural Network (ResNet), with the interpretability of the Support Vector Machine (SVM) for the accurate and reliable detection of diabetic retinopathy [3][4].
The ResNet architecture is employed to automatically extract discriminative features from retinal images, capturing intricate details that are indicative of DR progression [5]. This deep learning component is adept at handling the complexity and variations in retinal images, thus serving as a robust feature extractor [2].
Complementing the feature extraction process, SVM, a traditional machine learning classifier, is utilized to make binary classification decisions. SVMs are known for their ability to establish interpretable decision boundaries, a crucial aspect in medical diagnostics [6]. The synergy between ResNet's feature extraction and SVM's classification capabilities results in a powerful ensemble model that excels in DR detection [7].
We delve into the details of our implementation, discussing the architecture of the ResNet, the selection of layers, and any preprocessing steps applied to the retinal image dataset. Furthermore, we elucidate the training process of the SVM on the extracted features, along with insights into hyperparameter tuning for optimal performance.
Our approach exhibits promise in achieving high accuracy in the detection of diabetic retinopathy while providing valuable interpretability for healthcare professionals. This amalgamation of cutting-edge deep learning techniques with traditional machine learning principles represents a significant stride towards early DR diagnosis, thus facilitating timely medical intervention and improved patient outcomes.

Keywords : deep learning, RD, classification, machine learning.

Reference

[1] Abràmoff, M. D., Garvin, M. K., Sonka, M., Russell, S. R., Folk, J. C., & Bucur, B. (2010). Automated early detection of diabetic retinopathy. IEEE transactions on medical imaging, 29(11), 2036-2045.

ISSN: 0067-3064

[2] Wang, J., Chen, H., Li, F., & Wang, D. (2022). A deep learning framework with multi-scale feature extraction for diabetic retinopathy detection. Biomedical Signal Processing and Control, 70, 103151.
[3] Li, L., Shen, L., Zhang, Q., & Guo, Z. (2020). A residual learning framework with attention mechanism for diabetic retinopathy detection. Medical image analysis, 62, 101706.
[4] He, K., Zhang, X., Ren, S., & Sun, J. (2016). Deep residual learning for image recognition. In Proceedings of the IEEE conference on computer vision and pattern recognition (pp. 770-778).
[5] Quellec, G., Cazuguel, G., Lamard, M., Josselin, D., Danno, J., Gaudric, A., ... & Le Beux, S.(2018). Deep learning for the detection of diabetic retinopathy: A systematic review and meta-analysis. Frontiers in medicine, 5, 286.
[6] Chawla, N. V. (2005). Data mining for imbalanced datasets: An overview. In Data mining for imbalanced datasets. Springer, Boston, MA. pp. 1-22.
[7] Wang, Z., & Zhou, Y. (2021). A novel deep learning approach for diabetic retinopathy detection and classification based on ResNet and SVM. Biomedical Signal Processing and Control, 68, 102766.

ISSN: 0067-3064

Glioma Brain Tumor Segmentation using Deep Learning: A Review
OL 26

S.Ouitis, Y.Cherfa, A.Cherfa, N.Belkhamsa

Department of Electronics, Faculty of Technology, University of Blida 1, Blida, Algeria

Abstract: Brain tumor segmentation is a critical task in medical imaging, with profound implications for diagnosis and treatment planning. This study addresses the pressing need to compare and evaluate three distinct approaches to brain tumor segmentation: a conventional baseline method, a deep learning-based technique, and a semantic segmentation approach [1]. The primary objective of this research is to comprehensively assess the performance and efficacy of these three methods in accurately delineating brain tumors from medical imaging data [2].
Accurate diagnosis of brain tumors is crucial, as they account for a significant percentage of central nervous system tumors and pose a substantial threat to human lives [3]. Among these, gliomas present challenges due to their heterogeneity and ambiguous borders. This study explores the potential of deep learning, specifically Convolutional Neural Networks (CNNs), and semantic segmentation methods to streamline the diagnosis process [4].
In this context, this study aims to comprehensively compare and evaluate these three approaches to brain tumor segmentation. The study evaluates the accuracy, computational efficiency, robustness, and potential for hybrid approaches that combine the strengths of multiple methods. The findings offer valuable insights into selecting the most suitable method for specific clinical scenarios [5].
The article proceeds by providing detailed descriptions of the three segmentation methods employed basic, deep learning-based, and semantic segmentation. It covers the dataset, preprocessing steps, and performance evaluation metrics used. Experimental results are presented, including quantitative and qualitative assessments of the segmentation methods. The article concludes with a summary of key findings and suggestions for future research in this critical domain.
This research contributes to the ongoing dialogue in medical image analysis by offering a rigorous comparative analysis of brain tumor segmentation methods. The insights gained have the potential to guide medical professionals in selecting the most suitable approach for their specific diagnostic needs.

Keywords: tumor segmentation , MRI, deep-learning, CNN.
References:

ISSN: 0067-3064

[1] Stap, J., & Vincken, K. L. (2004). A review of image segmentation methods with a focus on brain tumor segmentation. IEEE transactions on medical imaging, 23(8), 932-949.
[2] Udupa, J. K., Srikanth, S. M., & Vemuri, B. C. (1999). Brain tumor segmentation using fuzzy c-means clustering. Computerized Medical Imaging and Graphics, 23(5), 343-350.
[3] Isensee, F., Kickingereder, P., Wick, W., Bendszus, M., Maier-Hein, K. H., & MICCAI BraTS 2017 Challenge. (2017). No New-Net: A convolutional neural network for brain tumor segmentation. In Medical Image Computing and Computer-Assisted Intervention – MICCAI 2017 (pp. 1-9). Springer, Cham.
[4] Havaei, M., Davy, A., Bengio, Y., Larochelle, H., Pal, C., Jodoin, P. M., & Bengio, Y. (2015). Brain tumor segmentation with deep neural networks. Medical image analysis, 35, 1-12.
[5] Ronneberger, O., Fischer, P., & Brox, T. (2015). U-net: Convolutional networks for biomedical image segmentation. In Medical image computing and computer-assisted intervention – MICCAI 2015 (pp. 234-241). Springer, Cham.
[6] Zhao, H., Zhao, X., Wang, Y., Zhang, J., & Tian, L. (2020). Deep convolutional neural network for brain tumor segmentation using cascaded U-Net. Biomedical Signal Processing and Control, 55, 101714.
[7] Bakas, S., Reyes, M., Van den Eynde, K., Aerts, H., Bakas, F., Beig, Z., ... & Ourselin, S. (2017). Identifying the best machine learning algorithms for brain tumor segmentation: Methods comparison to the BRATS 2017 challenge. IEEE transactions on medical imaging, 36(11), 2199-2212.
[8] Wang, Z., Zhao, X., Zhang, Y., Gong, D., Wei, L., Liu, Z., & Tian, L. (2021). A comparative study of deep learning-based brain tumor segmentation methods using a novel dataset. Medical image analysis, 73, 102093.

ISSN: 0067-3064

A Brief Survey of Transfer Learning in Breast Cancer Image Analysis Using Different Modalities OL 27

Oudjer Hayet1,2, Cherfa Assia1,3, Cherfa Yazid1,4, Noureddine Belkhamsa1,5
1Department of Electrical Engineering, University of Blida 1, BP 270 road Soumaa, Blida,
Algeria
2oudjerhayet@gmail.com, 3assia_bz@yahoo.fr, 4cherfa_yazid@yahoo.fr, 5nourbelk@hotmail.com

Abstract: Breast cancer is the most common cancer among women worldwide, including in Algeria,where it has the highest prevalence in terms of incidence and mortality. Research in the field of medical image processing is mainly focused on the analysis of images from the different modalities used to diagnose this cancer, because of the significant impact of early detection on reducing its mortality. Among the techniques used for image analysis, transfer learning appears to be a relevant approach, capable of adapting to the inherent limitations of small databases and the constraints of high computing time. In this paper, we summarize recent work on the application of transfer learning to different imaging modalities dedicated to breast cancer, in particular mammography, ultrasound, breast tomosynthesis, histology and MRI. We also present the most widely used public databases in this field. Finally, we analyze these studies and discuss future prospects for the application of transfer learning.

Keywords: Breast cancer, image processing, transfer learning, breast cancer modalities.

ISSN: 0067-3064

POSTER

ISSN: 0067-3064

Structural and FTIR characterization of tin oxide thin films deposited by Dip- coating method
P 01

H.OULDARAB [1,2,3], S.HAMZI [1], A.OUAGUED [3]

[1] LPCIMA Laboratory, Physics Department, Science Faculty of Blida1 University, 09000 Blida, Algeria.
[2] Material Sciences Department, Sciences and Technology Faculty of Djilali BOUNAAMA University, Algeria
[3] LEE Labratory, Physics department .Faculty of Technology. El Hassania .Chlef. Algeria

Abstract: Over the last decades transparent conducting oxides (TCOs) such as SnO2, ZnO, In2O3 have been of increasing interest. The most compelling motivation to study TCOs is the increasing number of applications including photovoltaic, Gas Sensors, Catalysis….. In this work we deposited thin films of tin oxide on glass substrates by the Sol Gel (Dip-Coating) method. We have investigated the structural properties in order to optimize the annealing temperature. The obtained samples were analysed by X- Ray Diffraction XRD, Energy Dispersive Spectroscopy EDS and FTIR Spectroscopy.

Keywords: SnO2, Thin film, Dip-coating, FTIR.

Experimental process: SnO2 thin films are deposited by the Sol-Gel dip coating technique on glass substrates, the solution was prepared from an amount of Tin Dichloride (SnCl2.5H2O) dissolved in ethanol (C2H5OH). The mixture was heated and stirred in a system reflux at 80°C for 2 hours until a white powder is obtained to which 50 ml of Ethanol is added and then heated with agitation at 50°C for 2 hours to have at the end a homogeneous solution. We have fixed the number of layers to 5 layers. After deposition the samples were annealed under air at 200°C, 300°C, 400°C and 500°C for 2 hours.

Results:

1. Structural properties: The study evaluated by the XRD analysis showed that the non-annealed samples are of amorphous structure, while annealed one revealed that at annealing temperatures above 200°C a poly crystalline phases of tin oxide appears. At 200°C, 300°C, 400°C annealing temperaturas, deposited films show the co-existence of metastable phases of tin oxide with appearance of SnO (110), Sn2O3 (101) and stable one SnO2(110),whereas at 500°C thin films crystallized only in a tetragonal rutile structure of the tin dioxide phase with presence of (110), (101) (200) and (110) a wich is in good agreement with the JCPDS card, No.01-41-1445. The intensity of (110)

ISSN: 0067-3064

exhibit a preferred orientation along this plane. The average crystallite size is found to vary between 44 and 10 nm with increasing temperature.

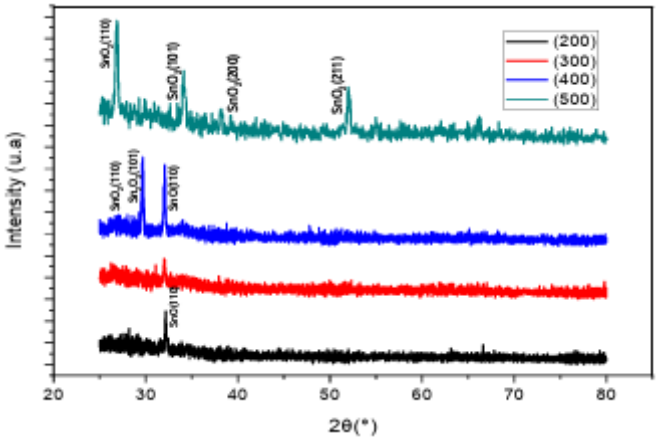

Figure 1. XRD spectra of Tin Oxide Thin Films annealed at 200°C, 300°C, 400°C and 500°C

FTIR charachterization: The identification of vibration modes and existant bonds were performed by FTIR ATR. Obtained spectra confirm the XRD results and show the existence of the Sn-O, Sn-OH, Sn-O-Sn bonds and the effect of Annealing temperature on this bonds.

Conclusion: From obtained results we can conclude that the annealing temperature have an important effect on the structural properties such as thin films nature, phases, and crystalline structure. We found that 500°C is the optimal annealing temperature. FTIR Analyses confirmed The structural results.

Acknowledgement: I gratefully acknowledge Miss BOUAMRA Faiza Director of Physical-Chemical Inorganic Materials and Their Applications (LPCIMA) who enabled me to achieve this research work in this laboratory.

References

[1] W. Hamd, Y.C. Wu, A. Boulle, E. Thune, R. Guinebretière "Microstructural study of SnO2 thin layers deposited on sapphire by sol–gel dip-coating" Journal Thin Solid Films 518 (2009) 1–5

[2] S.Haireche, A. Boumeddiene , A. Guittoumb, A. El Hdiy , A. Boufelfel "Structural, morphological and electronic study of CVD SnO2:Sb films" Materials Chemistry and Physics 139 (2013) 871e876

ISSN: 0067-3064

Physical Characterization Of Casein Biofilm
P 02

N. E. HADJ KADDOUR[1], N. ILES[1], B. UCPINAR DURMAZ[2], A. AYTAC[2,3]

[1]Laboratoire de Physique des Couches Minces et Matériaux pour l'Electronique, Université Oran 1 Ahmed Ben Bella, Algerie.
[2] Department of Chemical Engineering, Engineering Faculty, Kocaeli University, Kocaeli 41380, Türkiye
[3] Polymer Science and Technology Programme, Kocaeli University, Kocaeli 41001, Türkiye
Email: hadjkadour.nedjma27@gmail.com

Abstract: Thanks to the usage of biopolymers in various fields as packaging, biosensing, and drug design, these materials attracted the interest of scholars during the latest years. A subcategory of these biopolymers is fabricated using bio-sources like proteins. The Casein belong to this class of materials. In the current experiment work, casein-based films were fabricated using a wet technique. The films with a translucent appearance are obtained. Our stress tests show that the resulting film has a plastic quality and may be bent by up to 34% before it breaks. This outcome depends on the type of protein employed, the ratio of plasticizer, and other experimental conditions. The sodium caseinate-specific peaks in the FTIR spectrum of the excited film shows the O-H stretching vibration occurring at a wavelength of 3286.04 cm-1 whereas the C-H binding wavelength is found at 3067 cm-1, and the peak hallmark protein networks of 1639.69 cm-1 is characteristic of the amide I (C-O) band and 1517.38 cm-1 for the amide II (HN-CO) band, respectively.

ISSN: 0067-3064

Effect of Er doping TiO_2 thin films by Sol-Gel Technique P 03

A.SEDIK[1], A. YERBOUB[1], A.KEBIR[1], M.TRARI[2]
[1]Laboratory of Semiconductor Material and Metallic Oxides, Faculty of Physics, University of Sciences and Technology (USTHB), BP 32 Bab-Ezzouar Alger, Algérie
[2]Laboratory of Storage and Valorization of Renewable Energies, Faculty of Chemistry, University of Sciences and Technology (USTHB), BP 32 Bab-Ezzouar Alger, Algérie

Abstract: TiO_2 has an easily tunable bandgap and a great absorption dye ability being widely used in many fields and in a number of fascinating applications [1]
Experimental detail: TiO_2 films doped were prepared with TTIP solution as Titanium precursor and quantity of ($ErCl_3.6H_2O$) corresponding to the doping levels of 1%, 2% and 3%. The TiO_2 thin film doped with Erbium is deposed by sol gel spin coating, the layers were deposited on a glass substrate at 3500 rpm of speed for 45 seconds, the layers were crystallized in the air for 500°C for 1 hour, our study is under the influence of doping for 1%, 2% and 3% on the crystalline, optical, morphological and photocatalitic properties of the TiO_2 doped thin film.
Result and discussion
1. Crystallinity study: The results realized by Raman spectrometer confirm that the layers have an anatase phase in 144 cm^{-1}, 193 cm^{-1},519 cm^{-1}, we note that the intensity of the mean peak 144cm^{-1} decreases with increase of doping, that confirm influence in crystallite size with particles of Erbium doping
2. Optical study: Optical study is verified with UV Visible spectrometer, the transmittance spectra indicate a strong absorption, a good transmittance in the visible region about 80% is indicated in transmittance spectra, the band gap (Eg) is obtained from the plot $(\alpha h\nu)2$ against the incident photon energy ($h\nu$) we note a decrease in band gap energy from 3.11 to 2.85 eV
3. Morphological study: Atomic force microscopy technique was employed to investigate the morphology, roughness and grain structure of TiO_2 thin film doped Er, the results show uniform, homogeneous and dense films with small cereals, we observe also that the roughness of layer has been found to decrease with increase in doping, The doping significant effect on the film roughness with the addition of Erbium to solution
Photocatalytic activity: Photocatalytic activity of TiO_2 films doped Erbium was evaluated. Rhodamine B is a recalcitrant dye and TiO2 was successfully tested for its oxidation. An abatement of 33% was obtained under sunlight for an initial concentration of 10 mg/l.
Conclusion: The result on structural, morphological, optical properties and photocatalytic activity of TiO_2 thin film doped Er were studied, Based on the results

ISSN: 0067-3064

obtained, several perspectives are possible such as: photocatalyst, anti-reflective coating and magneto-optic

Reference

[1] Asma Sedik, Ana M. Ferraria, Ana P. Carapeto, Bouzid Bellal, Mohamed Trari, Ratiba Outemzabet, Characterization of TiO2 films obtained by a wet chemical process, Journal of ELECTRICAL ENGINEERING, VOL 68 (2017), NO7, 31–36

ISSN: 0067-3064

The influence of Boride and Nitride on Microstructure and Corrosion Behavior of 42CrMo4 Steel.

P 04

Benhabib Bensalah[a],*, Oulad saad Sofianea, Allaoui Omar[a]

[a] Laboratoire Génie des Procédés, Université de Laghouat, BP 37G, Laghouat, Algeria.

Abstract: This paper presents a study on the corrosion behavior of boriding and nitriding treatments of the low-alloy steel 42CrMo4. The thermochemical treatments were carried out in a solid medium by the powder technique: at a temperature of 900 °C for 4 hours for boriding, and at a temperature of 550 °C for 12 hours for nitriding. The structures of surface layers and diffusion zones were examined by Optical X-ray Diffraction (XRD). Analyses of the surface revealed the presence of FeB and Fe2B compounds for the boride layer, and CrN, Fe3N and Fe4N compounds for the nitride layer. The thickness of boride layer and nitride layer was found to be of 55 and 11 µm, respectively. The microhardness of the boride and nitride layers is between 800 HV0.2 and 1200 HV0.2. The corrosion was evaluated by electrochemical techniques. The potentiodynamic curves of corrosion tests immersed in a 1M HCL solution have shown the beneficial effect of boriding and nitriding treatments on the treated steel 42CrMo4. The samples acquired a high quality protection.

Keywords: boriding ,nitriding, corrosion, microhardness

References

[1] S. Sen, I. Ozbek, U. Sen, C. Bindal. Surf. Coat. Technol. 135 (2001) 173–177.
[2] M. KULKA, N. MAKUCH,P. DZIARSKI,et al., Gradient boride layers formed by diffusion carburising and laser boriding. Optics and Lasers in Engineering. 67(2015) 163–175
[3] M. Keddam, S.M. A diffusion model for describing the bilayer growth (FeB/Fe2B) during the iron powder-pack boriding. Applied Surface Science. 252(2)(2005) 393– 399. doi:10.1016/j.apsusc.2005.01.016
[4] O. Allaoui, N. Bouaouadja, G. Saindernan, Characterization of boronized layers on a XC38 steel. Surface and Coatings Technology. 201(6) (2006) 3475– 3482. doi:10.1016/j.surfcoat.2006.07.238
[5] M.Kulka, N.Makuch, M.Popławski, Two-stage gas boriding of Nisil inN2–H2–BCl3 atmosphere. Surf. Coat. Technol. 244 (2014) 78–86. doi: 10.1016/j.surfcoat.2014.01.057
[6] M. Keddam, M. E. Djeghlal, L. Barrallier, A diffusion model for simulation of bilayer growth (ε/γ′) of nitrided pure iron. Materials Science and Engineering: A. 378(1-2) (2004) 475–478.

ISSN: 0067-3064

Structural, elastic, electronic, and optic study of the anti-perovskite Rb_3BrO.
P 05

Fatiha SAADAOUI[1]*, Nadir CHAMI[2] , Hayat HOCINE[1] , Fatima Zohra DRISS-KHODJA[1], Halima HAMADA[1], Mohammed DRISS-KHODJA[1], Abdelkader ELIAS[1], and Mostefa ZEMOULI[1]

[1] Laboratoire des Etudes Physico-Chimiques, Université de Saïda, 20000 Saïda, Algérie
[2] Departments of Electronics, Faculty of Technology, University of Saïda Dr. Tahar Moulay, 20000 Saida, Algeria

Abstract: In this work, the structural, elastic, electronic, and optic properties of the anti-perovskites Rb3BrO compounds have been investigated using the full-potential linearised augmented plane waves (FP-LAPW) method based on the density functional theory (DFT) implemented in the code wien2k. The analysis of the structural and elastic properties of Rb3BrO were performed with mean of the generalized gradient potential (GGA-PBE, GGA-PBEsol) and the local density approximations(LDA) while the electronic, and optical properties have been performed using the GGA-PBEsol approximation. The obtained results of the lattice parameters are in good agreement with the available experimental data. On the other hand, the material is a narrow band-gap semiconductor of 0.41 eV.

Theoretical study: The calculations are carried out in the framework of the density functional theory DFT [1.2] with the full-potential linearised augmented plane waves method (FP-LAPW). To calculate the exchange and correlation potential, the tree approximations: the generalized gradient GGA-PBE [3], the generalized gradient GGA-PBEsol [4] and the local density LDA [5.6] are tested to find the best structural properties such as the lattice parameter, the bulk modulus and its pressure derivative. A number of k-points of 5000 corresponding to a Monkhorst-Pack grid of 17×17×17 in the first Brillouin zone is used with Rmt×Kmax = 8. The muffin-tin radius of Rb, Br, and O atoms are taken as 2.0, 2.5, and 2.0 au respectively

Results and discussion :

1. Structural properties : The lattice constant calculated with the GGA-PBEsol approximation is in good agreement with the experimental data [7] and the other theoretical calculation [8].

2. Elastic properties: the calculated values of the elastic parameters of Rb3BrO using GGA PBE, GGA-PBEsol and LDA approximations. Obviously, the conditions of mechanical stability in cubic crystals are well satisfied . The value of the bulk modulus obtained from the elastic constants Cij is close t o that obtained by fitting the Birch-Murnaghan equation of states.

ISSN: 0067-3064

3. Electronic properties: We note the existence of a small band-gap of 0.412 eV at point Γ between the valence band and the conduction band, which indicates that the material is a narrow direct-gap semiconductor.

2.4. Optic properties:

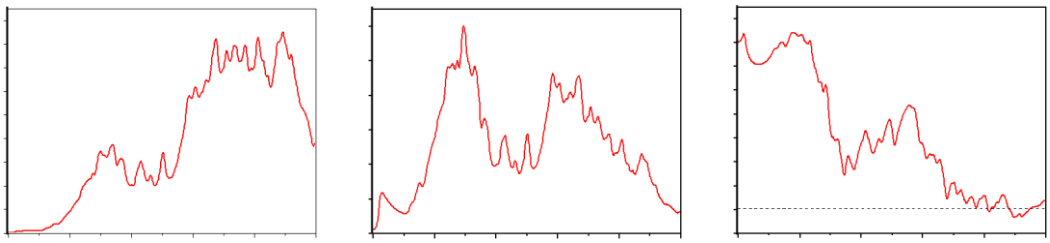

Fig. 1. a and b-The real ε1 (ω) and imaginary ε2 (ω) part of the dielectric function respectively; c-the absorption α(ω) for Rb3BrO

Conclusion: The lattice constant calculated with the GGA-PBEsol approximation is in good agreement with the experimental data and the other theoretical calculation. the conditions of mechanical stability in cubic crystals are well satisfied and anisotropy nature . the material is a narrow direct-gap semiconductor and The threshold value of the absorption coefficient for Rb3BrO is around 0.412 eV.

References

[1] P. Hohenberg and W. Kohn, Physical review. 136 (1964) B864. https://doi.org/10.1103/PhysRev.136.B864
[2] W. Kohn and L. J. Sham, Physical review. 140 (1965) A1133.
[3] J. P. Perdew, K. Burke, and M. Ernzerhof, Physical review letters. 77 (1996) 3865. https://doi.org/10.1103/PhysRevLett.77.3865
[4] J. P. Perdew, A. Ruzsinszky, G. I. Csonka, O. A. Vydrov, G. E. Scuseria, L. A. Constantin, X. Zhou, and K. Burke, Physical Review Letters. 100 (2008) 136406. https://doi.org/10.1103/PhysRevLett.100.136406
[5] D. M. Ceperley and B. Alder, Physical Review Letters. 45 (1980) 566. https://doi.org/10.1103/PhysRevLett.45.566
[6] J. P. Perdew and A. Zunger, Rev. B 23 (1981) 5048. https://doi.org/10.1103/PhysRevB.23.5048
[7] S. Sitta, K. Hippler, 19 Vogt, H. Sabrowsky, Z. anorg. allg. Chem. 597 (1991) 197
[8] Yinchang Zhao, Chao Lian,Shuming Zeng, Zhenhong Dai, Sheng Meng and Jun Ni PHYSICAL REVIEW B101, 184303 (2020)

ISSN: 0067-3064

Investigation of argon/methane cold atmospheric pressure plasma jet.
P 06

F. Bedrouni [1], M. Ochabane [2], F. Almabouada [2], N. Saidi-Amroun [1]

[1] Material Physics Laboratory, University of Science and Technology Houari Boumediene (USTHB), Bab Ezzouar, Algeria.
[2] Ionized Media and Lasers Division, Center for Development of Advanced Technologies (CDTA), Baba Hassen, Algeria

Abstract: In this study, atmospheric pressure plasma jet (APJ) of argon/methane mixture was sustained by 12 kHz sinusoidal ac power source. The optical emission spectroscopy (OES) was employed to investigate the plasma chemistry at three different positions along the plasma jet at flow rate 3 and 5 L/min. The spectra recorded at axial position (collinear to the plasma jet) present the highest intensity of the species.

References

[1] A. K. Srivastava, M. K. Garg, K. G. Prasad, V. Kumar, M. B. Chowdhuri, and R. Prakash, IEEE Transactions on Plasma Science, 35, 1135-1142, (2007).
[2] X. Lu, S. Reuter, M. Laroussi, and D. Liu, CRC Press, 2019
[3] R. Zaplotnik, G. Primc, and A. Vesel, Applied Sciences, 11, p. 2275, 2021
[4] J. Turicek, N. Ratts, M. Kaltchev, and N. Masoud, Plasma Sources Science and Technology, 30, 025005 (2021).
[5] N. Georgescu, C. P. Lungu, A. R. Lupu, and M. Osiac, IEEE Transactions on Plasma Science, 38, 3156-3162 (2010)

ISSN: 0067-3064

Magnetic perovskite nanostructure synthesis by hybrid solid state and solgel auto combustion for photocatalytic drug degradation.

P 07

Ilyes baba-Ahmed[1,2], Abdelkader Abderrahmane[3,4], Asma Tadji[5]

[1] Energy Processes and Nanotechnology Laboratory, Physics Department, Sciences Faculty, Saad Dahleb Blida 1 University, BP 270, Blida 09000, Algeria.
[2] Biomedical engineering Department, Technology Faculty, Aboubekr Belkaid University,
Tlemcen 13000, Algeria.
[3] Electrical Engineering Department, Faculty of Sciences and Technology, University Abdelhamid Ibn Badis Mostaganem, BP 188, Mostaganem 27000 Algeria.
[4] Department of Electrical Engineering, Chosun University, 375 Seosuk–dong, Dong–gu, Gwangju 501–759, Republic of Korea.
[5] Higher National School of Renewable Energy, Environment and Sustainable Development, Constantine Road. Fasdis, Batna 05078, Algeria.

Abstract: The photocatalytic efficiency of strontium titanate ($SrTiO_3$ or STO) can be significantly enhanced by improving its magnetic properties. As photocatalyst, $SrTiO_3$ is well known for its exceptional absorption of visible light, generating electron-hole pairs that facilitates the degradation of organic pollutants during the process. The introduction of magnetic ions, like iron (Fe) or cobalt (Co), into $SrTiO_3$ can augment its functionalities by harnessing the introduced magnetic properties [1]. In this research, we report the synthesis of new magnetic $NiFe_2O_4$/STO nanostructure. Due to its new magnetic properties of STO nanoparticles, the application of an external magnetic field enables precise control over photocatalytic reactions. Additionally, the photocatalyst can be more easily recovered after the reaction, allowing for its reuse, resulting in cost savings and reduced environmental impact. The redox properties of $SrTiO_3$ are strengthened by the magnetic effect, enabling the degradation of more complex organic pollutants, including pharmaceutical residues and toxic chemicals [2]. This ongoing development offers new opportunities for reliable and effective photocatalytic applications [3].

Keywords: perovskite, nanostructure, solid state , auto combustion, photocatalytic solgel,

References

[1] Baba-Ahmed, I., Ghercă, D., Iordan, A.R., Palamaru, M.N., Mita, C., Baghdad, R., Ababei, G., Lupu, N., Benamar, M.A., Abderrahmane, A. and Roman, T., 2021. Sequential synthesis

ISSN: 0067-3064

methodology yielding well-defined porous 75% $SrTiO_3$/25% $NiFe_2O_4$ Nanocomposite. Nanomaterials, 12(1), p.138.
[2] BAALOUDJ, O., Nasrallah, N., Assadi, A. and Kenfoud, H., 2020. Modeling of the photocatalytic degradation of ibuprofen using the nanocomposites $ZnCr_2O_4$.
[3] Matassi, S., Benrabaa, R., Benturki, O., Brahimi, R., Akkar, M., Zouaoui-Mahzoul, N. and Meddour-Boukhobza, L., 2022. Spinel Mixed Oxides Prepared by Soft Chemistry Methods for Catalytic Hydrogenation of 2-Nitrophenol to 2-Aminophenol. Arabian Journal for Science and Engineering, 47(6), pp.7171-7181.

ISSN: 0067-3064

First principles study on phonon dispersion, elastic and thermodynamic properties of LaBa compound for Hydrogen storage
P 08

Khadidja MISSOUM, Saïd MESKINE, Abdesamed BENBEDRA, BOUGUERRA Zakarya and HAMMADI Mohamed

e-mail: khadidja.missoum.etu@univ-mosta.dz

Abstract: Currently, the solid-state storage option of hydrogen has become a future energy carrier for electricity generation and storage. In the present study, the density functional theory (DFT) and the ab initio method of the full-potential linearized augmented plane-wave (FP-LAPW) method, as implemented in the code WIEN2K, have been used to calculate the phonon dispersion, structural, elastic, and thermodynamic properties of the binary intermetallic compound LaBa. The computed structural properties of LaBa compounds in various structures were studied to obtain the equilibrium lattice optimization parameters and formation energy. The structural stability is examined from phonon dispersion. We also investigate the elastic and thermodynamic properties of the above compound to prove its stability.

References

[1] Selvam P, Viswanathan B, Swamy CS, Srinivasan V. Studies on the thermal characteristics of hydrides of Mg, Mg2Ni, Mg2Cu and Mg2Ni1-xMx (M ¼ Fe, Co, Cu or Zn; 0 < x < 1) alloys.Int J Hydrogen Energy 1988;13(2):87e94. . https://doi.org/10.1016/0360-3199(88)90045-6.

[2] Xiao XB, Zhang WB, Yu WY, Wang N, Tang BY. Energetics and electronic properties of Mg7TMH16 (TM¼Sc, Ti, V, Y, Zr,, Nb): an ab initio study. Physica B 2009;404(16):2234e40. https://doi.org/10.1016/j.physb.2009.04.013.

[3] Prayoonsak Pluengphon , Prutthipong Tsuppayakorn-aek, Burapat Inceesungvorn, Thiti Bovornratanaraks. Pressure-induced structural stability of alkali trihydrides and H2-desorption occurrence: Ab initio study for hydrogen storage improvement. Hydrogen Energy Publications LLC, 2020.
https://doi.org/10.1016/j.ijhydene.2020.06.267.

[4] Lys, A.; Fadonougbo, J.O.; Faisal, M.; Suh, J.-Y.; Lee, Y.-S.; Shim, J.-H.; Park, J.; Cho, Y.W. Enhancing the Hydrogen Storage Properties of AxBy Intermetallic Compounds by Partial Substitution: AShort Review. Hydrogen 2020, 1, 38-63.

ISSN: 0067-3064

Spray-Coated assisted synthesise of Cu: SnS2thin films for antibacterial activities and photocatalytic properties. P 09

Imane Radja[1], Abdelkader Nebatti Ech-Chergui[2], Ali sadek Kadari[1], Nour el houda[1], Dris-Koudja[1], Bouhalouane Amrani[1],

[1]Laboratory of Theory and Simulation of Materials, Faculty of Exact and Applied Sciences, University of Oran1 Ahmed Ben Bella, Oran, Algeria
[2]Laboratory of applied hydrology and environment, University of Ain-Temouchent Belhadj Bouchaib, faculty of sciences and technology, Algeria.
Email: imaneradja@gmail.com and abdelkader.nebatti@univ-temouchent.edu.dz

Abstract: Tin Sulfide (SnS2) based material possess good photocatalytic activity for hydrogen evolution. To further improve photocatalytic efficiency, Cu atoms are doped into Sulphur vacancies. This incorporation of Cu atoms results into increase in charge carried density of photogenerated carriers. This work focuses on structural, optical, morphological & magnetic behavior of SnS2 thin films with different doping concentration of Cu prepared by spray pyrolysis method. XRD pattern reveals the characteristic peak of SnS2 along (101) plane. Crystallite size decreases while dislocation density increases with increase in Cu doping. Raman spectra reveals the characteristic peak of SnS2 at 314.4 which is assigned to the A1g mode. Optical transmittance of Cu doped SnS2 films is 45%. SEM image reveals the porous structure of films with decrease in porosity with increase in Cu doping concentration. The FTIR spectra confirms the Sn-S bond present at 753 cm-1. Electron Paramagnetic Resonance (EPR) studies reveals the Sulphur vacancies present in Cu doped samples. The outcome of these results indicates that Cu doped SnS2 are good candidate for antibacterial activities with good photocatalytic properties.

References

[1] Tair, S., et al., n-type SnS2 thin films spray-coated from transparent molecular ink as a non-toxic
[2] Zhang, J., R. He, and X.J.N. Liu, Efficient visible light driven photocatalytic hydrogen production from water using attapulgite clay sensitized by CdS nanoparticles. 2013. 24(50): p. 505401.
[3] Ech-Chergui, A.N., et al., Spray coated of newly La-doped SnS2 thin films for photocatalytic.

ISSN: 0067-3064

Electrical properties of CO_2 gas sensors based on Al/NiO/MPS/n-Si MOS structure. P 10

K. M'hammedi [1], M.Berouaken [2], A. Mansri [2], F. Bouamra[1], N. Gabouze [2]

[1] Saad Dahleb Blida 1 University, [1]Laboratory of Physical-Chemical Inorganics Materials and their Applications, Physics Department, 09000 Blida, ALGERIA
[2]Centre de Recherche en Technologie des Semi-conducteurs pour l'Energétique (CRTSE), 02 Bd, Frantz Fanon, B.P. 140, Algiers, ALGERIA

Abstract : A CO_2 gas sensor has been developed using an Al/NiO/MPS/n-Si MOS structure. The behaviour of the structure was analysed through the current–voltage (I-V) characteristics at room temperature when exposed to CO_2 gas. Furthermore, variations in capacitance-voltage (C-V) and conductance-voltage (G/-V) were observed across a frequency range of 10 Hz to 700 KHz at room temperature, both in the presence of air and CO_2 gas. At low frequencies, the conductance measurements indicate the presence of interface states that displayed a strong dependence on frequency.

Keywords: Macroporous Silicon, Nickel oxide, CO_2 Gas sensor, Capacitance, Conductance.

Introduction: The metal-oxide-semiconductor (MOS) structures have attracted considerable interest because of its large potential advantages in elaboration formation of electronic devices [1]. Early studies have presented the availability of macroporous silicon (MPS) in MOS diode for gas sensor application [2]. However, recent studies focus on improving the performance of the device by means of the insertion of new metal oxides at the metal/semiconductor interface, such as vanadium oxide, tin oxide, titanium oxide, and nickel oxide (NiO), etc [3].

Experimental study: Nanocomposite NiO/MPS was elaborated by the deposition of NiO solution into MPS films. The MPS films were formed using an electrochemical etching process under front side illumination Process, in addition to the standard etching solution of HF and ethanol for porous silicon, an oxidizing agent, H_2O_2, was introduced to enhance the etching process and achieve a faster etching rate. The sensing performances of the Al/NiO/MPS/n-Si structure were examined at room temperature using a gas sensing system. The sensor was mounted on a test holder and connected to a measuring instrument (Potensiostat–Galvanostat (VMP3 - 615, CRTSE)) that was controlled by a microcomputer piloted with Esclab software.

Results and discussion:

ISSN: 0067-3064

1. Structural properties: The XRD studies revealed that the nickel oxide films present a cubic structure with a (200) preferential orientation. The SEM images reveal that pores are filled with NiO nanocrystallites.
2. Optical properties: The optical properties were examined using UV-Vis spectrometer. The optical measurements indicated that the NiO films exhibit an energy gap of 3.8 eV [4].
3. Electrical properties: The current – voltage (I-V) characteristic of Al/NiO/MPS/n-Si structure was investigated at room temperature in the presence of CO_2 gas. In addition, the capacitance- Voltage (C-V) and Conductance- Voltage (G/ω- V) have been performed on Al/ NiO/MPS/n-Si structure in the range from 10Hz to 700 KHz at room temperature in the presence of air and CO_2 gas. It was shown that C-V and G/ω- V of the MOS structure are sensitive to frequency and that the sensor characteristics are modified in the presence of CO_2 gas. At low frequencies, the conductance measurements indicate the presence of interface states which are strongly frequency dependent that yield an excess capacitance and conductance.

Conclusion: In the present study, the current conduction mechanism across Al/NiO/MPS/n-Si structure using *I- V, C- V* and $G/\omega - V$ measurements in vacuum and under CO_2 gas at room temperature has been studied. The Al/NiO/MPS/n-Si characteristics are shown similar to those of metal-insulator semiconductor structures. The values of the ideality factor (n) and the series resistance (R_s) are shown to decrease when CO_2 gas is in contact with the structure, indicating the sensitivity effect of the structure to CO_2 gas. The capacitance- Voltage (C-V) and Conductance- Voltage (G/ω-V) performed on Al/ NiO/MPS/n-Si structure in the range from 10Hz to 700 KHz at room temperature in the presence of air and CO_2 gas indicated that both C-V and G/ω-V of the MOS structure are sensitive to frequency. The results showed that both the flat band potential of the heterojunction and doping level of the NiO are increased under CO_2 gas injection indicating that CO_2 creates holes at the NiO surface leading to increases the carrier concentration (N_A) and negative shift of V_{fb}.

References

[1] S. M. Sze, Physics of Semiconductor Devices, second ed. Willey & Sons, New York, 1981
[2] K. M'hammedi, M. Berouaken, N. Gabouze, Bull. Mater. Sci. (2023) 46:123
[3] O Pakma, N Serin, T Serin and S ¸ Altındal, Semicond. Sci.Technol. 23 (2008) 105014 (9pp).
[4] K. M'hammedi, H. Haine, N. Bourenane, H. Menari, Gabouze N, Arab. J. Sci. Eng (2019) 44 521

ISSN: 0067-3064

Sol-Gel Elaboration and X-Ray Diffraction analysis of SnO_2 thin films
P 11

Boudjemline Ihssen [1], Bouamra Faiza [1], M'hammedi Kawther [1], Zerhouni Noureddine [2]

1 LPCMIA, Physics Dept., Saad Dahlab University, Blida1, Route de Soumaa, BP 270, Blida 09000, Algeria.
2 FEMTO-ST, Franche-Comté Electronique Mécanique Thermique et Optique – Sciences et Technologies, France.

Abstract: The elaboration with sol-gel dip coating technique of the SnO_2 metal oxide thin films has been successfully released in this study. The Tin (II) dihydrate chloride ($SnCl_2$ $2H_2O$) has been used as precursor. This research hinges on the optimizing of two from more pivotal parameters: (1) the number of dipping steps and (2) the incorporation of additives. These performance variables wield profound influence in shaping the characteristics of the thin films, a critical requirement for gas sensing devices. Obtained SnO_2 thin films, are analyzed with X-ray diffraction and determine the structural parameters to improve the presence of the tetragonal phase through the distinct observation of peaks corresponding to SnO_2 diffraction planes.

Keywords: Detectors, Oxide nanomaterials, structural properties, thin films, DRX.

Introduction: One of the most significant TCO materials is Tin oxide SnO_2 thin films. It's an n-type semiconductor are highly significant in numerous applications. SnO_2 thin films have been always the fundamental of significant technological advancements. They ushered in significant technological advancements. Their versatility shines in a multitude of applications, encompassing sensing, thermal mirrors, and the coveted role of a transparent conductive coating for glass substrates [1-2]. Actually, it's within the domain of sensing that SnO_2 thin films claim their famous importance as the preferred choice for commercial sensor devices. This choice is a recognition to the challenging pursuit of optimal materials that meet the stringent demands of sensor performance as well as: sensitivity, minimal response time, linearity and stability. In this work, we explore meticulously the intricacies of preparing SnO_2 thin films via the sol-gel Deep Coating (SG-DC) technique, an endeavor that entails the optimization of diverse parameters including dip numbers and solution formulations. Subsequently, we go deeper into the elucidation of results stemming from X-ray pattern synthesis.

Experimental details and results: Our experiments commit on the construction of both pure and conditioned SnO_2 thin films, orchestrated with and without the strategic inclusion of additives. This process unfolds with the precise blending of Tin (II) chloride dihydrate, $SnCl_2$ $2H_2O$, and ethanol, yielding the tin acetate powder. The

ISSN: 0067-3064

formulation of SnO_2 solutions with additives has a similar process, with a unique distinction of incorporating additives. Specifically, the first sample fuses with DEA, while the second uses with HCl. These subsequent solutions serve as the canvas for the artful deposition of thin films through the dip coating technique. In addition, the meticulous execution of these experiments reaches its in positive limits in the context of the LPCMIA research laboratory. This might confirm the corresponding phase unfolds through an exhaustive characterization, skilfully performed via X-ray diffraction as visually illustrated in Figure 1 and Figure 2. Furthermore, the acquired patterns are subjected to in-depth analysis using the HighScore program, proving the omnipresence of the tetragonal phase within the elaborated SnO_2 thin films, obtained results are presented in the table.

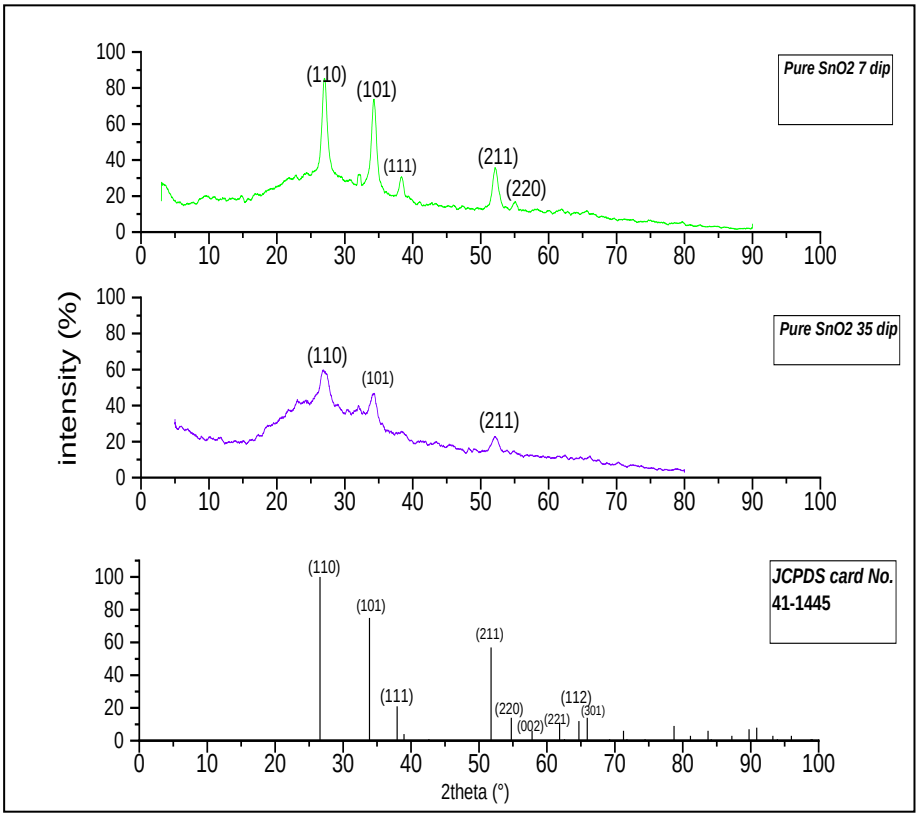

Fig. 01: X-ray diffraction spectra of pure SnO_2 composed of 07 and 35 dip.

ISSN: 0067-3064

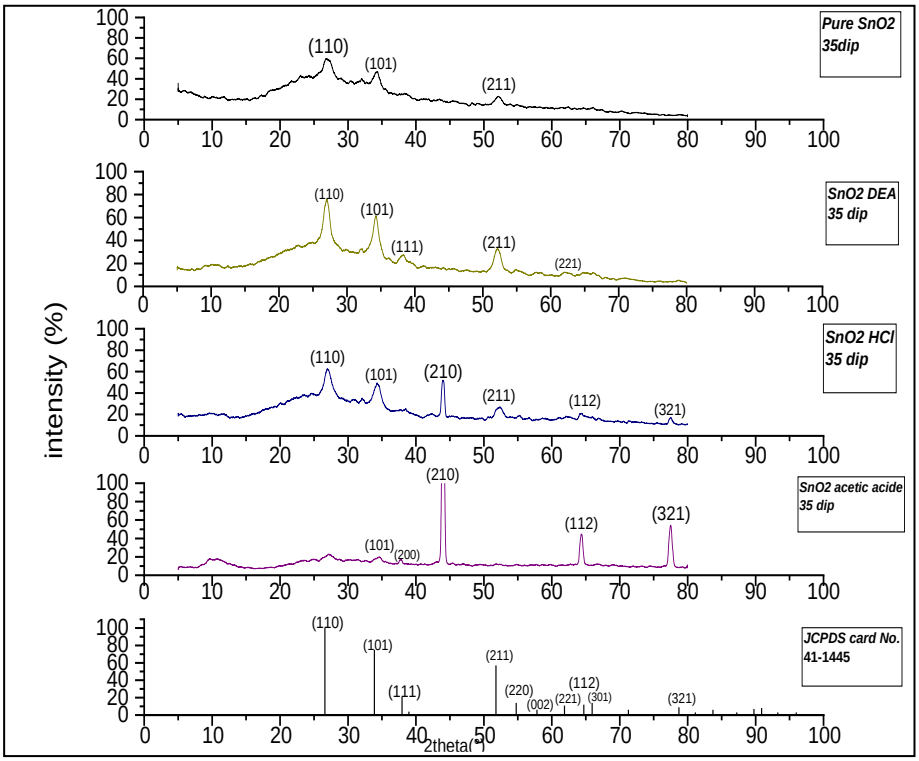

Fig. 02: X-ray diffraction spectra of pure SnO_2 with different additives.

Table 01: the lattice parameters and crystallite size calculated for all samples.

Samples	a=b (Å)	c (Å)	D (nm)
Pure SnO_2 (7 dip)	**4.6791**	**3 .1417**	**32,94**
Pure SnO_2 (35 dip)	**4.7179**	**3.1404**	**10.05**
SnO_2 DEA (35 dip)	**4.6504**	**3.1507**	**11,38**
SnO_2 HCl (35 dip)	**4.6719**	**3.1448**	**31,5**
SnO_2 acetic acid (35 dip)	**4.7613**	**3.1087**	**65,32**

Conclusion : In summary, this research show that elaborated thin films of pure and conditioned SnO_2 with optimizing parameters has successfully synthesized, asserting the realization of the coveted phase through the lens of XRD analysis. These findings bolster the promising potential of SnO_2 as a detection material in the sphere of metal oxide gas sensors. This study opens the door to the development of more metal oxide

ISSN: 0067-3064

gas sensors with the aim of improving their performance, paving the way for the development of more.

References:

[1] M.A. Gondal, Q.A. Drmosh, T.A. Saleh, Preparation and characterization of SnO_2 nanoparticles using high power pulsed laser, Appl. Surf. Sci. 256 (2010) 7067–7070.

[2] S.G. Onkar, F.C. Raghuwanshi, D.R. Patil, T. Krishnakumar, Synthesis, characterization and gas sensing study of SnO_2 thick film sensor towards H2S, NH3, LPG and CO2, Mater. Today Proc. 23 (2020) 190–201.

ISSN: 0067-3064

Mössbauer Spectroscopy Study of Iron-based Nano-particles Synthesized by Hydrothermal Method
P 12

Mohamed Walid HALIMI[1*], Abderrahim GUITTOUM[2], Messaoud HEMMOUS[2], Imane Bouelkreb[3]

[1] Department of Physics, University of Blida 1, Blida, 09000, Algeria
[2] Nuclear Research Centre Of Algeria CRNA, Algiers, 16000, Algeria
[3] Department of physics, University of Boumerdes , Boumerdes 35000, Algeria

Abstract: Mössbauer spectroscopy was used to characterize the synthesized $Fe_{30}Co_{70}$ and $Fe_{10}Co_{90}$ alloys prepared by hydrothermal method. The transmission ^{57}Fe Mössbauer spectra were measured at room temperature using ^{57}Co γ-ray source with an Activity ~50 mCi in order to learn about hyperfine interactions and parameters. Mössbauer spectroscopy results observe only one Zeeman sextet and one quadrupole doublet which confirms the body-centered cubic structure BCC. As a result of the analysis of the distributions hyperfine magnetic field the average values of the hyperfine parameters of the Mössbauer spectra were obtained $\langle B_{hf}\rangle_{Fe30Co70}$ = 32.68T and $\langle B_{hf}\rangle_{Fe10Co90}$ = 29.56 T. Therefore, it is observed that the increasing of the cobalt concentration decreases the hyperfine field.

Keywords: FeCo alloys; Hyperfine interactions; Mössbauer spectroscopy; Nanoparticules.

Introduction: FeCo nanoparticles (NPs) with their exceptional soft magnetic properties and mechanical properties have potential applications in ultrahigh magnetic recording, drug delivery and in biomedical field [1-5]. Such bimetallic NPs are highly challenging to synthesize [2]. The hydrothermal method has proven to be an efficient technique for synthesizing FeCo NPs for numerous advantages, such as it low-cost, simplicity, and facile adjusting the synthesis parameters, such as temperature, pressure, and reaction time [3-5]. One of the techniques used to probe the structural and magnetic properties is Mössbauer spectroscopy (MS), a non- destructive nuclear technique which provides valuable insights into the local environment and understanding of the crystallographic structure and magnetic behavior of the synthesized nanoparticles [3,5]. It is particularly effective in analyzing hyperfine interactions and parameters such as isomer shifts IS, quadruple splitting QS and hyperfine magnetic field $B_{hf,}$[5]. In this work, we present the analysis using MS of $Fe_{30}Co_{70}$ and $Fe_{10}Co_{90}$ NPs synthesized by the hydrothermal method. The main objectives are to investigate the structural characteristics of the NPs at the atomic level, to assess the distribution of Fe and Co

ISSN: 0067-3064

atoms within the alloy lattice, and to comprehend the magnetic properties exhibited by these nanoscale materials.

Materials and Methods: The synthesized $Fe_{30}Co_{70}$ and $Fe_{10}Co_{90}$ were prepared as NPs powders at the Nuclear Research Centre of Algeria (CRNA) laboratory. Hyperfine interactions and parameters information about the NPs as prepared were obtained by MS with conventional spectrometer apparatus setup of WISSEL instruments performed in transmission geometry. The radioactive source is a ^{57}Co γ-ray source with an Activity ~ 1.85 GBq. The analysis of Mössbauer spectra curves was by using WinNormos,. All measurements were calibrated at room temperature (RT) with a standard metallic α-Fe absorber foil.

Results and discussion: The spectra $Fe_{30}Co_{70}$ and $Fe_{10}Co_{90}$, fitted using WinNormos first with the "Site" option and then with the "Dist" option with two subspectra, according to the best fit by χ^2. A reasonable fit with Site in both cases, exhibit a sextet, with a relative area of 79.754% with parameter B_{hf} = 32.727 T and line width Γ=0.8404 mm/s for $Fe_{10}Co_{90}$ and 79.53% with parameter B_{hf} =34.429 T and Γ=0.958 mm/s for $Fe_{30}Co_{70}$. The main contribution to the spectra comes from the magnetic sextet which is assigned to ferromagnetic FeCo phase while the doublet is assigned to paramagnetic phase so the ferromagnetic phase is the dominant one. This result was used to do the distribution fit (Dist), the subspectrum isomer shift for the magnetic subspectrum block is incremented by a shift given by the parameter "DTI". The average hyperfine field value from these fits are $\langle B_{hf} \rangle_{Fe30Co70}$= 32.68 T with relative spectral area 80.995% and $\langle B_{hf} \rangle_{Fe10Co90}$= 29.56 T with relative spectral area 90.143%. The results observe indicates Co concentration dependence, for Co-rich alloys ($Fe_{10}Co_{90}$) the FCC (face-centered cubic structure) contributing to the decrease in B_{hf} due to the absence of BCC. The obtained NPs do not present any oxide shell, but it is still possible that there is a smaller amount of oxide surrounding the FeCo particles.

Conclusion: The MS studies of $Fe_{30}Co_{70}$ and $Fe_{10}Co_{90}$ synthesized by hydrothermal method have been carried out at RT and shown that with increasing the cobalt content, the sample decreases the hyperfine magnetic field. The obtained results support the suggestion that the applied ^{57}Fe MS method for investigation properties of alloys is a good tool in the case of hydrothermal synthesized iron-based NPs, and it can supply experimental data.

References

[1] S.-J. Oh et al. Mössbauer analysis on the magnetic properties of Fe–Co nanoparticles synthesized by chemical vapor condensation process Journal of Magnetism and Magnetic Materials 280 (2004) 147–157

[2] J. Zhou et al. Hydrothermal synthesis of polyhedral FeCo alloys with enhanced electromagnetic absorption performances. Journal of Alloys and Compounds 794 (2019) 68-75

[3] Zhen Liu et al. Hydrothermal synthesis of FeCo alloys with excellent microwave Absorption: Effect of reaction time. Journal of Magnetism and Magnetic Materials Volume 568, 2023, 170365

ISSN: 0067-3064

[4] Karipoth et al. Magnetic properties of FeCo alloy nanoparticles synthesized through instant chemical reduction. JOURNAL OF APPLIED PHYSICS 120, 123906 (2016)
[5] Z. Klencs_ar et al. Structure and magnetism of Fe-Co alloy nanoparticles. Journal of Alloys and Compounds 674 (2016) 153-161
[6] H. H. Hamdeh, B.Fultz, and D. H. Pearson Mossbauer spectrometry study of the hyperfine fields and electronic structure of Fe-Co alloys Physical review. B, Condensed matter VOLUME 39, NUMBER 16 PART A 1989

ISSN: 0067-3064

Two dimensional dipolar Bose gas with three-body interactions in weak disorder potential
P13

K. Redaouia[1] & A. Boudjemaa[2]

[1] Department of Materiel sciences , Jillian-Bounaama University of Khemis-Miliana, Khemis Miliana, 44225, Algeria*
[2]Laboratory of Mechanics and Energy, Hassiba Benbouali University of Chlef, P.O. Box 78, 02000, Ouled-Fares, Chlef, Algeria.
*Correspondance : k.redaouia@univ-dbkm.dz

Abstract: We study the effects of weak disorder with Gaussian correlation function on a dilute quasi-two-dimensional dipolar Bose-condensed with two- and three-body contact interactions using the Hartree-Fock-Bogoliubov theory. We analyze numerically the effects of three-body interaction on the energy spectrum, the quantum disorder fluctuations to the condensate depletion and the disorder energy, of the system. We show that increasing the three-body contact interactions leads to the appearance of rotonization and condensate instability at stronger dipole-dipole interaction. We also show that the intriguing interplay of the disorder, dipole-dipole interactions and three-body interactions plays a fundamental role in the physics of the system. Interestingly, we find that the three-body interactions release atoms localized in the respective minima of the random potential.

Keywords: Bose Einstein condensate, quantum gases, dipolar Bose gas, disorder potential.

.

ISSN: 0067-3064

Characterization of Seawater Reverse Osmosis Fouled Membranes From Large Scale Commercial Desalination Plant.

P 14

O. Naimi[1], A. Belatoui[2]

[1], Environmental Technologies Research Laboratory (LTE). National Polytechnic School of Oran Maurice Audin, B.P 1523 El M'naouer, Oran 31000 -Algeria.
[2] National Education Research Institute-INRE, BP 193,Zone Industrielle , Oued Romane El Achour – Algeria.
E-mail: Oussama.naimi91@gmail.com

Abstract: The objective of this study is to investigate the ageing state of a used reverse osmosis (RO) membrane taken in Algeria from the Benisaf Water Company seawater desalination unit. The study consists of an autopsy procedure used to perform a chain of analyses on a membrane sheet.
In most cases the effects of ageing are little or poorly known at the local level and global measurements such as (flux, transmembrane pressure, permeate flow, retention rate, etc.) do not allow characterization. Therefore, a used RO (reverse osmosis) membrane was selected at the site to perform the membrane autopsy tests.
These tests make it possible to analyze and identify the cause as well as to understand the links between performance degradation observed at the macroscopic scale and at the scale at which ageing takes place. External and internal visual observations allow seeing the state of degradation.
Materials and methods: The fouled RO membrane element (HYDRANAUTICS SWC 5) serial number: A1497030 selected for the autopsy study had been in service for nearly 2 years in a water treatment facility operated by Benisaf Water Company of Ain Temouchent in the Ouest of Algeria. Atomic absorption spectrometry (AAS) is an analytical technique that measures the concentrations of elements.
The Attenuated total reflectance infrared is a technique that can provide valuable information related to the chemical structure of membrane or characterize the fouling layer thet may be present on the membrane surface.
Results and discussion: Microscopic observation of samples reveals the importance of fouling deposition in the membrane surface. The SEM images show the morphological aspect of the fouling as well as the importance of the thickness of the layers as shown in figure 1. The main absorption bands were in the vicinity of 1020 cm-1(Si-O and Al-O) of silicate.

ISSN: 0067-3064

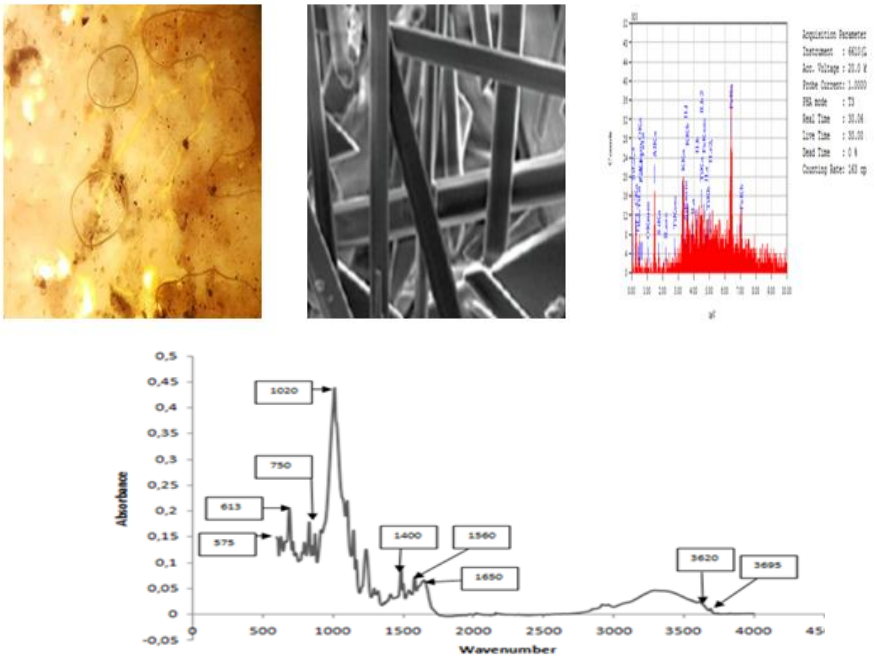

Figure 1. Microscopic observation, SEM images ar TIR spectrum of the fouled membrane extract.

Conclusion: The results obtained are consistent and complementary to each other. From the results of the study the following conclusions can be drawn:

- The extent of fouling was uneven on the membrane surface with the areas below or near the feed spacer being most affected. The fouling in areas further away from the strands was generally less loaded.
- Inorganic elements found with a high percentage are Fe, Al. The use of iron chlorides as coagulant and A maleic acid-based as antiscalant can contribute to the increase in the percentage of these elements in the fouling.

ISSN: 0067-3064

First-principles study on the Structural, electronic and optical properties of double perovskites K2AgAsBr6 for solar cell application.

P 15

Samir CHAREF [a], Abdenacer ASSALI [b], Abdelkader BOUKORTT [a]

[a] Elaboration and Characterization Physical Mechanics and Metallurgical of Materials (ECP3M) Laboratory, Abdelhamid Ibn Badis University-Mostaganem, Route Nationale N°11, Kharrouba, 27000 Mostaganem, Algeria.
[b] Research Unit in Optics and Photonics- Center for Development of Advanced Technologies (UROP- CDTA), University of Setif, 1, El-Bez, 19000 Setif. Algeria.
[*]Email : samir.charef.etu@univ-mosta.dz

Abstract: Double Perovskites are among the most promising materials for solar cells application. In this work, we will focus on the structural, electronic and optical properties of the lead-free double perovskite K2AgAsBr6, using the full-potential linearized augmented plane-waves method (FP-LAPW), based on density functional theory (DFT), implemented in the WIEN2K code, the exchange-correlation potential is treated with the approximations nKTP-mBJ-GGA. The structural parameters are calculated through optimization and analytical schemes. The bandgaps of K2AgAsBr6 has been calculated to be 1.34 eV, enabling various optoelectronic and transport applications. Furthermore, the absorption coefficient ranges from infrared to visible and ultraviolet regions, increasing their significance for diverse applications in optoelectronics.

Keywords: K2AgAsBr6, solar cell, WIEN2K, The absorption coefficient, electronic properties.

References

[1] Ali, Malak Azmat, et al. "The study of new double perovskites K2AgAsX6 (X= Cl, Br) for energy-based applications." *Journal of Taibah University for Science* 17.1 (2023): 2170680.
[2] Zanib, Maiza, et al. "A DFT investigation of mechanical, optical and thermoelectric properties of double perovskites K2AgAsX6 (X= Cl, Br) halides." Materials Science and Engineering: B 295 (2023): 116604.

ISSN: 0067-3064

The effects of boriding and boroaluminizing thermochemical treatments in solid medium on the microstructure and the surface properties of XC38 steel
P 16

OULADSAAD Sofiane *, BENHABIB Bensalah

Email: sofianesdm@yahoo.fr and b.benhabib@lagh-univ.dz

Abstract: In this work, the effects of boriding thermochemical treatment in solid medium on the microstructure and surface properties of XC38 steel were studied. The layers obtained are characterized by optical microscopy, X-ray diffraction and Vickers microhardness. The study shows the formation of a 70 µm diffusion layer with a significant improvement in the microhardness value which reaches 1422 HV.

Introduction: Surface modification of materials is an efficient and cost-effective solution to improve component life. Surface modification or surface engineering is done using coatings and thermochemical treatments. Boriding is a thermochemical treatment that involves the diffusion of boron atoms through the surface of treated materials to form borides with high mechanical characteristics (high hardness, low coefficient of friction, resistance to abrasive and adhesive wear [1,2,3]. Boroaluminizing is the saturation with boron and aluminum, this treatment has a fundamental offers a good combination of high hardness and oxidation-corrosion resistance[4 5] .The aims of this work is to produce boride and boroaluminide coatings on XC38 steel substrate using pack cementation technique and the characterization of obtained layers XC 38 AISI 1035 steel (0.35% low carbon ordinary steel) is selected as the substrate for boriding treatments because of its cost-effectiveness and extensive use in many industrial applications After boriding treatment, the treated steel is expected to improve the properties of the substrate in terms of corrosion resistance, high temperature oxidation resistance and wear resistance, which can reduce economic losses due to environmental deterioration

References

[1]Ucar N, Turku N, Ozdemir A F & Calik A, Acta Phys Pol A, 130 (2016) 492.
[2]Khenifer M, Allaoui O & Taouti M B, Acta Phys Pol A, 132 (2017) 518.
[3]Rayane K, Allaoui O & Allaoui L A, Acta Phys Pol A, [4]Sambogna G, Palombarini G, Carbucicchio M & Ciprian R,Hyperfine Interactions, 187 (2008) 131.
[5]Zakhariev Z, Marinov M, Penyashki T & Tsokov Pl, J Alloys Compd, 459 (2008) 501.132 (2017) 521.
[6] SUWATTANANONT, Naruemon. Surface treatment of ferrous alloys with boron. 2004.

ISSN: 0067-3064

Synthesis and Characterization of 15% Ni/MgO-CeO2and Its Application in Photocatalytic Degradation of Dyes. P 17

Nora Yahi

Laboratory LCPMM, Faculty of Science, University of Blida 1, B.P 270, Blida, Algeria

Abstract: Contemporary society grapples with a significant hurdle in the form of environmental pollution. Within this predicament, dyes play a pivotal role, instigating degradation and the subsequent decline of both f lora and fauna[1-3]. Photocatalysis emerges as a notably potent and progressive oxidation technique, particularly for addressing water contamination induced by azo dyes, presenting a compelling solution in this landscape. The process is rooted in the stimulation of a semiconductor, which acts as a catalyst, prompted by either visible or UV radiation. This mechanism facilitates swift oxidation, culminating in the comprehensive mineralization of a diverse range of organic compounds, including those with nitrogen content, which are adsorbed onto the catalyst. In this particular context, an investigation was carried out, focusing on the degradation of two cationic dyes: safranin and methylene blue. The degradation process was executed through exposure to visible light emitted by a 200-watt lamp. Notably, this procedure was conducted utilizing a 15% Ni/MgO-CeO2 photocatalyst (with a MgO/CeO2 ratio of 5/95) that was synthesized using sol-gel techniques and subjected to calcination at 700°C. Characterization of the catalyst was achieved through analytical methods such as X-Ray Diffraction (XRD), Scanning Electron Microscopy (SEM), and X-ray energy dispersive microanalysis (EDS X). The experimental results indicated a degradation rate of 70% for safranin and 71% for methylene blue under visible light exposure (200wt) and specific conditions (pH=10, C0=8ppm, T=22°C, and m=0.02g).

References

[1] Abid, M. F., Zablouk, M. A. & Abid-Alameer, A. M.2012 Experimental study of dye removal from industrial wastewater by membrane technologies of reverse osmosis and nanofiltration. Iranian Journal of Environmental Health Science & Engineering 9, 9–17.

[2]Adam, F., Chew, T.-S. & Andas, J. 2011 A simple template-free sol–gel synthesis of spherical nanosilica from agricultural

[3]biomass. Journal of Sol-Gel Science and Technology 59 (3), 580–583. Adebowale, K. O., Olu-Owolabi, B. I. & Chigbundu, E. C. 2014 Removal of safranin-O from aqueous solution by adsorption onto kaolinite clay. Journal of Encapsulation and Adsorption Sciences 4 (03), 89.

ISSN: 0067-3064

Study of new materials DMS: preaching DFT
P 18

Nadjet ZEGGAI, lalia Messaoudi, [2,3] Chaimaa Mohammed krarroubi, [4] Mostefa DJERMOUNI

[1] Laboratoire de Physique Computationnelle des Matériaux (LPCM), Université Djilali Liabès de Sidi Bel-Abbès
[2] Département de Physique, Faculté des Sciences et Technologies, Université Ahmed ZABANA de Relizane
[3] Département de Physique, Faculté des Sciences et Technologies, Université Ahmed ZABANA de Relizane
[4] Département de Physique, Faculté des Sciencesexactes, Université Djilali Liabès de Sidi Bel-Abbès
Corresponding author: zeggainadjet17@gmail.com

Abstract: In all the prototype dilute magnetic semiconductor materials (DMS) of groups III-V and II-VI, such as GaAs or ZnO doped with Mn, the maximum Curie Temperature (TC) remains limited to 180-200 K [1] . So far, the magnetic mechanism is not fully understood. These difficulties could be overcome in the recently discovered family of semiconductors (SC) I-II-V [2] and I-III-IV. In these families of SCs, the manipulation of charge and spin is independent. In contrast, the record TC value reported for Ferromagnetic III-V Semiconductors doped with Iron (Ga, Fe) Sb, reaches 340 K, restoring hope in DMS projects. These materials have certain advantages over those doped with Mn. In addition, the similarity between SC III-V GaSb with I-III-IV semiconductors (NaGaSi) gives us the idea to look for an Iron-based DMS which can present an ease of characterization with a Curie temperature relatively high. To achieve this goal, we used DFT theory to describe the electronic structure of the proposed DMSs.

References

[1] K. Olejník, M. H. S. Owen, V. Novák, J. Mašek, A. C. Irvine, J. Wunderlich, and T. Jungwirth, Phys. Rev. B 78, 054403 (2008).
[2] Z. Deng, C. Q. Jin, Q. Q. Liu, X. C. Wang, J. L. Zhu, S. M. Feng, L. C. Chen, R. C. Yu, C. Arguello, T. Goko, F. Ning, J. Zhang, Y. Wang, A. A. Aczel, T. Munsie, T. J. Williams, G. M. Luke, T. Kakeshita, S. Uchida, W. Higemoto, T. U. Ito, B. Gu, S. Maekawa, G. D. Morris, and Y. J. Uemura, Nat. Commun. 2, 422 (2011).

ISSN: 0067-3064

Mouving single dipolar BEC
P 19

Bakhta. Cherifi, Abdelaali. Boudjemaa.

Hassiba Benbouali University of chlef, P.O Box 78, 02000, Ouled- Fares, Chlef, Algeria

Abstract: We study the properties of dipolar Bose-Bose mixtures using the full Hartree- Fock-Bogoliubov theory. The analytical and numerical calculations emphasize that the competition between the relative motion of two fluids and the interspecies dipole-dipole interactions may affect the behavior of the condensed spectrum.

Generalized coupled Gross-Pitaeveskii equations: We consider weakly interacting two-component dipolar BECs with equal masses m1 = m2 = m confined in an external trap u(r).the above coupled GP equations can be rewritten as follows [1, 2]:

$$i\hbar\dot{\Phi}_j(r,t)=\left[\frac{P^2}{2m}+p.v+\frac{1}{2}mv^2+U(r)\right]\Phi_j(r,t)+\int dr' V_{12}(r-r')n_{3-j}(r')\Phi_j(r,t)$$
$$+\int dr' V_j(r-r')\left[n_j(r',t)\Phi_j(r,t)+\tilde{n}_j(r,r',t)\Phi_j(r,t)+\tilde{m}_j(r,r',t)\Phi_j^*(r',t)\right] \quad (1)$$

The intraspecies two-body interaction potential is defined as:

$$V_j(r)=g_j d(r)+d_j^2\frac{1-3\cos^2 q}{r^3} \quad \ldots\ldots\ldots\ldots\ldots\ldots\ldots\ldots\ldots\ldots\ldots\ldots(2)$$

Collective excitations: The Bogoliubov excitations energy. The quasi-particle amplitudes ujp(r) and vjp(r) satisfy the generalized nonlocal Bogoliubov- de-Gennes (BdG) equations [3]:

$$\varepsilon_p u_{jp}=\left[E_P+P.v+\tilde{V}_j(p)n_{cj}\right]u_{jp}+\tilde{V}_j(p)n_{cj}\vartheta_{jp}+\tilde{V}_{12}(p)\sqrt{n_{cj}n_{c3-j}}\left(u_{jp}+\vartheta_{jp}\right) \quad \ldots(3)$$
$$-\varepsilon_p u_{jp}=\left[E_P+P.v+\tilde{V}_j(p)n_{cj}\right]\vartheta_{jp}+\tilde{V}_j(p)n_{cj}\mu_{jp}+\tilde{V}_{12}(p)\sqrt{n_{cj}n_{c3-j}}\left(u_{jp}+\vartheta_{jp}\right)$$

Let us start with a moving single dipolar BEC $\chi^{dd}=0$[4]. In such a case, the excitations spectrum becom :

$$e_{P\pm}=\sqrt{E_P^2+2E_P n_c d\tilde{V}_\pm(p)} \quad \ldots\ldots\ldots\ldots\ldots\ldots\ldots\ldots\ldots\ldots\ldots\ldots\ldots\ldots (4)$$

Let us now look at how the ground-state energy of each component behaves in the regime of small velocities.

ISSN: 0067-3064

Fluctuations and equation of state : At zero temperature, the condensate depletion and the anomalous density for each component are defined, respectively as:

$$\tilde{n}_{\pm} = \frac{1}{2}\int \frac{dp}{\left(2\pi\hbar^3\right)}\left[\frac{E'_p + mc^2_{s\pm}}{\varepsilon_{p\pm}} - 1\right] \quad \text{.....(5)}$$

$$\tilde{m}_{\pm} = -\frac{1}{2}\int \frac{dp}{\left(2\pi\hbar^3\right)}\frac{mc^2_{s\pm}(\theta)}{\varepsilon_{p\pm}} \quad \text{.....(6)}$$

The ground state energy can be written as:

$$E_j = \frac{1}{2}mv^2 n_j + \frac{1}{2}\tilde{V}_j(\mathbf{p}=0)n_j^2 + \frac{1}{2}\tilde{V}_{12}(\mathbf{p}=0)n_{3-j}^2 \quad + \bar{E}_{\mathrm{LHY}\pm}, \text{ .....(7)}$$

where

$$E_{\mathrm{LHY}\pm} = \frac{1}{2}\int \frac{d\mathbf{p}}{(2\pi\hbar)^3}\left[\varepsilon_{\mathbf{p}\pm} - E'_{\mathbf{p}} - mc^2_{s\pm}(\theta_{\mathbf{p}})\right], \quad \text{.....(8)}$$

accounts for corrections to the ground-state energy owing to the LHY quantum fluctuations for Bose mixtures. Equation.

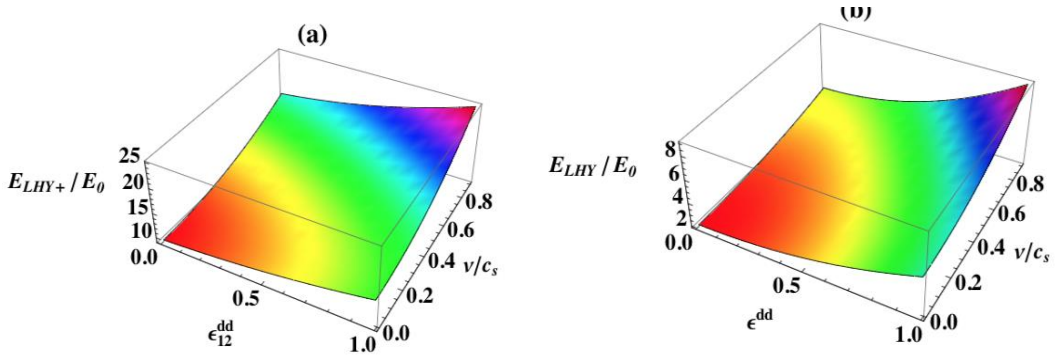

FIG. 1 (Color online) (a) The LHY corrected energy as a function of edd and v/cs. (b) the same but for the lower branch. Parameters are: a = 141a0 [5], a12 = 115.1a0, r∗ = 131a0 [6], and n ≈ 1020m−3.

Conclusion: For v = 0, one recovers the energy of an immovable dipolar Bose mixture . Equation (5) shows that the dipolar mixture fluid gains an extra kinetic energy due to the relative motion leading to increase the total energy of the mixture.
We observe that ELHY increases with both the relative motion effects and the dipolar interactions. For small velocities v ≪ vc = $c_{s\pm}(\theta)$, the energy can be easily computed by integrating term by term the power series representation of integral (18). To overcome the ultraviolet divergence, we use dimensional regularization.

ISSN: 0067-3064

References

[1] L. Landau, Physical Review, 60,356 (1941).
[2] L. Tisza, Nature 141, 913 (1938).
[3] A. Boudjemaa, Sci. Rep. 11, 21765 (2021).
[4] B. Cherifi, A. boudjemaa
[5] M. Wenzel, F. Bottcher. J-N. Schmidt, M. Eisenmann, T. Langen, T. Pfau, and I. Ferrier-Barbut, Phys. Rev. Lett. 121, 030401 (2018).
[6] L. Cacciapuoti, D. Hellweg, M. Kottke, T. Schulte, W. Ertmer, J. J. Arlt, K. Sengstock, L. Santos, and M. Lewenstein, Phys. Rev. A 68, 053612 (2003).

ISSN: 0067-3064

Experimental and Numerical study of spherical Taylor-Couette flow
P 20

Z. Tigrine[1,2], S. Lecheheb[1], F. Mokhtari[1] and A. Bouabdallah[1]

[1]Faculty of Physics, Thermodynamics and Energetic Systems Laboratory, University of Houari Boumediene, B.P32 El Alia, 16111 Bab Ezzouar, Algiers, Algeria
[2]Unité de Développement des Equipements Solaires, UDES/Centre de Développement des Energies Renouvelables, CDER, Bou-Ismail 42415, W. Tipaza, Algeria,

Abstract: This work presents an experimental and numerical study of hydrodynamic instabilities of an incompressible viscous fluid contained between two concentric spheres whose the inner one rotating ($\Omega 1 \neq 0$) while the outer is at rest ($\Omega 2 = 0$). The flow system, totally or partially filled through the aspect ratio $\Gamma = H/d$ of the fluid is defined by clearance ratio $\delta = d/R1$ in small gap configuration ($\delta = 0.11$). The main aim is to investigate the effect of the aspect ratio on the instabilities in field flow system with free surface using water as working fluid. Experiments are performed for different aspect ratio values and Laser photometric technique is used for visualization. Our observations are compared to the flow system totally filled. The effect of free surface on the onset of axisymmetric Taylor vortices instability and oscillating vortices are examined in the spherical Couette flow annulus. A good agreement was observed between experimental and numerical results showing that the wavy mode is accelerated for weak aspect ratio.

Keywords: Spherical Couette flow, free surface, aspect ratio, instabilities, CFD

ISSN: 0067-3064

INFLUENCE OF INCREASING ALUMINUM RATE ON MECHANICAL PROPERTIES OF STAINLESS STEEL P 21

BOUGUETTAF Soufyane, TAZROUT Mansour

,Mhamed Bougara university, Boumerdes
Email: s.bouguettaf@univ-boumerdes.dz
Email: btazrout@yahoo.fr

Abstract: For high temperature applications, Aluminum is added to stainless steels for the purpose of enhancing the oxidation resistance by forming a surface alumina layer. This advantageous effect does not refrain the research for the best mechanical properties of the steel. The effect of Al on the mechanical properties of an austenitic stainless steel has been investigated. The studied alloys were elaborated with the industrial process by Increasing the Al rate from 0,3% to 1,85% , the chemical composition of the studied alloys was analyzed, hardness was measured , tensile test and Impact test were realized. The obtained results reveal an enhancement in the ductility when increasing Al to 0,77% and 1,19 %, by increasing Al to 1,85% The ductility of the steel decreased to be almost the same with the base alloy which contains 0,3% of Al.

Keywords: stainless steel, mechanical properties, ductility.

ISSN: 0067-3064

Natural Radioactivity Dose Assessment in Beach Sands of Béjaia, Algeria
P 22

Ghada Mellak [a@], Wassila Boukhenfouf [a], Fatma Zohra Dehimi [b], Adnane Messai [c] Nour Eddine Hebboul [c]

aDAC Laboratory, Physics Department, Faculty of Sciences, Ferhat ABBAS University, Sétif 19000, Algeria
bNuclear Research Center of Algiers, Algeria
cNuclear Research Center of Birine, Djelfa, Algeria

Abstract: Natural radioactivity has been the primary external source of radiation exposure to the human body. Beach sands encompass varying degrees of natural radioactivity, which can have health implications. It is crucial to understand the distribution, composition, and background of these soils. A radiological study was initiated to estimate the level of radioactivity and absorbed doses, using gamma spectrometry for sands collected from twelve beaches spanning from Souk El Tenine to Bejaia. The average concentrations of activity for radionuclides 226Ra, 232Th and 40K were respectively 31, 10.8 and 255 Bq / kg. The values of the radium equivalent activity (Raeq) for all the studied samples were lower than the value recommended by the United States Scientific Committee on the Effects of Atomic Radiation (UNSCEAR) which is 370 Bq / kg. The values of absorbed dose rate and annual effective dose for the samples studied vary from 17.98 4.3 to 51.57 7.2 nGy/h and from 0.02 to 0.06 mSv/y respectively. The average values of the external and internal hazard indices were respectively 0.17 and 0.25. The results were compared to the values given by other countries. The hazard indices are less than the allowable values recommended by the UNSCEAR.

References

[1] UNSCEAR, United Nations Scientific Committe on the Effects of Atomic Radiation. Sources and Effects of Ionizing Radiation, Report to the General Assembly, (New York: United Nation) (2000).
[2] M.W. Yii, A. Zaharudi, I. Abdul-Kadir, Distribution of naturally occurring radionuclides activity concentration in east Malaysian marine sediment, Journal of Radiation Research and Applied Sciences, 2009, 67, 630-635.
[3] M. Krmar, E. Varga, J. Slivka, Correlations of natural radionuclides in soil with those in sediment from the Danube and nearby irrigation channels, Journal of Environemental Radioactiv, 2013, 117, 31 35.

ISSN: 0067-3064

NLO Gluon Self Energy in Real Time Formalism
P 23

K, BENCHALLAL[1], A. ABADA[2],

[1] Ecole Normale Supérieure, Physics Department,, Alger, Algeria
[2] United Arab Emirates University, Physics Department,, Al Ain, UAE
benchallal.k@gmail.com, a.abada@uaeu.ac.ae

Abstract: The problem of gauge dependence for physical quantities in high-temperature perturbation theory was resolved by Braaten and Pisarski, who showed that an effective perturbation that sums the hard thermal loops into dressed propagators and vertices is necessary to consistently calculate at high temperatures. In the context of QCD research, it is essential to explore the next-to-leading order calculations for gluon self-energy by appropriately resumming propagators and vertices, as the leading-order expression for self-energy.
This resummation technique, known as hard thermal loop resummation, has led to significant advancements in the study of QCD at finite temperature, such as the understanding of infrared divergences and gauge dependence issues. This approach is necessary to obtain physical, gauge-independent results and prevent issues such as infrared divergence.
We used this techenique to get the analytic expression of the self energy for longitudinal gluons with soft momentum at the next-to-leading order using the closed time path-formulation of the real-time formalism of the finite temperature quantum field theory.
.
Keywords*:* Hot QCD, Quark-Gluon plasma, Real time formalism, Hard thermal loop.

ISSN: 0067-3064

Effects of Level Densities and Those of a-Parameter in the Framework of Preequilibrium Model for 58N(n, xp) reaction in neutrons at 8 to 11 MeV
P 24

Yettou Leila[a]*, Belgaid Mohamed[a], Belouadah Naima[a], Amrani Naima[b] and Kadem Fatiha[a]

[a] University of Sciences and Technology of Bab Ezzouar, Faculty of Physics, Laboratory SNIRM, Algiers, Algeria
[b] University of Sétif, Sétif, Algeria

Abstract: in this study, the calculations of proton emission spectra produced by 58Ni (n, xp) reactions are used in the framework of preequilibrium model with the TALYS code. The two-component exciton model is used and the level density with the level density a-parameter have been investigated for our calculations. The comparison with experimental data shows clear improvement over the Preequilibrium Exciton Model calculations. 1. Introduction: Nickel is a major component of austenitic steel that is widely employed in the nuclear industry and it is important structural material for nuclear applications [1]. The main purpose of this work is to investigate the sensitivity on the input parameters from the level density [2] with the level density a-parameter [3] considered in our calculations affect strongly the results compared to the experimental data. The cross sections for the emission of proton for incident neutron energy 8, 9.4 and 11MeV on 58Ni are calculated in the framework of pre-equilibrium [4], and equilibrium [5] models by using the TALYS code [6]. The plots are presented with the comparison between the results from the TALYS code [6] calculations and the experimental data which are retrieved from the EXFOR database [7]. The obtained results have been discussed and compared with the available experimental data [7] and found in agreement with each other.

References

[1] Dispersive coupled-channels optical-model potential with soft-rotator couplings for Cr, Fe, and Ni isotopes. Rui Li et al., PHYSICAL REVIEW C87, 054611 (2013).
[2] A.J. Koning, S. Hilaire and S. Goriely, “Global and local level density models”, Nucl Phys. A 810, 13-76 (2008).
[3] A.V. Ignatyuk, G.N. Smirenkin and A.S. Tishin, Sov. J. Nucl. Phys. 21, no. 3, 255 (1975). 2ndInternational Conference on Computational & Applied Physics- ICCAP 2023
[4] A.J. Koning and M.C. Duijvestijn, “A global pre-equilibrium analysis from 7 to 200 MeV based on the optical model potential”, Nucl. Phys. A 744, 15 (2004).

ISSN: 0067-3064

[5] W. HAUSER and H. FESBACH, Phys. Rev., 87, 366 (1952),http://dx.doi.org/10.1103/PhysRev.87.366; see also L. WOLFENSTEIN, Phys. Rev., 82, 690 (1951), http://dx. doi.org/10.1103/PhysRev.82.690.
[6] A. J. KONING, S. HILAIRE, and M. C. DUIJVESTIJN, “Talys-1.0,”Proc. Int. Conf. Nuclear Data for Science and Technology (ND-2007), Nice, France, April 22–27, 2007.
[7] Experimental Nuclear Reaction Data (EXFOR) Database Version of March 16, 2015,

ISSN: 0067-3064

Application Of Artificial Intelligence In Engineering
P 25

Madour Fouzia

Department of Electronics, Faculty of Physics, University of Ferhat Abbas Setif, Algeria
madour_fouzia@yahoo.fr

Abstract: This paper describes the implementation of hierarchical control on a robotic manipulator. In our work, we have developed a fuzzy neural network controller using supervised training in order to decrease the position tracking errors. The simulation results show the effectiveness of this approach to track reference trajectories.

Introduction: To develop effective control laws and achieve the precision required by a manipulator robot, it is necessary to start by modeling the robot mathematically. After having modeled the robot, it is necessary to solve these functions to perform the dynamic simulation of the manipulator robot. In our work, we made a comparative study between the classical method and a more precise but somewhat time-consuming method. This method is the Runge Kutta method of order 4.

The manipulator arm : The manipulator arm is a mechanism having a structure more or less similar to that of the human arm in the case of manipulator robots. Its architecture is a kinematic chain of bodies, assembled by links called joints [1].

References

[1] J.-P. Lallemand, S. Zeghloul. « Robotique. Aspects fondamentaux ». Edition Masson,1994.
[2] Sylvain G. et al., « Modélisation Dynamique d'un Robot Parallèle à 3-DDL : l'Orthoglide». Discover research, Institut de Recherche en Communications et Cybernétique de Nantes France, 2007.
[3] B. Stout, « Méthodes numériques de résolution d'équations différentielles Marseille, France : Université de Provence, 2007.
[4] R. Kelly, V. Santibáñez and A. Loría, « Control of Robot Manipulators in Joint Space», Springer, 2005.
[5] J. Butcher, « Runge–Kutta methods for ordinary differential equations ».Wellington, New Zealand: The University of Auckland, 2005
[6] W. Afzal, S. Iqbal, Z. Tahira, and M. E. Qureshi, "Gesture Control Robotic Arm Using Flex Sensor," Applied and Computational Mathematics, vol. 6, no. 4, pp. 171–176, Jan. 2017, doi: 10.11648/j.acm.20170604.12
[7] C. Chavez-Olivares, F. Reyes Cortes, and E. Gonzalez-Galvan, "On Explicit Force Regulation with Active Velocity Damping for Robot Manipulators," Automatika, vol. 56, no. 4, pp. 478–490, Jan. 2015, doi: 10.7305/automatika.2016.01.399.

ISSN: 0067-3064

Determination of the fast neutron flux by activation method P 26

Naima Belouadah[a], Fatiha Kadem[a], Khelifa Boukeffousa[b], Liela Yettou[a], Mohamed Belgaid[a] ,Nabila.Taibouni[a] and Zahir Idiri[b]

[a]USTHB, Faculté de Physique, Laboratoire SNIRM, B.P. 32, El-Alia, 16111 Bab Ezzouar, Algeria
[b]Centre de Recherche Nucleaire d'Alger, 02 Bd Frantz Fanon, B.P.399, Alger-Gare, Algeria
Corresponding author: Email: b_belouadah@yahoo.fr

Abstract: Flux measurement of an accelerator based D-T neutron generator was achieved by the activation technique. The neutron generator can produce maximum neutron yield of 1.8 10^8 n/sec at the Tritium-target For the measurement of 14.7 MeV neutron flux , ^{56}Fe(n, p)^{56}Mn and ^{27}AI(n, p)^{27}Mg reactions are most suitable because of their higher threshold energies. The fast neutrons were produced, via the ^{3}H(d,n)^{4}He reaction by Neutron Generator at the Research Nuclear Center of Algiers. The Neutron Activation Analysis (NAA) technique was adopted, the half-lives, isotopic branching ratios and resulting intensities of emitted gamma-rays after activation are essential factors in selecting what type of foil to activate. If the half-lives of the activated isotopes are too short, not many activated nuclei survive to the beginning of the counting. Also, intensities (branching ratios) and energies of characteristic gamma-rays emitted from activated nuclei must be suitable to accumulate enough net counts above background to be detected during gamma-ray spectroscopy. The γ ray spectra for the Fe and Al were detected for the Germanium Hyper Pure coupled in the Genie 2000 data acquisition software. The resolution of this detector was of ~1.92 keV for 1332.5 keV (^{60}Co) with a relative measured efficiency of 46.6%. The collected data were analyzed by using the gamma spectrometry Genie 2000 data acquisition software.
In the present paper, we report on the measurement of the fast neutron flux via at the neutron energy of 14.7 MeV. Iron and Aluminum have been selected to measure the neutron flux of D-T neutron generator. The measured flux values via the ^{56}Fe(n, p)^{56}Mn and ^{27}AI(n, p)^{27}Mg reactions is (1.32±0.04) 10^7 and (1.12±0.03) 10^7n.cm^{-2}.s^{-1}. The activation technique can be expanded to measure the cross section for the reactions (n,2n), (n,p), and (n,α) as well as to determine the neutron spectra over any desired energy range by employing the proper stack of metal foils.

Keywords: D-T neutron generator, neutron activation analysis, fast neutron, neutron flux.

ISSN: 0067-3064

Optical and structural properties of pure ZnO and Sr-doped ZnO nanocomposites synthesized by SILAR method. P 27

MOKRANI Nourelhuoda[1,*], GHETTAF TEMAM Elhachemi[1], BEN TEMAM Hachemi[1], BARKAT Hadjer[1]

1Physics Laboratory of Thin Layers and Applications, Biskra University, BP 145 RP, Biskra 07000, Algeria

Abstract: In this work, pure ZnO and Sr doped ZnO nanocomposites, in three different concentrations were successfully prepared using the low-cost and simple method of SILAR. X-ray diffraction patterns confirmed the formation of the ZnO wurtzite structure in all of the nanocomposites. SEM images showed that surface morphology of the Sr-doped ZnO thin films varied and the doping can alter the shape of grains. Optical absorption spectra showed the shifts somewhat towards the longer wavelength area and the band gap energy (Eg) of pure ZnO and Sr-doped ZnO nanocomposites decreased with adding Sr and pure ZnO from 3.127 eV and 3.06 eV for Sr-doped sample (5%). Hence, doping Sr enhanced the optical sensitivity issue of nanocomposites. Collectively, our results can be useful in the photocatalytic purification of wastwater from colorants.

Keywords: pure ZnO ,ZnO/Sr, thin films, SILAR

ISSN: 0067-3064

Structural, elastic, and electronic properties of cubic perovskite compound $BaTiO_3$: ab initio study.
P 28

BOUGUERRA Zakarya [a], BENNACER Hamza [a, b], BOUKORTT Abdelkader [a], HAMMADI Mohamed [a], MISSOUM Khadidja [a],

Abstract : The study featured ab initio calculations with the Wien2k code, which used the FP-LAPW method and the EV-GGA method to handle the exchange-correlation potential in the framework of density functional theory (DFT). The objective was to predict the structural, elastic, and electrical properties of the cubic ($Pm\bar{3}m$) perovskite compound $BaTiO_3$, with a lattice constant of 4.0248 Å. While thorough research of electrical characteristics, including the density of states (DOS) and band structure, was being done, the study of elastic properties confirmed the stability for a wide range. The compound preliminary findings show semiconductor behaviors with a gap energy of Eg = 1.95 eV, and because of this, it is a strong contender for use in a variety of technological applications, particularly for photovoltaic uses.

Keywords: Ab initio, Wien2k, FP-LAPW, EV-GGA, DFT, DOS.

ISSN: 0067-3064

Deconfinement phase transition in a finite volume
P 29

Abdelkader Cheddad*, Amal Ait El Djoudi and Faiza Ramdani

Laboratoire de Physique des Particules et Physique Statistique, Ecole Normale Supérieure-Kouba, B.P.92, 16050, Vieux-Kouba, Algiers, Algeria
*Corresponding author: abdelkader.cheddad@g.ens-kouba.dz

Abstract: This work deals with the investigation of the scaling behavior of the thermal deconfinement phase transition (DPT) at zero chemical potential, occurring between a hadronic phase of massive pions and a color-singlet quark gluon plasma (QGP) phase, coexisting in a finite volume. To achieve this, we describe the DPT in a finite volume using a phenomenological coexistence model [1], whithin the MIT bag model. We consider the QGP consisting of gluons, massless up and down quarks and massive strange quarks, and we calculate the relevant partition function projected on the SU(3) color-singlet representation [2], using a density of states containing the volume term only. In order to probe the system at the transition, we may examine some characteristic quantities, such that the order parameter, which is in this case the mean value of the fraction of volume occupied by the HG phase relatively to the total volume of the mixed system. It turns out that the transition temperature is shifted to higher values in small volumes, and the shift relatively to the transition temperature in an infinite volume varies with the inverse of the volume as a power law, characterized by a scaling exponent λ. By means of a numerical f inite size scaling analysis, we extract the shift critical exponent and we find that its value is equal to: $\lambda=0.913\pm0.015$. Let us note that previous results found in [3,4], gave a shift scaling exponent around 0.86 with the difference of considering therein massless pions in the HG phase and massless up and down quarks in the QGP phase. Finally, we conclude that our results are compatible with the first order phase transition and agree very well with the predictions of other Finite-size scaling analysis (FSS) approaches.

References

[1] C. Spieles, H. Stöcker and C. Greiner, Phys. Rev. C57, 908 (1998).
[2] K. Redlich and L. Turko, Z. Phys. C 5, 201 (1981); L. Turko Phys. Lett. B 104, 153 (1981).
[3] A. Ait El Djoudi, Doctorat thesis in theoretical physics, "Finite-Size Effects on the Deconfinement Phase Transition", Université Mouloud Mammeri (April 2008). [4] M. Ladrem and A. Ait El Djoudi, Eur. Phys. J. C44, 257 (2005); A. Ait El Djoudi et al., J. Phys.: Conf. Ser. 1766, 012017 (2021).

ISSN: 0067-3064

Synthesis and study of LnAO3 (Ln=Y, Gd, Lu and A; transition element) doped Er+3
P 30

Hamzi Soumia [1], Lanez imane[1], Rekik Brahim[1], Guerbous Lakhder[2]

[1] LPCMIA, Physics Dept., Saad Dahlab University, Blida1, Route de Soumaa, BP 270, Blida 09000, Algeria
[2] Nuclear research center of Algiers CRNA, Algeria

Abstract: GdAlO3 (GAP) perovskite phosphor undoped and doped 2% Erbium ion (Er3+) was synthesized by the co-precipitation method with presses revers strike, using NH5CO3as a precipitant agent with different sources of precursors (Aluminum Nitrate……) The crystal structure along with all other parameters was determined by (XRD). The selected samples are calcined at different temperature 1000, 1150 1300°C they found in polyphase structure contains monoclinic phase Gd4Al2O9 and orthorhombic phase with Pnma space group and lattice parametersare a=5,48766477Å b=5,34885722Å c=6,92102837Å α=β=ɤ=90°. The X-Ray powder diffractogram of the obtained sample of GAP with different sources of precursors. (Figure. 1) indicates that sample of GAP nitrates sources can crystalize in orthorhombic phase with Pnma space group as verified by the existence of ten characteristic peaks corresponding to (002), (111), (200), (022), (202), (004), (114), (321), (224) and (116) plans Aset of some other peaks was also observed, corresponding to the secondary phases Gd4Al2O9. The ten peaks are also exist in the sample of GAP sulfate source but they tow peaks of monoclinic phase are (110) (312)

Keywords: Perovskite– co-precipitation– orthorhombic– Erbium– XRD

ISSN: 0067-3064

Electron impact ionization of atoms: An improved BBK mode
P31

BECHANE Kawther, *Pr S. HOUAMER*

LPQSD, Department of Physics, Faculty of Sciences, University Sétif1, Sétif 19000, Algeria

bechanekawther34@gmail.com

Abstract: Ionization of atoms by electron impact is part of basic research which enables to study the strength and importance of fundamental interactions. The triple differential cross section (TDCS) measured in (e,2e) experiments provides the probability that the scattered and ejected electrons are selected in energy and direction and detected in coincidence. We present a new model which called BBK2CWZ model to study the dynamics of electron impact ionization of atoms (and molecules). In this model, the two outgoing electrons are both described by a Coulomb wave with variable charges Z(r) while the incident electron is described by a plane wave. The fully (TDCS) is then calculated in (e,2e) reactions for several atomic targets taking into account the post collision interaction (PCI), the results are compared with available experiments.

Keywords: Ionization, cross section, Coulomb wave, variable charge

1.Introduction: Atomic collision play a fundamental role in the development of quantum mechanics, in the present work we introduce an improved theoretical approach to describe the (e,2e) reaction for atoms, it is in fact an extension of our earlier studies which provided rather good agreement between experiment and theory, The present theoretical description is a fully quantum mechanical approach, it is actually a kind of BBK model in which the ejected and the scattered electrons are both represented by Coulomb waves with variable charge Z(r) instead of an effective charge (Z=1 for single ionization generally), the (PCI) is introduced and treated exactly to all orders.

2.Theory: In an (e,2e) reaction the projectile of energy E_0 and momentum k_0 collides with the target and ionizes it. The scattered and ejected electrons, with energy and momentum (E_a, K_a) and (E_b, K_b) respectively, are detected in coincidence.
The probability of single ionization is obtained by calculating triple differential cross section expressed as:

$$\boldsymbol{\sigma^3 = (2\pi)^4 \frac{k_a k_b}{k_0} |T_{if}|^2}$$

The matrix element T_{if} is given by:

ISSN: 0067-3064

$$T_{if} = \langle \Psi_f | V | \Psi_i \rangle$$

Where Ψ_i and Ψ_f represent respectively the initial and final states. In the framework of the single particle approximation, the interaction between the projectile and the target is written as:

$$V = \frac{1}{r_{01}} - \frac{1}{r_0}$$

Ψ_i is described by a plane wave, while the final state is written as:

$$\Psi(\vec{r}_0, \vec{r}_1, \vec{r}_{01}) = \varphi^z(\vec{r}_0, \vec{k}_a)\varphi^z(\vec{r}_1, \vec{k}_b)C(\vec{r}_{01}, \vec{k}_{01}, \alpha_{01})$$

Where $\varphi^z(\vec{r}, \vec{k})$ represents a Coulomb wave with variable charge Z(r) and $C(\vec{r}_{01}, \vec{k}_{01}, \alpha_{01})$ deals with the (PCI) with $\vec{k}_{01} = \frac{1}{2}(\vec{k}_a - \vec{k}_b)$ and $\alpha_{01} = \frac{1}{2k_{01}}$

3. Results: We have calculated triply differential cross sections (TDCS's) for electron impact ionization of some atomic targets, especially the following targets Ne2p and Ar2p

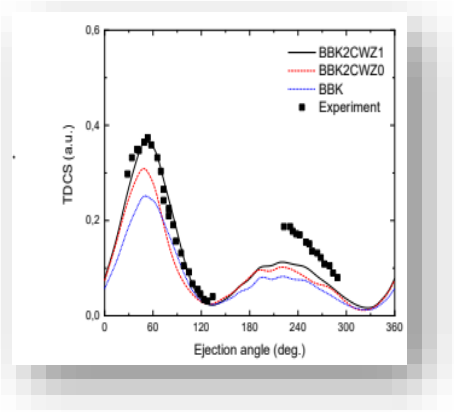

Figure 1: Absolute TDCS for the ionization of neon 2p as a function of the ejection at fixed scattering angle . The scattered and ejected electrons have respective energies

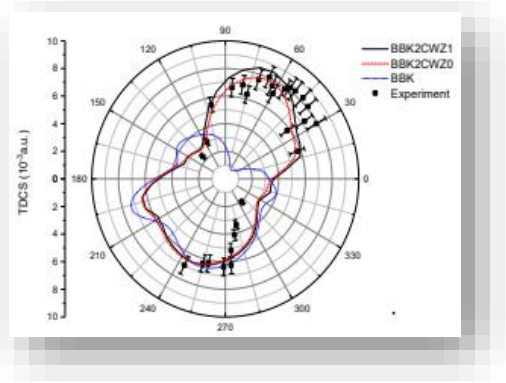

Figure 2: Absolute polar plot of the TDCS, for the ionization of argon 2p by an impact energy as a function of the ejection angle . The projectile is scattered at an angle in coincidence with the ejected electron with an energy.

4.Conclusion: In conclusion, sophisticated model called BBK2CWZ as well as the standard BBK model were applied to investigate the (e,2e) process for atoms in several kinematics, it was found that:
The two models are nearly equivalent for low momentum transfer kinematics **[3].**

ISSN: 0067-3064

References :

[1] Hargreaves R L, Stevensen M A and Lohmann B 2010 J. Phys. B 43 205202
[2] Lahmam-Bennani A, Wellenstein H F, Duguet A and Daoud A 1984 J. Phys. B 30 1511
[3] Attia M, Houamer S, Khatir T, Bechane K and Dal Cappello C 2023 J. phys. B 56 075201

ISSN: 0067-3064

Study of electronic, thermoelectric, and optical properties of 3d orbitals doped ceria: Based on First Principles
P 32

Benmalek.Aida*, Doughmane Malika, Chettibi Sabah

Département sciences de la matière, Université8 Mai 1995, Guelma, Alegria

Abstract: According to the recent investigations, based on a series of supercell density functional calculations of Zn doped CeO2 both with and without O vacancy (VO), we show that VO plays an important role in determining the exceptional thermoelectric and optical properties. In this context, present study reports the effect of Zn doping on the electronic, thermoelectric, and optical properties of CeO2 through DFT [1] calculations implemented in Wien2k code [2]. These results are obtained, supposedly due to the ability of ceria nanoparticles to rapidly store and release oxygen, as it acts as an oxygen buffer. Further optimization can be expected by doping Zn which can increase the electrical conductivity of the ceria nanoparticles, thereby increasing the figure of merit. Effect of Zn can also be seen in the electronic and optical behavior of ceria nanoparticles as the band-structure of the system changes. All these changes result in thermoelectric figure of merit approaching to 2 ± 0.2 at room temperature and above.

References

[1]-Blaha, P., Schwarz, K., Sorantin, P., & Trickey, S. B. (1990). Full-potential, linearized augmented plane wave programs for crystalline systems. Computer physics communications, 59(2), 399-415. doi.org/10.1016/0010-4655(90)90187-6

[2] Blaha, P., Schwarz, K., Tran, F., Laskowski, R., Madsen, G. K., & Marks, L. D. (2020). WIEN2k: An APW+ lo program for calculating the properties of solids. The Journal of Chemical Physics, 152(7), 074101. doi.org/10.1063/1.5143061.

ISSN: 0067-3064

Harmonic and anharmonic frequencies of hydroxyl groups adsorbed on SnO2(110) surface: first principle study
P 33

N. Bouchelarem[1], F. Bouamra[1], M. Derbal[1]

[1] LPCMIA Laboratory, Department of physics, University of Blida 1, Blida, Algeria.

Abstract: Rutile tin dioxide SnO2is one of transparent conductive oxide materials (TCO) combined high transparency (>80 %) and high conductivity with a large band gap of 3.6 eV [1, 2]. SnO2(110) surface is known to be the most stable one thermodynamically among the low index surfaces that has an important potential of applications in solar cell, photo-electronic, catalysis and gas sensing [3-5]. SnO2 (110) surface is usually covered with hydroxyl groups formed from the dissociative adsorption of H2O molecule. The stoichiometric SnO2(110) surface was modelled by a periodic slab of three layers (3L) and was represented by p(1x1) unit cell, p(2x1) and p(4x1) supercells to simulate OH groups adsorption at 1, 1/2 and 1/4 monolayers (ML) coverages, respectively. First principle calculations have carried out with CRYSTAL17 package [6] in the framework of the density functional theory (DFT) at the hybrid B3LYP level [7, 8] with effective core pseudopotentials (ECP) basis set. The harmonic frequencies of OH stretching modes are calculated as function of the coverage from 1 to 1/4 ML. At 1 MLcoverage, negative values of frequencies are found, which indicates instable adsorption configuration. We found that the OH stretching modes at the harmonic level are overestimated than the experimental OH frequencies. These frequencies can be obtained in very good agreement with experiment by DFT-B3LYP calculation if anharmonic correction are included. The anharmonicity constant for OH groups has found to be constant.

References

[1] V. E. Henrich, P. A. Cox, Cambridge University Press, Cambridge, U. K., 1994.
[2] C. Sun, A. Du, J. Liu, S. Qiao, J. Lu, S. C. Smith, Solid State commun., 150 (2010) 957-960.
[3] M. Batzill, U. Diebold, Prog. Surf. Sci., 79 (2005) 47-154.
[4] R. Li, Z. Yuan, F. Meng, T. Jiao, G. Li, Micro. Eng., 236 (2021) 111469.
[5] W. Chen, Q. Zhou, F. Wan, T. Gao, J. Nano., 2012 (2012) 1-9.
[6] R. Dovesi, R. Saunders, C. Roetti, R. Orlando, C. M. Zicovich-Wilson, F. Pascale, B. Civalleri, K. Doll, N. M. Harrison, I. J. Bush, Ph. D'Arco, M. Llunel, M. Causa, Y. Noel, L. Maschio, A. Erba, M. Rérat, S. Casassa, CRYSTAL17, University of Torino, 2018.

ISSN: 0067-3064

A DFT Computational Study of the Antioxidant Activities of Antivitamins K
P34

Fella Ati[a,b,*], Soraya Abtouche[a], Moumna El Kebiche[a] and Meziane Brahimi[a]

[a] Department of Physical Chemistry, Faculty of Chemistry, USTHB, Algiers, Algeria
[b] Department of Chemistry, Faculty of Sciences, University Saad Dahlab BLIDA 1, Algiers, Algeria

Abstract: Antivitamins K(AVK), also known as vitamin K antagonists, are a class of medications used as anticoagulants, which means they help prevent blood clot formation. They are used in the treatment of phlebitis, pulmonary embolisms or in certain cardiac disorders. Although their effectiveness is widely recognized, their common use is still difficult due to the many drug interactions. In order to provide more information on the structural and electronic properties as well as the mode of action of AVK, we are therefore interested in the theoretical study of electronic structure and antioxidant activity of the most used AVK using DFT method. The study included three coumarin-type AVK molecules , acenocoumarol, phenprocoumon and warfarin in addition to coumarin core.

Keywords : AVK, Antioxidant activity; DFT, HAT mechanism, SET-PT mechanism, SPLET mechanism.

ISSN: 0067-3064

Computation of Quantum Plasma: Contribution of Exchange-Correlation Potential
P 35

Rachid Fermousa, Rima Mebrekb and Mohamed Douicia

(a) Laboratoire de Valorisation des Substances Naturelles (LVSN), Khemis Miliana University, Route de Theniet El Had, 44225 Khemis Miliana, Algeria.
(b) Theoretical Physics Laboratory, Faculty of Physics, USTHB, B.P. 32 Bab-Ezzoura, 16079 Algiers, Algeria.

Abstract: Plasma expansion is an important physical process that takes place in laser interactions with solid targets. Within a self-similar model for the hydrodynamic multi-fluid equations, we investigated the expansion of dense plasma. The weakly relativistic electrons are produced by ultra-intense laser pulses, while ions are supposed to be in a non-relativistic regime. It is shown that dense plasma expansion is found to be governed mainly by quantum contributions in the fluid equations that originate from the degenerate pressure in addition to the nonlinear contributions from exchange and correlation potentials. The quantum degeneracy parameter profile provides clues to set the limit between under-dense and dense relativistic plasma expansions at a given density and temperature.

Quantum hydrodynamic equations : For sufficiently large plasma density, some level of understanding can be achieved by considering independent electrons. However, a more accurate description requires the use of a self-consistent model, where electron-electron interaction is included. Thus, to avoid solving complicated full N-body problem, mean field models are used. One of these models, the quantum hydrodynamic fluid model, based on the generalization of plasma classical fluid model, allows straightforward investigation of the collective dynamics.

Conclusion: Dense plasma expansion is governed by a quantum statistical pressure term in the momentum equation as well as the combined exchange-correlation potentials. Quantum effects originating from degenerate pressure led to faster ion density depletion. Compared to the latter case the nonlinear combination of exchange and correlation potentials becomes important and can be detected through a slowdown of ion front motion. Dense plasma expansion evolves with different acoustic speeds which are associated with different expansion time scales.

References

[1] Y. Lyubarsky and M. Liverts, Astrophys. J. 682, 1436 (2008).
[2] P. K. Shukla, A. A. Mamun, and D. A. Mendis, Phys. Rev. E 84, 026405 (2011).
[3] Y. Ma, S. Mao, and J. Xue, Phys. Plasmas 18, 102108 (2011).
[4] L. Brey, J. Dempsey, N. F. Johnson, and B. I. Halperin, Phys. Rev. B 42, 1240 (1990).[5] Ch. Sack and H. Schamel, Phys. Rep. 156, 311 (1987).

ISSN: 0067-3064

The structural, electronic properties of Mg2Ge compounds doped Mo
P 36

[1]M. HAMMADI, [2]S. MESKINE, [3] A. BOUKORTT, [4] Z. Bouguerra, [5] W. Maafa

[1] Physics, University of Mostaganem, ECP3M, Algeria
[2] Electrical engineering, University of Mostaganem, ECP3M, Algeria
[3] Electrical engineering, University of Mostaganem, ECP3M, Algeria
[4] Physics, University of Mostaganem, ECP3M, Algeria
[5] Physics, University of Mostaganem, ECP3M, Algeria
e-mail: hammadi.mohamed14@gmail.com

Abstract: In this study, we have investigated the structural, electronic properties of Mg_2Ge compounds doped Molybdenum. The calculations have been performed by using the full potential linearized augmented plane wave (FP-LAPW) method within the density functional theory (DFT). We have calculated lattice parameters, band gap energies, density of states, parameters for Mg_2Ge compounds doped and undoped. The impurity atom is Mo. We have found that the deformation energy under the pressure decreases with the impurity atom.

Keywords: doped, GAP, compound; DFT;electronic properties; FP-LAPW

Introduction : The magnesium germanide is one of the family of the Mg2× compounds where X can be Ge, Si and Sn elements. Mg2Sn has been used Li-ion batteries In addition, it is expected that a material should have low thermal conductivity, high electrical conductivity As can be seen from the literature review, Mg-based compounds are widely studied by researchers due to their different properties.

In this paper, we have investigated the structural, electronic, properties of Mo . doped (impurity atoms) Mg2Ge compounds based on the first principal calculations. In order to add selected impurity atoms, we have used supercell approach with 12 atoms per cell. It means that the unit cell contains four Ge atoms and eight Mg atoms. The impurity atom has been replaced with the Mg atom.

Computational details

In this study, the first principle calculations have been executed the full linear augmented plane wave method (FP-LAPW) within the density functional theory (DFT) by using WIEN2k code. The structural properties have been analyzed from optimizing lattice parameter and ground state energy of the system. The structural parameters are calculated using Perdew-Burke-Enzerhof (PBE) generalized gradient approximation (GGA). In order to improve band gap and electronic structure

ISSN: 0067-3064

calculations Tran-Blaha modification of the Beckee-Johnson potential (mBJ) has been treated in the self-consistent cycle (SCF) calculations . The convergence parameter is defined as RMT*KMAX. In our study, this parameter is set to 7. RMT is the smallest atomic sphere radius in the unit cell and KMAX is the magnitude of the largest K vector. The plane wave vector is magnitude of the largest vector (GMAX). GMAX has been adjusted to 12. The cut-off is defined as energy for separating core from valence state which is set to − 6.0 Ry. Finally, we have used 100 k-point in our study.

Conclusion: In this study, the structural, electronic properties of undoped and impurity doped Mg2Ge compounds have been presented. The lattice parameter and deformation energy under the pressure have decreased with the impurity doping . The calculated band gap energy of Mg2Ge is in a good agreement with experimentally and theoretically reported band gap values. As a result of this the mBJ method is suitable to perform calculations. doped compounds exhibits semiconductor characteristics. The Mo doped compounds exhibits metallic properties.

References

[01] M. Petersen, F. Wagner, L. Hufnagel, M. Scheffler, P. Blaha, K. Schwarz, Improving the efficiency of FP-LAPW calculations, Comput. Phys. Commun. 126 (2000) 294–309, https://doi.org/10.1016/S0010-4655(99)00495-6.
[02] K. Schwarz, DFT calculations of solids with LAPW and WIEN2k, J. Solid State Chem. 176 (2003) 319–328, https://doi.org/10.1016/S0022-4596(03)00213-5.
[03] K. Schwarz, P. Blaha, G.K.H. Madsen, Electronic structure calculations of solids using the WIEN2k package for material sciences, Comput. Phys. Commun. 147 (2002) 71–76, https://doi.org/10.1016/S0010-4655(02)00206-0.
[04] K. Schwarz, P. Blaha, Solid state calculations using WIEN2k, Comput. Mater. Sci. 28 (2003) 259–273, https://doi.org/10.1016/S0927-0256(03)00112-5.
[05] K. Schwarz, P. Blaha, S.B. Trickey, Electronic structure of solids with WIEN2k, Mol. Phys. 108 (2010) 3147–3166, https://doi.org/10.1080/00268976.2010.506451.
[06] J.P. Perdew, K. Burke, M. Ernzerhof, GGA-PBE (1996) 3865–3868, https://doi.org/ 10.1103/PhysRevLett.77.3865.
[07] F. Tran, P. Blaha, Accurate band gaps of semiconductors and insulators with a semilocal exchange-correlation potential, Phys. Rev. Lett. 102 (2009) 5–8, https://doi.org/10.1103/PhysRevLett.102.226401.
[08] D. Koller, F. Tran, P. Blaha, Improving the modified Becke-Johnson exchange potential, Phys. Rev. B Condens. Matter 85 (2012) 1–8, https://doi.org/10.1103/ PhysRevB.85.155109.
[09] P. Jund, R. Viennois, C. Colinet, G. Hug, M. F`evre, J.C. T´edenac, Lattice stability and formation energies of intrinsic defects in Mg2Si and Mg2Ge via first principles simulations, J. Phys. Condens. Matter 25 (2013), https://doi.org/10.1088/0953- 8984/25/3/035403.

ISSN: 0067-3064

[10] A. Stella, A.D. Brothers, R.H. Hopkins, D.W. Lynch, Pressure coefficient of the band gap in Mg2Si, Mg2Ge, and Mg2Sn, Phys. Status Solidi 23 (1967) 697–702, https:// doi.org/10.1002/pssb.19670230231.

ISSN: 0067-3064

Innovative Biosensing Approach: 1D Photonic Crystal for Glucose Concentration Detection
P 37

Asma Tadji[1], Abdelkader Abderrahmane[2], Ilyes baba-Ahmed[3,4], Senouci Khaled[5], Pil Ju Ko[6]

[1] Higher National School of Renewable Energy, Environment and Sustainable Development, Constantine Road. Fasdis, Batna 05078, Algeria.
[2] Electrical Engineering Department, Faculty of Sciences and Technology, University Abdelhamid Ibn Badis Mostaganem, BP 188, Mostaganem 27000 Algeria.
[3] Energy Processes and Nanotechnology Laboratory, Physics Department, Sciences Faculty, Saad Dahleb Blida 1 University, BP 270, Blida 09000, Algeria.
[4] Biomedical engineering Department, Technology Faculty, Aboubekr Belkaid University, Tlemcen 13000, Algeria.
[5] Laboratoire de Structure, Elaboration et Application des Matériaux Moléculaires (SEA2M), Université Abdelhamid Ibn Badis Mostaganem, B.P. 227, Mostaganem 27000, Algeria.
[6] Department of Electrical Engineering, Chosun University, 375 Seosuk–dong, Dong–gu, Gwangju 501–759, Republic of Korea.

Abstract: In recent years, diabetes has become a major global health concern that affects a large number of people around the globe. According to statistics, 642 million individuals may be affected by diabetes by the year 2040 [1]. Photonic crystals (PCs) have been explored as a potential solution for the development of biosensors with the aim of measuring blood glucose concentrations with high precision and high sensitivity. PCs consist of a periodic structure with alternating refractive indices, which leads to the formation of photonic band gaps and the ability to control electromagnetic wave propagation, i.e., transmit or reflect certain wavelengths. Two-dimensional (2D) gallium sulfide (GaS) exhibits a wide direct band gap of ~3.1 eV in its monolayer form and ~2.6 eV in its bulk form [2], a high refractive index of 2.7152 at a wavelength of 633 nm [3], and a very broad spectral range, making it an excellent candidate for 1D photonic crystals [4]. In this research, we report novel design of 1D photonic crystal biosensor based on multilayered 2D GaS with prism/Au/$[GaS/T]^6T[GaS/T]^6$ structure, where T refers target glucose solution. We investigated numerically the photonic properties of the 1D PC with respect to the target concentrations. The successful integration of 2D materials within 1D photonic crystal structures highlights a promising avenue of research in biosensing.

Keywords: Biosensing, Photonic Crystal, Blood Measuring, Glucose Detection

References

ISSN: 0067-3064

[1] Ng, A.C., Delgado, V., Borlaug, B.A. and Bax, J.J., 2021. Diabesity: the combined burden of obesity and diabetes on heart disease and the role of imaging. Nature Reviews Cardiology, 18(4), pp.291-304.
[2] Jung, C.S., Shojaei, F., Park, K., Oh, J.Y., Im, H.S., Jang, D.M., Park, J. and Kang, H.S., 2015. Red-to-ultraviolet emission tuning of two-dimensional gallium sulfide/selenide. ACS nano, 9(10), pp.9585-9593.
[3] Kato, K. and Umemura, N., 2011. Sellmeier equations for GaS and GaSe and their applications to the nonlinear optics in GaS x Se 1− x. Optics letters, 36(5), pp.746-747.
[4] Abderrahmane, A., Senouci, K., Hachemi, B. and Ko, P.J., 2023. 2D Gallium Sulfide-Based 1D Photonic Crystal Biosensor for Glucose Concentration Detection. Materials, 16(13), p.4621.

ISSN: 0067-3064

Structural and Optical properties of LiGd1-x Lux$(WO_4)_2$co-doped Yb^{3+}/Er^{3+}
P 38

N. NAIMI[1], B.REKIK[1], M. DERBAL[1],I. LANEZ[1], L. Benharrat[2], Z. Bendaoud

[1]LPCMIALaboratory, Faculty of sciences, Saad Dahleb Blida1 University.
[2]CRTSE,Algeria

Abstract: Tungstate crystals with the general formula A(RE)(WO4)2, where A is the alkaline element; K,Li Na, Cs and Rb; the (RE) is trivalent element such rares earth have attracted a great attention, for their great optical properties [1] and high performance for many applications, such as optical fibers[2], scintillator materials[3],humidity sensors ,catalys [4], phosphor's and laser's light[5]. In the family of the double alkaline rare earth tungestates, The LiGd(WO4)2material crystallizes in the tetragonal structure with space symmetry group I4(1)/a and cell parameter (a = b = 5.20 Å, c = 11.17 Å) with Z = 2, we are synthesized a series of LiGd1-xLux(WO4)2 doped and co-doped Yb3+/Er3+ phosphors by a solid-state method. The XRD,XRF,MEB, PL, IR, and Raman analysis characterize the co-doped LiGd1- xLux (WO4)2 structure and optical properties . In this work we talk about the effect of the presence of Lutetium (Lu) in the compound LGW on the 2H11/2→4I15/2 and 2S3/2→4I15/2 emissions of the Erbium (Er3+) ion, in the case of the presence of ytterbium (Yb3+) as co-doping or lack thereof. we are analyzed the decay times of the these levels for the compounds LiGd1-xLux(WO4)2. : 1%Yb3+ / 0.4% Er3+x=90%,95% ,prepared at temperatures 800 °C and 850°C and compared with this results of LiLu(WO4) 2 co-doped Yb3+/ Er3+studied in reference [6].

References

[1] A.M. Kaczmarek, R. Van Deun, Chem. Soc. Rev. 42 (2013) 8835e8848.
[2] S. Dutta, S. Som, J. Priya, S. Sharma, Solid State Sci. 18 (2013) 114e122.
[3] L. You, Y. Cao, Y. Sun, P. Sun, T. Zhang, Y. Du, G. Lu, Sensor. Actuator. B Chem.161 (2012)799-804
[4] B. Rekik, M.Derbal, O.Benamara, K.Lebbou Yb-doped LiGd1-xLux(WO4)2 single crystal fibers grown from the melt and optical characterization. J Crystal Growth (2014).
[5] V. Petrov, M.C. Pujol, X. Mateos, O. Silvestre, S. Rivier, M. Aguil_o, R.M. Sol_e,J. Liu, U.Griebner, F. Díaz, Laser Photon. Rev. 1 (2007) 179 212
[6] Xiangyan Yun, Jun Zhou, Yaohui Zhu, Xiong Li, Shan Liu, Chen Fang, Mingxia Lv, Denghui Xu , Green up-conversionluminescence and optical thermometry of Yb3+/Er3+ co-doped LiLuW2O8 phosphor, Journal of Physics and Chemistry of Solids, 2022 .

ISSN: 0067-3064

Zr and Nb effects on Thermal and Mechanical properties of the Ti_2AlC MAX Phase
P 39

Lyacine Rabahi[a], Abdessabour Benamor[b], Youcef Hadji[b], and Riad Badji[a]

[a] Research Center In Industrial Technologies (CRTI) P. O. Box 64, Cheraga 16014, Algiers, Algeria .
[b] Laboratoire d'études et recherche en technologie industrielle, University of Saad Dahlab Blida 1, BP 270 Route de Soumaa, Blida, Algeria

Abstract: MAX phases are a fascinating class of materials with an unusual and sometimes unique set of properties that successfully combine the metallic and ceramic characteristics under various conditions [1, 2]. The scientific community's interest in these materials is growing steadily. A few years ago, only 155 MAX phases were known and studied, involving 16 A elements (mostly groups 13 and 14) and 14 M (early transition metal) elements of the periodic table [3]. However, the recent discovery of both solid solution and ordered MAX phases that contain either two M, two A, or two X elements has opened the door to the discovery of many new quaternary MAX phases. Besides obtaining new properties, which generally do not exist in the starting material, alloying elements can make possible the formation of new, non-existent MAX phases or the establishment of a close relationship between the composition and properties of materials in order to get modulable properties depending on the targeted application [4].
In this context, the main objective of the present work is to study the effects of Zr and Nb alloying (fourth) elements on the thermal and mechanical properties of the Ti_2AlC MAX phase by means of DFT calculations. The elastic constants, as well as several mechanical properties such as young modulus *E*, shear modulus *G*, and Poisson's ratio υ, were derived from the strain-stress curves. The temperature effects on the studied properties were considered when applying the quasi-harmonic Debye's model [5]. The obtained results display a strong dependency of the studied properties on the Zr and Nb concentrations (presence). Nb and Zr elements prefer to substitute for the Ti atom. However, Nb insertion increases the rigidity of Ti_2AlC, while the stability of this material is found to be decreased by Nb and Zr insertion. Moreover, Ti_2AlC, $(TiNb)_2AlC$, and $(TiZr)_2AlC$ are found to be brittle materials and mechanically stable at 0 K with their hexagonal structure. The Ti_2AlC alloy is the most rigid even at elevated temperatures, and Nb/Zr insertion decreases its rigidity.

Keywords: DFT-calculations, MAX Phases, Elastic properties, Thermal Properties, Quasi-Harmonic Debye's model.

ISSN: 0067-3064

References

[1] D. Yu-Lei, Electronic Structure and Elastic Properties of Ti_3AlC from first-principles calculations, Chin. Phys. Lett. Vol.26, N 11(2009).
[2] M. W. Barsoum, The $M_{n+1}AX_n$ Phases and their Properties, Ceramics Science and Technology Vol 2: Properties. 2010.
[3] M. Radovic, M. W. Barsoum, MAX phases: Bridging the gap between metals and ceramics, American Ceramic Society Bulletin, Vol. 92, No. 3.
[4] M. Sokol, V. Natu, S. Kota, M. W. Barsoum, On the Chemical Diversity of the MAX Phases, Trends in Chemistry, Vol 1, N°2 (2019), 210-223.
[5] M.Blanco, E. Francisco, V. Luana: GIBBS: isothermal-isobaric thermodynamics of solids from energy curves using a quasi-harmonic Debye model, Comput. Phys. Commun. 158 (57) 00104655 (2004).

ISSN: 0067-3064

The Influence of Electric Field on the Energy Spectrum "Stark Effect" P 40

M'hamed HADJ MOUSSA

Theoretical Physics and Radiation Matter Interactions Laboratory (LPTHIRM),
Physics Department, Sciences Faculty , University of Saad Dahlab-Blida 1 ,
PO box 270 SoumaaRoad , 09000 , Blida, Algeria.
E-mail: hadj2009@gmail.com , hadjmoussa-mhamed@univ-blida.dz

Abstract: In this study, we present the solution of the Duffin-Kemmer-Petiau Oscillator (DKPO) equation in the presence of an electric field ε. We use the displacement operator to investigate the influence of the electric field ε on the energy spectrum E_n, a phenomenon known as the "Stark effect." Our calculations demonstrate the modified energy spectrum E_n levels resulting from the presence of the electric field ε, and we illustrate these results graphically to enhance visualization.

ISSN: 0067-3064

Study of performance neural model to predict PIMs permeability of CH4 gas.
P 41

Maroua Henni, Mohamed Krea, Hanaa Hasnaoui

Laboratoire LME, Faculté de Technologie, Université de Médéa

Abstract: Polymeric microporous materials are gaining popularity due to their potential applications in gas separation membranes, sorption resins, chromatographic materials, and gas storage media. The concept of PIMs can be traced back to Prof. McKeown's research on phthalocyanine materials at Cardiff University in the 1990s [1]. Since Budd and McKeown's groundbreaking work on PIM-1 in 2004 and the invention of linear-chain polyimides with intrinsic microporosity (PIM-PIs) in 2008, hundreds of new ladder PIMs and PIM-PIs with a wide range of custom-designed polymer architectures have been synthesized and evaluated for their gas separation performances [2].

In this work, a database of 121 PIMs with various structural variations was built and used to create a neural model that could forecast their permeability to CH4 gas. This study focus on comparing experimental permeability values reported in the literature for each class of PIMs (15 compounds of ladder PIMs and 15 compounds polyimides of intrinsic microporosity (PIM-PIs)) for CH4 gas in order to assess how well the elaborated model performs. Figure 1 illustrates the results of the comparative analysis for Ladder PIMs family, which showed good performance.

Results

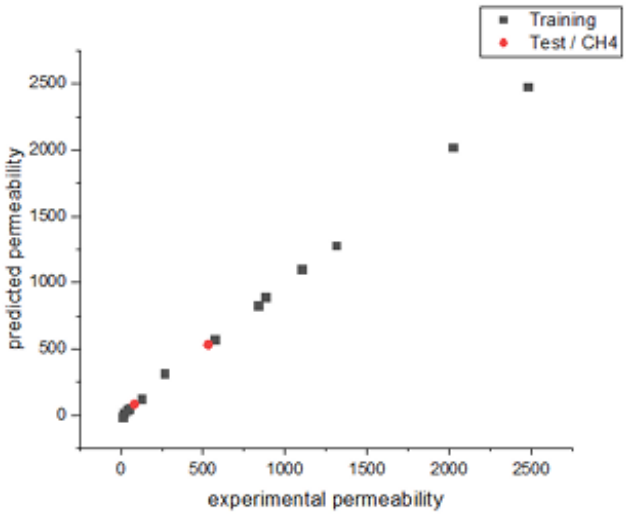

Figure I: Comparison between experimental and predicted permeability of Ladder PIMs family by the elaborated ANN model.

ISSN: 0067-3064

References

[1 Mckeown, N. B. Polymers of Intrinsic Microporosity. 2012, (2012)
[2] Y. Wang, X. Ma, B.S. Ghanem, Polymers of intrinsic microporosity for energy-intensive membrane-based gas separations, 2018

ISSN: 0067-3064

Study of structural, electronic and magnetism properties of ZZrTiAl (Z=Pd and Ru)quaternary heusler alloys by FP-LAPW method for spintronic application
P 42

Lalia. MESSAOUDI [1,2], Mostefa. DJERMOUNI [1,3], Habib Rached[4],Chaimaa.MOHAMMED KRARROUBI[1,2]*, and Nadjet ZEGGAI [1,2]

[1] Laboratory of Computational Physics of Materials (LPCM), Djilali Liabès University of Sidi-Bel-Abbès,Algeria
[2] Department of Physics, Faculty of Science and Technology, Ahmed ZABANA University of Relizane, Algeria
[3] Department of Physics, Faculty of Exact Sciences, Djillali Liabès University of Sidi Bel-Abbès,Algeria
[4] Department of Physics, Faculty of Exact Sciences, Hasiba Ben Bouali, University of chlef
Adresse Email : messaoudilalia28@gmail.com

Abstract: The main goal of the present work is to provide a report on the structural and magnetic stabilities and study the electronic, properties of ZZrTiAl (Z=Pd and Ru)quaternary Heusler alloys by using the ab-initio first-principles method, based on the Density Functional Theory (DFT). The ground state properties and magnetic stabilities reveal that all our compounds are ferromagnetic materials and crystallize in type III phase.. The magneto-electronic calculation reveals the half metallic ferromagnets behaviours for all the investigated compounds.

Keywords: Heusler alloys; magnetic properties ; Density functional theory.

References:

[1] R.M.Martin.Electronic structurs,basis theory and practical methods. Combrige. (2004).
[2] D.S.Shall and J.A.Steckel.Density Functional Theory,a practical introductions Wiley. (2009).
[3] J.M.Wills,O.Eriksson,P.Anderson,A.Delin,O.Grechnyev and M.Alouani(auth). Full potential Electronic Structure Method,Energy and Force Calculations With Density Func-tional and Dynamical Mean Field Theory.Springer.(2010).

ISSN: 0067-3064

Structural and optical properties of Erbium-doped $(Gd_{1-x}Lu_x)_3Al_5O_{12}$ cubic garnet elaborated by co-precipitation
P 43

Imane LANEZ[1*], Brahim REKIK[1], Walid MEHIS[1], Mourad DERBAL[1], Amina KEZZIM[1], Soumia HAMZI[1]

[1]LPCMIA Laboratory, Department of Physics, Faculty of Sciences, University of Saad Dahleb Blida 1, ALGERIA
Email: imanelanez@hotmail.com

Abstract: Due to their exceptional optical properties, efficient energy transfer, and chemical durability, rare earth aluminate garnet compounds, particularly $Gd_3Al_5O_{12}$ doped rare earths serve as a highly promising host matrix for phosphor materials **[1,2]**. In order to inhibit the thermal decompositions and enhance the stability of the crystal structure of $Gd_3Al_5O_{12}$ garnet, a substitution approach was employed, specifically, GdAG was substituted with considerably smaller Lutetium (Lu^{3+}) ions, considering the formation of solid solutions known as $(Gd, Lu)_3Al_5O_{12}$**[2]**. Erbium-doped $(Gd_{1-x}Lu_x)_3Al_5O_{12}$ with x=0.2 and 0.3, were elaborated by co-precipitation method with NH_4OH and NH_5CO_3 precipitating agents, calcined at different temperatures. The evolution of the structure and the formation of the pure garnet phases elaborated with these methods were discussed through XRD results. FTIR results have confirmed the appearance of vibrations of elements :(**M Gd, Lu, Er, Al)**. The existence of a highly intense band at 270 nm in the excitation spectrum (PLE), has confirmed the efficient transfer of energy between $\mathbf{Gd^{3+}}\rightarrow\mathbf{Er^{3+}}$ ions. The emission (PL) spectra, monitored at 270 nm of excitation wavelength show the most intensive band at 450 nm which is responsible for the blue color of synthesized phosphors.

Keywords: Garnet, Erbium, Co precipitation, phosphor materials, PLE, PL

ISSN: 0067-3064

Investigating the Crossover Region in the QCD Phase Diagram
P 44

Mohamed Amine Lakehal[a,b]* and Amal Ait El Djoudi[b]

[a] Physics departement, Université M'hamed Bougara Boumerdes, 35000, Algeria
b Laboratoire de Physique des Particules et Physique Statistique
Ecole Normale Supérieure - Kouba, B.P. 92, 16050, Vieux Kouba, Algiers, Algeria

Abstract: We investigate the crossover region in the QCD phase diagram in the μ-T plane, by using the equation of state of a hadronic gas (HG) phase consisting of massive pions and a Quark-Gluon Plasma (QGP) phase, consisting of massless up and down quarks and massive, strange quarks, based on the bag model. We calculate some physical quantities that describe well the system and study their variations with varying temperature at zero baryochemical potential. We examine the behavior of these quantities in the temperature range: $100<T<400$ *MeV*, corresponding to the crossover region, and compare with Lattice QCD results.

Keywords: QCD phase diagram, Quark-Gluon Plasma, Density of states, Lattice QCD.

References

[1] A. M. Halasz et al. Phys. Rev. D **58**, 096007 (1998).
[2] L. P. Csernai, J. I. Kapusta and L. D. McLerran, Phys.Rev. Lett. **97**, 152303 (2006).
[3] M. Albright, J. Kapusta and C. Young, Phys. Rev. C **90**, N 2, 024915 (2014).
[4] C. J. Plumberg, T. Welle and J. I. Kapusta, nucl-th/1812.01684 (2018).
[5] W. Greiner, L. Neise and H. StÖker , *Thermodynamics and statistical mechanics* (Springer Science & Business Media, 2012).
[6] R. Balian and C. Bloch, Ann. Phys. (N. Y.) **60**, 401 (1970).
[7] M. Ladrem and A. Ait El Djoudi, Eur. Phys. J C **44**, 257 (2005); A. Ait El Djoudi, Canad. J. Phys. Vol. **91** N°10, 793 (2013).
[8] A. Bazavov et al, Phys. Rev. D **90**, 094503 (2014).

ISSN: 0067-3064

Quantum Computational energies in spin symmetry limit using Feynman path integral method.
P 45

Mohamed Douici[a], Hocine Boukabcha[b] and Rachid Fermous[a]
(a) Laboratoire de Valorisation des Substances Naturelles (LVSN), Khemis Miliana University, Route de Theniet El Had, 44225 Khemis Miliana, Algeria
(b) Laboratory of Energy and Smart Systems, Khemis Miliana University, 44225 Khemis Miliana, Algeria

Abstract: The study of the energies spectra is an important tool to get useful information about the properties of atomic physics. In these latter, obtaining exact solutions of the nonrelativistic and relativistic wave equations, such as the Schrödinger and Dirac equations, is a critical problem when dealing with mixed vector V(r) and scalar S(r) potentials. The aim of the present contribution is to study the bound state solution in the relativistic limit of the Dirac wave equation with Coulomb-like potential plus a new generalized Morse-like potential using the Feynman path integral method. As a first step, an expression relativistic of the energy spectrum in the spin symmetry limit is established. As a second step, the energy spectra are calculated for various values of the quantum numbers n, l and k. The obtained results are compared to those obtained by the Nikiforov-Uvarove method [3].
Conclusion: In this work, we have solved the relativistic Dirac wave equation in the presence of Coulomb-like potential plus the new generalized Morse-like potential using the Feynman path integral method with an arbitrary spin-orbit state k under the conditions of the spin symmetry limit. The energy eigenvalues are obtained in relativistic case. We have also shown that in the presence of a Coulomb-like potential, the degeneracy is removed for all the pairs of spin doublets.

References

[1] Njoku I J, Onyenegecha C P, OkerekeC J and Omugbe E, 2022 Eur. Phys. J. Plus 137.
[2] Douic M, Boukabcha H and Fermous R, 2023 Phys. Scr. 98 075405.
[3] Ikot A N, Maghsoodi E, Zarrinkamar S and Hassanabadi H 2013 Journal of Theoretical and Applied Physics 7 53.
[4] Khandekar D C, Bhaguht K Vand Lawande S V 1991 Path Integral Methods and Their Applications (Singapore: World Scientific Publishing).

ISSN: 0067-3064

DFT Calculations Revealing the Electronic and Structural Characteristics of Half Heusler Alloys: Case Study of TiIrSb, ZrIrSb and TaIrGe.
P 46

MohammedHADBI[1], Kamel DEMOUCHE[1], Mohammed Lamine FODIELI[2], Hiba ELARABI[3], Khawla CHAOUI[4], Meriem BENAISSA[5]

[1] Materials Science and Applications Laboratory. Faculty of Sciences and Technology. University of Ain Temouchent Belhadj Bouchaib, B.P. 284. 46000 Ain Temouchent. Algeria
[2]Laboratoire de Physique des Matériaux, Université Amar Telidji de Laghouat; BP37G, Laghouat 03000, Algeria
[3]Laboratoire d'études physico-chimiques, Université Dr Moulay Tahar, Saida 20000, Algeria
[4]Laboratoire De Physique, Université 8 Mai 1945, BP 401, 24000 Guelma, Algeria
[5]Laboratoire De Physique Techniques Expérimentales Et Ses Applications, Université De Médéa, Alger.

Abstract: A theoretical investigation was conducted on ternary intermetallic Half-Heusler (HH) compounds MIrSb (M= Zr, Ti) and TaIrGe with 18 valence electrons, focusing on their structural and electronic characteristics. To carry out this study, the Vienna ab-initio Simulation Package (VASP)1 was employed, utilizing density functional theory (DFT)2 with the GGA-PBE approximation3 PBE+U and SCAN for evaluating the energy of exchange and correlation. The results obtained were compared to both previous experimental and theoretical studies. The compounds under investigation were found to crystallize in a cubic system with the $F\bar{4}3m$ space group (N°:216)4. In terms of structural properties, the cell parameter was calculated and exhibited results in close agreement with experimental findings. Regarding the electronic properties, it was observed that these materials exhibit a semiconductor nature characterized by an indirect band gap.

Keywords: Structural, Electronic, DFT, VASP, Half-Heusler Alloys, Semiconductors.

References

[1] Kresse, G. & Hafner, J. Ab initio molecular dynamics for liquid metals. Phys. Rev. B 47, 558– 561 (1993).
[2] Kohn, W. & Sham, L. J. Self-Consistent Equations Including Exchange and Correlation Effects. Phys. Rev. 140, A1133–A1138 (1965).
[3] Perdew, J. P., Burke, K. & Ernzerhof, M. Generalized Gradient Approximation Made Simple. Phys. Rev. Lett. 77, 3865–3868 (1996).

ISSN: 0067-3064

[4] Gautier, R. et al. Prediction and accelerated laboratory discovery of previously unknown 18 electron ABX compounds. Nature Chem 7, 308–316 (2015).

ISSN: 0067-3064

Study of the influence temperature on the electrical structure of supraconductors
P 47

Chaimaa. MOHAMMED-KRARROUBI[1,2]*, Mostefa. DJERMOUNI[1,3], Asmaa. MOHAMMED-KRARROUBI[4], Lalia.MESSAOUDI[1,2,] and Nadjet ZEGGAI [1,2]

[1] Laboratory of Computational Physics of Materials (LPCM), Djilali Liabès University of Sidi-Bel-Abbès,Algeria
[2] Department of Physics, Faculty of Science and Technology, Ahmed ZABANA University of Relizane,Algeria
[3] Department of Physics, Faculty of Exact Sciences, Djillali Liabès University of Sidi Bel-Abbès,Algeria
[4] Renewable energy research unit in the Saharan (URERMS)-CDER, Adrar ,Algeria
Email author : mk_chaimaa@hotmail.fr

Abstract: Motivated by the theoretical predictions of the high critical temperature (TC) hydride in many hydride superconductors (SCs), experiments were performed to confirm that the compressed sulfur hydride H3S exhibits a TC of 203 K at pressures around of 150 GPa. To this end, the objective of this work on the one hand, to know the microscopic mechanism of superconducting hydride materials; and on the other hand, to contribute to the exploration of new high-pressure SC hydrides. And in order to achieve our goals, we will use a first-principle method based on DFT theory. This theory helps us to predict the electronic, chemical, and phononic properties of hydride materials.

Keywords: Superconductivity, electron-phonon coupling, critical temperature, DFT

References

[1] H. Liu, I. I. Naumov, R. Hoffmann, N. W. Ashcroft, and R. J. Hemley, Proc. Natl. Acad. Sci. USA 114, 6990 (2017).
[2] A. P. Drozdov, M. I. Eremets, I. A. Troyan, V. Ksenofontov, and S. I. Shylin, Nature (London) 525, 73 (2015)
[3] P Blaha, K Schwarz, G K H Madsen, D Kvasnicka, and J LuitzAn Augment. Pl. Wave+ Local Orbitals Program for Calculating Crystal Properties (Karlheinz Schwarz, Techn. Universität Wien, Austria), 2018. ISBN 3-9501031-1-2. (2001).

ISSN: 0067-3064

Structural and electronic properties of Mg_2FeH_6 hydride: DFT study
P 48

N. MOSTEGHANEMI[1], L. RABAHI[1,2], L. ROUAIGUIA[1], A. KELLOU[1]

1 Theoretical Physics Laboratory, Faculty of Physics, USTHB, BP 32 Bab-Ezzouar Algiers, Algeria
2 Research Center in Industrial Technologies (CRTI), BP 64, Cheraga, Algiers, Algeria

Abstract: The diamagnesium iron hydride, Mg_2FeH_6, has attracted more attention as candidate for hydrogen storage applications. Because of their light density, high hydrogen capacity and abundance of its constituent elements [1-2]. However, there is scarce literature available on physical properties of this material, especially DFT based investigations. In the present work, the structural and electronic properties of Mg_2FeH_6 are investigated using the Density Functional Theory (DFT) based pseudo potential method. The obtained results are in a good agreement with available data[3]. Mg_2FeH_6 exhibits cubic (fcc) phase with space group Fm-3m (N° 225). Our calculated values of band gap revealed that Mg_2FeH_6 is a semiconductor with an energy gap of 1.96 eV.

Key-words: Mg_2FeH_6 hydride, DFT calculations, electronic properties, thermo plane wave program.

References

[1] Zhang, J., et al. "First-principles investigation of Mg_2Ni phase and high/low temperature Mg_2NiH_4 complex hydrides." Journal of Physics and Chemistry of Solids 70.1 (2009): 32-39.
[2] Zhang, J., et al. "First-principles investigation of Mg_2TH_y (T= Ni, Co, Fe) complex hydrides." Physica B: Condensed Matter 403.23-24 (2008): 4217-4223.
[3] Zareii, S. M., & Sarhaddi, R. (2012). Structural, electronic properties and heat of formation of Mg_2FeH_6 complex hydride: an ab initio study. *Physica Scripta*, *86*(1), 015701.

ISSN: 0067-3064

The effect of a biaxial strain on the electronic structure of indium nitride
P 49

Ouahiba Namir[1, a] * and Imad Belabbas [2, b]

[1,2] Equipe de Cristallographie et de Simulation des Matériaux, Laboratoire de Physico-chimie des Matériaux et Catalyse, Université de Bejaia, 06000, Algeria
[a] ouahiba.namir@univ-bejaia.dz, [b] imad.belabbas@univ-bejaia.dz

Abstract: The effects of homogeneous biaxial strain on the electronic structure of wurtzite indium nitride (InN) have been investigated through first principles calculations based on density functional theory. Our calculations demonstrate that InN undergoes a structural phase transition from wurtzite to a graphitic-like phase (Figure 1 (a, b)) at a tensile strain of +6%, which has been identified as a first-order transition. This transformation is accompanied by a transition from a direct to an indirect band gap. Keywords: InN, DFT, biaxial strain, wurtzite, graphitic, electronic structure, phases transition. 1. Introduction Group-III nitride semiconductors, particularly InN, have gained significant attention due to their potential in applications such as short-wavelength LEDs and high-frequency electronic devices. InN stands out among these semiconductors due to its exceptional properties, including the largest lattice parameter and the smallest bandgap (0.7 eV). By applying strain, the structure and electronic properties of semiconductors can be modified [1]. In this study, we used first principles calculations to investigate the impact of homogeneous biaxial strain on the electronic properties of wurtzite InN. Both compressive and tensile strains were considered, ranging from -10% to +10%. The simulations were performed using the ABINIT code with the local density approximation and the pseudo-potentials modified à la Christensen. Well-converged results were obtained using a cutoff energy of 200 Ry and a Monkhorst Pack k-point mesh of 22×22×22. 2.

Results :

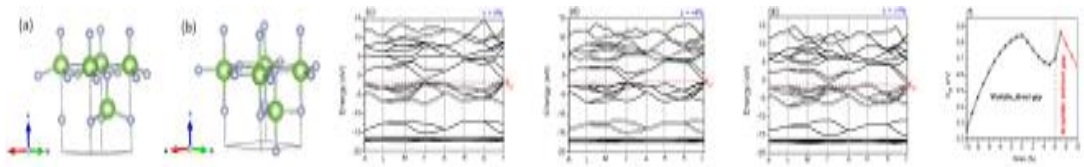

Figure 1. (a) wurtzite structure, (b) graphitic-like structure of InN.(c-e) Band structures of InN in different strain states. (f) Evolution over biaxial strain from −10% to +10% of wurtzite InN's band gap.

ISSN: 0067-3064

Figure 1 (f) shows the band gap energy (Eg) evolution of InN under biaxial strain. The band gap is initially 0.85 eV with a direct nature (both the valence band minimum (VBM) and the conduction band maximum (CBM) located at the center of the Brillouin zone (Γ point) at zero strain (Figure1 (c)). It nonlinearly decreases under compression (0% to -10%) and extension (0% to +6%) while remaining direct. From +6% to +7% strain, Eg increases and then linearly decreases from +7% to +10%, resulting in an indirect band gap where the VBM and CBM are located at the and H points, respectively (Figure 1 (e)). This indicates that the wurtzite to graphitic-like phase transition involves a transformation from a direct to an indirect band gap.

Conclusion: Our DFT calculations have demonstrated the occurrence of a phase transition in InN from a wurtzite to a graphitic-like structure at a tensile strain of +6%. This transition is of first-order nature, indicating a sudden change in the crystal arrangement. Additionally, we have observed a transition in the electronic band gap property of InN, where it shifts from a direct band gap to an indirect band gap.

References

[1] O. Namir, J. Kioseoglou, Ph. Komninou, Th. Karakostas and I. Belabbas, Modelling and Simulation in Materials Science and Engineering, 29 (2021) 065013

ISSN: 0067-3064

Electronic and optical properties of 2D-bilayer systems: graphene, boron nitride and carbon-boron nitride
P 50

S. Tazekritt, A. Kellou, M. Gallouze

Theoretical Physics and Didactic Laboratory, Faculty of Physics, University of Science and Technology Houari Boumediene (USTHB), P.B. N°32 El-Alia, Bab Ezzouar, Algiers.
stazekritt@usthb.dz

Abstract: Research into 2D materials has accelerated as a result of the discovery of graphene in 2004, and this is anticipated to have a significant impact on our understanding of material properties at small dimensions. Among other materials, boron nitride (BN) and carbon-boron nitride (C-BN) have exceptional characteristics with the possibility of being used in a large variety of devices, including energy storage, catalysts, thermoelectric devices, and medicine.
In this work, we examined the physical properties of two-dimensional bilayer graphene (C), boron nitride (BN), and carbon-boron nitride (C-BN) using the density functional theory. The energetic, electronic, and optical properties have been calculated. The results indicate that bilayer graphene always remains a semiconductor with a zero bandgap. However, BN is an isolator, and C-BN is a semiconductor with a small bandgap.
Next, the optical observables such as absorption and reflectivity are calculated in both polarizations. The results show that the absorption is zero in the infrared region. After that, it reaches its maximum value in the ultraviolet region. Reflectivity is also improved in the ultraviolet region.

Keywords: 2D materials, bilayer systems, energetic properties, electronic gap, and optical properties.

ISSN: 0067-3064

Atomistic simulation of III-Nitride semiconductors
P 51

OUMESSAOUD Sara [1,a], BELABBAS Imad [2,b]

1,2 Equipe de Cristallographie et de Simulation des Matériaux, Laboratoire de Physico-chimie des Matériaux et Catalyse
Université de Bejaia, 06000, Algeria
sara.oumessaoud@univ-bejaia.dz

Abstract :
We have investigated, by using computer atomistic simulations some of the physical properties, such as structural and elastic properties, of binary III-nitride semiconductors (GaN, AlN and InN) in the wurtzite phase. Our calculations were performed using the CASTEP code, which is based on Theory Density Functional (DFT), where we used ultra-soft type pseudo-potentials and the two functional exchanges and correlations LDA-PZ and GGA-PBE. Our study made it possible to reproduce the general tendencies of the DFT by employing the two standard functionals, i.e. LDA-PZ and GGA-PBE.

Keywords: GaN, InN, AlN, structural and elastic properties, DFT, CASTEP

Introduction: Due to their excellent properties which makes them attractive for the development of electronic and optoelectronic devices for a wide range of applications, such as: LASERs used in high density optical data storage and high-resolution laser printing, LEDs (light emitting diodes), for signaling, color display or lighting. Semiconductors belonging to the family of III-nitride materials have attracted considerable attention within the scientific community. They are mainly formed by the three binary compounds, which are: gallium nitride (GaN), aluminum nitride (AlN) and indium nitride (InN), as well as by their ternary and quaternary alloys. The value of the direct bandgap varies continuously between 3.4 eV for GaN and 6.2eV for AlN and thus, extending over the spectral range from visible to ultraviolet. In a recent discovery, it was shown that InN has a gap of only 0.7 eV which extends the range of direct gaps covered by nitrides-III to the near infrared region.
Computational methods: We have carried out computer atomistic simulations to investigate some of the physical properties, such as structural, elastic and thermodynamic of III-nitride semiconductors (GaN, AlN and InN) in the wurtzite phase. Our calculations were performed using the CASTEP code, which is based on Density Functional Theory (DFT), where we used ultra-soft pseudo-potentials and the two exchanges and correlations functionals, i.e. LDA-PZ (Perdew-Zunger) and GGA-PBE (Prdew-Becke-Ernzerhof).
Results and discussions:

ISSN: 0067-3064

- **Structural properties**

In this study, we have focused on lattice parameters of primitive cell of hexagonal structure of three materials; GaN, AlN and InN. Two convergences tests were carried out; the first the grid of k-points "k_g" used to sample the Brillouin zone and the second on the cut-off energy "E_{cut}" which defins the size of the plane waves basis set. As shown in Figure.1, The variation of lattice parameters versus kg and Ecut respectively, presents a decrease then a stabilization. The best convergence of the lattice parameter is obtained at a value of 40 of the number of points reduced by symmetry and at a cutoff energy of 80 Ry.

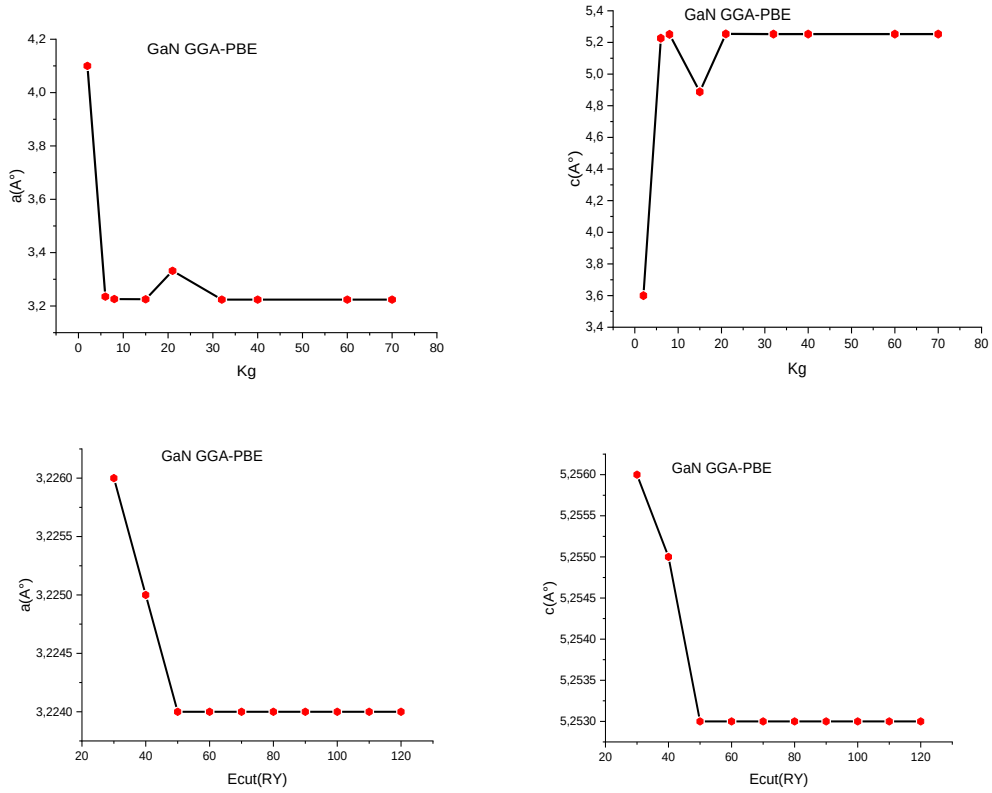

Figure 1: Evolution of lattice parameter a and c of GaN versus Kg and Ecut, respectively with the functional GGA-PBE

For all materials (table 1), the values of the lattice parameters obtained with the GGA-PBE functional are higher than the experimental values and those obtained with the LDA-PZ functional are lower. This reflects general trends of the DFT and those of so-called standard exchange functionals and correlations. Furthermore, our results are in good agreement with the results of other theoretical studies based on DFT and obtained with the same type of exchanges and correlations functionals.

ISSN: 0067-3064

Table 1 : values of the calculated and experimental lattice parameters of the three materials (GaN, AlN and InN) with the GGA-PBE and LDA-PZ functionals.

Exchanges and correlations functionals	LDA-PZ		GGA-PBE		Experimental values [1] [2]	
Lattice parameter	a(Å)	c(Å)	a(Å)	c(Å)	a(Å)	c(Å)
GaN	3,155	5,145	3,224	5,253	3,189	5,185
AlN	3,0637	4,9	3,125	5,007	3,112	4,982
InN	3,528	5,709	3,608	5,835	3,540	5,705

- **Elastic properties**

The elastic constant tensor of hexagonal structure is defined as a following form:

$$C_{ij}=\begin{bmatrix} C_{11} & C_{12} & C_{13} & 0 & 0 & 0 \\ C_{11} & C_{11} & C_{13} & 0 & 0 & 0 \\ C_{13} & C_{13} & C_{33} & 0 & 0 & 0 \\ 0 & 0 & 0 & C_{44} & 0 & 0 \\ 0 & 0 & 0 & 0 & C_{44} & 0 \\ 0 & 0 & 0 & 0 & 0 & C_{66} \end{bmatrix} \text{ with: } C_{66} = \frac{1}{2}(C_{11}\text{-}C_{12})$$

Four convergence tests were carried out. The first was in relation to the grid of k-points, the second in relation to the cut-off energy E_{cut}, the third in relation to the number of points in the parabolic fit Np and the last in relation to a maximum value of the deformation parameter δ_{max} (amplitude of deformation).

ISSN: 0067-3064

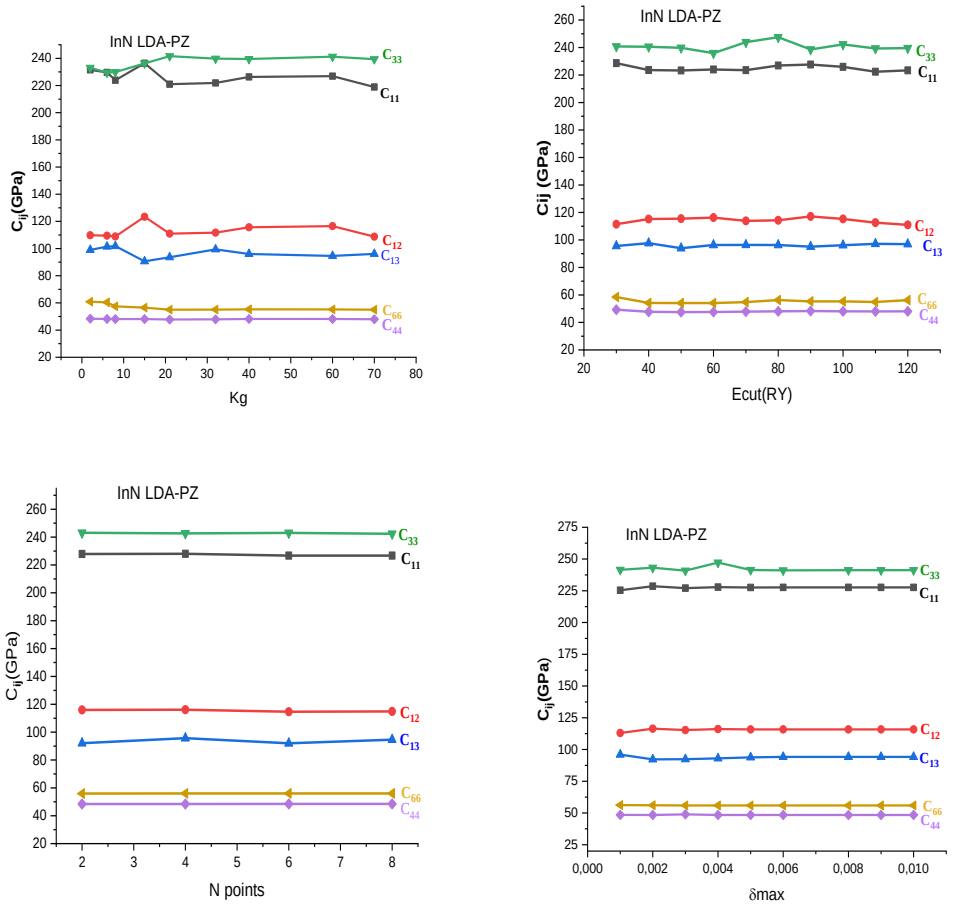

Figure 2: Evolution of the elastic constants of InN versus Kg, Ecut, the number of points of the parabolic fit Np and the maximum amplitude deformation δmax, respectively; case of the LDA-PZ functional

As shown in figure 3 the best convergence of elastic constant for all materials is obtained at a value of 40 of the number of points reduced by symmetry, cut-off energy Ecut at 80 Ry, Np at 4 and finally at a value of 0.003 of δ_{max}.

The values of the elastic constants of three materials GaN, AlN and InN (table 2) obtained with the LDA-PZ functional present a better agreement with the experimental results compared to the results obtained with the GGA-PBE functional.

Conclusion : We were able to reproduce the values of the different physical properties (structural, elastic and thermodynamic) of the three III-Nitride semiconductors such as GaN, AlN and InN, which are in good agreement with the experimental results published in the literature. Furthermore, our study allowed us to reproduce the general trends of density functional theory (DFT) which effectively treats physical properties in the ground state by using the standard LDA-PZ(Perdew-Zunger) and GGA-PBE (Prdew-Becke-Ernzerhof) functionals.

ISSN: 0067-3064

Table 2 : values of the calculated and experimental of elastic constant the three materials (a-GaN, b-AlN and c-InN) with the GGA-PBE and LDA-PZ functionals.

C_{ij}	C_{11}	C_{12}	C_{13}	C_{33}	C_{44}	C_{66}	
C_{ij} (GPa) LDA-PZ	336,7 (5,98%)	136,1 (6,14%)	99,9 (5,75%)	408,5 (2,65%)	95,3 (7,03%)	115,3 (7,03%)	**a**-GaN
C_{ij} (GPa) GGA-PBE	323,6 (16,9%)	110,4 (23,88%)	79,4 (25%)	354,7 (10,83%)	88,1 (16%)	106,5 (13,27%)	
C_{ij} (GPa) Exp [3]	390	145	106	398	105	124	
C_{ij}	C_{11}	C_{12}	C_{13}	C_{33}	C_{44}	C_{66}	
C_{ij} (GPa) LDA-PZ	406,7 (1%)	132,1 (11,11%)	105,6 (6,8%)	374,3 (3,64%)	121,4 (2,53%)	137,3 (4,84%)	
C_{ij} (GPa) GGA-PBE	337,4 (8%)	119 (19,87%)	96,1 (3,15%)	348,9 (9,88%)	113,9 (8,46%)	129,2 (1,28%)	**b**-AlN
C_{ij} (GPa) Exp [4]	410,5	148,5	98,9	384,5	124,6	131	
C_{ij}	C_{11}	C_{12}	C_{13}	C_{33}	C_{44}	C_{66}	
C_{ij} (GPa) LDA-PZ	227,1 (0,93%)	115,3 (5,78%)	92,4 (14,44%)	240,9 (17,51%)	48,9 (11,1%)	56,9 (1,89%)	**c**-InN
C_{ij} (GPa) GGA-PBE	195,1 (13,3%)	90,1 (17,36%)	72,8 (32,6%)	206,2 (22,19%)	45,1 (17,92%)	52,9 (9,5%)	
C_{ij} (GPa) Exp [5]	225	109	108	205	55	58	

Reference

[1] I. BELABBAS, P. RUTERANA, J. CHEN, G. NOUED. Philosophical Magazine, Taylor Francis, 2006,86 (15)
[2] I. Vurgaftman and J.R. Meyer, journal of Applied physics, Vol.94, pp.3675-3696,2003
[3] P. POLIAN, M. GRIMSDITCH and I. GRZEGORY. J.Appl. Phys, 79(1996)
[4] L. E. McNeil, M. Grimsditch, and R. H. French, J. Am. Ceram. Soc. 76, 1132 (1993). DOI: 10.1111/j.1151-2916. 1993.tb03730. x.
[5] A.F. Wright : J. Appl. Phys. Vol. 82 (1997), p. 5259

ISSN: 0067-3064

Effect of total isovalent replacement of (Cu) by (Ag) on the structural properties of the CZTS absorber
P 52

Kouaci Khaled [1,2]*, Belkhettab Ilyas[1], Latreche Slimane[3], Khelfane Amar[1], Derbal Mourad[2], Tablaoui meftah[1]

[1] Research Center in Semiconductors Technologies for the Energetics (CRTSE), BP 140, Alger 7 Merveilles, 16200 Algiers, Algeria
[2] LPCMIA, Physics Dept., Saad Dahlab University, Blida1, Route de Soumaa, BP 270, Blida 09000, Algeria
3 Technical platform for physico-chemical analysis (PTAPC), microstructural and microanalysis division, University of Science and technology (USTHB), BP 32 El-Alia, Bab-Ezzouar, Algiers 16111, Algeria

Abstract: Quaternary compound Cu2ZnSnS4 (CZTS) is a promising material in the domain of photovoltaic applications. Alloying with appropriate elements allows better control of its properties. To this end, considerable efforts have been directed toward exploring the effect of isomorphic substitutions on the general features of quaternary chalcogenide compounds [1] with the main aim to increase the formation energy of detrimental defects. In this sense, Ag2ZnSnS4 obtained by total substitution of Cu with isovalent element (Ag) is considered to be an approach of significant interest to improve the performance of photovoltaic chalcogenide semiconductors. In this work we describe the synthesis of high-purity bulk multi-element semiconductor compound Ag2ZnSnS4 (AZTS) via solid state reaction method. The synthesis has been undertaken in an evacuated quartz ampoule loaded with the constituent elements Ag, Zn, Sn and S [2]. The sealed ampoule was heated then to above the melting point of the AZTS compound. The X-Ray powder diffractogram of the obtained Ag2ZnSnS4 sample (Figure. 1) indicates that this material can crystalize with Pirquitasite-type structure in the tetragonal space group I-42m (N°121), as verified by the existence of nine characteristic peak corresponding to (101), (110), (112), (200), (204), (224), (132), (116) and (226) plans. A set of some other peaks were also observed, and have been attributed to binary (ZnS) and ternary (ATS) secondary phases. The lattice vibrational modes were researched by means of RAMAN spectroscopy using two different excitation wavelengths (Figure. 2). Two similar Raman spectra were obtained under 633 nm and 785 nm excitations showing two main peaks located at 345 and 269cm-1 which were attributed to AZTS pirquitasite phase [3], [4]. Moreover, electron probe microanalysis (EPMA) analysis (Table. 1) showed that the chemical composition of the obtained Ag2ZnSnS4 compound is close to the desire composition. Our results provide useful insights that are needed as a standard for fundamental property characterization as well as the starting materials for thin film disposition.

ISSN: 0067-3064

Keywords: Chalcogenides - Tetragonal – Solid state reaction - Secondary phases – Substitution.

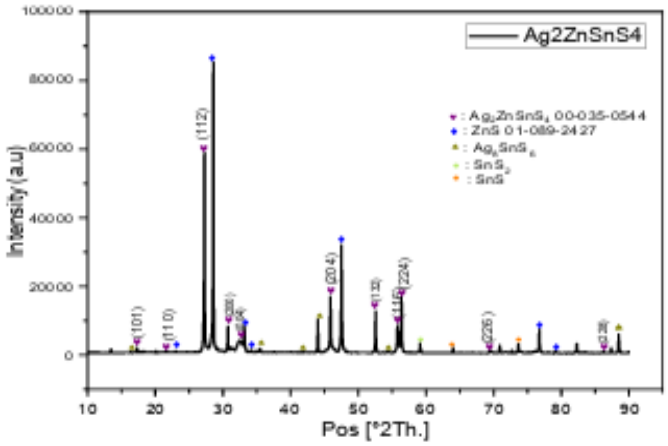

Figure 1 : X ray powder diffraction profil of the as prepared bulk polycristallin Ag2ZnSnS4.

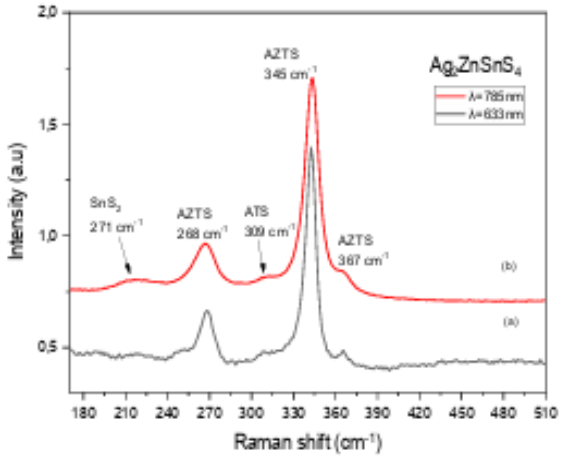

Figure 2: Raman spectra of the obtained polycrystalline Ag2ZnSnS4; (a) recorded at 633 and (b) at 785 nm excitation wavelength.

Table. 1: The detailed composition of the obtained AZTS polycrystalline

	Measured composition				**Cation ratios**	
Ag_2ZnSnS_4	**Ag** (at%)	**Zn** (at%)	**Sn** (at%)	**S** (at%)	Ag/(Zn+Sn)	Zn/Sn
EPMA Analysis	24,64	10,62	11,92	52,81	1.09	0,89

References

[1]: Y. E. Romanyuk et al., “Doping and alloying of kesterites,” JPhys Energy, vol. 1, no. 4, Oct. 2019, doi: 10.1088/2515-7655/ab23bc.

ISSN: 0067-3064

[2]: M. Tablaoui, M. Derbal, and K. Lebbou, “Discussion on the purity and the crystallization of CZTS compound,” J Cryst Growth, vol. 452, pp. 131–134, Oct. 2016, doi: 10.1016/j.jcrysgro.2016.04.008.
[3]: S. M. Abdullah, N. A. Bakr, and S. A. Salman, “STRUCTURAL, OPTICAL, AND ELECTRICAL PROPERTIES OF Ag 2 ZnSnS 4 SPRAYED THIN FILMS BY CHEMICAL PYROLYSIS METHOD,” 2021.
[4]: K. Pietak, C. Jastrzebski, K. Zberecki, D. J. Jastrzebski, W. Paszkowicz, and S. Podsiadlo, “Synthesis and structural characterization of Ag2ZnSnS4 crystals,” J Solid State Chem, vol. 290, Oct. 2020, doi: 10.1016/j.jssc.2020.121467.

ISSN: 0067-3064

(e-3e) process with electronic impact
P 53

Sakhraoui Wafa, Kada Imen

Department of Physics, University of Farhat Abbas, Setif, Algeria.
Wafa.sakhraoui@univ-setif.dz

Abstract: The exploration of matter and its structure necessitates a profound comprehension of its fundamental constituents and behavior. One field of research that focuses in this area is atomic and quantum studies. In our research, we delve into the intricate processes of collision and double ionization in diverse atoms and molecules. To achieve this, we employ approximation models such as plane and distorted wave function, Hartree-fock, Brauner, Briggs, and Klar… These models elucidate how the targets react and how interactions influence their trajectory. 1. Introduction The double ionization by electron impact is a physical process that occurs when a high-energy electron strikes an atomic or molecular target, resulting in the simultaneous loss of two electrons by the target. This phenomenon can be observed in various systems, from simple atoms to complex molecules. It depends on multiple factors, such as the energy of the incident electron, the electronic structure of the target, the geometry of the interaction, etc. Theoretical and experimental studies have been conducted to understand these factors and predict the probabilities of double ionization in different systems. In recent years, experiments on double ionization have made significant progress due to the use of ultrafast electron sources and more sophisticated detection techniques. Theoretical studies have also advanced with the utilization of more advanced calculation methods. In our work we focus on the different approximation to describe the process and calculate the cross section.

References

[1] C. Schroter, B. El Marji, A. Lahmam-Bennani, A. Duguet, M. Lecas, L. Spielberger, J. Phys. B 31, 131 (1998)

ISSN: 0067-3064

Synthesis and characterization of silver nanorods by chemical reduction method
P 54

Bessi Assia*[1], Bahria Hiba[2], Hadji Manel[2], Boudin Boubkeur [3]

1 LCPMM Laboratory , faculty of science ,Blida-1 university ,Algeria.
2 department of chemistry ,faculty of sciences, Blida-1 university.Algeria.
3 crystallography laboratory ;mentouri university ,algeria.

Abstract: In recent years, the synthesis of metal nanorods has received researchers' interest due to their excellent optical and electronic properties. In particular, silver nanorods (Ag NRs) have attracted a lot of attention due to their antibacterial effects.
In this study, we focused on the elaboration of silver nanorods using a chemical reduction method based on hydrazine. All samples were characterized using deferent technique such as UV-Vis, SEM and XRD.
The appearance of a bathochrome effect on the UV-Vis spectrum during the reaction synthesis of Ag nanorods reveals a notable shift in the characteristic absorption bands of the reagents used. The spectrum of synthesized Ag NPs shows an absorption band at λ_{max}=400nm, which confirms the formation of Ag nanorods. Color changes of the solution that occur at the end of the reaction confirm the Ag nanorods formation.
On the XRD pattern, the characteristic silver peaks were observed. By comparing the positions of these peaks with those reported on the JCPDS sheet (04-0783) relating to Ag, it was possible to deduce that the synthesized powder has a cubic structure with a lattice parameter: a=b=c= 4.0862 A°, V= 68.23*10^6 μm^3.The size of Ag crystallites is 31nm and the majority of them are orientated in the (1 1 1) direction.
The SEM morphological analysis reveals that the produced Ag powder takes the shape of nanorods with nanometric sizes.

Keywords: nanorods, silver, chemical reduction, synthesis.

ISSN: 0067-3064

Analyzing mixing quality in a T-shaped micromixer for moderate Reynolds number flow
P 55

O.Hadj rahmoun[1],T.Tamsaout[1], K. Kheloufi1, E. H. Amara[1], F. Hamadi[1], K. Boughrara[1] and S. Aggoun[1]

[(1)]Centre de Développement des Technologies Avancées, Laser Material Processing Team, PO. Box 17 Baba-Hassen, 16303 Algiers, Algeria

Abstract: The micromixers are one of the most important components for microreaction technology in the wide range of industries, especially in chemical and biological fields where mixing is used to facilitate chemical and biological effects. In this work, a numerical study of a T-shaped micromixer channel for laminar regime flow. The continuity and momentum equations, as well as the advection-diffusion equation are solved to evaluate the mixing performance.
The main objective is to identify the critical values of the transition from the stratified regime to the vortex regime as well as to the engulfment regime for three different dimensions of the T-shaped micromixer and to describe the relationship between the flow characteristics and the values of mixing to suggest possible geometrical modifications to promote mixing. The results show that for the three different dimensions of T-shaped micromixer, the maximum values of mixing index is attended in the beginning of engulfment flow regime**.**

Key words: T-shaped micromixers; microreactors; microreaction technology, CFD-simulation.

ISSN: 0067-3064

Doping effect of Co on structural and optical properties of nickel oxide thin films deposited by sol-gel (dip-coating) method.
P 56

K. M'HAMMEDI*,F. BOUAMRA and I.BACHIR

Laboratory of Physical-Chemical Inorganics Materials and their Applications, Physics Department in Science Faculty of Blida1 University, 09000 Blida, Algeria.

Abstract: Undoped and cobalt (Co) doped nickel oxide thin films were deposited on a glass substrate by sol-gel (dip-coating) method at different doping concentrations from 0 to 4%. The effect of doping content on structural and optical properties was explored by X-ray diffraction and UV–visible spectroscopy, respectively. X-ray diffraction result shows the NiO thin films were polycrystalline in nature having a cubic crystal structure. The utilised parameters such as crystallite size, micro-strain and dislocation density are presented from structural data. The average crystallite size is found between 20 and 26 nm with cobalt doping (Co) concentration. Co doping concentration led to an increase in the band gap energies in the range between 3.32 and 3.40 eV.

Keywords: NiO, Dip-coating, Thin film, Doping.

Introduction: Currently, semiconducting metal oxide are considered one of the most effective materials for use as gas sensor, fuel cells and batteries [1]. In particular, NiO has gained much consideration by researchers because of its numerous properties and applications that depend on doping. This study presents the effect of Co doping on structural and optical properties of nickel oxide thin films.

Experimental study: The undoped and Co doped NiO thin films were prepared on glass substrates using 0.5M (Ni(AC)2.4H2O, 98%) and cobalt chloride (CoCl2, 99%) in ethanol (C2H5OH, 96%) in the presence of a small amount of hydrochloric acid (HCl, 36%). Then the solution is left under stirring and heating for one hour. The cobalt doping concentrations (1, 2, 3 and 4%) were added to the solution at a constant temperature. Following the completion of the deposition, the NiO films were dried in air for 10 minutes and subsequently annealed at 300°C for one hour.

Results and discussion

1. Structural properties: XRD analysis was used to investigate the crystal structure, crystallite size, micro-strain, dislocation and lattice parameters of both undoped and Co doped NiO thin films. The identification of peaks using the "JCPDS" card reveals that the NiO layers are polycrystalline with cubic structure, which is in agreement with the JCPDS card, No.01-75-0269. All the layers exhibit a preferred orientation along the (200) plane. Moreover, a shift in the diffraction peaks towards higher angles appears

ISSN: 0067-3064

with the increase in Co orientation, Which are consistent with those reported in the literature [2,3].

2. Optical properties: The optical properties were examined using UV-Vis spectrometer. The spectra of Co-doped NiO show relatively low transmittance in the visible range. The values of the band gap increase as the cobalt doping concentration increases [4].

Conclusion: In summary, the study focused on Co doped NiO thin films, and it examined the impact of Co doping on the structural and optical properties. Various techniques were employed to characterize the synthesized samples. The crystallite size of NiO and Co doped NiO, as determined from the XRD pattern, was found between 20 and 26 nm. The structural parameters, including crystallite size, dislocation density and micro-strain were changed with varying Co doping concentration. The optical gap is modified with Co doping concentration within the range of 3.32 to 3.4 eV.

References

[1] K. M'hammedi, H. Haine, N. Bourenane, H. Menari and Gabouze N, 2019 Arab. J. Sci. Eng. 44 521
[2] R. S. Kate et al, Optical and Quantum Electronics, (2019) 51-319
[3] N. A. Bakr et al, International Letters of Chemistry, Physics and Astronomy, Vol. 41, (2015) 15-30
[4] R. Kaneko et al, Solar Energy, 181 (2019) 243–250

ISSN: 0067-3064

Design and Performance Analysis of PbTiO3 1D Photonic Crystal-Based Near Infrared Biosensors
P 57

Abdelkader Abderrahmane[1], Ilyes baba-Ahmed[2], Asma Tadji[3], Senouci Khaled[4], Pil Ju Ko[4]

[1] Laboratoire de Structure, Elaboration et Application des Matériaux Moléculaires (SEA2M), Université Abdelhamid Ibn Badis Mostaganem, B.P. 227, Mostaganem 27000, Algeria
[2]Laboratory of Fundamental and Applied Physics (FUNDAPL), Physics Department, Sciences Faculty, Saad Dahleb Blida 1 University, BP 270, Blida 09000, Algeria.
[3]University of Sciences and Technology of Oran –Mohamed Boudiaf, USTOMB, El Mnaouar, BP 1505, Bir El Djir, 31000 Oran, Algeria.
[4]Department of Electrical Engineering, Chosun University, 375 Seosuk–dong, Dong–gu, Gwangju 501–759, Republic of Korea.

Abstract: Photonic crystals (PCs) are structures composed of alternating materials with different refractive indices leading to the manipulation of electromagnetic waves. One potential application of PCs is biosensing, particularly, the detection of proteins, urine, biomarkers, and cancer cells [1]. The lead (II) titanate ($PbTiO_3$) has excellent physical and optical properties, including high refractive index, large electro-optic coefficient, and excellent piezoelectric properties [2]. On the other hand, magnesium fluoride (MgF2) possesses unique physical and optical properties that make it ideal for the unidimensional photonic crystal (1D PC). In fact, the MgF_2 has a high transmittance in the UV and visible regions [3] and a low refractive index compared to the refractive index of $PbTiO_3$. In this research, we investigated the optical performance of [$PbTiO_3$/MgF_2] heterostructure and we studied its suitability for the 1D PC based biosensor (1D PC-BIO) for extracellular vesicles (EVs) detection.

Theoretical model and proposed design: Figure 1 shows the 1D PC-based biosensor (1D PC-BIO) proposed in our study. The structure consists of alternating layers of material A, which represents the $PbTiO_3$ (refractive index given by the equation 1) and material B, which represents MgF_2 (refractive index given by the equation 2).

$$n_{PbTiO_3} = \left[1 + \frac{5.3635\lambda^2}{\lambda^2 - 0.050267^2}\right]^{0.5} \quad (1)$$

$$n_{MgF_2} = \left[1 + \frac{0.48755\lambda^2}{\lambda^2 - 0.04338^2} + \frac{0.39875\lambda^2}{\lambda^2 - 0.0941^2} + \frac{2.31203\lambda^2}{\lambda^2 - 23.793^2}\right]^{0.5} \quad (2)$$

ISSN: 0067-3064

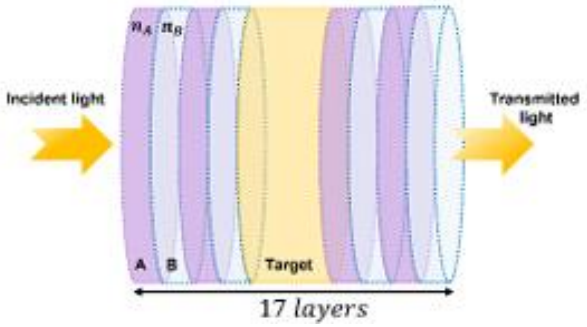

Figure 1. Schematic of the proposed 1D photonic crystal-based biosensor (1D PC-BIO). (1) (2)

The thicknesses of $PbTiO_3$ and MgF_2 were calculated according to the equation $d=\lambda_0/4n$. The defect layer (or cavity region), created in the middle of the periodic structure, is the nanochannel (the orange colored layer in Figure 1) in which EVs can be injected for the detection process. We used transfer matrix method for the simulation and calculation of the optical properties [1].

Numerical results and discussion: Figure 2(a) and (b) show the variation of the transmittance as a function of the wavelength and defect layer thicknesses at two incidence angle values of light. Thereafter, the incidence angle was chosen as 85˚ and the thickness of the defect was fixed as 1.8 μm. The transmittance was then numerically calculated as shown in Figure 2(c) and (d). Finally, the biosensing performance was deduced from the defect mode peak shift.

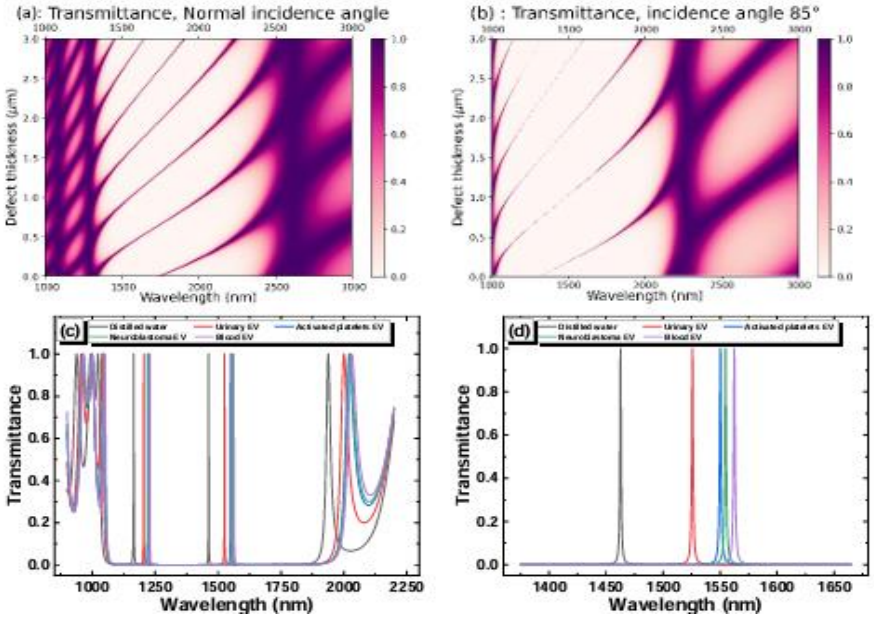

Figure 2. Variation of the transmittance as a function of the wavelength and defect layer thicknesses at (a) normal incidence angle. (b) incidence angle of 85˚, and (c) transmittance variation and (d) shift in the defect mode position, with respect to various EV samples.

ISSN: 0067-3064

Conclusion: In conclusion, we successfully enhanced the biosensing performance of $PbTiO_3$ 1D photonic crystal-based near-infrared biosensor from a value of 510 [1] to a value 3 folds higher (i.e., S = 1535 nm/RIU). Moreover, the figure of merit (FOM), and quality factor (Q) were measured as 1078 RIU-1 and 1167. The results of this study may contribute to the development of high-performance biosensors for various applications, including disease diagnosis and monitoring the response to cancer therapy

References

[1] Abderrahmane, A., Senouci, K., Hachemi, B. and Ko, P.J., 2023. Design and Performance Analysis of Perovskites Unidimensional Photonic Crystal-Based Biosensors for Extracellular Vesicles Detection: A Numerical Investigation. Crystals, 13(6), p.945.

[2] Zhang, J.; Xu, B.; Wang, Y.S.; Qin, Z.; Ke, S.H. First-principles investigation of the ferroelectric, piezoelectric and nonlinear optical properties of LiNbO3-type ZnTiO3. Sci. Rep. 2019, 9, 1–14.

[3] Zarei Moghadam, R.; Omrany, A.H.; Taherkhani, M.; Shokrian, F. Fabrication of multi-layer antireflection coating consisting of ZnS and MgF2. Prog. Physi. Appl. Mater. 2021, 1, 7–13

ISSN: 0067-3064

A comparative study of LiH, O2and GaCl energies under a three-dimensional hyperbolic potential
P 58

A. Haddouche [a,b]* , and R. Yekken [b]

[a] Laboratoire de Physique Théorique et de didactique, Faculté de Physique, USTHB. BP 32, Al-Alia, 16111, Bab Ezzouar, Alger, Algeria.
[b] Ecole Nationale Supérieure des Travaux Publics, BP 32 Rue Sidi Garidi, 16006, Kouba, Alger, Algeria. * a.haddouche@enstp.edu.dz

Abstract: In this study, we provide a solution of Schrödinger equation with the three-dimensional hyperbolic Pöschl-Teller potential [1]. To this end, we considered three methods: Quantum supersymmetry, Nikiforov-Uvarov and numerical method. On the one hand, we compared energies that are obtained, taking the numerical method's results as a reference; on the other hand, we extended the study by inserting linear energy dependence into the potential to see how this dependence affects the results and the methods themselves.

Theoretical overview:

1. Quantum supersymmetry: This method [2] is based on the factorization of the Hamiltonian, the latter provides us two scaling operators and whose successive allows us to determine the energy spectrum and the application eigenfunctions thanks to the shape invariance property. We recall that, the introduction of energy dependence [3] induces some theoretical modifications on the method as well as to the usual rules of quantum mechanics [4] (scalar product and so on…).

2. Nikiforov-Uvarov (NU) method: It constitutes a polynomial method developed by Nikiforov and Uvarov [5]. The first step of this method is the transformation of the Schrödinger stationary equation to a generalized hypergeometric one. This method is based on soluting second order linear differential equations with the help of special orthogonal functions. The solution of Schrödinger equation with energy dependent potential by this method is, as we will see, straightforward.

3. Numerical method: our numerical solution [6] is based on the fourth order Runge-Kutta method. It has been extended to encompass energy-dependent wave equations.

Results and discussion: Wave functions and energy spectra of diatomic molecules are derived by using the three mentioned methods. Application is done to LiH, O2 and GaCl molecules. These latter diatomic molecules have different reduced masses. The results show the effects of mass difference on the exactness and the effect of energy dependence.

Conclusion: a- Both SQM and NUmethods give satisfyingly exact and analytic results. b- Energy-dependence affects the wave functions as well as the energy eigenvalues. c- Lower reduced-mass molecules are in better approximation in their results.

ISSN: 0067-3064

References

[1] G. Pöschl, E. Teller, Z. Phys. 83, 143 (1933).
[2] F. Cooper, A. Khare, U. Sukhatme, Phys. Rep. 251, 267 (1995).
[3] R. J. Lombard, J. Mareš, and C. Volpe. Journal of Physics G : Nuclear and Particle Physics,34(9) :1879 (2007)
[4] R. Yekken, M. Lassaut, and R. J. Lombard, Annals of Physics, 338 :195– 206, (2013).
[5] A. F. Nikiforov, V. B. Uvarov, Birkh a ¨ user, Basel (1988).
[6] W. Lucha, F.F. Schöberl, Int. J. Mod. Phys. C, 10, 607 (1999)

ISSN: 0067-3064

Surface analysis and wettability of Ba doped ZnO thin films created via SILAR for self-cleaning application
P 59

Hadjer Barkat[a]*, Elhachmi Guettaf Temam[a], Hachemi Ben Temam[a], Nour Elhouda Mokrani[a], Mohammed Althamthami[a]

[a] Physics Laboratory of Thin Films and Applications, Biskra University, BP 145 RP, Biskra 07000, Algeria. * hadjer.barkat@univ-biskra.dz

Abstract: This study discusses the effect of barium doping at low concentrations on the self-cleaning of ZnO thin films which fabricated via a cost-effective SILAR method, the acronym for Successive Ionic Layer Adsorption and Reaction. The XRD analysis exhibited the wurtzite hexagonal structure and confirmed the crystallinity of all films. Surface roughness is studied using atomic force microscope (AFM) which depicted that the highest value is at Ba 5 wt. %. Furthermore, contact angle test exhibited the direct relationship between the roughness and wettability, whereas the major value of wettability was illustrated at Ba 5 wt. %. As a general trend, doping nanomaterial such as barium doped zinc oxide, is considered to be an effective candidate for use in self-cleaning applications. Keywords: Ba-ZnO, SILAR method, wettability.

References

[1] Anandh BA, Sakthivel R, Ganesh AS, Subramani S, Rajamanickam AT. ANALYZING ANTIMICROBIAL ACTIVITY OF ALUMINIUM DOPED ZnO THIN FILMS. Rasayan J Chem. 2022 Jan 1;15(1):387–94.
[2] González LA, Ramírez-Rodríguez SE. Al and F co-doped ZnO films prepared by the SILAR method: Characterization and performance as active layers in TFTs. Mater Sci Semicond Process. 2022 May 142.
[3] Mohammed, Temam H Ben, EI Hachmi GT, Malf N, Hasan GG, Brakat H. Structural Analysis and Hydrophilic Behavior of Co_3O_4 Thin Film for Enhanced Photocatalytic Activity under Visible Light with Hole Scavengers. Int Conf Sci Innov Stud. 2023;1(1):73–6.
[4] N'Konou K. Influence of Barium Doping on Physical Properties of Zinc Oxide Thin Films Synthesized by SILAR Deposition Technique. Adv Mater. 2014;3(6):63.
[5] Rabeel M, Javed S, Khan R, Akram MA, Rehman S, Kim DK, et al. Controlling the Wettability of ZnO Thin Films by Spray Pyrolysis for Photocatalytic Applications. Materials (Basel). 2022;15(9).

ISSN: 0067-3064

Nonextensive thermostatics of q-Bose-Einstein condensation P 60

Lebba GHENAM

Physics Department, Ecole Normale Supérieure El-Cheik Mohamed El-Bachir El-Ibrahimi, BP 92, 16050, Vieux-Kouba, Algiers, Algeria

Abstract: Our work has based upon the mean value of occupational number which is given by Tuszyski et al. Our study's primary goal is to examine the thermodynamic characteristics of the Bose-Einstein condensation of non-interacting q-boson gas (ultrarelativistic case) in the thermodynamic limit. This study is shown to exhibit Bose-Einstein condensation with higher critical temperature (which depends on the density and deformation parameter and is always greater than zero).

Keywords: q-deformed algebra, quantum groups, Jackson derivative, Bose-Einstein condensation.

ISSN: 0067-3064

Monte Carlo Simulation of the GZK Limit for Ultra High Energy Cosmic Rays
P 61

Rafik Sedrati [A]*, Dallel Bouchachi[B]

[A] Department of Material Sciences, Faculty of Science and Technology, Mohamed-Cherif Messaadia University, Souk Ahras 41000, Algeria
[B] Department of Physics, Faculty of Science, Badji Mokhtar University, B. P. 12, Annaba 23000, Algeria
* Corresponding author Email: r.sedrati@univ-soukahras.dz

Abstract: The Greisen–Zatsepin–Kuzmin (GZK) limit sets an upper energy boundary for cosmic rays originating from distant sources, determined by their interaction with cosmic microwave background radiation. The limit stands at approximately 5×1019 eV, but accurately simulating the propagation of ultra high energy cosmic rays over long distances necessitates detailed modeling of particle interactions and energy losses. Monte Carlo methods offer a valuable numerical technique to simulate these intricate processes. This study employs a Monte Carlo approach to investigate the propagation of ultra high energy cosmic rays and the resulting GZK cutoff. Energy loss mechanisms are simulated at each step, tracking a significant number of cosmic rays to build an energy spectrum. The results confirm a pronounced steepening of the spectrum around 6×1019 eV, aligning with the anticipated GZK cutoff. This technique enables a detailed validation of the GZK limit through numerical modeling, demonstrating its power by comparing the predicted spectrum with recent experimental data from ultra high energy detectors like the Pierre Auger Observatory. Monte Carlo methods thus exemplify their efficacy in simulating fundamental astrophysical processes at high energies.

ISSN: 0067-3064

Study of the phase separation of a binary alloy by Numerical simulation

P 62

Salaheddine Seghiri[A], Sid Ahmed Sabeur[B]

[A,B] LEPM, Faculty of Physics, University of Science and Technology of Oran Mohamed-Boudiaf, El Mnaouar, BP 1505, Bir El djir. Oran 31000
[A]salahphysique13@gmail.com [B]sidsabeur@gmail.com

Abstract: In this work, we present the simulation of the phase separation of a binary alloy with the finite differences algorithm and we will show how to solve the Cahn-Hilliard equation. The simulation is performed in two dimensions for a square cell. The advantages and disadvantages of this modeling approach are presented and discussed.

Aim and scopes: The Cahn-Hilliard equation describes the temporal evolution of a conserved field that is a continuous, sufficiently differentiable function of position. It was originally proposed to model the spinodal decomposition of a binary A–B system at a fixed temperature, for which an initially homogeneous system with a uniform composition of c, the mole fraction of component B, spontaneously decomposes into two phases with the same crystal structure, but with different compositions. In this case, the spatial distribution of the two phases during decomposition could be described by the composition field, c(x, t), which is a continuous, differentiable function of position x and time t:

$$\frac{\partial c}{\partial t} = \nabla \cdot (M \nabla \mu) \tag{1}$$

Methodology: The Cahn-Hillard equation is discretized by simple finite difference method in this work. The 1st order Euler method is used for time-integration. The 2nd-order central finite difference method is used for spatial derivatives. the discretized time evolution equation is given as[3]:

$$C_{i,j}^{t+\Delta t} = C_{i,j}^{t} + M_c A_{i,j} + B_{i,j} C_{i,j} \tag{2}$$

$$M_c = \frac{D_A}{RT}\left[c_{i,j}^{t} + \frac{D_B}{D_A}\left(1 - c_{i,j}^{t}\right)\right] c_{i,j}^{t}\left(1 - c_{i,j}^{t}\right) \tag{3}$$

$$\frac{\partial^2 \mu}{\partial x^2} + \frac{\partial^2 \mu}{\partial y^2} \simeq A_{i,j} = \frac{\mu_{i+1,j}^{t} - 2\mu_{i,j}^{t} + \mu_{i-1,j}^{t}}{(\Delta x)^2} + \frac{\mu_{i,j+1}^{t} - 2\mu_{i,j}^{t} + \mu_{i,j-1}^{t}}{(\Delta y)^2} \tag{4}$$

$$\frac{\partial M_c}{\partial c} \simeq B_{i,j} = \frac{D_A}{RT}\left[\left(1 - \frac{D_B}{D_A}\right) c_{i,j}^{t}\left(1 - c_{i,j}^{t}\right) + \left(c_{i,j}^{t} + \frac{D_B}{D_A}\left(1 - c_{i,j}^{t}\right)\right)\left(1 - 2c_{i,j}^{t}\right)\right] \tag{5}$$

$$\frac{\partial c}{\partial x}\frac{\partial \mu}{\partial x} + \frac{\partial c}{\partial y}\frac{\partial \mu}{\partial y} \simeq C_{i,j} = \frac{\left(c_{i+1,j}^{t} - c_{i-1,j}^{t}\right)\left(\mu_{i+1,j}^{t} - \mu_{i-1,j}^{t}\right)}{4(\Delta x)^2} + \frac{\left(c_{i,j+1}^{t} - c_{i,j-1}^{t}\right)\left(\mu_{i,j+1}^{t} - \mu_{i,j-1}^{t}\right)}{4(\Delta y)^2} \tag{6}$$

Results and finding: The phase separation process starts with a homogeneous system in which the two phases are evenly distributed and the order parameter remains

ISSN: 0067-3064

constant, indicating the uniformity of B atom concentration. The lowering of free energy is the driving force behind spinodal decomposition. As the system evolves, it approaches an equilibrium defined by maximum domain size. The resulting microstructure is often composed of broad, discrete phases, the specifics of which are determined by parameters like as diffusion coefficients and interaction energy.

Keywords : Finite differences method ; The Cahn–Hilliard equation ; Binary alloy; Phase separation.

ISSN: 0067-3064

Study of the structural, elastic and electronic properties of cubic perovskites RbXF3 (X = Co, Fe): Ab-initio calculation. P 63

A.Sekkal[1, 2], M. Kaderi[1], M. Sahlaoui[3], C. Esling[4], and J. M. Raulot[4].

[1]Ecole Supérieure Des Sciences Appliquées (E.S.S.A) d'Alger, 16001 Algérie
[2] Division Etude et Prédiction des Matériaux DEPM-URMER, Université Abou Bekr Belkaid,Tlemcen, 13000 Algérie,
[3]Ecole Supérieure en Sciences Appliquées de Tlemcen, Tlemcen, Algérie
[4]Laboratoire d'Etude des Microstructures et de Mécanique des Matériaux, LEM3 UMR CNRS 7239, Université de Lorraine UL, Metz 57045, France.

Abstract: Perovskites, known for their structural simplicity, are the most abundant minerals on earth. They are characterized by various electrical properties. These materials can be insulators, semiconductors, ionic conductors, metallic type conductors and high temperature superconductors. Perovskites are of great interest in materials science due to the unusual combination of their magnetic, electronic, spintronic and transport properties [1]. The ideal perovskite structure corresponds to the general formula ABX3. In this work, we studied the structural, elastic and electronic and magnetic properties of cubic perovskite compounds RbXF3 (X = Co, Fe) using the PAW pseudo-potential method in the framework of density functional theory (DFT), developed in the VASP code.

Keywords: Cubic perovskite RbXF3 (X = Co, Fe), electronic structure, elastic properties, Ab initio calculations..

References

[1] M. R. Hashmi *e*t al. Chinese Physics. B Vol. 25, No. 11 (2016) 117401, http://iopscience.iop.org/1674-1056/25/11/117401)

ISSN: 0067-3064

Modification of Algerian nanoclay for the production of a polypropylene-based nanocomposite
P 64

M. TRIAK [1, *], A. BENMOUNAH [2]

[1, 2]. Research Unit Materials, Processes and Environment (URMPE), University M'Hamed Bougara of Boumerdes 35000, Algeria.
[1.] E-mail : triakim@yahoo.fr

Abstract: Our challenge is to promote local materials at low cost to manufacture nanocomposites with improved properties. Particular interest has been paid to clay nanoplatelets and their composites with non-polar thermoplastic polyolefin matrices, namely polypropylene
The goal of this work was to prepare nanoclay; this last will be introduced during the preparation of nanocomposite based on the Polypropylene. Polypropylene / nanoclay nanocomposites have been prepared via a co-rotational twin screw extruder machine with nanoclay content varied between 0 and 11 Wt. %. The maleic anhydride grafted polypropylene (PP-g-MA) was used as compatibizer to improve the dispersibility of the nanoclay. The influence of nanoclay in a thermal property of polypropylene nanocomposites has been studied. The obtained results indicate that the incorporation of a small amount of nanoclay has a significant effect on the thermal properties of nanocomposites. The nature and size of nanoclay directly affects the properties of nanocomposite.

Keywords: Nanomposites, Polypropylene, Nanoclay, Thermal stability.

ISSN: 0067-3064

1D Confined Gas of Magnetic Colloidal Nanoparticles: Theoretical Model and Monte Carlo Simulations
P 65

S.Meddour [1] , L.Bouzar [1] , R.Messina [2]

[1] Laboratoire de Physique des Matériaux, Faculté de Physique USTHB, BP 32 Bab-Ezzouar Alger, Algérie.
[2] Laboratoire de Physique et Chimie Théoriques, LPCT – UMR CNRS 7019, Université de Lorraine, 1 Boulevard Arago 57070 Metz, France.

Abstract: Dipolar nanoparticles offer the extraordinary ability to be manipulated at will and at a distance through external magnetic fields [1,2]. In this communication, we focus on the collective properties that emerge at the mesoscopic scale from interactions between nanoparticles at the nanoscale. The nanoparticles under consideration possess permanent dipolar moments and are confined in a channel while exposed to a magnetic field such as to generate a purely repulsive interaction. Through analytical, numerical calculations, and Monte Carlo simulations, we determine, according to the strength of the coupling, the various phases exhibited by these particle assemblies (fluid-like or solid-like phases). This study may offer a roadmap for experimentalists or engineers seeking to exploit these particular properties of dipolar particles.
Conclusion: In this communication, we have presented various models and techniques for studying the behavior of a 1D dipolar gas. We have observed that the system exhibits different degrees of ordering depending on the strength of the magnetic coupling. This study may be useful for other research such as to identify the suitable values of magnetic fields/temperatures for specific applications.

References

[1] MOURAD, A., MOHRBACH, H., et MESSINA, R. Dipolar particles trapped in a cylindrical pore. Europhysics Letters, 2023, vol. 141, no 6, p. 67001.
[2] LIU, Ping, DE FOLTER, Julius WJ, PETUKHOV, Andrei V., et al. Reconfigurable assembly of superparamagnetic colloids confined in thermo-reversible microtubes. Soft matter, 2015, vol. 11, no 31, p. 6201-6211.
[3] HANSEN, Jean-Pierre et MCDONALD, Ian Ranald. Theory of simple liquids: with applications to soft matter. Academic press, 2013.

ISSN: 0067-3064

Performance Comparison between LMS and RLS Algorithms for Active Noise Control
P 66

[a] A. Chiheb and [a,b] H. Khelladi
[a] Faculty of Electrical Engineering, BP 32 El Alia, Bab-Ezzouar, 16111, Algeria
[b] Material Physics Laboratory, Faculty of Physics, BP 32 El Alia, Bab-Ezzouar, 16111, Algeria

Abstract: The aim of this study is to implement two different types of adaptive algorithms for the noise cancellation. The study explores the least mean squares (LMS) adaptive algorithm, which is based on stochastic gradient approach, and its performances in terms of convergence in active noise control (ANC). Another algorithm is considered in this investigation based upon the use of the least squares estimation (LSE), commonly named, the recursive least squares algorithm (RLS), and will be compared to the LMS in terms of convergence speed and control performances. The numerical experiments are performed by using several recordings tested on the two proposed adaptive algorithms. From this numerical study, the RLS algorithm reveals a faster convergence speed and better control performances than the LMS algorithm.

Keywords: Active noise control, LMS algorithm, RLS algorithm, FIR filter

Active Noise Control: Acoustic noise can occur in different forms and variety of environments. For the acoustic comfort, it is necessary to reduce it by using different methods. Active noise control refers to the cancellation of the noise by electronically generating an anti-noise, in order to reach the silence [1-2]. The component responsible of this operation is the adaptive filter, and the adaptation of the filter coefficients is done with an adaptive algorithm. An adaptive filter is a filter that can adjust its coefficients, using a specific adaptation algorithm, each time a new sample of the signal is available [3]. The adaptation algorithm is responsible of updating the filter coefficients in such a way that the filter output must minimize the error signal between the desired signal and the filter output. The most common adaptation algorithms are the LMS and the RLS algorithm.

1. LMS algorithm: Based on stochastic gradient approach, the LMS algorithm updates its coefficients by minimizing the mean square error (MSE) between the desired signal and the filter output [4-5]. It is widely used due to its simplicity, robustness, and stability in different signal conditions [3].

2. RLS algorithm: The RLS algorithm is an extension of the LSE, where a combination of previous and new set coefficients is used in the adaptation process. The computation is started with specific initial conditions, and then the information contained in new data samples is used to update the old estimate [6-7].

ISSN: 0067-3064

Simulation experiments: The two above-mentioned algorithms are implemented on different types of noise.

1. Implementation of the LMS algorithm: The LMS algorithm is implemented on several noises and the obtained results are displayed on different figures. Referring to these figures, the input signal is concurrently attenuated with the generation of the adaptive filter output, which represents the "anti-noise".

2. Implementation of the RLS algorithm: The same process is done for the RLS algorithm, where this latter is applied to the same noises to observe its attenuation rate and convergence speed.

3. Comparison between LMS and RLS: In this section, the noise attenuation is displayed for the two algorithms, where the same noise sources are examined. A comparison is established by plotting on the same graph the noise suppression ability of the two proposed techniques.

Conclusion: The obtained results attest that the RLS algorithm presents an efficient performance and a faster convergence in attenuating different types of noise, compared to the LMS algorithm.

References

[1] Behrouz Farhang-Boroujeny, "Adaptive Filters Theory and Applications", second edition, John Wiley & Sons, 2013.

[2] Atar Mon, Thiri Thandar Aung, Chit Htay Lwin, "Active Noise Cancellation in Audio Signal Processing", International Research Journal of Engineering and Technology (IRJET), 2016.

[3] Paulo S. R. Diniz, "Adaptive Filtering Algorithms and Practical Implementation", Fifth Edition, Springer 2020.

[4] L.V.Rajani Kumari, Asha jyothi sabavat, Y.Padma Sai, "Performance Evaluation of Adaptive Filtering Algorithms for Denoising the ECG Signal", Second International Conference on Electronics and Sustainable Communication Systems (ICESC), IEEE 2021.

[5] Muzamil Ahmed, Amber Farooq, Fatima Farooq, Nasir Rashid, Ayesha Zeb, "Power Line Interference Cancellation from EEG Signals Using RLS Algorithm", International Conference on Robotics and Automation in Industry (ICRAI), IEEE 2019.

[6] Simon Haykin, "Adaptive Filter Theory", Fifth Edition, published by Pearson Education, 2014.

[7] M. Sugadev, Malladi Kaushik, V. Vijayakumar, I. T. Ilayaraja, K. T. Ilayaraaja, "Performance Analysis of Adaptive Filter Algorithms on Different Noise Sources", International Conference on Computer Communication and Informatics (ICCCI), IEEE 2022

ISSN: 0067-3064

Adsorption of transition metals on armchair carbon nanoribbons: Magnetic and electronic properties

P 67

Zoubir BENKHANOUCHE[1, a *], Khaled BOUFALA [2, a]

[a] A/Mira University of Bejaia, Faculty of Exact Sciences, Department of Physics, Laboratory of Physical Chemistry of Materials and Catalysis, Algeria

Abstract: Graphene, a planar object composed of carbon atoms, is a prospect material for nanoelectronics and spintronics due to its unique electronic and magnetic properties. It was discovered that graphene reveals a spin polarization effect, that is, its magnetic characteristics increase when crystal defects (vacancies and groups of vacancies) are introduced. Carbon nanoribbons are fractions of graphene with properties different from graphene. Indeed, they have electronic and magnetic properties which strongly depend on the configuration of the edges (armchair or zigzag), width and the adsorption or doping by of transition metal atoms (Fe). The systematic analysis is carried out by ab initio simulation using the siesta code to indicate the spin. in our work we will dope nanoribbons based on graphene with atoms of transition metals (Fe). We carried out several configurations and noted differences in the magnetic, electronic and geometric properties.

Keywords: Graphene, Siesta code, Magnetic properties, electronc properties.

Introduction: Graphene [1] is a two dimensions design with hexagonal crystallographic structure, it has been discovered recently [2]. It has a good electronic and mechanical properties but has an inconvenient which is his zero-energy gap. To overcome this problem, researchers performed a new unit-dimension materials like nanoribbons, and shown that a strong dependence on the larger and doped atoms [3,4] leads to news properties which are absent in graphene and pure nanoribbons. These materials are used in several applications and mainly in electronic media junctions at the nanometric scale and spintronic [5]. In this study, we have simulated by siesta code armchair nanoribbons doped with two Fe atoms. The object is to learn more the effect of the Fe atoms in the electronic and magnetic properties of the doped ribbons compared to pure one.

Mathematical model: The SIESTA method [6] is an ab initio technique based on DFT with pseudopotentials [7] with conserved norms and a basis formed from digitized atomic orbitals. The calculation was carried out with a polarized triple zeta basis. The exchange-correlation energy was treated by the GGA [8,9]. The relaxation of the geometric structure was carried out by the conjugate gradient method implemented in siesta.

ISSN: 0067-3064

Conclusion: In this work, we have studied structural, electronic and magnetic properties of Carbone armchair nanoribbons doped with two iron atoms. We have observed that the nanoribbon has semiconductor behavior with a small indirect gap energy, which can be attributed to the presence of iron states inside the gap where the valence layer is horizontal, who reduces it considerably. The spin moments along the OX axis are larger than those along the OZ axis, and the anisotropy energy is equal to 0.47meV. These results are in good correlation with Bruno model.

References

[1] AOKI, Hideo et DRESSELHAUS, Mildred S. (ed.). Physics of graphene. Springer Science & Business Media, 2013.
[2] Novoselov K S, Geim A K, Morozov S V, Jiang D, Zhang Y,Dubonos S V, Grigorieva I V and Firsov A A 2004 Science 306 666.
[3] K. Nakada, M. Fujita, G. Dresselhaus, and M. S. Dresselhaus, Phys. Rev. B 54, 17 954 (1996).
[4] An infinite (straight) graphene ribbon is characterized as an armchair type or a zigzag type if its edges parallel to its axis exhibit the armchair or the zigzag structure.
[5] Gambardella, P., Dallmeyer, A., Maiti, K., Malagoli, M. C., Eberhardt, W., Kern, K., & Carbone, C. (2002).
[6] Oda, T., Pasquarello, A., & Car, R. (1998). Fully unconstrained approach to noncollinear magnetism: application to small Fe clusters.
[7] https://www.researchgate.net/post/Why_we_need_to_use_Pseudopotentials_for_Density_Functional_Theory_Calculations.
[8] Perdew, J. P., Burke, K., & Ernzerhof, M. (1996). Generali zed gradient approximation made simple.
[9] Hajlaoui, C. (2014). Etude des propriétés structurales et électroniques des nanofil semiconducteurs III-V (Doctoral dissertation, INSA de Rennes).

ISSN: 0067-3064

STUDY Of THE EFFECT OF THE MATERIAL SOURCE ON ZINC FERITTE PROPERTIES
P 68

Guettaf Mohamed[1], Kezzim Amina[1], Souad Saadi[2] , Mouattah Dalila[3], Rekik Brahim[1]

[1]LPCMIA Laboratory, Department of Physics, Faculty of Sciences, University of Saad Dahleb Blida 1, Algeria .
[2] LABCAM Laboratory, University of Boumerdes,Algeria .
[3] LPCM Laboratory Department of Physics Laghouat., Algeria

Abstract: The growing interest in the Spinel study due to its importance and applications in many areas, including gas sensing devices [1], lithium-ion batteries (LIBs) [2,3], heterogeneous catalysis [4], and nanomedicine. In the most recent instance, this novel class of magnetic nanoparticles (MNPs) has shown promise as contrast agents in MRI [5] or as heat sources in magnetic hyperthermia applications [6] in this work we have prepared tow zinc ferrite nano-powders by both zinc nitrate ZFO-N and zinc acetate ZFOA as the source of the substance in order to know the extent of the effect of these sourcee on the sol-gel process and to reach the precursor that gives good results .The X Ray diffraction, the FTIR, and the UV,Visible analysis were used to confirm the crystallinity and the purity of Spinel phases and to study their properties.

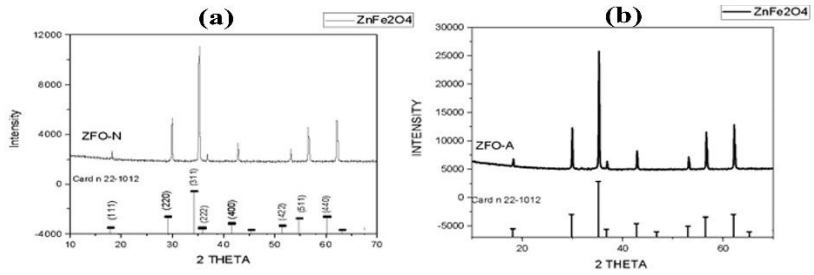

Fig.1: XRD parameters, (a) XRD patterns of source Nitrate, (b) XRD patterns of source Acetate.

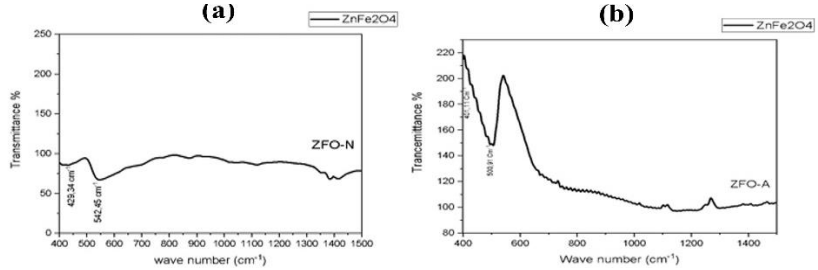

Fig.2: FTIR spectroscopy, (a) FTIR spectroscopy of zinc ferrite prepared by nitrate precursor, (b) FTIR spectroscopy of zinc ferrite prepared by Acetate precursor

ISSN: 0067-3064

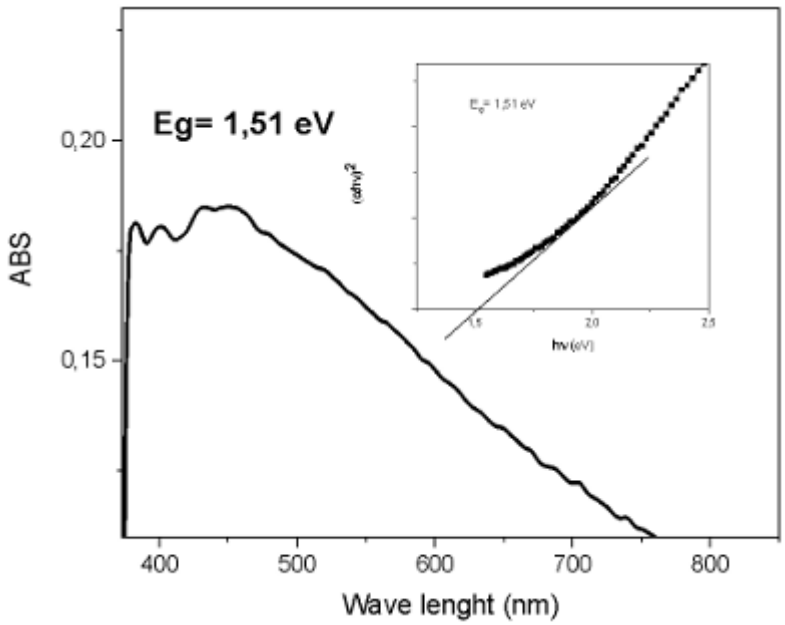

Fig.3. UV-Vis absorption spectra and Tauc plots (to determine the energy band-gap) Spinel powders

Conclusion: In this work, pure Zinc Ferrite Spinel nano-powders were successfully synthesized by the sol-gel method used two different source of Zinc as Starting materials. The average sizes were calculated using the Scherrer formula, and their optical properties were studied, confirming the good crystallinity of Spinel pure phases and their nano-metric particle sizes. On the other hand, the band-gap of spinel nano-powders prepared by using nitrate precursor were found to be: Eg =1,51 eV which present a smallest energy band gap.

References

[1] T. Liu, J. Liu, Q. Liu, L. Rumin, H. Zhang, X. Jing, J. Wang, Shape-controlled fabrication and enhanced gas sensing properties of uniform sphere-like ZnFe2 O4 hierarchical architectures, Sensors Actuators B Chem. 250 (2017) 111–120
[2] N. Wang, H. Xu, L. Chen, X. Gu, J. Yang, Y. Qian, A general approach for MFe2O4 (M = Zn Co, Ni) nanorods and their high performance as anode materials for lithium ion batteries, J. Power Sources. 247 (2014) 163–169
[3] Y. Qu, D. Zhang, X. Wang, H. Qiu, T. Zhang, M. Zhang, G. Tian, H. Yue, S. Feng, G. Chen, Porous ZnFe2O4 nanospheres as anode materials for Li-ion battery with high performance, J. Alloys Compd. 721 (2017) 697–704
[4] Y.S. Fu, X. Wang, Magnetically separable ZnFe2O4-graphene catalyst and its high photocatalytic performance under visible light irradiation, Ind. Eng. Chem. Res. 50 (2011) 7210–7218,

ISSN: 0067-3064

Artificial Intelligence Enhanced Solutions for the Elementary Shortest Path Problem with Time Windows P 69

Abdelkader LAMAMRI

a.lamamri@univ-blida.dz
Department of Mathematics, University of Blida 1, Algeria.

Abstract: Artificial Intelligence Approaches (AI) are becoming increasingly relevant in tackling complex optimization problems. This includes the Elementary Shortest Path Problem with Time Windows (ESPPTW), which seeks to find the minimum cost elementary path in a valuated graph while adhering to time windows. ESPPTW is known to be an NP-hard problem frequently encountered in the context of column generation for vehicle routing problems.

In this paper, we introduce an innovative AI-based solution procedure to address ESPPTW for both acyclic and cyclic graphs. Our approach combines established mathematical optimization techniques, such as Lagrangian Relaxation, with cutting-edge AI methodologies. By applying AI to selectively dominate a subset of resource constraints, we effectively reduce the search space, facilitating the efficient computation of solutions to enhance the column generation procedure.

We conducted extensive experimental evaluations that encompass a range of techniques, demonstrating the effectiveness of our hybrid approach. This proposed method strikes a compelling balance between computational efficiency and solution quality, marking significant advancements over existing state-of-the-art techniques in the domain of Artificial Intelligence Approaches.

Keywords: Elementary shortest path, Artificial intelligence, Dynamic programming, Lagrangian relaxation, Vehicle routing

ISSN: 0067-3064

MODELING, OPTIMIZATION AND SIMULATION OF PYROELECTRIC INFRARED DETECTOR BASED ON P(VDF-TrFE) COPOLYMER.

Mohamed BEHLOUL [1*], Nour Eddine DERGUINI [2], Djamel KENDIL [3], Essaid BOUSBIAT [4]

[1] Department of Physics, University of Boumerdes, Algeria*
[1, 2, 3, 4] Laboratory of sensor-based integrated systems (LSIC) ENS Kouba, Algiers, Algeria

Email [1] - m.behloul@univ-boumerdes.dz
Email [2] - noureddine.derguini@g.ens-kouba.dz
Email [3] - djamel.kendil@g.ens-kouba.dz
Email [4] - essaid.bousbiat@g.ens-kouba.dz

Abstract:

This article presents a thermal model of the pyroelectric detector based on copolymer P(VF2-TrFE).
A one-dimensional of the heat equation was solved for the simulation of the response of the pyroelectric detector based on P (VF2-Tr FE).
We studied the temperature, current and voltage response of the pyroelectric detector in different possible structures and arrangements and their influence either by the nature or by the thickness of the layers, these studies allowed to find an optimal response in the structure (copo/ porous silicon) without addition of thermal insulation.
Keyword: Pyroelectric, P (VF2 -TrFE), Thermal model, Detector.

1. Introduction:

The development of infrared sensors using pyroelectric detection based on the copolymer P(VF2-TrFE) has been accompanied by an increase and diversification of their applications. we find them both in imaging (medical and thermal infrared) remote monitoring, hot spot detectors …. etc. [1]
In this work we are interested in the thermal behavior of the integrated structure on silicon based on a pyroelectric layer, to study the effect of the thermal insulator layer on the temperature response and their influence either by the nature of the materials or by the thickness on the detector response and the best way to arrange the sensitive elements to the silicon substrate.

ISSN: 0067-3064

1. Heat Transfer Equation:

The studied system is a pyroelectric detector based on copolymer P(VF2-TrFE) in a ratio of 70/30 mol%. P(VF2-TrFE) is statistical copolymer 70 % of vinylidene fluoride ($CH_2 - CF_2$) or VF2 and 30 % of trifluoroethylene ($CHF - CF_2$) or TrFE. they are linear chain copolymers, randomly distributed along the chain. this composition appeared as the most promising way to obtain crystalline ferroelectric thin films.

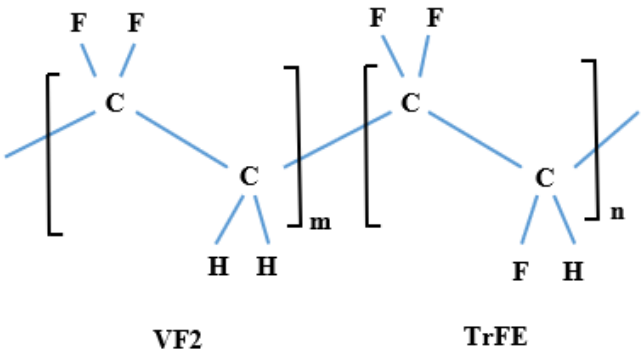

Figure 1. The chemical formula which characterizes the ferroelectric crystalline phase of P (VF2 - TrFE).

The structure described consists of a layer of copolymer with a surface area exposed to radiation measuring (2 mm x 2 mm). Additionally, the layer has two electrodes located on the outer and inner surfaces of the copolymer. Studying the temperature distribution of the three mentioned structures - (copolymer suspended in the air), (copolymer/substrate), and (copolymer/thermal insulator/substrate) - is essential for understanding the thermal behavior and performance of these configurations in different applications.

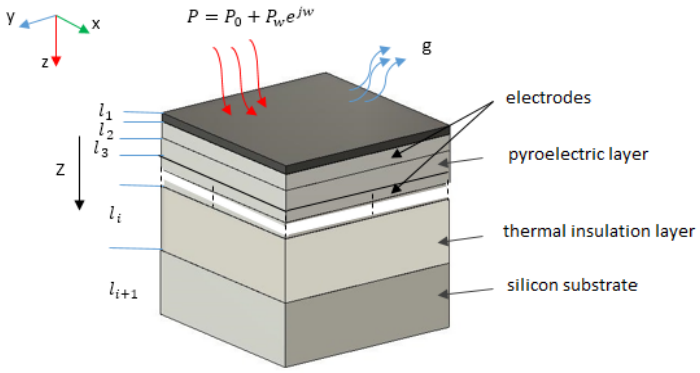

Figure 2. Diagram of a multi-layer pyroelectric sensor integrated on a silicon substrate.

ISSN: 0067-3064

The general heat conduction equation in rectangular coordinates. In the case of constant thermal conductivity is.[2]

$$\frac{\partial}{\partial x}\left(\frac{\partial T}{\partial x}\right)+\frac{\partial}{\partial y}\left(\frac{\partial T}{\partial y}\right)+\frac{\partial}{\partial z}\left(\frac{\partial T}{\partial z}\right)=\frac{1}{\alpha}\frac{\partial T}{\partial t} \quad \ldots\ldots\ldots (1)$$

T is the temperature.

1.1. Mathematical model.

Assumptions:

- the lateral surfaces are very small compared to the surface exposed to the flow.
- The thin metal electrodes have a low thermal capacity and a low thermal resistance, which led us to neglect their thermal effects.

these assumptions lead us to solve the system with the general one-dimensional equation of heat transfer, using the analytical method, according to z-axis.

$$\frac{\partial T(z,t)}{\partial t}=\alpha_i\frac{\partial^2 T(z,t)}{\partial z^2} \quad \ldots\ldots\ldots (2)$$

and

$$\alpha_i=\frac{k_i}{\rho_i .C_i} \quad \ldots\ldots\ldots (3)$$

where α is a thermal diffusivity, (i) is the index of the layer, t is time, T is temperature, z is distance. C_i is calorific capacity, ρ_i is density, k_i is thermal conductivity.

the general solution of the heat conduction equation for each layer is [3]

$$T(Z_i)=A_i\cosh(\lambda_i z_i)+B_i\sinh(\lambda_i z_i) \ldots\ldots (4)$$

and

$$\lambda_i=(1+j)\sqrt{\frac{\omega_0}{2\alpha_i}} \quad \ldots\ldots\ldots (5)$$

ω_0 is the angular frequency, A_i and B_i are complex constants can be calculated by a system of linear equation using elimination.

ISSN: 0067-3064

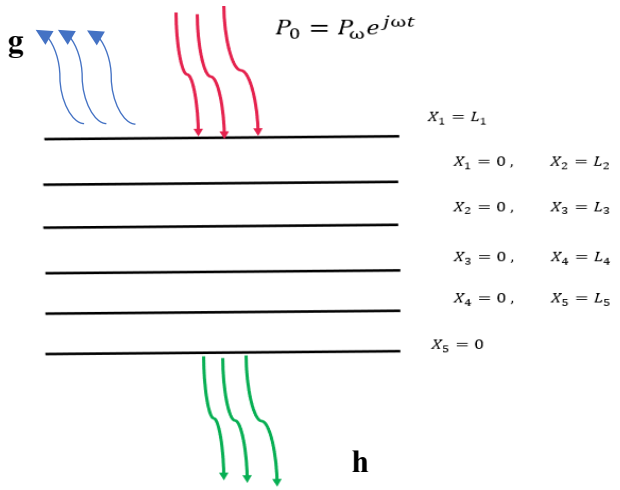

Figure 3. Multi-layer pyroelectric structure according to z-axis.

The boundary conditions:

The frequency domain equation system can be solved by considering the boundary conditions that ensure:

a. Radiation:

for the layer exposed to the flows:

$$k_1\left(\frac{\partial T_1}{\partial z}\right) = Q \ldots\ldots (6)$$

the layer exposed to the flux receives a fraction η of incident power which is the modulated power P_ω and the other part will be lost by radiation characterized by a coefficient of heat exchange by radiation g.

$$-k_1\left(\frac{\partial T_1}{\partial z}\right) = \eta P_w - gT_1 \ldots\ldots (7)$$

b. Conduction:

- Temperature continuity at the interface:

$$T_1|_{z=l_1} = T_2|_{z=0} \ldots\ldots (8)$$

$$\text{Cosh}\,(l_i\lambda_i)\,.A_i + \text{Sinh}\,(l_i\lambda_i).B_i - A_{i+1} = 0 \ldots\ldots (9)$$

suppose that $l_i\lambda_i = \mu_i$, equation (9) becomes:

$$\text{Cosh}\,(\mu_i)\,.A_i + \text{Sinh}\,(\mu_i).B_i - A_{i+1} = 0 \ldots\ldots (10)$$

ISSN: 0067-3064

- Continuity of heat flow density at interfaces:

$$-k_i\left(\frac{\partial T_i}{\partial z}\right)_{z=l_i} = -k_{i+1}\left(\frac{\partial T_{i+1}}{\partial z}\right)_{z=0} \quad \ldots\ldots (11)$$

$$k_i\mu_i A_i Sinh(\alpha_i l_i) + k_i\mu_i B_i Cosh(\alpha_i l_i) - k_{i+1}\alpha_{i+1}A_{i+1} = 0 \quad \ldots\ldots (12)$$

suppose that $k_i\mu_i = \delta_i$, equation (12) becomes:

$$\delta_i A_i Sinh(\mu_i) + \delta_i B_i Cosh(\mu_i) - \delta_{i+1}B_{i+1} = 0 \quad \ldots\ldots. (13)$$

c. Convexion:

for bottom layer in contact with air:

a convective exchange is established between the layer in contact with the air expressed by the following relation:

$$-k_{i+1}\left(\frac{\partial T_i}{\partial z}\right)_{z=l_{i+1}} = hT_{i+1}(l_{i+1}) \quad \ldots\ldots. (14)$$

$$[h.Cosh(\alpha_{i+1}l_{n+1}) + \delta_{i+1}Sinh(\alpha_{i+1}l_{n+1})]A_{i+1} + [\delta_{i+1}Cosh(\alpha_{i+1}l_{n+1}) + h.\cosh(\alpha_{i+1}l_{n+1})]B_{i+1} = 0 \quad \ldots\ldots. (15)$$

$$[h.Cosh(\mu_{i+1}) + \delta_{i+1}Sinh(\mu_{i+1})]A_{i+1} + [\delta_{i+1}Cosh(\mu_{i+1}) + h.\cosh(\mu_{i+1})]B_{i+1} = 0 \ldots (16)$$

h is coefficient of heat exchange by convexion.

Using boundary conditions, the system equations to solve for N layers is: [4]

$$\begin{cases} g.A_1 - \delta_1 B_1 = \eta P_w & i = 0 \\ \left.\begin{array}{l} \text{Cosh}(\mu_i).A_i + \text{Sinh}(\mu_i).B_i - A_{i+1} = 0 \\ \delta_i A_i Sinh(\mu_i) + \delta_i B_i Cosh(\mu_i) - \delta_{i+1}B_{i+1} = 0 \end{array}\right\} & i = 1\ldots n-1 \\ [h.Cosh(\mu_{i+1}) + \delta_{i+1}Sinh(\mu_{i+1})]A_{i+1} + [\delta_{i+1}Cosh(\mu_{i+1}) + h.\cosh(\mu_{i+1})]B_{i+1} = 0 & i = n \end{cases}$$

ISSN: 0067-3064

The system of linear equations is a multilayer structure represent the temperature distribution in the pyroelectric structure using the thermal parameters in the table.1 and with the determination of the complex constants A_i and B_i by elimination.

Materials	Density ρ (g /m^3)	Thermal conductivity K (w/m. k)	calorific capacity C (j/kg. K)
Aluminium	2.708 [a]	236 [a]	896 [a]
P (VDF-TrFE)	1.800 [a]	0.13 [a]	1400 [a]
Polyamide	1.420 [a]	0.147 [a]	1087 [a]
Air	0.02184 [a]	0.026 [a]	1047 [a]
SiO_2	2.2 [c]	1.3 [c]	750 [c]
Silicon	2.330 [a]	153 [a]	712 [a]
Porous silicon	1.320 [b]	0.02 [b]	780 [b]

Réf a = [5], Réf b = [7], Réf c = [8]

Table 1. Thermal parameters of materials.

1.2. Pyroelectric detector model.

a) Pyroelectric layer suspended in the air

This structure likely involves a layer of copolymer suspended in the air without direct contact with a solid substrate. [6]

$$T_{m1} = \frac{(\eta/g)P_W}{(\chi_p - \chi_0)\mu_1}\{\chi_p sh(\mu_1) + [ch(\mu_1) - 1]\} \quad \ldots\ldots (17)$$

Where:

$$\chi_0 = \frac{\delta_p}{g} \quad \ldots\ldots\ldots (18)$$

$$\chi_p = \frac{\delta_p.\chi_f - \delta_m.Tanh(\mu_p)}{\delta_m - \delta_p.\chi_f.Tanh(\mu_p)} \quad \ldots\ldots\ldots (19)$$

$$\chi_f = -\frac{\delta_m + h.Tanh(\mu_m)}{h + \delta_m.Tanh(\mu_m)} \quad \ldots\ldots\ldots (20)$$

ISSN: 0067-3064

b) Pyroelectric layer deposited on silicon substrate:

This structure involves the copolymer layer in direct contact with a solid substrate. The temperature distribution study can reveal how heat is transferred between the copolymer layer and the substrate, providing insights into the thermal conductivity and thermal resistance of the copolymer-substrate interface.

$$T_{mp} = \frac{(\eta/g)P_W}{(\chi_p - \chi_0)\mu_p}\{\chi_p sh(\mu_p) + [ch(\mu_p) - 1]\} \ldots\ldots\ldots (21)$$

Where:

$$\chi_0 = \frac{\delta_p}{g} \ldots\ldots\ldots (22)$$

$$\chi_p = \frac{\delta_p \cdot \chi_{si} - \delta_{si} \cdot Tanh(\mu_p)}{\delta_{si} - \delta_p \cdot \chi_{si} \cdot Tanh(\mu_p)} \ldots\ldots\ldots (23)$$

$$\chi_{si} = \frac{\delta_m \cdot \chi_m - \delta_m \cdot Tanh(\mu_{si})}{\delta_m - \delta_{si} \cdot \chi_m \cdot Tanh(\mu_{si})} \ldots\ldots\ldots (24)$$

$$\chi_m = -\frac{\delta_m + h \cdot Tanh(\mu_m)}{h + \delta_m \cdot Tanh(\mu_m)} \ldots\ldots\ldots (25)$$

c) Pyroelectric layer/ thermal Insulator/ silicon substrate:

This structure includes a layer of copolymer sandwiched between a thermal insulator and a substrate. The temperature distribution study can elucidate the thermal resistance provided by the insulator, the heat transfer characteristics between the copolymer and the insulator, and the overall temperature profile across the structure.

$$T_{mp} = \frac{(\eta/g)P_W}{(\chi_p - \chi_0)\mu_p}\{\chi_p sh(\mu_p) + [ch(\mu_p) - 1]\} \ldots\ldots\ldots (26)$$

Where:

$$\chi_0 = \frac{\delta_p}{g} \ldots\ldots\ldots (27)$$

$$\chi_p = \frac{\delta_p \cdot \chi_{is} - \delta_{is} \cdot Tanh(\mu_p)}{\delta_{is} - \delta_p \cdot \chi_{is} \cdot Tanh(\mu_p)} \ldots\ldots (28); \qquad \chi_{is} = \frac{\delta_{is} \cdot \chi_{is} - \delta_{is} \cdot Tanh(\mu_{is})}{\delta_{si} - \delta_{is} \cdot \chi_{si} \cdot Tanh(\mu_{is})} \ldots\ldots\ldots (29)$$

$$\chi_{si} = \frac{\delta_{si} \cdot \chi_m - \delta_m \cdot Tanh(\mu_{si})}{\delta_m - \delta_{is} \cdot \chi_m \cdot Tanh(\mu_{si})} \ldots\ldots (30); \qquad \chi_m = -\frac{\delta_m + h \cdot Tanh(\mu_m)}{h + \delta_m \cdot Tanh(\mu_m)} \ldots\ldots\ldots (31)$$

ISSN: 0067-3064

2. Simulation and optimization of pyroelectric detector:

The temperature response was analyzed using the equation $|T_m/T_0|$, where T_m is the temperature of the pyroelectric layer at a specific frequency and T_0 is the initial temperature.

For the free copolymer structure, the temperature response was compared to the copolymer with a thermal insulator layer and the copolymer with a porous silicon layer. The nature of the substrate, the nature of the thermal insulation, and the thickness of the thermal insulator were varied to observe their influence on the temperature response at different frequencies.

The goal of this analysis was to deduce the optimal structure for infrared imaging at frequencies of 10, 25, 100, 500, and 1000 Hz. By considering the technology parameters and the influence of the different structural components, the study aimed to determine the most effective configuration for infrared imaging applications.

2.1. Influence of the nature of heat insulation:

In the simulation, the temperature response was analyzed as a function of the thickness of the sensitive copolymer layer in the structure (copolymer/ thermal insulator/ silicon). This allowed for the investigation of the influence of the nature of the thermal insulation on the sensitivity to temperature changes.

The results of the simulation were presented in Figure 3, which likely depicted the relationship between the thickness of the sensitive copolymer layer and the corresponding temperature response. This visualization would have provided insights into how the nature of the thermal insulation affects the sensitivity of the structure to temperature variations.

the thermal insulators respectively are: Polyamide (PA), Silicon dioxide (SiO_2), Air (O_2).

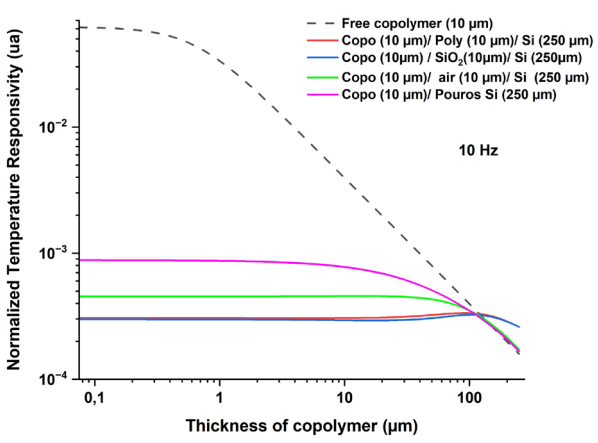

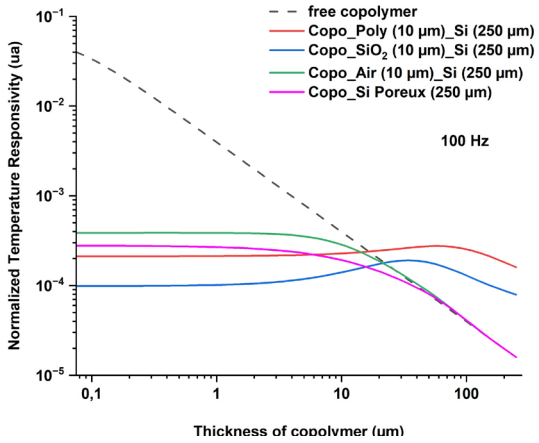

ISSN: 0067-3064

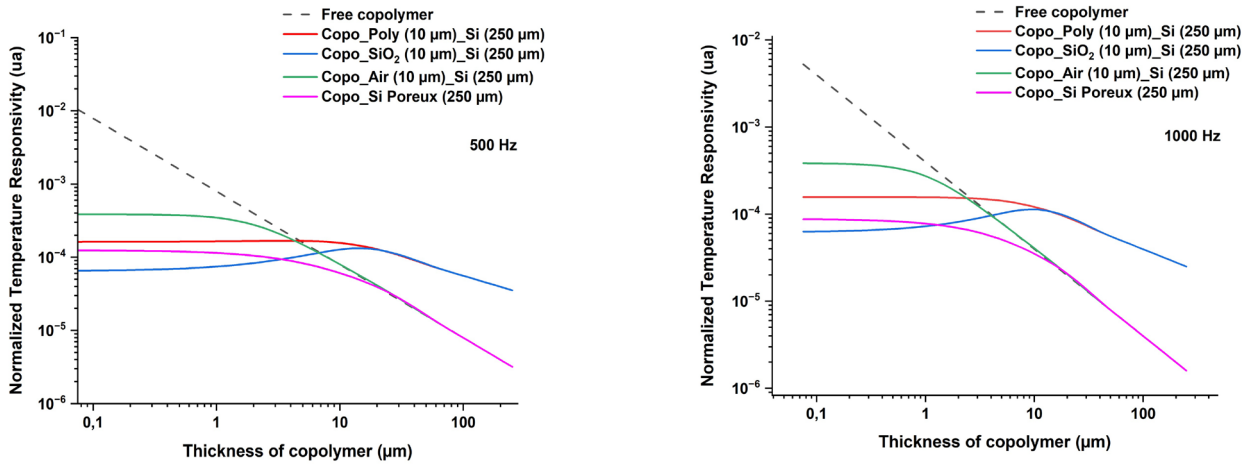

Figure 4. Influence of the thermal insulation nature on the temperature response ($|T_m/T_0|$) for different frequency (10 Hz, 100 Hz, 500 Hz, 1000 Hz) for (copo/ thermal insulator/ silicon) structure.

The comparison of different insulating materials in the structure (copolymer/ thermal insulator/ silicon) revealed that a 10 µm layer of air exhibited superior insulating properties compared to a 10 µm layer of polyamide and a 10 µm layer of silicon dioxide. This finding suggests that air may be a more effective thermal insulator within this specific structure.

When comparing the responses of structures using different thermal insulators at a modulation frequency of 10 Hz, it was observed that the structure (copolymer/ porous silicon) exhibited the best sensitivity to temperature changes. This superior sensitivity can be attributed to the presence of pores within the porous silicon substrate layer.

The presence of pores in the porous silicon layer can indeed act as a form of thermal insulation. The porosity of the porous silicon layer can be represented by an equation that describes the relationship between the porosity and its impact on thermal insulation.

A typical equation that represents porosity in the context of thermal insulation could be:

$$P_t = \frac{V_p}{V_t} \quad \ldots\ldots\ldots (32)$$

with V_p: *Pore Volume* V_t: *Total Volume of material*

ISSN: 0067-3064

This equation provides a measure of the fraction of the porous silicon layer that consists of voids or pores, and it helps to quantify the impact of porosity on the thermal insulation properties of the material. Understanding this relationship is crucial for assessing the thermal performance and sensitivity of structures incorporating porous silicon in various applications.

The porosity depends on thermal conductivity, when porosity increases the thermal conductivity decreases and this explains the increase in thermal resistance:

$$R_{th} = (^{d}/_{k}).S \quad \ldots\ldots (33)$$

In the frequency range of 100 Hz to 500 Hz, the structure consisting of 10 µm of copolymer, 10 µm of air, and 250 µm of silicon substrate was found to provide the best response to temperature changes. This indicates that this specific combination of materials and thicknesses within the structure is particularly effective at responding to temperature variations within the specified frequency range.

In the context of a 1000 Hz modulation frequency, the structure consisting of 10 µm of copolymer, 5 µm of air, and 250 µm of silicon was observed to provide the best response to temperature changes.

2.2. Influence of the thickness of substrate:

figure 4. suggests that there is a graphical representation or data in the study that illustrates the relationship between the thickness of the porous silicon substrate and the temperature response of the pyroelectric structure. This figure likely shows how the temperature response varies with different substrate thicknesses, supporting the assumption that a thin layer of porous silicon yields the best temperature response.

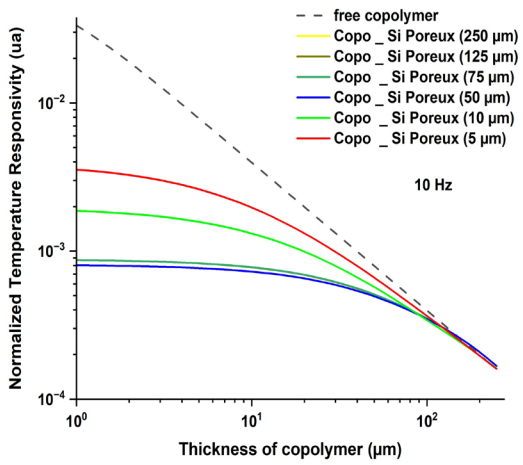

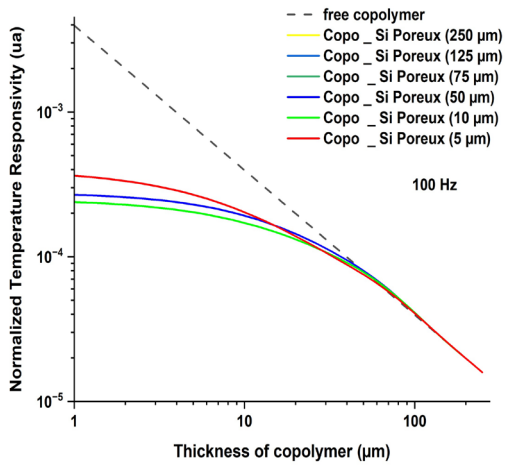

ISSN: 0067-3064

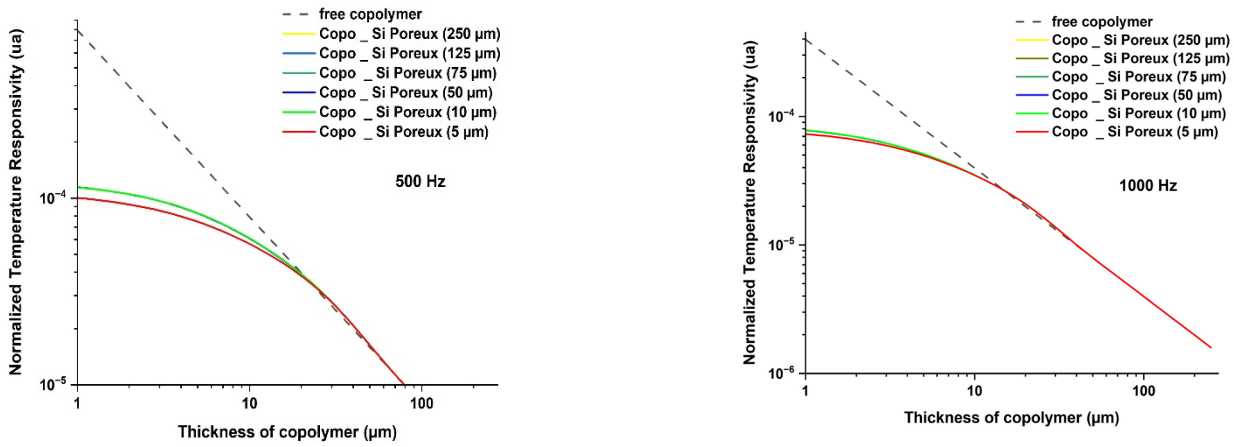

Figure. 5 Influence of the substrate thickness on the temperature response ($|T_m/T_0|$) at different frequencies (10 Hz, 100 Hz, 500 Hz, 1000 Hz) for the (copolymer/ porous silicon) structure.

2.3. Optimal geometry study of structure:

The study focuses on investigating the optimal geometry of the (copolymer/thermal insulator/silicon) structure. Table 2. provides important data regarding the minimum thickness of the copolymer layer, the thermal capacity, and the thermal resistance of some electrodes within this structure.

Materials	C_{th} (J / k)	R_{th} (K/ w)	Minimum thickness of Copolymer (µm)
P (VDF_TrFE)	$(7.56).10^{-7}$	$(2.3).10^{-12}$	-
Ni-Cr	$(7.50).10^{-8}$	$(9.44).10^{-15}$	0.075
Aluminium (Al)	$(2.91).10^{-7}$	$(5.08).10^{-16}$	0.29
Or (Au)	$(2.96).10^{-7}$	$(3.75).10^{-16}$	0.295

Table 2. Thermal parameters and minimum thickness of electrodes.

ISSN: 0067-3064

The heat capacity equation is:

$$C_{th} = \rho . C_s . S . d \quad \ldots\ldots\ldots (34)$$

To define the minimum thickness of the pyroelectric layer (copolymer) based on the given condition that the thermal capacity of the copolymer must be ten times that of the electrodes can be expressed as follows:

$$C_{th\_copo} = 10 \, . C_{th\_NiCr} \quad \ldots\ldots\ldots (35)$$

C_{th_copo} is thermal capacity of the copolymer; C_{th_NiCr} is thermal capacity of the electrodes.

Analyzing the data in Figure 5 can provide a comprehensive understanding of how copolymer thickness influences the temperature response at various chopper frequencies, allowing for the identification of optimal thicknesses for specific operational conditions. This can contribute to the development of more effective and responsive (copolymer/polyamide/silicon) structures for practical use. The thickness of the polyamide layer fixed at 10 µm.

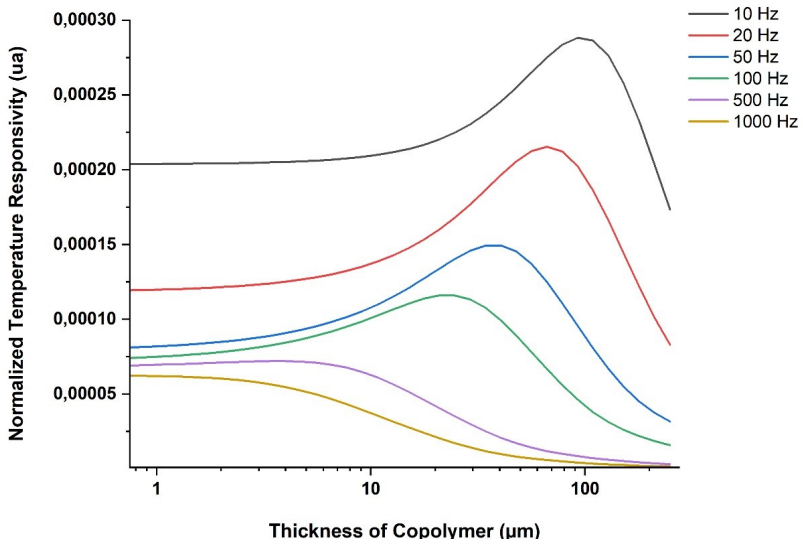

Figure 6. Influence of the thickness of the copolymer on the temperature response in different modulation frequencies.

ISSN: 0067-3064

The study has identified a frequency-dependent behavior in the optimal thickness of the copolymer layer within the (copolymer/polyamide/silicon) structure. Specifically, it seems that at low frequencies, a thicker copolymer layer is preferred, while at high frequencies, a thinner copolymer layer is more suitable, as indicated in Table 3.

Frequency	10 Hz	20 Hz	50 Hz	100 Hz	500 Hz	1000 Hz
Copolymer	92 µm	66 µm	40 µm	24 µm	4 µm	0.075 µm

Table 3. Thickness of the copolymer layer corresponding to the maximum response in temperature for the (copolymer/ polyamide/ silicon) structure.

3. Conclusion:

The resolution of one-dimensional equation of heat transfer, by analytical method and construction of pyroelectric detector model.

The temperature responses of the detector revealed depending on the modulation frequency, thickness and nature of the materials.

The result suggests that air might be a good thermal insulator, which could be useful for improving temperature response and sensitivity in structures. This insight could be valuable for optimizing the design and performance of systems used in applications like temperature sensing and infrared imaging.

The use of porous silicon can also eliminate the need for an additional thermal insulating layer, which can simplify the design and fabrication of the temperature sensing structure. This can be particularly beneficial in applications where space and weight constraints are critical factors.

ISSN: 0067-3064

References

[1] Vui V. Pham, Daniel Esteve, Essaid Bousbiat, Jean Farre, Rene Laguerre, et Jean Simonne, « Parameters Controlling the Design of a Pyroelectric PVDF Matrix Array », present à Proc.SPIE, mars 1989, p. 35-39. doi: 10.1117/12.950256.

[2] Y. A. Çengel et A. J. Ghajar, *Heat and Mass Transfer: Fundamentals & Applications*. in Asia Higher Education Engineering/Computer Science Mechanica. McGraw Hill Education,P. 80, 2015.

[3] B. R. Holeman, « Sinusoidally modulated heat flow and the pyroelectric effect », *Infrared Phys.*, vol. 12, n° 2, p. 125-135, juin 1972, doi: 10.1016/0020-0891(72)90016-4.

[4] H. Zhang, W. Wang, S. Zhang, et Z. Zhao, « Semi-analytic solution of three-dimensional temperature ……response functions », Int. J. Heat Mass Transf., vol. 118, p. 208-222, mars 2018.

[5] A. Mahrane, M. Djafari-Rouhani, A. Najmi, et D. Esteve, « Effects of the Substrate on the Response of P (VDF-TrFE) Pyroelectric Detector », MRS Proc., vol. 299, p. 297, 1994.

[6] Derguini Noureddine, thèse de Magister « Modélisation et simulation d'un capteur infrarouge ..... carte d'acquisition à base d'un CPLD », ENS Kouba-Algérie, Page (58-60), 2007.

[7] L. Li, L. Zhang, X. Yao, et B. Li, « Computer simulation of temperature field of multilayer pyroelectric thin film IR detector », Ceram. Int., vol. 30, no 7, p. 1847-1850, janv. 2004.

[8] Shu-Yau Wu, « Effects of the substrate on the response of pyroelectric detectors », IEEE Trans. Electron devices, vol. 27, no 1, p. 88-91, janv. 1980, doi: 10.1109/T-ED.1980.19825.

ISSN: 0067-3064

Synthesis and characterization of $LaAl_{0.9}Fe_{0.1}O_3$ perovskite: Application to oxygen photo-production

H. Medjadji [a 1], A. Boulahouache [a, b], K. Derkaoui [c] and M. Trari [d] N. Salhi [a, b,]

[a]Laboratoire LCPMM, Faculté des Sciences, Université BLIDA1, B.P 270, Route de Soumaa, BLIDA, Algérie.
[b]Laboratoire de Chimie du Gaz Naturel, Faculté de Chimie, USTHB, BP32, El-Alia, 16111 Bab Ezzouar, Alger, Algérie.
[c] Research Center On Semiconductors Technology for Energetic, CRTSE-TESE - 02, Bd. Dr. Frantz Fanon, 7 Merveilles, Box 140, 16038 Algiers, Algeria.
[d]Laboratoire de Stockage et valorization de l'énergie renouvelable, Faculté de Chimie, USTHB, BP32, El-Alia, 16111 Bab Ezzouar, Alger, Algérie.

Abstract

Iron-substituted perovskite $LaAl_{0.9}Fe_{0.1}O_3$ material prepared by sol-gel route using nitrates precursors salts as raw materials and propionic acid as a chelating agent was characterized by (TG-ATD), X-ray diffraction (XRD), FT-IR spectroscopy, UV-visible spectrophotometry, Scanning Electron Microscopy (SEM-EDX) analysis, X-ray Photoelectron Spectroscopy (XPS), Photoluminescence (PL) and electrochemical analysis. $LaAl_{0.9}Fe_{0.1}O_3$ was applied as photocatalyst for oxygen production under visible light irradiation. The thermal analysis (TG/DSC) shows that oxide phase formation is complete beyond 500°C. The XRD patterns indicates the formation of pure phase $LaAl_{0.9}Fe_{0.1}O_3$ at 800 °C with an average crystallite size of 29 nm. The optical band gap determined by diffuse reflectance is 2.28 eV. The EDS analysis indicates the presence of only La, Al, Fe and O. XPS analysis revealed the presence of La, Al, Fe in the oxidation state (III) on the surface of the material. The positive slope of the capacitance-potential plot (C-2 - E) indicates an n-type semiconductor with a flat-band potential of 0.36 VSCE and an electron density of 5.37×10^{18} cm^{-3}. Tested in the photo reduction reaction of water, $LaAl_{0.9}Fe_{0.1}O_3$ perovskite leads 37 µmol of O_2 at neutral medium (pH~ 7), whereas a notable enhancement to 91 µmol is observed in a basic medium (pH ~ 12).

Keyword: Perovskite; Sol Gel; Semiconductor; Photocatalyst; Visible light; Oxygen-production.

[1] *Corresponding authors*
nas.salhi@yahoo.fr *(N. Salhi)* ; hamzamedjadji1990@gmail.com *(H.Medjadji)*

ISSN: 0067-3064

1. Introduction

Photocatalysis-based semiconductors are considered as green technology [1,2], which has attracted significant attention due to its various applications such as air purification [3], wastewater treatment [4], degradation of various organic and inorganic pollutants [5], production of green hydrogen [6,7] and photogenerated oxygen [8,[9]. In this regard, water splitting into H_2 and O_2 represents an interesting challenge. O_2 evolution occurs with many high-potential oxides, so that the valence band is greater than the oxidation potential of water [10]. In this field, perovskite oxides with the structural formula ABO3, where A and B represent cations of different sizes, the atomic size of the atoms in position A being greater than that of the atoms in position B [11,12], have promising applications in various fields due to their suitable potential valence band and unique structural properties, high chemical stability and excellent optical characteristics. Undoped lanthanum aluminate ($LaAlO_3$) has been the subject of much interest in the photocatalytic water splitting to generate O_2 [13,14], and its applications are diverse. It is used as a dielectric resonator, substrate and insulating pad for high-temperature superconducting thin films for microwave devices, as a catalyst support, electrolyte or electrode for solid oxide fuel cells [15,16]. The good catalytic activity and high surface area of $LaAlO_3$ make it to be used as a catalyst for the oxidative coupling of methane [17] and the hydrogenation and hydrogenolysis of hydrocarbons [18]. Due to its wide energy gap, $LaAlO_3$ does not respond in the visible light range [19,20]. The catalytic and optical properties of $LaAlO_3$ perovskite can be modified by partial cation substitution or doping [21,22], this broadens the response to the visible light spectrum. In addition, it reduces recombination between pairs of electrons (e^-) and holes (h^+) [23,24], giving the material high photocatalytic performance [25,26]. Numerous studies have shown that the crystal structure of $LaAlO_3$ is a good host for $^+$III cations as long as they have an ionic radius similar to that of the La^{3+} ion, different rare earth ions meet this requirement [27]. Additionally, the B site occupied by aluminum can be doped with transition metal ions, giving rise to a large variety of $LaAlO_3$. The $LaAlO_3$ perovskite was doped with rare earth ions, such as Tb^{3+}, Fe^{3+}; as well as noble metal ions, such as, Cu^{2+}, Zn^{2+} [28-30].

In this study, $LaAlO_3$ doped by 10% Fe was synthesized by sol-gel route using propionic acid as a chelating agent. The phase structure, morphology, particle size, gap energy, and electrochemical study of the prepared $LaAl_{0.9}Fe_{0.1}O_3$ powder were studied. The photocatalytic activity of $LaAl_{0.9}Fe_{0.1}O_3$ was conducted for the photo reduction of water to oxygen production under visible light irradiation, in neutral and basic pH.

ISSN: 0067-3064

II Materials and methods

II 1 Synthesis of material

$LaAl_{0.9}Fe_{0.1}O_3$ was synthesized by sol-gel method, using stoichiometric amounts of $La(NO_3)_3,6H_2O$ and $Al(NO_3)_3,9H_2O$, $Fe(NO_3)_3,9H_2O$ with purity greater than 99%. Due to their hygroscopic nature, the precursor salts previously dried in desiccator under vacuum for several days owing, were dissolved separately in propionic acid $C_6H_7O_6$ under heating and stirring until total dissolution. The solutions are then mixed and evaporated at 160°C with vigorous stirring, and the resulting gel is dried overnight in an oven and finally calcined at 800°C (2°C min^{-1}) for 4 h.

II 2 Characterization techniques

The thermogravimetric analysis coupled with differential thermal analysis (TG-DTA) of non-calcined material was performed using a Perkin Elmer SDT-Q500 thermal balance in an inert N_2 flow at a heating rate of 5°C min^{-1} in the temperature range (ambient-900 °C).The XRD analysis was performed on a Panalytical X'Pert PRO diffractometer with the Cu Kα line (λ = 1.54056 Å) in the 2θ range (20-80°). The chemical bands in the $LaAl_{0.9}Fe_{0.1}O_3$ perovskite were obtained by the ATR analysis (ATR platinum Diamond) in the region (400 - 4000 cm^{-1}). The morphology of the powder was characterized using an emission scanning electron microscope (SEM, JEOL JSM-7610FPlus). The XPS analysis was carried out on an Escalab 220 XL spectrometer (Vacuum enerator). A monochromatic Al Ka X-ray source was used and the electron energy was measured in constant analyzer energy mode. All binding energies were referred to C1s core level (285eV). The diffuse reflectance data were collected between 190 and 900 nm with a double-beam UV-visible spectrophotometer (Jasco V- 650). The electrochemical analysis was performed in a standard cell, filled with NaOH electrolyte (0.1 M) containing a Pt auxiliary electrode, an SCE as reference, and the working electrode (WE). J(E) current-potential profiles were plotted using a PGZ 301 potentiostat under N_2 bubbling at a sweep rate of 10 mV. s^{-1}. The capacitance of the $LaAl_{0.9}Fe_{0.1}O_3$/electrolyte junction was measured at 10 kHz. The electrochemical impedance spectroscopy (EIS) was realized between 100 kHz and 10 MHz). The free potential is an intrinsic property of the material independent of its morphology and must be stabilized before characterization. The electrochemical measurements were carried out in the dark and under the irradiation of a LED lamp. The photoluminescence (PL) spectra were recorded at room temperature by a model 320DFX spectrophotometer using a xenon lamp as excitation source.

ISSN: 0067-3064

II 3 Photocatalytic activity

The photo-catalytic test was carried out in a hermetically sealed, double-walled Pyrex reactor thermostated at 50 (± 1°C). 100 mg of catalyst powder were magnetically dispersed (300 rpm) in 100 mL of aqueous electrolyte. After bubbling the solution with N_2 for 30 minutes, the reaction mixture was irradiated with a system of three LED lamps (13 W) arranged symmetrically around the reactor, delivering an intensity of 23 mW/cm^2 (2x1019 photons.s^{-1}).

III Results and discussion

The TGA curve of the gel (**Fig. 1**), shows an initial weight loss (~15%) occurring in the range 74 -170°C, attributed to the release of water. The second major weight loss in the region (200-500°C, 31%) is attributed to the simultaneous decomposition of organic matter from residual solvent and lanthanum, aluminum and iron nitrates into NOx fumes and. The plateau zone above ~500°C indicates the formation of oxide phases. The peaks of the derived curve (DTA) corroborate these temperatures.

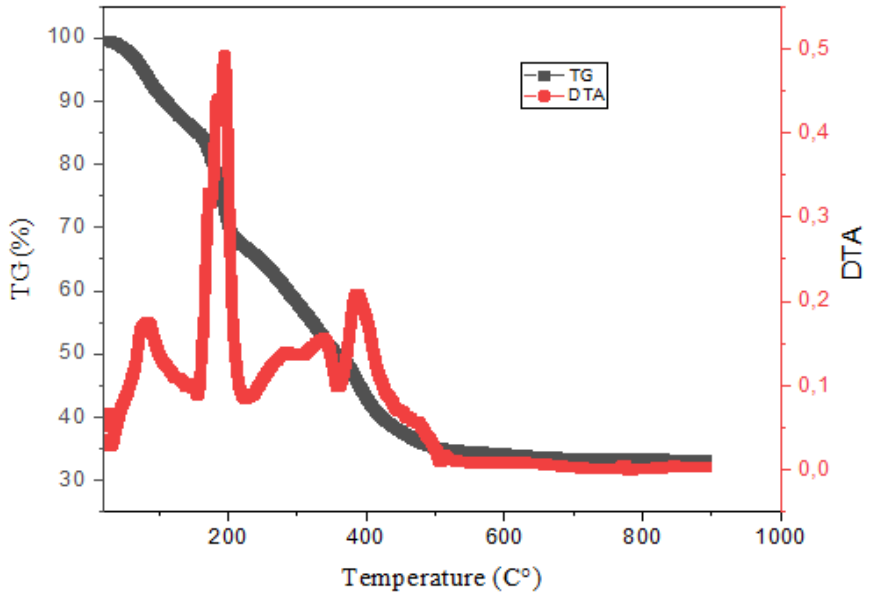

Fig.1: TG- DTA curves of non calcined gel

The single-phase diffractogram of $LaAl_{0.9}Fe_{0.1}O_3$ is depicted in **(Fig.2)**. All peaks correspond to the perovskite structure and rhombohedral symmetry (space group R-3c, N° 167) with no detectable impurities. The absence of Fe_2O_3 peaks confirms that Fe entre the $LaAlO_3$ lattice. The refined lattice constants: *a*= 5.360 Å and *c* =13.089 Å are in good agreement with the JCPDS Card (01-070-4097).

ISSN: 0067-3064

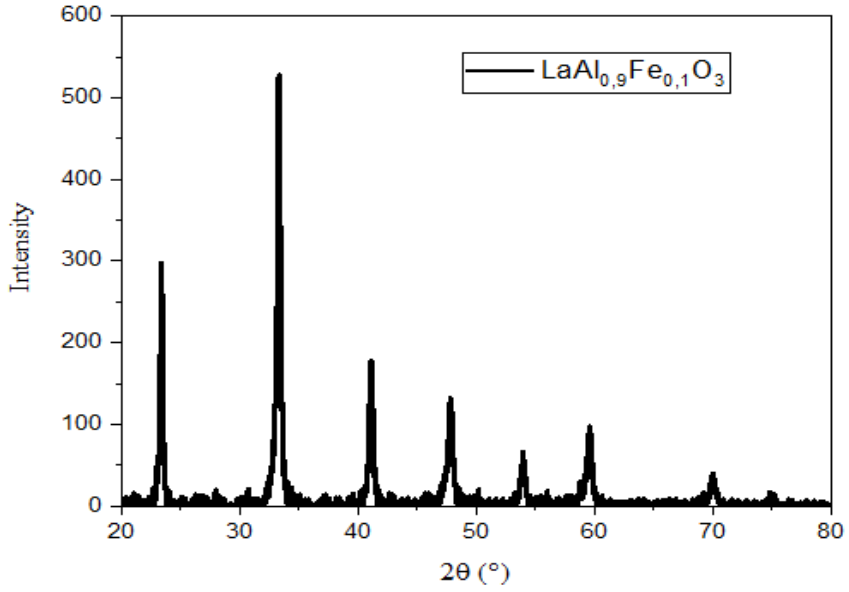

Fig.2: XRD pattern of $LaAl_{0.9}Fe_{0.1}O_3$ calcined at 800 °C

The crystallite size (D =29 nm) was evaluated by Debye Scherrer (Eq 1) from the full width at half maximum (= β, rd.) of the intense XRD line (104); and referring to the nanometric scale.

$$D = \frac{0.9\lambda}{\beta \cos\theta} \qquad \text{(Eq 1)}$$

The ATR spectroscopy **(Fig. 3)** was achieved to identify the chemical bands of the material.

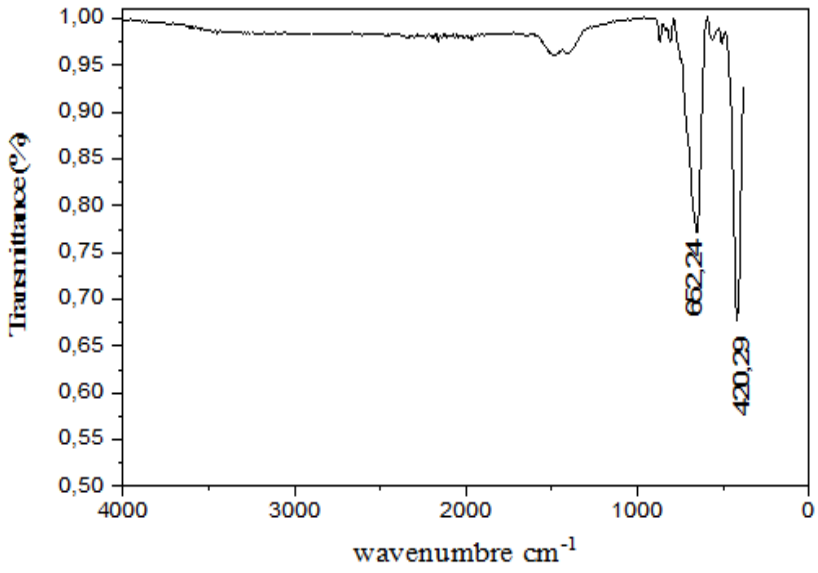

Fig. 3: ATR spectrum of $LaAl_{0.9}Fe_{0.1}O_3$ calcined at 800°C

ISSN: 0067-3064

The absorption bands of $LaAl_{0.9}Fe_{0.1}O_3$ at low wavenumbers (<1500 cm^{-1}) at 652 and 420 cm^{-1}, are associated to the stretching vibration of La-O and Al-O respectively with the LaO_{12} and AlO_6 system in the octahedral site [31,32].

SEM analysis of LaAl0.9Fe0.1O3 (**Fig. 4a**) reveals a semi-spherical structure with moderate homogeneity and medium porosity. As expected, EDS analysis **(Fig. 4b)** shows the presence of La, Al, Fe and O, indicating the formation of $LaAlO_3$ with high purity.

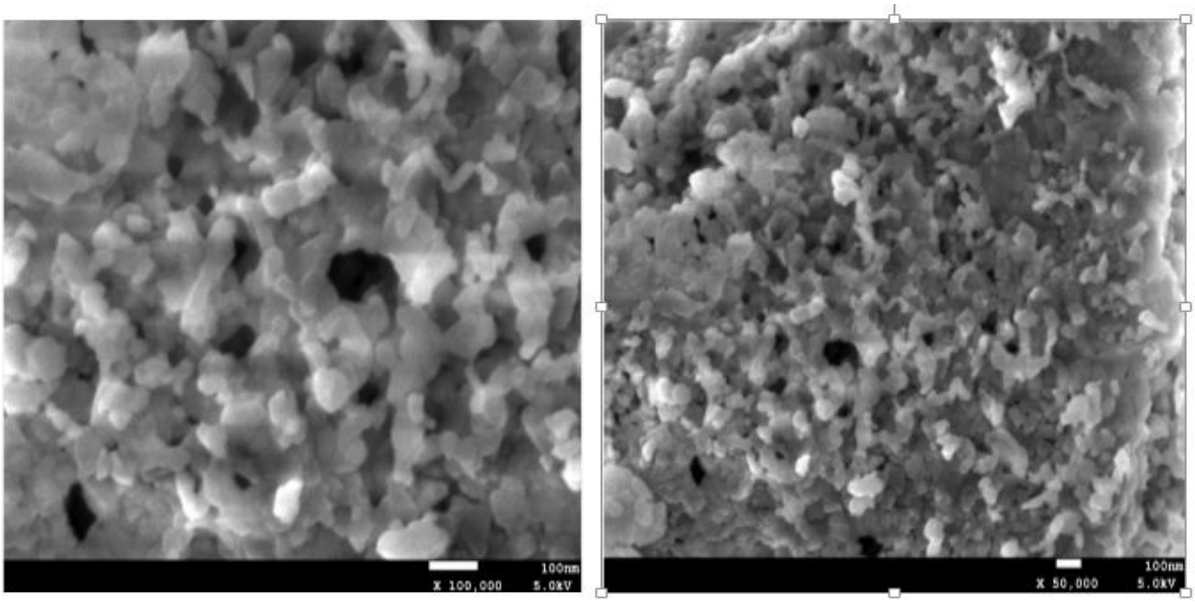

Fig.4a: SEM micrographs of $LaAl_{0.9}Fe_{0.1}O_3$

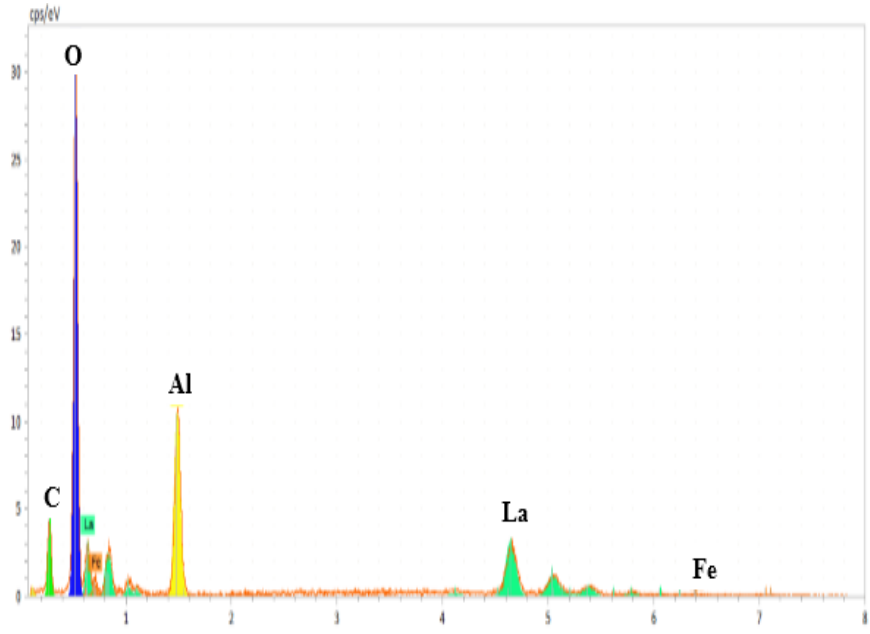

Fig.4b: EDS analysis of $LaAl_{0.9}Fe_{0.1}O_3$

ISSN: 0067-3064

The optical properties of the $LaAl_{0.9}Fe_{0.1}O_3$ nanoparticles are illustrated in **(Fig. 5)**. The energy band gap (E_g) was determined from the Kubelka-Munk equation (Eq 2) using the Tauc plot:

$$(\alpha h\nu)^n = K \times (h\nu - E_g) \qquad \text{(Eq 2)}$$

α: the optical absorption coefficient, ν: the irradiation frequency, and β: a constant intrinsic property of the semiconductors. The exponent *n* indicates the transition type i.e. indirect (*n* = 1/2) or direct (*n* = 2).

For the direct transition of the semiconductor $LaAl_{0.9}Fe_{0.1}O_3$, the gap E_g is obtained from the linear graph $(\alpha h\nu)^n$ versus the incident energy (hν). The indirect gap is evaluated at 2.28 eV.

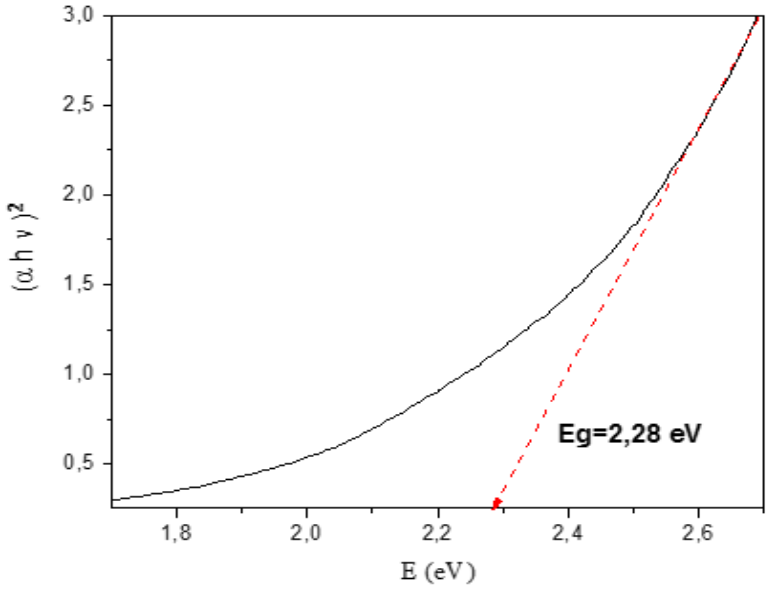

Fig.5: Direct optical transition of $LaAl_{0.9}Fe_{0.1}O_3$ synthesized by Sol-Gel

The surface composition and some specific changes in valence states of $LaAl_{0.9}Fe_{0.1}O_3$ calcined at 800°C (4h) were examined by XPS analysis. Survey scan XPS spectrum **(Fig. 6a)** shows the presence of La, Al, Fe, and O, beside C1 (284.8 eV) signal caused by the incidental surface carbon. The high resolution spectrum of La *3d* **(Fig.6b),** Al *2p* **(Fig.6c)** and Fe *3d* **(Fig.6c)** indicate the lanthanum, aluminum and iron are in the (III) valence oxidation state. La (III) **(Fig.6b)** is detected by $La3d_{5/2}$ (833.6 eV) and $3d_{3/2}$ (850.3eV) peaks [33], while Al (III) **(Fig.6c)** is present as a single symmetrical peak in the Al2p spectrum (74 eV) [34]. Two major peaks in the Fe2p spectra (Fig.6c) at (710.98 eV) and (725.7 eV), are attributed to 2p3/2 and 2p1/2 respectively [35]. **Fig.6d** depicts the O*1s* spectra with binding energies at 529.9, 531.1 and 532eV related to La-O, Al-O and Fe-O crystal [36].

ISSN: 0067-3064

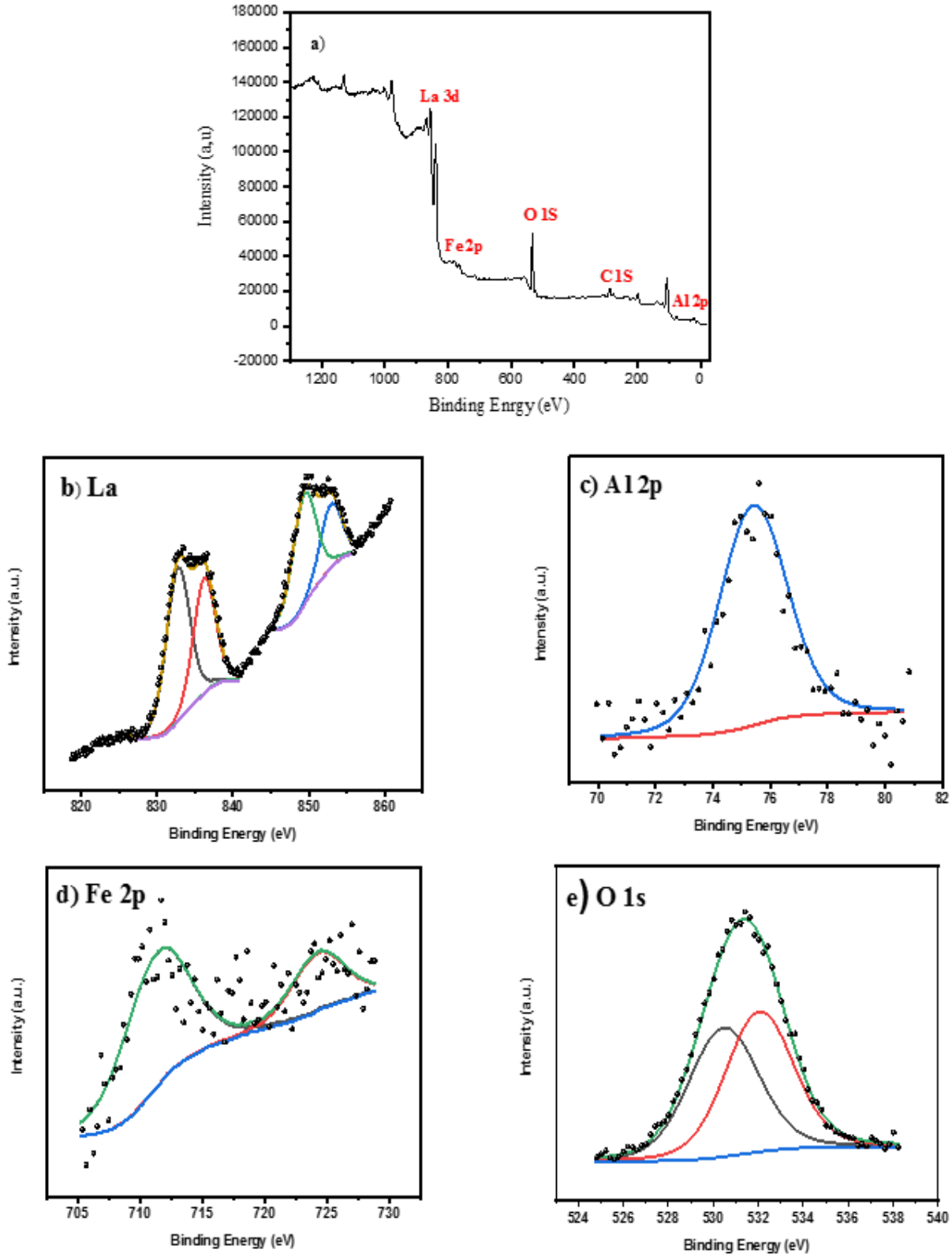

Fig. 6: (**a**): Survey XPS spectrum of $LaAl_{0.9}Fe_{0.1}O_3$

(**b, c, d and e**): High resolution spectra of, La 3d, Al 2p, Fe 2p and O 1s.

ISSN: 0067-3064

Photo-electrochemistry

The flat band potential (E_{fb}) is an important factor in determining the levels of the valence band (VB) and conduction band (CB) for material $LaAl_{0.9}Fe_{0.1}O_3$, a prelude for the photocatalysis application. The determination of the potential E_{fb} and the resulting data are plotted in Figure **(Fig. 7a).** The extrapolated plot to the E-axis gives a potential E_{fb} of 0.36V.

$$\frac{1}{C^2} = \frac{2}{\varepsilon\varepsilon_0 e N_A}(E - E_{fb}) \qquad \text{(Eq 3)}$$

The positive slope of the C^{-2} line confirms the n-type nature of $LaAl_{0.9}Fe_{0.1}O_3$ with electrons as the dominant charge carriers. The flattening below 0.3 V corresponds to the accumulation region with a charge surface of massive levels, while the deviation from the line below ~0.44 V is due to an accumulation zone with a high recombination process. In contrast, above 0.45 V a total separation of (e^-/h^+) pairs is observed. The n-type character is also confirmed by photo-chrono amperometry **(Fig.7b)**, which shows an increase in current under visible irradiation.

The potentials/energies of VB and CB are (2.44 V/7.19eV) and (0.16 V/4.91 eV) respectively, and are calculated from the following relations:

$$E_{CB} = 4.75 + eE_{fb} - Ea \qquad \text{(Eq 4)}$$

$$E_{VB} = E_{CB} - E_g \qquad \text{(Eq 5)}$$

In general, for n-type semiconductors, E_{CB} is 0.2 V more negative than E_{fb} [37]. EIS analysis was carried out in the dark and under free-potential irradiation **(Fig. 7c)**. The diagram showing a semicircle at high frequency is attributed to charge transfer, thus corroborating the semi-conductivity of $LaAl_{0.9}Fe_{0.1}O_3$ perovskite with enhanced photocatalysis. The current potential characteristics J(E) shown in **(Fig.7d)** are plotted to determine the electrochemical stability range and to predict the interfacial reaction. Water oxidation is observed at ~0.6 V, while the increase in current below ~0.05 V is due to the release of H_2.

ISSN: 0067-3064

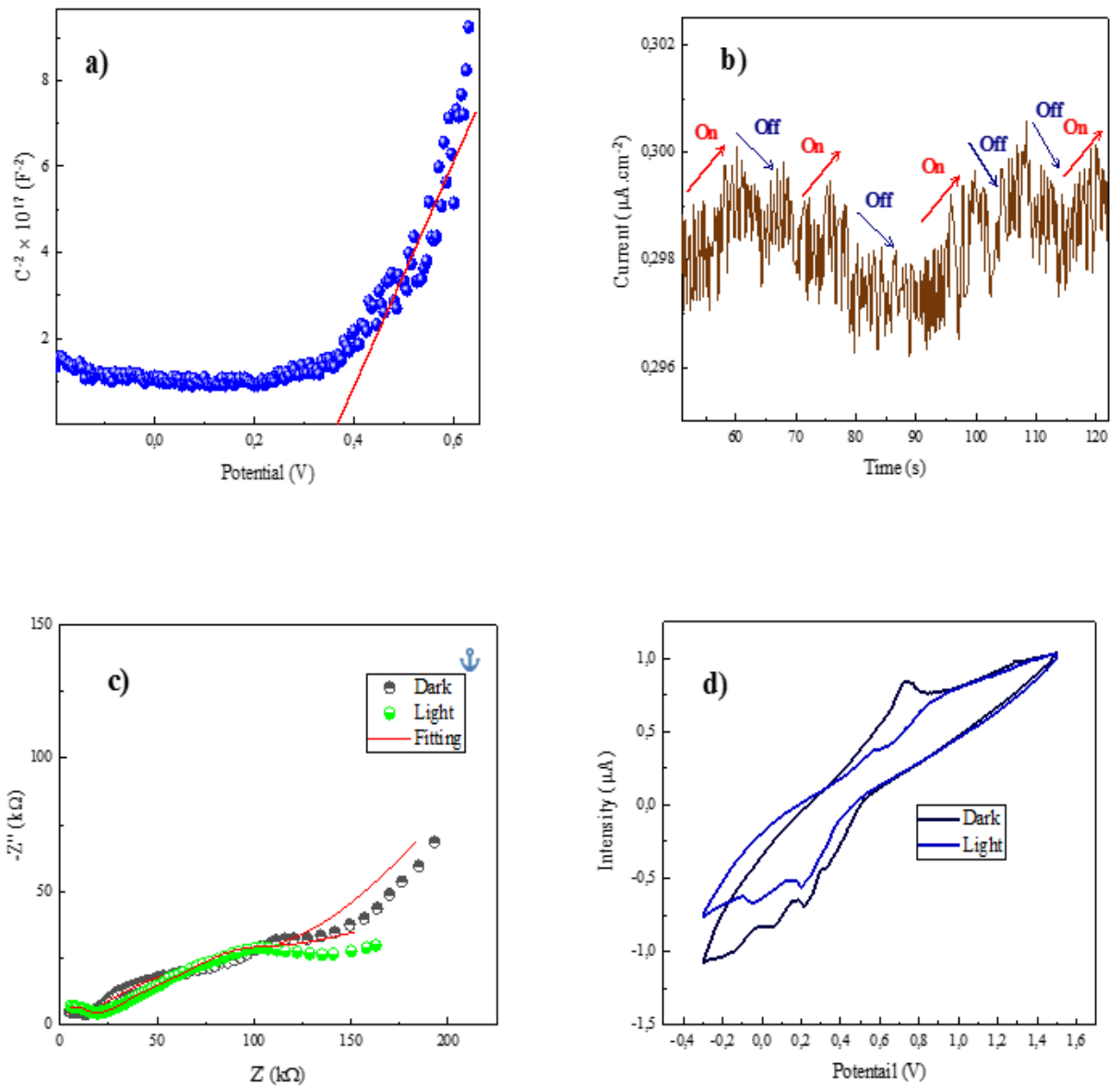

Fig. 7: a): Mott-Schottky plot, b): Chrono-amperometry of $LaAl_{0.9}Fe_{0.1}O_3$ in NaOH solution (0.1 M) under UV light, c): J(E) characteristics under UV light, d) :Electrochemical impedance spectroscopy

The photoluminescence (PL) is an important analysis to investigate the electronic structure, optical and photochemical properties of the semiconductor. **Fig.8** illustrates the PL emission spectrum of $LaAl_{0.9}Fe_{0.1}O_3$ calcined at 800°C with the excitation wavelength of 300 nm. The emission signals in the range 390-550 nm are attributed to 3.1,3 and 2.5eV respectively.

ISSN: 0067-3064

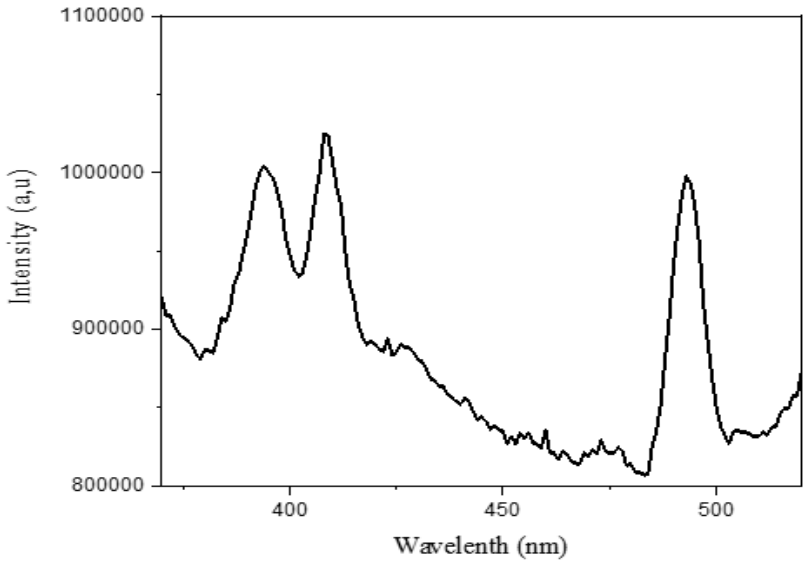

Fig. 8: Photoluminescence emission spectrum of $LaAl_{0.9}Fe_{0.1}O_3$

IV Photocatalyticactivity

Photochemical production of O_2 and H_2 on semiconductors from water and sunlight is an attractive process due to the clean and renewable energy. In general, the photocatalytic water reduction reaction mechanism involves three main steps: light absorption with energy greater than or equal to the band gap of the $LaAl_{0.9}Fe_{0.1}O_3$ perovskite to generate electrons (e^-) hole (h^+) pairs, charge separation and migration to the semiconductor surface and the interfacial reactions for water reduction [38]. **Fig.9** depicts the energy diagram of $LaAl_{0.9}Fe_{0.1}O_3$ semiconductor.

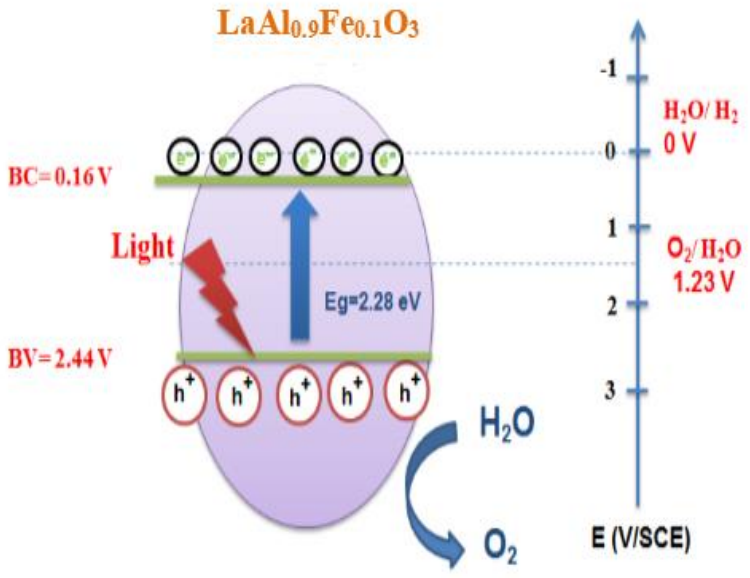

Figure.9- Energy diagram for $LaAl_{0.9}Fe_{0.1}O_3$

ISSN: 0067-3064

The E_{CB} = 0.16V is more positive than the standard potential to reduce water to hydrogen $E°(H_2O/H_2)$ = 0 V, therefore the photo-generated electrons (e-) cannot reduce water to hydrogen [39], While H_2O can oxidized by photo-generated holes (h^+) due to the E_{VB}=2.44 V which is more positive than oxidation water potential $E°(O_2/ H_2O)$=1.23V [40], so the photocatalyst produces only oxygen gas.

Fig.10 shows the O_2 evolution at pH~7, a volume ~ 37 µmol of oxygen is recorded after 30 min. A significant increase of oxygen production is generated leading to ~ 91 µmol at pH~12 after 10 min of reaction test. The oxygen volume increase by a factor of 2.45 with pH rising.

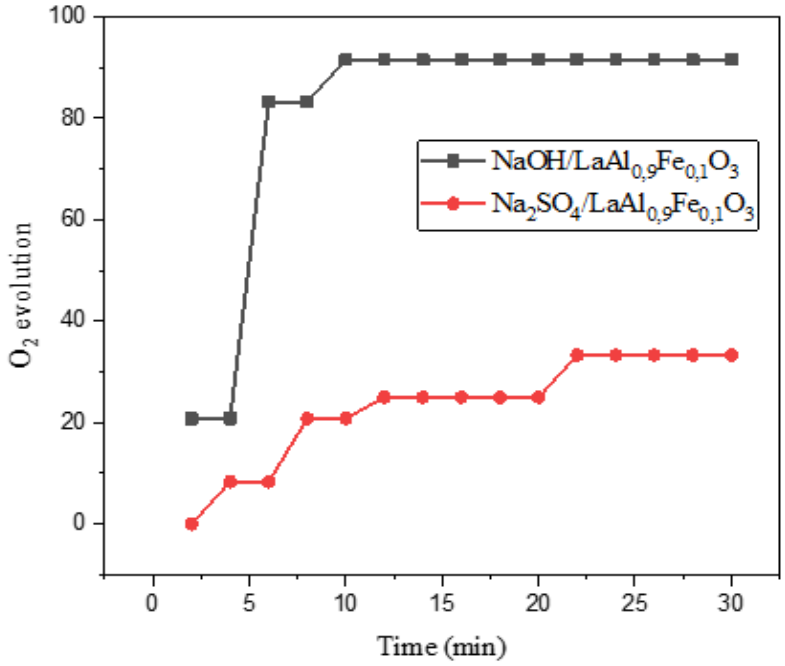

Figure.10: Oxygen (O_2) evolution on $LaAl_{0.9}Fe_{0.1}O_3$ versus time

The water photo reduction for oxygen production over $LaAl_{0.9}Fe_{0.1}O_3$ semi-conductor takes place as follow:

$LaAl_{0.9}Fe_{0.1}O_3$ + light = pervoskite ($e^-_{CB} + h^+_{VB}$)

$2h^+_{VB} + 3H_2O \rightarrow 1/2O_2 + 2H_3O^+$ (Eq 6)

The quantum efficiency (η) is expressed by:

$\eta(\lambda) = 1 - \exp(-\alpha_\lambda L_D)$ (Eq 7)

α_λ is the absorption coefficient which is λ-dependent and the O_2 release is a two electron reaction and the quantum yield is given by the expression:

$\eta = 2 \times V \times N / \{\Phi \times V_m \times t\}$ (Eq 8)

ISSN: 0067-3064

V and V_m are respectively the volume of generated and the molar volume of O_2, N Avogadro number, Φ the photons flux falling (6.28×10^{16} photons s^{-1}), and t the saturation time.

V Conclusion

$LaAl_{0.9}Fe_{0.1}O_3$ was successfully prepared at 800°C via sol-gel method. X-ray diffraction analysis indicated the formation of a pure phase with an average crystallite size of 29 nm. A less homogeneous semi-spherical shape and the presence of La, Al, Fe and O were recorded by SEM-EDS analysis. XPS analysis revealed the existence of the valence state III of La, Al and Fe. The electrochemistry study showed an n-type semiconductor with 0.36 V potential of E_{fB}. $LaAl_{0.9}Fe_{0.1}O_3$ was tested in water photo reduction for oxygen production under visible light irradiation. An evolution rate of 91.59 μmol of O_2 is obtained in 0.1 M NaOH solution at pH~12.

Bibliography

[1] A. Boulahouache *et al.*, "Preparation, characterization and electronic properties of lafeo3 perovskite as photocatalyst for hydrogen production," *International Journal of Hydrogen Energy*, vol. 48, no. 39, pp. 14650–14658, 2023. doi:10.1016/j.ijhydene.2022.12.327

[2] F. Zhang *et al.*, "Recent advances and applications of semiconductor photocatalytic technology," *Applied Sciences*, vol. 9, no. 12, p. 2489, 2019. doi:10.3390/app9122489

[3] S. Weon, F. He, and W. Choi, "Status and challenges in photocatalytic nanotechnology for cleaning air polluted with volatile organic compounds: Visible light utilization and Catalyst Deactivation," *Environmental Science: Nano*, vol. 6, no. 11, pp. 3185–3214, 2019. doi:10.1039/c9en00891h

[4] F. Opoku, K. K. Govender, C. G. van Sittert, and P. P. Govender, "Recent progress in the development of semiconductor-based photocatalyst materials for applications in photocatalytic water splitting and degradation of pollutants," *Advanced Sustainable Systems*, vol. 1, no. 7, 2017. doi:10.1002/adsu.201700006

[5] M. B. Tahir *et al.*, "Role of nanophotocatalysts for the treatment of Hazardous Organic and inorganic pollutants in wastewater," *International Journal of Environmental Analytical Chemistry*, vol. 102, no. 2, pp. 491–515, 2020. doi:10.1080/03067319.2020.1723570

[6] H. Kenfoud *et al.*, "Opto-electrochemical characteristics of synthesized BAFE2O4 nanocomposites: Photocatalytic degradation and hydrogen generation investigation," *International Journal of Hydrogen Energy*, vol. 47, no. 24, pp. 12039–12051, 2022. doi:10.1016/j.ijhydene.2022.01.232

[7] O. A. Carrasco-Jaim, J. M. Mora-Hernandez, L. M. Torres-Martínez, and E. Moctezuma, "A comparative study on the photocatalytic hydrogen production of ATiO3 (A = zn, Cd and pb) perovskites and their photoelectrochemical properties," *Journal of Photochemistry and Photobiology A: Chemistry*, vol. 371, pp. 98–108, 2019. doi:10.1016/j.jphotochem.2018.11.004

[8] S. Boumaza, L. Boudjellal, R. Brahimi, A. Belhadi, and M. Trari, "Synthesis by citrates sol-gel method and characterization of the perovskite lafeo3: Application to oxygen photo-production," *Journal of Sol-Gel Science and Technology*, vol. 94, no. 2, pp. 486–492, 2020. doi:10.1007/s10971-020-05275-2

[9] A. Mahmoud Idris *et al.*, "A novel double perovskite oxide semiconductor SR₂Cowo₆ as bifunctional photocatalyst for photocatalytic oxygen and hydrogen evolution reactions from water under visible light irradiation," *Solar RRL*, vol. 5, no. 3, 2021. doi:10.1002/solr.202000702

[10] Z. Zou, "Photocatalytic water splitting into H2 and/or O2 under UV and visible light irradiation with a semiconductor photocatalyst," *International Journal of Hydrogen Energy*, vol. 28, no. 6, pp. 663–669, 2003. doi:10.1016/s0360-3199(02)00159-3

[11] C. Moure and O. Peña, "Recent advances in perovskites: Processing and properties," *Progress in Solid State Chemistry*, vol. 43, no. 4, pp. 123–148, 2015. doi:10.1016/j.progsolidstchem.2015.09.001

[12] S. K. Vatti, K. K. Ramaswamy, and V. Balasubramanaian, "Shape controlled palladium nano particles for hydrogenation of Cinnamaldehyde," *Journal of Advances in Nanomaterials*, vol. 2, no. 2, 2017. doi:10.22606/jan.2017.22006

[13] W. Zhang, J. Tang, and J. Ye, "Structural, photocatalytic, and photophysical properties of perovskite MSnO₃ (M = ca, sr, and BA) photocatalysts," *Journal of Materials Research*, vol. 22, no. 7, pp. 1859–1871, 2007. doi:10.1557/jmr.2007.0259

[14] L. I. Ibarra-Rodriguez, A. M. Huerta-Flores, J. M. Mora-Hernandez, and L. M. Torres-Martínez, "Photocatalytic evolution of H2 over visible-light active LaMO3 (M: Co, Mn, Fe) perovskite materials: Roles of oxygenated species in catalytic performance," *Journal of Physics and Chemistry of Solids*, vol. 136, p. 109189, 2020. doi:10.1016/j.jpcs.2019.109189

[15] R. Ianoş, R. Lazău, S. Borcănescu, and R. Băbuță, "Single-step combustion synthesis of laalo3 powders and their sintering behavior," *Ceramics International*, vol. 40, no. 5, pp. 7561–7565, 2014. doi:10.1016/j.ceramint.2013.12.107

[16] J. Chandradass, Y.-J. Cha, E. Yu, J. Kim, and K. H. Kim, "Stearic acid assisted synthesis of Laalo₃Nanopowder by sol–gel self propagation process," *Materials and Manufacturing Processes*, vol. 25, no. 7, pp. 679–683, 2010. doi:10.1080/10426914.2010.489789

[17] G. Lee *et al.*, "Effects of the preparation method on the crystallinity and catalytic activity of LaAlO3 perovskites for oxidative coupling of methane," *Applied Surface Science*, vol. 429, pp. 55–61, 2018. doi:10.1016/j.apsusc.2017.08.092

[18] Q. N. Tran *et al.*, "Transition metal B-site substitutions in LAALO3 perovskites reorient bio-ethanol conversion reactions," *Catalysts*, vol. 11, no. 3, p. 344, 2021. doi:10.3390/catal11030344

[19] O. A. Dicks, A. L. Shluger, P. V. Sushko, and P. B. Littlewood, "Spectroscopic properties of oxygen vacancies in," *Physical Review B*, vol. 93, no. 13, 2016. doi:10.1103/physrevb.93.134114

[20] S. Chettri *et al.*, "A systematic study of Laalo₃ with variation of ND doping, case of band Gap Tuning: A first principles method," *Modern Physics Letters B*, vol. 30, no. 04, p. 1650028, 2016. doi:10.1142/s0217984916500287

[21] A. A. Ansari *et al.*, "Catalytic performance of the CE-doped lacoo3 perovskite nanoparticles," *Scientific Reports*, vol. 10, no. 1, 2020. doi:10.1038/s41598-020-71869-z

[22] A. A. Ansari *et al.*, "Physico-chemical properties and catalytic activity of the sol-gel prepared CE-ion doped LaMnO3 Perovskites," *Scientific Reports*, vol. 9, no. 1, 2019. doi:10.1038/s41598-019-44118-1

[23] H. Khan and I. K. Swati, "Fe³⁺-doped anatase tio₂ with D–D transition, oxygen vacancies and Ti³⁺ centers: Synthesis, characterization, UV–vis photocatalytic and mechanistic studies," *Industrial & Engineering Chemistry Research*, vol. 55, no. 23, pp. 6619–6633, 2016. doi:10.1021/acs.iecr.6b01104

[24] U. Alam *et al.*, "Highly efficient Y and V co-doped zno photocatalyst with enhanced dye sensitized visible light photocatalytic activity," *Catalysis Today*, vol. 284, pp. 169–178, 2017. doi:10.1016/j.cattod.2016.11.037

[25] X. Zhang, Y. Chen, S. Zhang, and C. Qiu, "High photocatalytic performance of high concentration al-doped zno nanoparticles," *Separation and Purification Technology*, vol. 172, pp. 236–241, 2017. doi:10.1016/j.seppur.2016.08.016

[26] F. Huang, A. Yan, and H. Zhao, "Influences of doping on photocatalytic properties of tio2 photocatalyst," *Semiconductor Photocatalysis - Materials, Mechanisms and Applications*, 2016. doi:10.5772/63234

[27] Y. Guo, S. H. Park, B. C. Choi, J. H. Jeong, and J. H. Kim, "Effect of la3+ ion doping on the performance of eu2+ ions in novel Sr3CeNa(Po4)2SiO4 phosphors," *Journal of Alloys and Compounds*, vol. 724, pp. 763–773, 2017. doi:10.1016/j.jallcom.2017.07.114

[28] P. J. Dereń, M. A. Weglarowicz, P. Mazur, and W. Strek, "Spectroscopic properties of LaAlO3 nanocrystals doped with tb3+ ions," *Journal of Luminescence*, vol. 122–123, pp. 780–783, 2007. doi:10.1016/j.jlumin.2006.01.287

[29] K. Wang *et al.*, *Novel cu2+-fe3+ co-doped LAALO3 ceramic with High Infrared Radiation Performance for energy-saving application*, 2023. doi:10.2139/ssrn.4514280

[30] A. V. Egorova, K. G. Belova, I. E. Animitsa, Y. A. Morkhova, and A. A. Kabanov, "Effect of zinc doping on electrical properties of Laalo₃ Perovskite," *Chimica Techno Acta*, vol. 8, no. 1, 2021. doi:10.15826/chimtech.2020.8.1.03

ISSN: 0067-3064

[31] V. N. Stathopoulos *et al.*, "Evolution of bulk and surface structures in stoichiometric LAALO3 mixed oxide prepared by using starch as template," *Materials Chemistry and Physics*, vol. 207, pp. 423–434, 2018. doi:10.1016/j.matchemphys.2017.12.056

[32] I. S. Silveira, N. S. Ferreira, and D. N. Souza, "Structural, morphological and vibrational properties of laalo3 nanocrystals produced by four different methods," *Ceramics International*, vol. 47, no. 19, pp. 27748–27758, 2021. doi:10.1016/j.ceramint.2021.06.201

[33] J. Cheng *et al.*, "Perovskite la0.6sr0.4co0.2fe0.8o3 as an effective electrocatalyst for non-aqueous lithium air batteries," *Electrochimica Acta*, vol. 191, pp. 106–115, 2016. doi:10.1016/j.electacta.2016.01.058

[34] K. Djebaili, Z. Mekhalif, A. Boumaza, and A. Djelloul, "XPS, FTIR, EDX, and XRD analysis of Al2O3Scales grown on PM2000 alloy," *Journal of Spectroscopy*, vol. 2015, pp. 1–16, 2015. doi:10.1155/2015/868109

[35] M. Ismael and M. Wark, "Perovskite-type lafeo3: Photoelectrochemical properties and photocatalytic degradation of organic pollutants under visible light irradiation," *Catalysts*, vol. 9, no. 4, p. 342, 2019. doi:10.3390/catal9040342

[36] M. Schindler, F. C. Hawthorne, M. S. Freund, and P. C. Burns, "XPS spectra of uranyl minerals and synthetic uranyl compounds. II: The O 1s spectrum," *Geochimica et Cosmochimica Acta*, vol. 73, no. 9, pp. 2488–2509, 2009. doi:10.1016/j.gca.2008.10.041

[37] X. Ma, D. Li, P. Su, Z. Jiang, and Z. Jin, "S-scheme W18O49/MN0.2Cd0.8s heterojunction for improved photocatalytic hydrogen evolution," ChemCatChem, vol. 13, no. 9, pp. 2179–2190, 2021. doi:10.1002/cctc.202002069

[38] J. Tang, J. R. Durrant, and D. R. Klug, "Mechanism of photocatalytic water splitting in tio₂. reaction of water with photoholes, importance of charge carrier dynamics, and evidence for four-hole chemistry," *Journal of the American Chemical Society*, vol. 130, no. 42, pp. 13885–13891, 2008. doi:10.1021/ja8034637

[39] T. Puangpetch, T. Sreethawong, and S. Chavadej, "Hydrogen production over metal-loaded mesoporous-assembled srtio3 nanocrystal photocatalysts: Effects of metal type and loading," *International Journal of Hydrogen Energy*, vol. 35, no. 13, pp. 6531–6540, 2010. doi:10.1016/j.ijhydene.2010.04.015

[40] A. Olivo *et al.*, "Flexible solutions for lab-based phase contrast and dark field CT and micro-CT," *e-Journal of Nondestructive Testing*, vol. 24, no. 3, 2019. doi:10.58286/23652

ISSN: 0067-3064

Electron Transport Analysis For GaSb MOSFET n+nn+ Channel

Y.LAIDOUNI [a*], C. SAYAH [a]
B. BOUAZZA[b], S. FEROUANI [c]

[a]Smart Structures Laboratory (SSL),
Department of Electronic and Telecommunications
University Belhadj BOUCHAIB of Ain Témouchent.
Po Box 284, 46000, Algeria.
Authors[a] E-mail: *yousfia.laidouni@univ-temouchent.edu.dz*
chou28dz@gmail.com

Abstract: Velocity is a crucial factor in defining the electrical properties and performance of MOSFETs. The shrinking of transistor size from submicron to nanometer domain makes the calculation and measurement of this physical quantity increasingly problematic. Through this study, we try to determine how the velocity evolves with temperature. We conducted electron transport calculations on a 45-110-45 nm MOSFET n+nn+ GaSb channel structure using a three-valley model. Our analysis employed a bipolar Monte Carlo simulator coupled with the Poisson solver, including polar, non-polar optical phonon, and acoustic deformation potential. We present carrier transport phenomena for a two-dimensional submicronic structure and discuss the effect of temperature on the dispersion rate for strong values ranging from 77 K to 600 K. Our results showed that increasing temperature leads to a higher dispersion rate, causing a decrease in carrier velocity and the maximum drift velocity is reduced.

Keywords: Ensemble Monte Carlo, III-V compounds, Poisson equation, particle dynamics.

1. Introduction:

The fields of electronics and optoelectronics have greatly benefited from the use of new materials in semiconductor manufacturing. Solid-state physics has allowed for the prediction of the behavior of these materials, resulting in more efficient devices. Extensive research has led to the discovery of a new class of semiconductor materials, known as III-V compounds, in the late 1950s [4]. These materials possess unique qualities that make them essential in optoelectronics, with a wide range of applications. Among this array of materials, GaSb emerges as a notably auspicious candidate for channel material in the domain of field-effect transistors (FETs), marking a significant stride in the post-silicon era [1]. To improve the design of GaSb-based devices, it is essential to understand the electron transport that occurs within these materials. While electron transport in this bulk has already been studied [2], this article aims to provide devices that can serve in the microwave domain.

ISSN: 0067-3064

The n+–n–n+ diode is one of the simplest and most popular devices that represent highly favored components within submicron systems due to their uncomplicated fabrication techniques and minimal concerns related to dopant diffusion issues.

Our research delves into the intricacies of temperature dependencies on electron transport in an n+-n-n+ structure composed of GaSb. To achieve this, we employed an Ensemble Monte Carlo (EMC) technique, which operates in tandem with the Poisson equation.

2. Self-Consistent Monte-Carlo Model

The Monte Carlo method has found extensive application across diverse scientific domains, underscoring its robustness and reliability. Nevertheless, it is imperative to acknowledge that the efficacy of this method is contingent upon the inherent particle nature of electrons within submicron devices[3].

In our study, we explore the effects of temperature variation upon the electron transport within an n+-n-n+ structure comprised of GaSb. To achieve this investigation, we employed an Ensemble Monte Carlo (EMC) technique, operating in conjunction with the Poisson equation. The EMC method computes particle dynamics within brief time intervals, followed by the solution of the Poisson equation at the end of each interval to ascertain the potential distribution [4].
The Poisson equation is given by the following form:

$$\nabla^2 \varphi = \frac{\rho}{\varepsilon} \tag{1}$$

To ensure precision, a consistent time interval of approximately 0.3 femtoseconds was employed across all cases. Furthermore, our analysis accounted for electron scatterings induced by polar optical, non-polar optical and acoustic deformation phonons. The foundation of our EMC approach relied on the band and material parameters of a spherically symmetric no-parabolic conduction band extracted from the reference [5] .

The approach comprises generating random free-flight times for individual particles by specifying the type of diffusion occurring at the end of each flight, adjusting the particle's energy and momentum post-diffusion, and subsequently iterating the process for the next free flight. Observing particle movements at various points in the simulation allows for statistical estimation of essential physical parameters. Examples include the average drift velocity under an applied electric field and the average energy of particles, providing valuable insights into the system's behavior [6].

During its free flight, the particle traverses both real space and wave vector space, influenced by a constant electric field E that alters its wave vector. If k and r represent its initial wave vector and initial position vector, in the presence of a constant external electric field, the

ISSN: 0067-3064

particle transitions from the initial state (k, r) at a time t to a final state (k′, r′) at time $t'=t+\Delta t$. This transition leads to the form:

$$k'(t+\Delta t) = k(t) - \frac{eE}{\hbar}\Delta t \tag{2}$$

If we consider the evolution of the wave vector and the position vector of an electron treated in a semi-classical manner, without the influence of an external magnetic field, they can be described respectively by the following two equations:

$$\hbar \frac{\partial \vec{k}}{\partial t} = e\vec{E} \tag{3}$$

$$\frac{\partial \mathrm{r}}{\partial \mathrm{t}} = \frac{\hbar.\vec{\mathrm{k}}}{\mathrm{m}^*} \tag{4}$$

Where e, $\hbar$ and E are respectively: the elementary charge of the electron, reduced Planck constant and electric field.

The change in vector r over the same time interval Δt, considering the initial and final states, can be derived from equation (4) as follows:

$$r'(t+\Delta t) = r(t) + \frac{\hbar}{m^*}.\frac{k(t)+k'(t+\Delta t)}{2}.\Delta t \tag{5}$$

In typical Self-Consistent Monte Carlo simulations, the process unfolds through distinct stages, following the subsequent steps [7] :

- **Three-Valley Conduction Band Model:** A three-valley model for the conduction band is utilized as the basis.

- **Consideration of Scattering Mechanisms:** Various scattering mechanisms are considered, including ionized impurity, polar and non-polar optical phonon, and acoustic deformation potential.

- **Geometry and Discretization Setup:** The geometry and discretization scheme are defined. Parameters like plasma frequency and Debye length significantly influence the choice of time step and grid size.

- **Charge Assignment:** Each particle's charge is assigned to a specific mesh point. Since simulating all electrons in a real device is impractical, each particle represents a cloud of electrons

ISSN: 0067-3064

for estimating currents, charge, and field distributions. For other purposes, individual particles carry their elementary charge, and doping charge is incorporated into the mesh based on its distribution.

- **Potential Solution:** Poisson's equation is solved to determine the electrostatic potential at mesh points. In EMC simulations, a finite difference scheme is typically employed for this purpose.

- **Particle Flights:** Each particle, now considered as an individual electron, experiences the standard Monte Carlo sequence of scatterings and free flights. These events are governed by the local field derived from the solution of Poisson's equation. The Monte Carlo sequence is terminated at fixed intervals, with field adjustments made following specific steps outlined above.

- **Initial and Boundary Conditions:** Initial conditions, while not crucial, are set. The focus is on obtaining self-consistent steady-state results. Boundary conditions, especially in sub micrometer devices, are vital. Contact properties significantly influence the device's overall behavior, making precise boundary conditions essential for accurate simulations.

3. Simulated Device:

We employed a 2D self-consistent Monte Carlo transport model to simulate a one-dimensional n+-n-n+ device with a symmetric profile. The central region of the device has a width of 0.11 μm, maintaining a uniform hosting concentration of $4x10^{23}$ cm^{-3}. Both the emitter and collector regions feature symmetrical rectangular shapes, each measuring 45 nm in width, and possess uniform doping with a specific concentration of 2×10^{21} cm^{-3}.
In order to maintain charge neutrality and thermal equilibrium at the contact interfaces, ideal Ohmic contacts were considered throughout the implementation process.

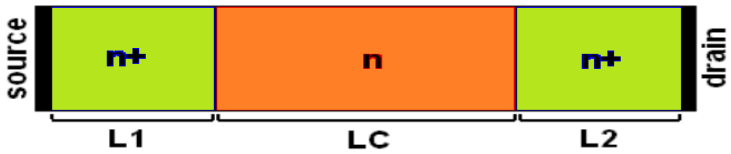

Figure 1: The device architecture employed in the simulation.

4. Results and Discussion:

ISSN: 0067-3064

In In Figure 2, we scrutinize the average energy of electrons throughout the device under varying bias voltages (0.5V, 1 V, and 1.5V) at a temperature of 77 K. As the bias voltage increases, the electron energy elevates correspondingly. However, a noteworthy observation is the shifting position of this energy peak within the active region, which moves towards the cathode. This displacement is attributable to multiple factors, including the amplification of back-scattering effects. Additionally, a greater number of electrons near the anode in the active region acquire sufficient energy to transition to the L valley, further contributing to this observed phenomenon[8].

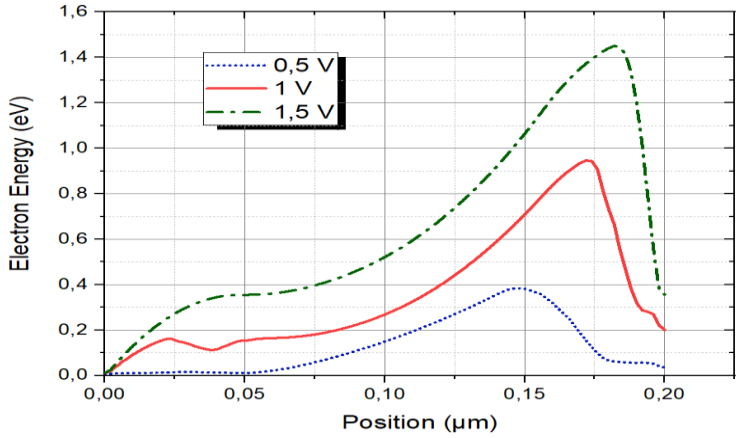

Figure 2: Electron energy distribution across the device for various anode voltages V_A=0,5 V, 1 V and 1,5 V, at 77 K

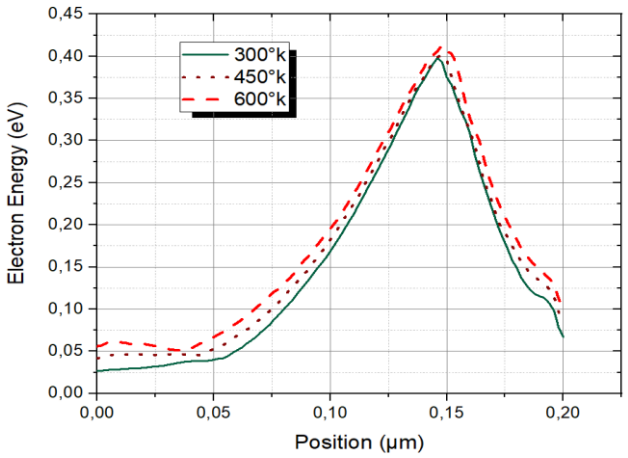

Figure 3: Electron energy distribution across the device for an applied voltage of 0.5 V and various lattice temperature

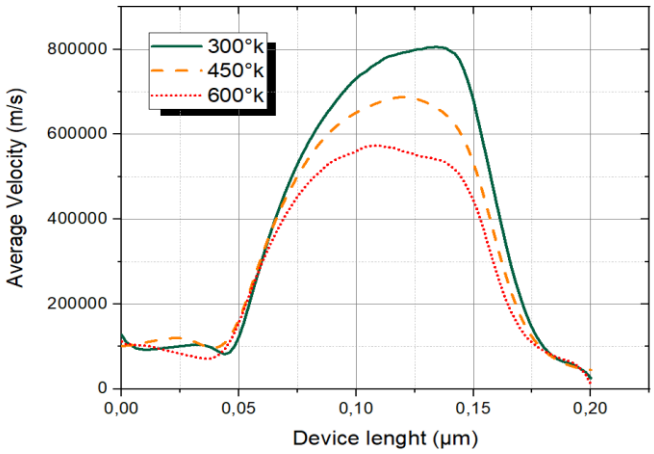

Figure 4: Average Velocity across the device for bias voltage of 0.5 V and various lattice temperature

Figures 3, and reveals a noteworthy accumulation of electrons proximal to the anode within the active region. Importantly, this phenomenon is not a consequence of internal scattering within the active

ISSN: 0067-3064

layer; rather, it results from the back-scattering of electrons originating from the anode n+-layer. This back-scattering is observed when electrons, moving almost ballistically through the active layer, acquire energies substantial enough to penetrate the L-valleys in the n+ anode layer. Within these L-valleys, electrons undergo isotropic scattering with notable probabilities before being redirected to the Γ valley. It is crucial to emphasize that the maximum drift velocity attained within the active layer greatly exceeds the stationary-state bulk velocity for various anode voltages, as evidenced in Figure 4. Consequently, ballistic transport emerges as a fundamental determinant in the behavior of the investigated device [9] [10].

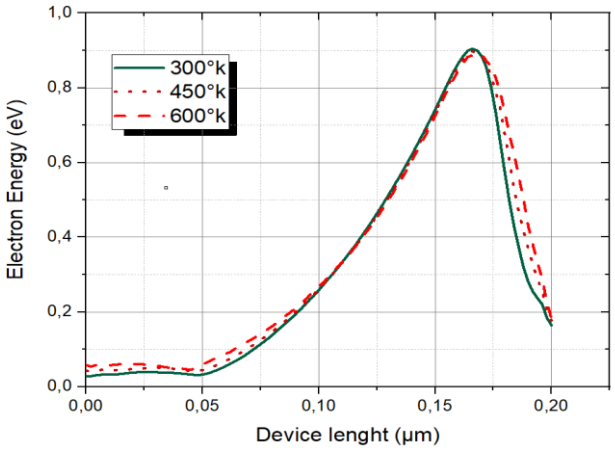

Figure 4: Electron energy distribution across the device for an applied voltage of 1 V and various lattice temperature

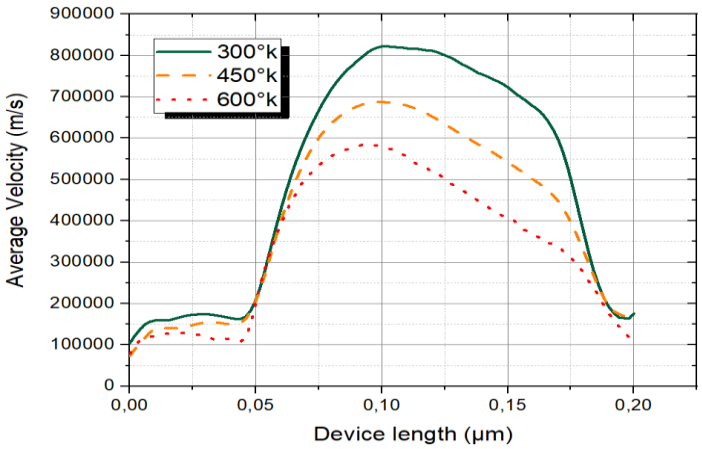

Figure 5: Average Velocity across the device for a bias voltage of 1 V and various lattice temperature

The increase in the temperature range from 300 K to 600 K results in a slight reduction in the average electron velocity of the simulated device. This phenomenon arises from heightened phonon scattering, impeding carrier heating by the electric field. It is noteworthy, however, that this effect remains relatively minor, especially when contrasted with the substantial temperature increase. Figures 3 and 4 illustrate that the device maintains stability in electron energy even at elevated temperatures, yet it continues to garner increasing interest within industrial applications.

5. Conclusion:

Our study was focused on the energy of electrons and their velocity as the bias voltage increases and the lattice temperature becomes progressively higher.

Our results reveal a pronounced electron accumulation near the anode within the active region. Elevating the network temperature to 600 K leads to a reduction in the maximum drift velocity.

Electrons injected from the cathode initially undergo quasi-ballistic travel, but a significant transfer to the upper satellite valleys occurs as the anode is approached, leading to a reduced average electron velocity in that region.

ISSN: 0067-3064

At low temperatures and high bias voltages, backscattering effects become prominent. Consequently, under such conditions, electrons accumulate near the anode within the active region. Elevating the lattice temperature to 600 K results in a reduction of the peak drift velocity, indicating that increasing the network temperature leads to a decrease in average velocity.

Elevating the temperature range from 300 K to 600 K under high bias voltage leads to a noticeable reduction in the electron transport properties of the simulated diodes. This phenomenon arises due to intensified phonon scattering, impeding carrier heating by the electric field. It is noteworthy, however, that this effect remains relatively minor, particularly when compared to the substantial temperature increase.

References

[1] P. Wang, S. Han, et R. Quhe, « Quantum transport simulation of the two-dimensional GaSb transistors », *J. Semicond.*, vol. 42, nº 12, p. 122001, déc. 2021, doi: 10.1088/1674-4926/42/12/122001.
[2] Y. Belhadji et B. Bouazza, « Steady State and Transient Study of The Electron Transport In N-Type GaSb Using Three Valley Monte Carlo Model », vol. 9, nº 1, 2012.
[3] J. M. Sellier, J. E. Fonseca, et G. Klimeck, « Archimedes, the free Monte Carlo simulator: A GNU package for submicron semiconductor devices on nanoHUB », in *2012 15th International Workshop on Computational Electronics*, Madison, WI, USA: IEEE, mai 2012, p. 1-4. doi: 10.1109/IWCE.2012.6242861.
[4] « Thése de doctorat_SAYAH.pdf ».
[5] A. Guen-Bouazza, C. Sayah, B. Bouazza, et N. E. Chabane-Sari, « Comparison of electron transport properties in submicrometer InAs, InP and GaAs n+-n-n+ diode using ensemble Monte Carlo simulation », 2014.
[6] A. Guen-Bouazza, C. Sayah, B. Bouazza, et N. E. Chabane-Sari, « Steady-State and Transient Electron Transport within Bulk InAs, InP and GaAs: An Updated Semiclassical Three-Valley Monte Carlo Simulation Analysis », *JMP*, vol. 04, nº 05, p. 616-621, 2013, doi: 10.4236/jmp.2013.45089.
[7] C. Sayah, B. Bouazza, A. Guen-Bouazza, et N. E. Chabane-Sari, « Simulation of Electron Transport in GaN Based MESFET Using Monte Carlo Method », *World Applied Programming*.
[8] M. R. Khalvati, H. Arabshahi, M. Izadifard, A. M. Gerami, et H. Rahimpour, « Comparison of electron transport properties in submicrometer ZnS and ZnO n+nn+ diode using ensemble Monte Carlo simulation », *Int. J. Phys. Sci.*.
[9] M. Galler, *Multigroup equations for the description of the particle transport in semiconductors*, vol. 70. World Scientific, 2005. Consulté le: 1 novembre 2023. [En ligne].
[10] M. Galler et F. Schürrer, « A direct multigroup-WENO solver for the 2D non-stationary Boltzmann–Poisson system for GaAs devices: GaAs-MESFET », *Journal of Computational Physics*, vol. 212, nº 2, p. 778-797, 2006.

ISSN: 0067-3064

The influence of Boride and Nitride on Microstructure and Corrosion Behavior of 42CrMo4 Steel

Benhabib Bensalah[a,*], Oulad saad Sofiane[a], Allaoui Omar[a]

Laboratoire Génie des Procédés, Université de Laghouat, BP 37G, Laghouat, Algeria

Abstract: This paper presents a study on the corrosion behavior of boriding and nitriding treatments of the low-alloy steel 42CrMo4. The thermochemical treatments were carried out in a solid medium by the powder technique: at a temperature of 900 °C for 4 hours for boriding, and at a temperature of 550 °C for 12 hours for nitriding. The structures of surface layers and diffusion zones were examined by Optical X-ray Diffraction (XRD). Analyses of the surface revealed the presence of FeB and Fe_2B compounds for the boride layer, and CrN, Fe_3N and Fe_4N compounds for the nitride layer. The thickness of boride layer and nitride layer was found to be of 55 and 11 µm, respectively. The microhardness of the boride and nitride layers is between 800 $HV_{0.2}$ and 1200 $HV_{0.2}$. The corrosion was evaluated by electrochemical techniques. The potentiodynamic curves of corrosion tests immersed in a 1M HCL solution have shown the beneficial effect of boriding and nitriding treatments on the treated steel 42CrMo4. The samples acquired a high quality protection.

Keywords: boriding ,nitriding, corrosion, microhardness

1. Introduction

It is possible to modify the chemical composition of the surface of a metallic material by the diffusion of one or more elements in order to improve a certain number of functional properties such as fatigue, wear and tear resistances, or corrosion. This concerns the thermochemical treatment process by diffusion of metalloids and metals. Thermochemical surface treatments (cementation, nitriding, boriding) are carried out by introducing the elements C, N, B, by diffusion to modify the chemical composition and the microstructure of the surface. In general, these treatments are used to improve the mechanical and chemical performance of surfaces against wear, fatigue and corrosion.

Boriding is a thermochemical surface hardening process in which boron atoms, due to their relatively small size, diffuse easily into the surface of the workpiece. The

ISSN: 0067-3064

boron atoms react with the atoms of the base material by forming two types of borides: FeB and Fe_2B. The hardness of such a layer can reach values close to 2000 HV. Temperature process range between 973 to 1273 K for a period of time ranging from 1 to 10 h [1]. It can be applied to ferrous and nonferrous materials. After boriding, a coating with a ragged or flat interface is formed on the surface improving its hardness, wear and corrosion properties [2]. The boriding process can be performed in a solid medium with powders [3] or in molten salts with or without electrolysis [4], or in a gaseous medium [5]. Nitriding is a process for hardening the surface of steel objects by introducing nitrogen (N) into it at elevated temperatures, usually between 773 and 853 K [6]. The nitriding process begins at the surface of the part with the formation of a compound layer. The phases formed within this surface layer consist of the iron nitrides γ'-Fe_4N_{1-x} and ε-Fe_2N_{1-z}. This layer is responsible for improving the tribological properties and corrosion resistance [7-10]. The nitriding process can be performed in the following types: gas nitriding, ion (plasma) nitriding, solid nitriding and salt-bath nitriding [11-13].

In the present work, we study corrosion behaviors of nitrided and borided 42CrMo4 steel. The effect of boriding and nitriding on the microhardness and corrosion resistance of the treated steel was investigated using optical microscopy, microhardness tests and XRD. The corrosion resistance was evaluated and data were obtained through the linear polarization and the open circuit electrochemical techniques. The corrosion resistance of borided and nitrided samples was compared with untreated samples.

2. Experimental procedures

2.1 Characterization of Boriding and Nitriding

The low-alloy steel 42CrMo4 was used for the boriding and nitriding treatments. The chemical composition of this steel, determined by spectrometric analysis, is given in Table 1.

Table 1 - Chemical composition of the steel 42CrMo4 to be coated (%)

elements	C	Si	Mn	Cr	P	Mo
Weight%	0.449	0.32	0.80	1.006	0.026	0.195

The test specimens were cut into the cylinders with the dimensions of ø 20 mm ×10 mm. Samples surface preparation before testing generally involves silicon carbide paper up to grade 1000 to facilitate the azote and bore diffusion through the surface. This was realized on both stages: boriding and nitriding. The boriding of the steel 42CrMo4 was achieved in a solid medium using a powder with the following composition: 90% SiC as a diluen, 5% B_4C as boron source and 5% $NaBF_4$ as activator. The test samples were packed with the boriding medium and heated in an electrical resistance furnace at a temperature of 900 °C for 4 hours. The nitriding

ISSN: 0067-3064

process was realized in a powder consisting of Fe_4KCN as a nitrogen source, NH_4Cl as an activator and SiC as a diluent at a temperature of 550 °C during 12 h. After the treatments, the boride and the nitride steel parts were removed from the furnace then cooled in air.

The microstructures of polished and etched cross-sections of the specimens were observed under a LEICA DMLM optical microscope. The identification of nitrides and borides formed in the coating layer was performed by the X-ray diffraction using Cu Kα_radiation. The hardness of the nitride and the boride 42CrMo4 steel samples was measured using a microhardness tester, by a Mitutoyo MVK-H2 with a load of 200 g. Thickness values given in the results section are averages of at least 8 measurements.

2.2 Electrochemical Corrosion

The corrosion resistance testing of nitride and boride and untreated 42CrMo4 steel parts immersed in 1M of HCl with open circuit potential as a function of time, as well as polarization resistance experiments, were performed on a Radiometer model PGZ 301 potentiostat controlled by a PC and supported by Voltamaster 4.0 software for the experimental control and data acquisition. All experiments were performed at room temperature and open circuit potential in a classical three-electrode cell with a Platinum cylindrical rod as counter electrode and an Ag/AgCl mini-electrode as a reference electrode. The corrosion test was performed at a scanning rate of 1 mV/s. The samples were immersed in an electrolyte solution for approximately 30 min to stabilize the open circuit potential at room temperature.

3. Results and discussions

3.1 Characterization of Nitride and Boride Coatings

The cross-sectional views by optical micrographs of the nitrided steel 42CrMo4 at the temperature of 550 °C during 12 hours are given in Figure 1, which shows the structural zones obtained on typical morphology. The first layer observed in all cases is the white layer or compound layer. According to literature, it is mainly composed of iron nitrides ($Fe_{2-3}N$) and γ' nitrides (Fe_4N) [14,15]. This layer, estimated to be around 11 µm thick, is more or less homogeneous with uniform contrast. The second layer obtained by the diffusion of nitrogen below the compound layer is named the diffusion layer and it is made up of nitrogen solid solution in insertion and possibly of fine nitride precipitates or carbo nitrides. The present phases of nitrided layers were determined by X-ray diffraction (XRD) analysis. Figure 3 shows that the dominant phases formed in the coating layer are Fe_3N, Fe_4N and CrB. The present results are in accordance with the literature [16,17]. The cross-sectional views by optical micrographs of the low-alloy steel 42CrMo4 borided at a temperature of 900 °C during 4 hours are shown in Figure 2. The two boride layers FeB and Fe_2B

ISSN: 0067-3064

formed on the steel substrate have a saw-tooth morphology, which is in agreement with the works of other researchers [18,19]. Optical cross-sectional examination of the borided steel surfaces revealed a morphology with a depth that reaches 55 μm. The present phases of borided layers were determined by X-ray diffraction (XRD) analysis. Figure 4 shows that the dominant phases formed in the coating layer are FeB and Fe_2B. The present results are in good accordance with the literature [20,21].

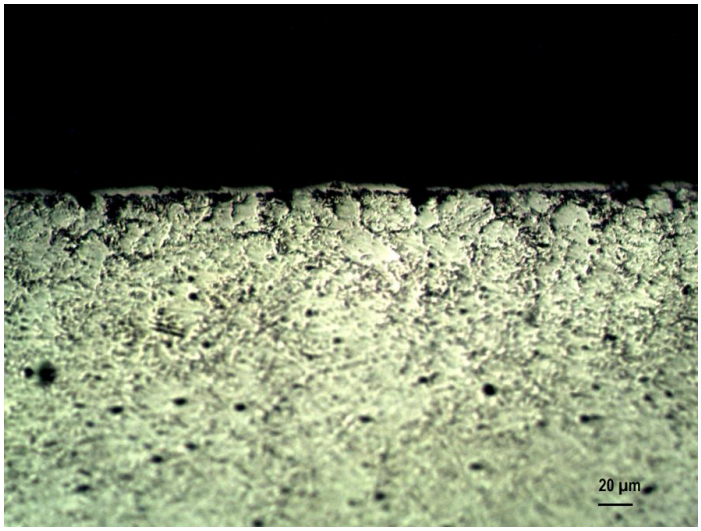

Fig. 1 – Microstructure after nitriding in (550 °C, 12 hours): steel 42CrMo4

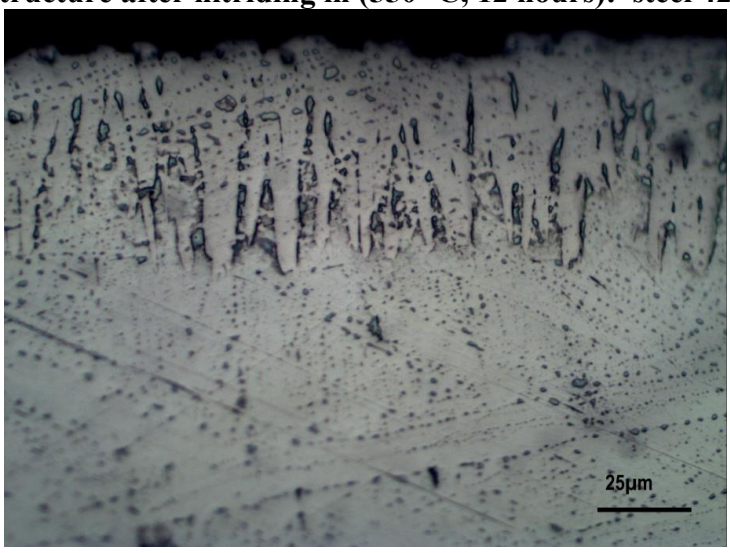

Fig. 2 – Microstructure after boriding in (900 °C, 4 hours): steel 42CrMo4

3.2 XRD Analysis

Figure 3 shows the X-ray diffraction spectra of 42CrMo4 steel, nitrided at a temperature of 550 °C for 12 hours. In this figure, the peaks of Fe_3N, Fe_4N, and CrN appear and the surface indicates a compound layer of phase ε, phase γ', and chromium nitride. Fig.4 shows the X-ray diffraction analysis pattern in solid, borided at the temperature 900 °C for 4 hours. The different boride layer phases obtained on the specimen surface after boriding consist mainly of Fe_2B and FeB. The boride

ISSN: 0067-3064

layers essentially consist of intermetallic phases as a result of the diffusion of boron atoms from the boriding compound to the metallic lattice [22].

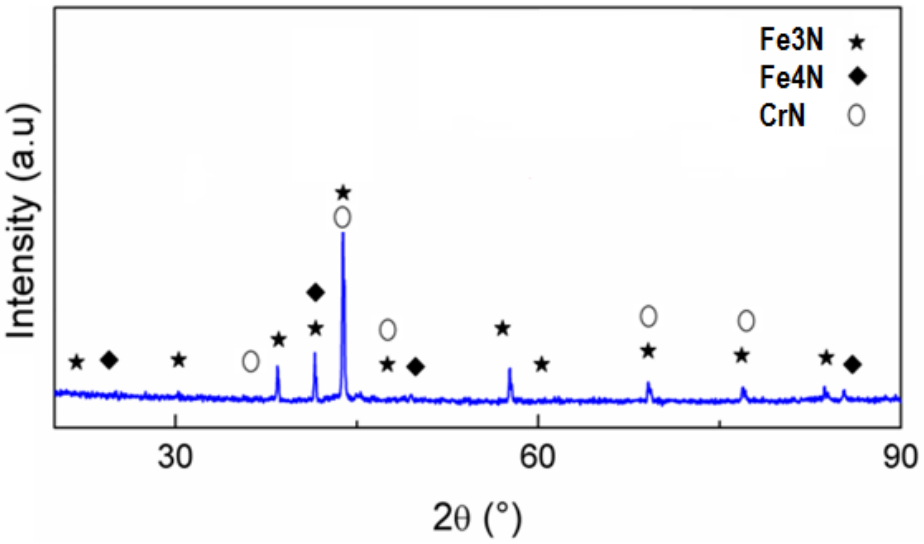

Fig. 3 – X-ray diffraction patterns of borided steel: 42CrMo4

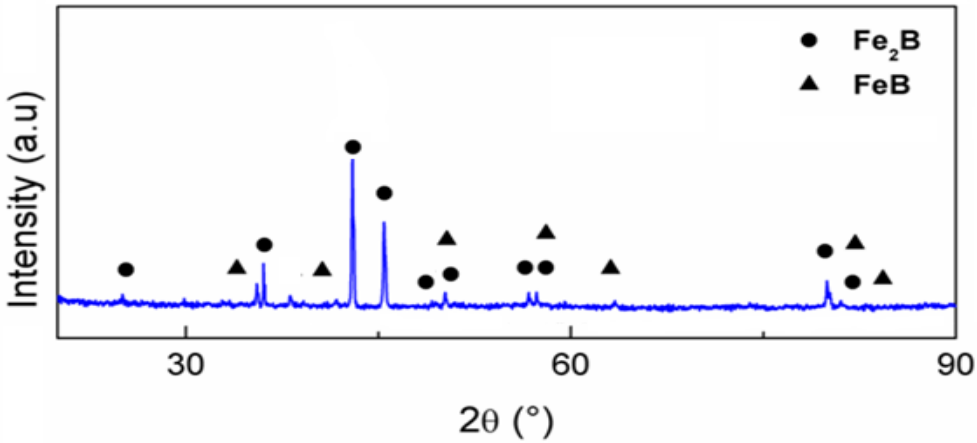

Fig. 4 – X-ray diffraction patterns of borided steel: 42CrMo4

3.3 Microhardness Profile

Figure. 5 shows the microhardness measurements that were carried out on cross-sections from the surface to the interior along a line of specimens of the steel 42CrMo4 with different treatments: borided at a temperature of 900 °C for 4 hours and nitrided at a temperature of 550 °C for 12 hours. The microhardness of the boride layers and nitride layers was measured at 8 different locations at the same distance from the surface and the average value was taken as the hardness. The microhardness of the borided specimen is around 1200 $HV_{0.2}$ in the boride layer zone, while that of the substrate is around 300 $HV_{0.2}$. The nitrided steel shows a hardness of 800 $HV_{0.2}$. It is clear that the cross-section microhardness can be significantly increased by boriding and nitriding. The specimen treated by boriding

ISSN: 0067-3064

has a higher cross-section microhardness than that treated by nitriding. The boride layer hardness is approximately four times greater than that of the substrate.

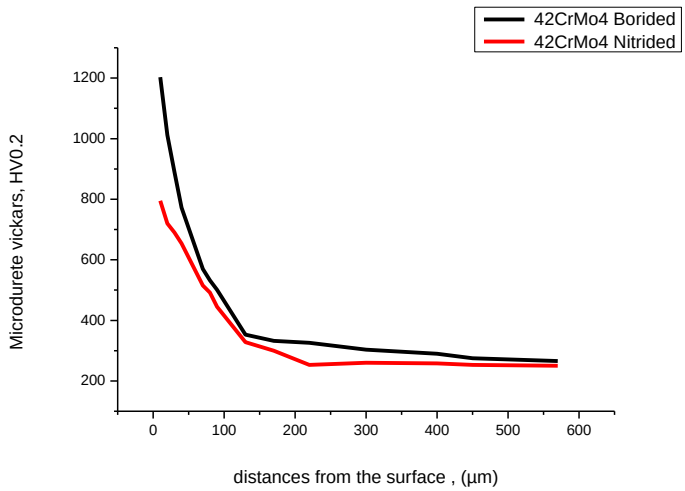

Fig. 5– The variation of hardness depth in the borided and nitrided steel: 42CrMo4

3.4 Corrosion Test Results

Electrochemical parameters from polarization curves of samples treated with boriding and nitriding and tested in 1M HCl solution are obtained in Table 2.
Potentiodynamic polarization curves of samples tested in 1M HCl solution and treated with boriding at the temperature 900 °C for 4 hours and nitriding at the temperature 550 °C for 12 hours are shown in Figure 6.The higher value of corrosion potential (Ecorr) is observed for borided layer compared with nitrided layer. The more corrosion potential is on the positive side; the more steel is considered corrosion resistant, and in comparison with the untreated steel It can be seen in this figure that all the borided and nitrided samples have more positive corrosion potential than the untreated substrate. The best corrosion resistance is obtained by the boriding sample, as it showed more positive potential at lower current (Figure 6 and Table 2). This indicates that the treated samples are less susceptive than the untreated samples, thus they show a better corrosion resistance.This means that the boriding treatement can act as a protective barrier for the steel in corrosion middle . This result is similar to that reported in the literature [23,24].

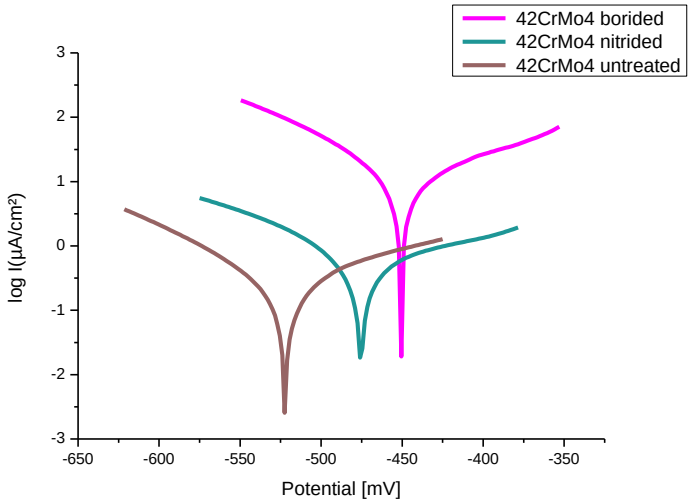

Fig. 6– The Tafel curves for the untreated, borided, and nitrided steel in 1M HCl solution.

Table 2 - Corrosion data as determined by Tafel extrapolation method for untreated, nitrided and borided steel in 1M HCl solutions.

Treatments	42CrMo4 Borided	42CrMo4 Nitrided	42CrMo4 unteated
E_{crro}	- 450.5 mv	- 475.4 mv	- 522.2 mv
I_{corr}	10.49 µA/cm^2	51.49 µA/cm^2	182.5 µA/cm^2
Corrosion Rate	0.122 mm /y	0.60 mm/y	2.134 mm/y

4. Conclusion

The following conclusions may be derived from the present study:

- Thermochemical boriding and nitriding treatments on 42CrMo4 steel lead to the formation of boride (Fe_2B and FeB) and nitride (Fe_3N, Fe_4N and CrN) layers. This result was confirmed by XRD analysis.
- The Microhardness tests indicate that boriding and nitriding treatments lead to an increase of the surface hardness compared with that of the matrix.
- The borided steel shows a higher corrosion resistance than the nitrided and untreated steels.
- Corrosion tests have shown the beneficial effect of boriding and nitriding treatments on steel.

References

[1] S. Sen, I. Ozbek, U. Sen, C. Bindal. Surf. Coat. Technol. 135 (2001) 173–177.

[2] M. KULKA, N. MAKUCH, P. DZIARSKI,et al., Gradient boride layers formed by diffusion carburising and laser boriding. Optics and Lasers in Engineering. 67(2015) 163–175 .

[3] M. Keddam, S.M. A diffusion model for describing the bilayer growth (FeB/Fe2B) during the iron powder-pack boriding. Applied Surface Science. 252(2)(2005) 393–399. doi:10.1016/j.apsusc.2005.01.016

[4] O. Allaoui, N. Bouaouadja, G. Saindernan, Characterization of boronized layers on a XC38 steel. Surface and Coatings Technology. 201(6) (2006) 3475–3482. doi:10.1016/j.surfcoat.2006.07.238

[5] M.Kulka, N.Makuch, M.Popławski, Two-stage gas boriding of Nisil inN2–H2–BCl3 atmosphere. Surf. Coat. Technol. 244 (2014) 78–86. doi: 10.1016/j.surfcoat.2014.01.057

[6] M. Keddam, M. E. Djeghlal, L. Barrallier, A diffusion model for simulation of bilayer growth (ε/γ′) of nitrided pure iron. Materials Science and Engineering: A. 378(1-2) (2004) 475–478. doi:10.1016/j.msea.2003.11.066

[7] V.G. Gavriljuk, H. Berns, High Nitrogen Steels: Structure, Properties, Manufacture, Applications. Springer-Verlag: Berlin/Heidelberg, Germany. 1999.

[8] D. DOBROCKY, D. KUSMIC ,The effect of plasma nitriding process on the change of dynamic param-eters of steeel DIN 1654/4. In: Manufacturing technology. 15 (3) (2015) 14-20. ISSN 1213-2489.

[9] U. Kamachi Mudali, H. S. Khatak, B. Raj, M. Uhlemann, Surface Alloying of Nitrogen to Improve Corrosion Resistance of Steels and Stainless Steels. Materials and Manufacturing Processes. 19(1) (2004) 61–73. doi:10.1081/amp-120027501

[10] G. Stein, I. Hucklenbroich, H. Feichtinger, Current and future applications of high nitrogen steels. Materials Science Forum. 318–320(1999) 151–160. doi.org/10.4028/www.scientific.net/MSF.318-320.151

[11] J.Yang, Y. Liu, Z. Ye, D. Yang, S. He, Microstructural and tribological characterization of plasma- and gas-nitrided 2Cr13 steel in vacuum. Materials &Design.32(2)(2011) 808–814. doi:10.1016/j.matdes.2010.07.022

[12] I. GUNES, S. TAKTAK, Surface characterization of pack and plasma paste boronized of 21NiCrMo2 steel. Journal of the Faculty of Engineering and Architecture of Gazi University. 27(2012) 99-108.

[13] C. BINDAL, A.H. UCISIK, Characterization of borides formed on impurity-controlled chromium-based low alloy steels. Surface and Coatings Technology. 122(1999) 208-213.

[14] S. Ahangarani, F. Mahboubi, A. R. Sabour, Effects of various nitriding parameters on active screen plasma nitriding behavior of a low-alloy steel. Vacuum, 80(9)(2006) 1032–1037. doi:10.1016/j.vacuum.2006.01.013

[15] A. Şelte, B. Özkal, K. Arslan, S. Ülker, A. Hatman, Effect of Nitriding on the Wear Resistance of Tool Powder Steels with Different Contents of V, Cr and Mo. Metal Science and Heat Treatment. 59(11-12) (2018) 729–734. doi:10.1007/s11041-018-0218-1

ISSN: 0067-3064

[16] M. A. Terres, S. B. Mohamed, H. Sidhom, Influence of ion nitriding on fatigue strength of low-alloy (42CrMo4) steel. Experimental characterization and predictive approach. International Journal of Fatigue. 32(11) (2010) 1795–1804. doi:10.1016/j.ijfatigue.2010.04.004

[17] K. Sakoshi, C. Kagaya, E. Kagaya, Development of Solid Nitriding Method Using Thermosetting Waste Plastic. Solid State Phenomena. 118(2006) 121–130. doi:10.4028/www.scientific.net/ssp.118.121.

[18] M. Erdogan, I. Gunes, Corrosion Behavior and Microstructure of Borided Tool Steel. Matéria (Rio de Janeiro). 20(2) (2015) 523–529. doi:10.1590/s1517-707620150002.0052.

[19] S. Taktak, Some mechanical properties of borided AISI H13 and 304 steels. Materials & Design. 28(6) (2007) 1836–1843. doi:10.1016/j.matdes.2006.04.017

[20] O. Azouani, M. Keddam, A. Brahimi, A. Sehisseh, Diffusion kinetics of boron in the X200CrMoV12 high-alloy steel. Journal of Mining and Metallurgy, Section B: Metallurgy, 51(1) (2015) 49–54. doi:10.2298/jmmb140404009a.

[21] A. Günen, B. Kurt, N. Orhan, E. Kanca, The investigation of corrosion behavior of borided AISI 304 austenitic stainless steel with nanoboron powder. Protection of Metals and Physical Chemistry of Surfaces, 50(1) (2014) 104–110. doi:10.1134/s2070205114010195.

[22] Y. Ergun, I. Gunes, M. Erdogan, N. Cankaya, Effect of Boriding Treatment on the Corrosion Behavior of Steels. Journal of Nanoscience and Nanotechnology, 17(12) (2017) 8946–8951. doi:10.1166/jnn.2017.14251

[23] A. Kaouka, H. Allaf , M. Keddamb , O. Alaouia , Evaluating the Corrosion Behaviour of Borided Carbon Steel C35. Materials Research, (2022) https://doi.org/10.1590/1980-5373-mr-2020-0591

[24] Ergun, Y., Gunes, I., Erdogan, M., & Cankaya, N. (2017). Effect of Boriding Treatment on the Corrosion Behavior of Steels. Journal of Nanoscience and Nanotechnology, 17(12), 8946–8951. doi:10.1166/jnn.2017.14251

ISSN: 0067-3064

New piezoresistive flow sensor design and fabrication based on PDMS and Conductive-PDMS Using soft-lithography

Abdelkader Hassein-Bey[(1)], Nadir Belgroune[(1)], Asma Leila Hassein-Bey[(1)], Burhanuddin Yeop Majlis[(2)] and Rafik Serhane[(3)]

[(1)] Physical Chemical Laboratory of Inorganics Materials and their Applications (LPCMIA), University of Blida1 Blida 09000, Algeria.

[(2)] Institute of Microengineering and Nanoelectronics (IMEN) Universiti Kebangsaan Malaysia UKM Bangi, Selangor, Malaysia.

[(3)] Centre for Development of Advanced Technologies. 20 Août 1956 City, Baba Hassen, P.O. Box 17, DZ-16303 Algiers, Algeria

Abstract: In this paper, we present the design and fabrication of a piezoresistive flow sensor utilizing PDMS and CPDMS materials. The sensor's working principle is based on the deflection of a CPDMS microbridge due to fluid motion within a PDMS microchannel. Finite Element Method (FEM) simulations, as previously reported, were conducted to optimize the sensor design using Comsol Multiphysics software [7]. We showcase the fabrication of the flow sensor using the soft lithography technique and present the results of experimental performance testing. This flow sensor was swiftly prototyped at a low cost. The measured sensitivity of 0.361% ml^{-1}.min aligns with the predicted value of 0.234% ml^{-1}.min obtained from simulations. Furthermore, the sensor can effectively measure the flow rate of biological fluids with a wide range of properties. Consequently, the sensor's electrical response open a new horizon for various applications in microfluidic systems and BioMEMS.

1. Introduction

Over the last two decades, microfluidic has become a major vector of the development for several applications [1–2]. The growing interest for this technology can be explained by the wide variety of microfluidic devices based on labs-on-chip (LOC) and micro Total Analysis Systems (µTAS) applications

ISSN: 0067-3064

[3–4]. Thus, they can contain elements for fluid control, trapping, separation of biological cells and data acquisition to accomplish many tasks (transporting, manipulating and analyzing small samples of the fluid).

In practical, the amount of fluid handled should be controlled accurately using a flow rate sensor. Various designs of flow sensors are proposed in the literature according to the sensing principle, e.g. thermal phenomena [5], pressure phenomena [6], mechanical bending measured by optical microscopy [7], laser interferometry [8] or piezoresistivity in a specific case of airflow [9].

The material generally used to fabricate this kind of microfluidic systems is PolyDiMethylSiloxane (PDMS) [4, 10]. PDMS has acquired new and interesting electric properties that transform it from an insulating polymer to a conductive one by adding conducting particles such as carbon black (CB) nanoparticles, carbon nanotubes (CNT), silver and nickel particles [11–12]. Additionally, the conductive PolyDiMethylSiloxane (CPDMS) is piezoresistive [9, 13]. A common approach to fabricate devices based on PDMS is the use of thin multilayer soft lithography process. It consists of pouring a liquid PDMS on a rigid SU-8 mold fabricated using a conventional photolithography. This low-cost process requires less than 24 hours of time fabrication [14].

In this work, we present a design and a fabrication of a piezoresistive flow sensor based on PDMS and CPDMS materials. A multi-layer fabrication method, based on the common microfluidic network fabrication technique so called soft-lithography technique, is used for the flow sensor fabrication. Thus, the proposed sensor structure consists of three PDMS layers forming the CPDMS microbridge integrated within a microchannel.

In order to optimize the design and dimensions of the sensor, finite element method (FEM) simulations, previously discussed [15], were carried out using Comsol Multiphysics software (version 4.3a). The simulation results give more efficiency to the design of the sensor by verifying the fluid structure interaction between the microbridge and the fluid flow in the microchannel [15–16]. A complete and functional sensor was fabricated and tested by introducing various flow rates into the microchannel and measuring the corresponding changes in the electrical resistance of the CPDMS microbridge. The experimental measurements and simulation results were finally compared to estimate the range of model validity and the sensor actual behavior.

2. Design and simulations

2.1. Description of the working principle: The proposed fluid flow sensor consists of a piezoresistive microbridge made of CPDMS integrated within a PDMS microchannel as reported in [15]. Basic elements and operating principle of this flow sensor are shown in figure 1. The fluid is introduced to the microchannel

through the inlet and exited through the outlet. The sensing element is a CPDMS microbridge obstacle suspended at the middle of the microchannel. The fluid flow motion in microchannel causes a mechanical deflection of the piezoresistive microbridge. The transduction mechanism based on the piezoresistivity property of CPDMS composite converts the mechanical deflection of microbridge to an electrical resistance variation [9, 11–13].

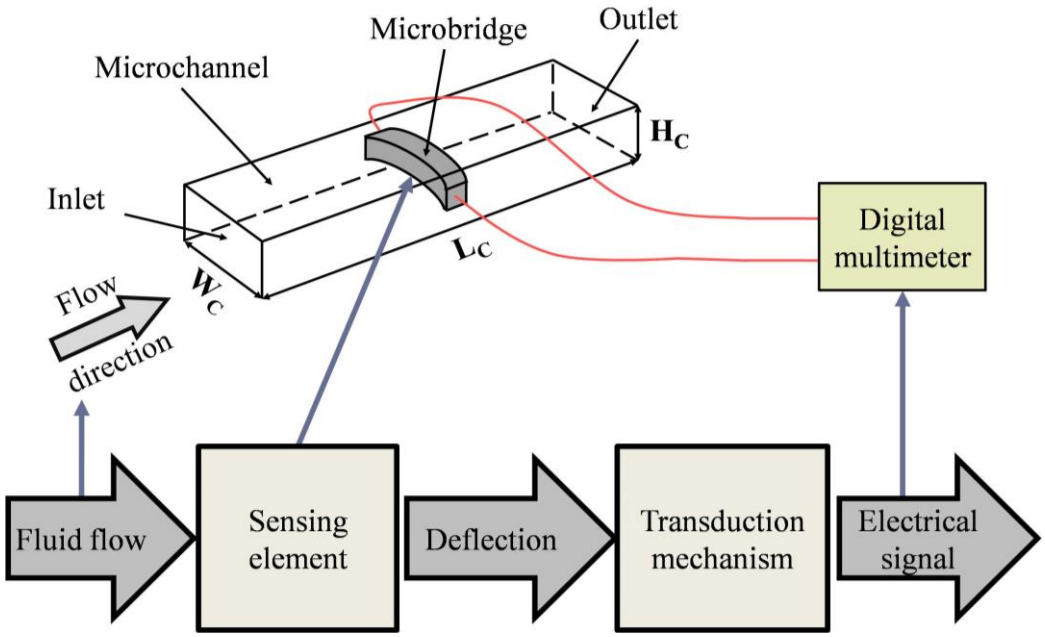

Figure 1: *Diagram of the basic elements and the operating principle.*

2.2. Sensor design: The 3D schematic of the fluid flow sensor design is depicted in figure 2. The proposed sensor structure consists of three PDMS layers forming the microbridge integrated within a microchannel, as discussed in the previous report [15]. The geometry includes the fluid inlet and outlet with rectangular microchannel section W_c x H_c (Figure 1) and a squared section H_b x W_b CPDMS microbridge. With respect to our deliberate design choice, we preferred to fabricate the flow sensor using the soft-lithography technique with multi-layers approach. The upper and the middle layers are patterned with two circular punch holes connections. The intermediate layer is patterned with the flow microchannel structure supporting the embedded Conductive-PDMS microbridge. The PDMS lower layer is acting as a platform. The square section microbridge obstacle is suspended in the channel half-height. The electrical connection of the sensor device is realized through a copper wire. Note that when we simulate the sensor behavior, we follow approaches and fluid-materials properties presented in previous simulations [15]. Table 1 summarizes all these simulations parameters and the fluid flow conditions.

ISSN: 0067-3064

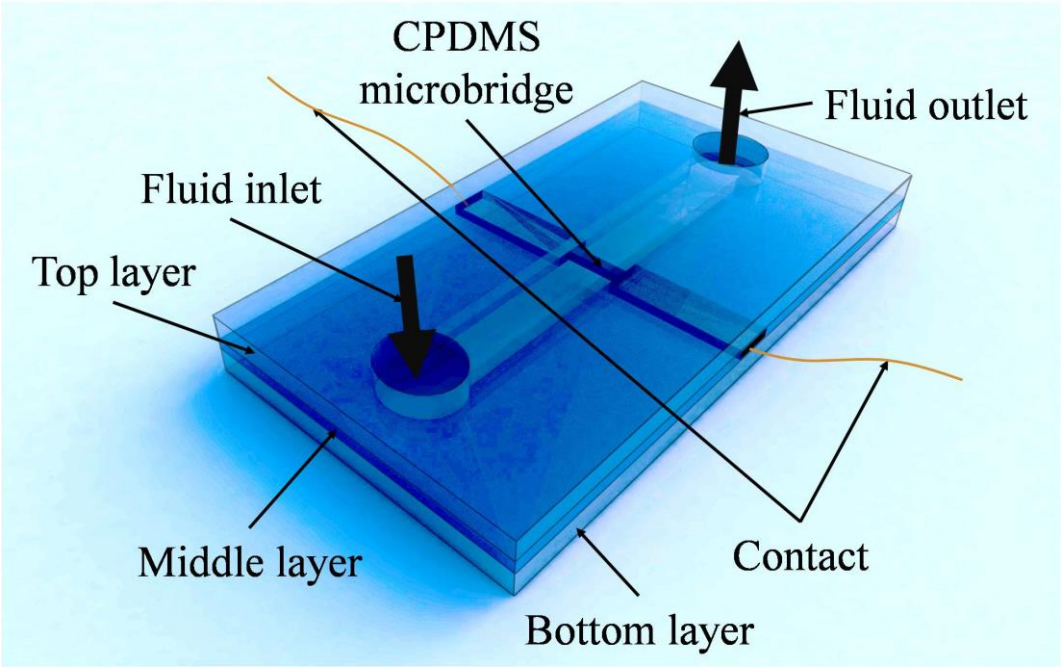

Figure 2: *3D schematic design of the proposed flow sensor*

Table 1 Parameters list used in simulations

Parameters		Value
Density of water	P	1000kg/m3
Dynamic viscosity of water	H	0.001Pa.s
Fluid inlet velocity	U	0.0484m/s
Weight ratio of CB-PDMS	wt.%	16wt.%
Density of CB-PDMS	$\rho_{CB\text{-}PDMS}$	970kg/m^3
Young modulus of CB-PDMS	$E_{CB\text{-}PDMS}$	2.45MPa
Poisson ratio of CB-PDMS	$\nu_{CB\text{-}PDMS}$	0.45
Initial electric resistivity	$\rho(0)_{CB\text{-}PDMS}$	1.6Ω.m

2.3. Simulation results: Three-dimensional simulations were performed to verify the sensor design using finite element method (FEM) implemented in Comsol Multiphysics software (Figure 3*a*). Various fluid flow rates were computed to predict the microbridge mechanical deflection and the piezoresistive response (Figure 3*b*). In figure 3*b*, the zero-flow electrical resistance of the microbridge is R_0=35.45kΩ. The relative change in electric resistance $\Delta R/R_0$ evolves from 0.027% @ 0.2ml.min^{-1} to 0.122% @ 1.0ml.min^{-1} for microbridge made of CB-PDMS composite.

From our previous analysis [15], two geometric parameters strongly influence the sensor behavior: the microbridge thickness and the microchannel height. Several simulations were carried out to optimize the values of these two key design parameters. Simulation results give more efficiency to the sensor design by verifying the fluid structure interaction between the microbridge and the fluid flow in the microchannel. Indeed, to avoid the strangling effect, the design must take into account two key-parameters: the microchannel height and the adapted microbridge dimensions [15]. Our design allows the microbridge sensing element to transduce any mechanical stress to an electrical signal owing to the CPDMS piezoresistive property.

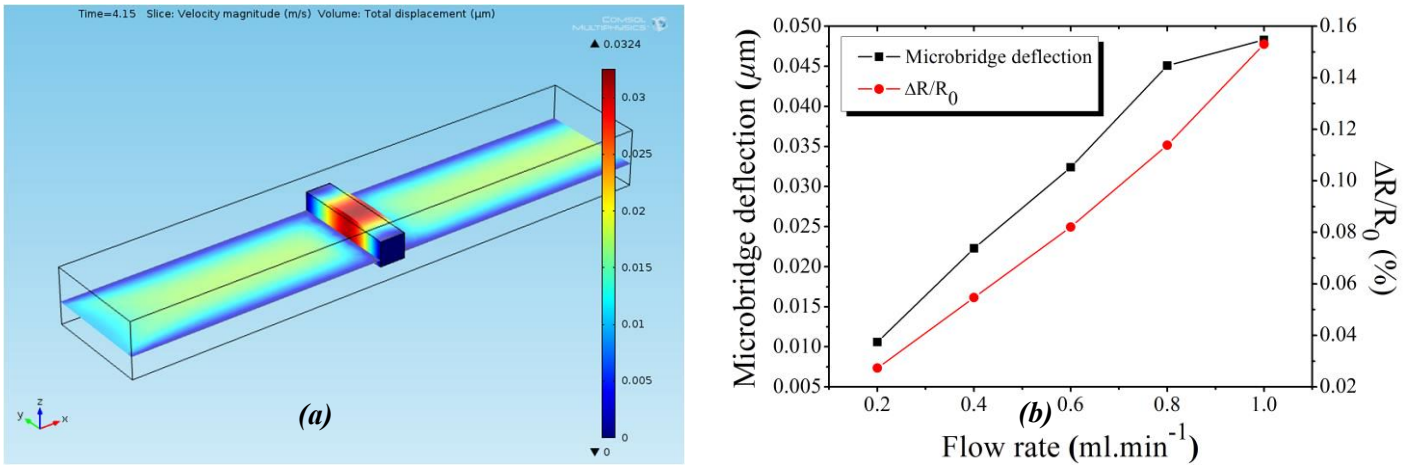

Figure 3 *Simulation results of the microbridge behavior, (a) 3D FEM simulation using Comsol Multiphysics (b) The microbridge mechanical deflection and the piezoresistive response under various flow rates*

3. Sensor fabrication process and results

3.1. Materials preparation: The nanocomposite material with homogeneous electrical conductivity properties needs a specific preparation. In focus to obtain a homogeneous and uniform nanoparticles distribution within a PDMS polymer matrix, a mixing operations must be done [17]. The key-operation is the dispersion operation using an organic solvent [18]. CPDMS was prepared by mixing 20 wt.% conductive CB nanoparticles filler (Vulcan XC-72R, Cabot Co.) with liquid PDMS (Sylgard 184, Dow Corning), using a series of operation as schematically detailed in figure 4. The CB weight ratio was optimized in the previous design study [15] to be in the range of 16-20 wt.% to obtain an acceptable piezoresistive property hence a good manufacturability of the CPDMS [13, 15, 17–20].

ISSN: 0067-3064

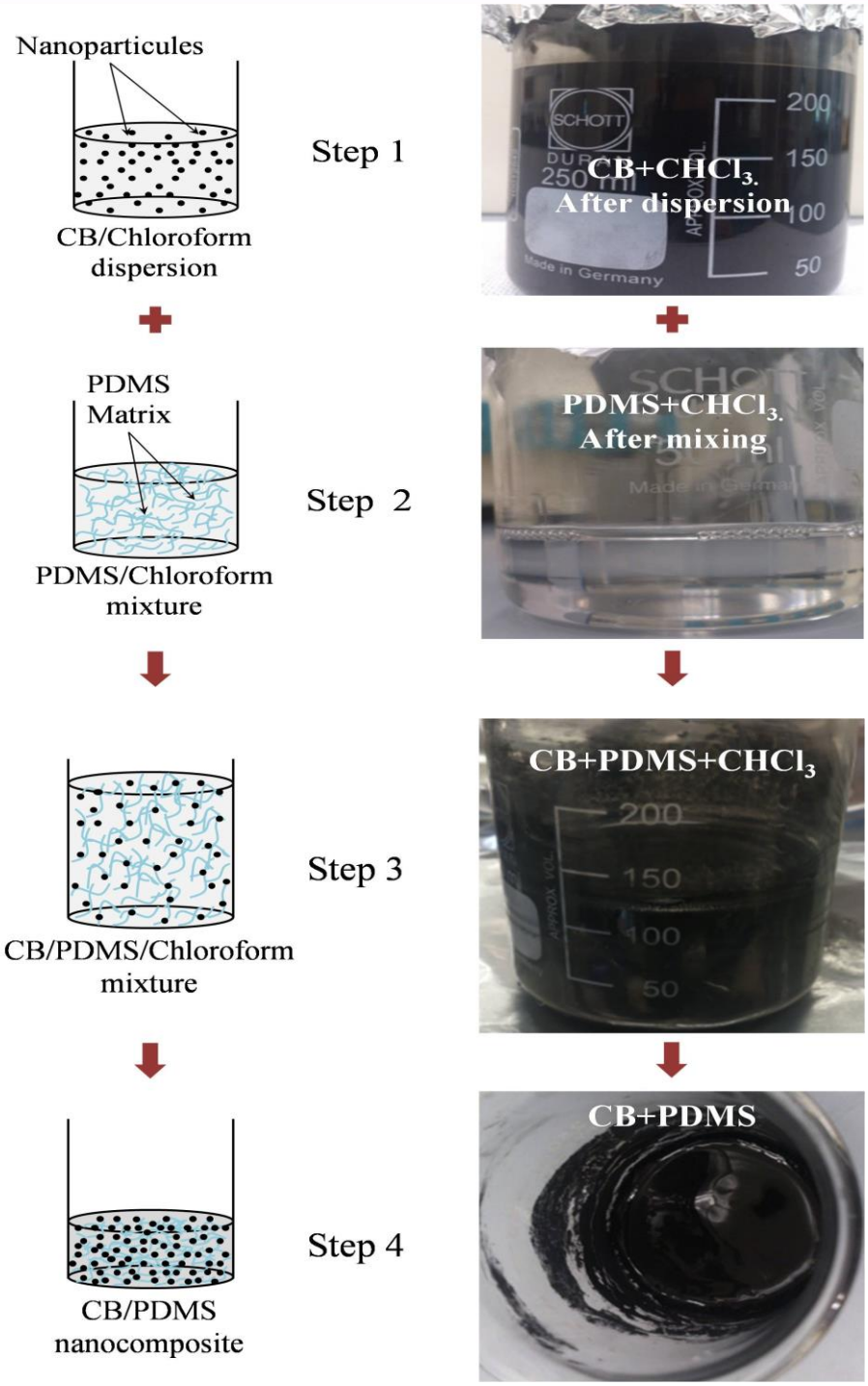

Figure 4: *Synthesis procedures schematic illustrations of CB-doped conductive composites and CB-PDMS preparation procedures*

In order to make the CB nanoparticles dispersion easy into the viscous PDMS liquid, CB nanoparticles were mixed with a volatile solvent (chloroform $CHCl_3$). The mixing ratio was 1g of CB for 300ml of chloroform.

ISSN: 0067-3064

This mixture (CB/chloroform) was sonicated for 2h to disaggregate the CB nanoparticles using sonicator (Desen Ultrasonic Cleaner DSA50-GL1, FUZHOU DESEN PRECISION INSTRUMENTS Co. Ltd.) with a fixed frequency of 28kHz. Subsequently, the above mixture (CB/chloroform) was mechanically stirred for 30min at room temperature (C-MAG HS7, IKA). The stirred mixture is shown in the step 1 of figure 4. The liquid PDMS was also mixed with chloroform to reduce strongly its viscosity to obtain later easy dispersion of the CB. This mixture (PDMS/chloroform) was prepared in ratio of 4.5g of PDMS for 15ml of chloroform. This mixture was stirred mechanically for 30min at room temperature and sonicated for 10min (Step 2 of figure 4).

The two mixtures (CB/chloroform and PDMS/chloroform) were mixed together. This mixture was sonicated for few hours at 60°C, then stirred mechanically for 30min at 50°C under a fume hood until a complete evaporation of the volatile chloroform (Step 3 of figure 4). Step 4 of the figure 4 is the final step of the CPDMS preparation process. At this point, CB/PDMS mixture became ready to be molded by adding manually a PDMS curing agent at weight ratio of 0.1:1. Figure 5 illustrates the cross-section image of the cured composite polymer using scanning electron microscopy (SEM; Quanta 650, FEI). This indicates the efficiency of the synthesis procedure which gives a relative uniform distribution of the CB nanoparticles within the PDMS matrix.

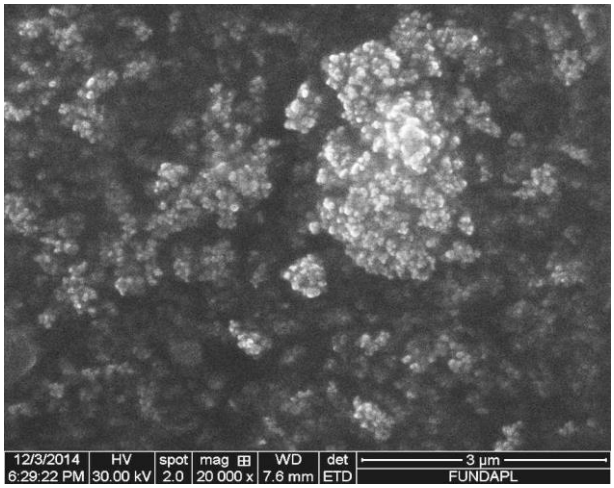

Figure 5: *The cross-sectional SEM image of CB-PDMS composites*

3.2. Fabrication process flow of the device: Based on the previous design (figure 2), fabrication process flow is shown in figure 6. This process flow uses a soft lithography technique, which entails PDMS molding and multilayer technique. This device, fabricated with three layers, involves a middle thin layer including the microbridge and two additional top and bottom PDMS layers. The fabrication process is divided into three steps: mold preparation, replication and bonding.

ISSN: 0067-3064

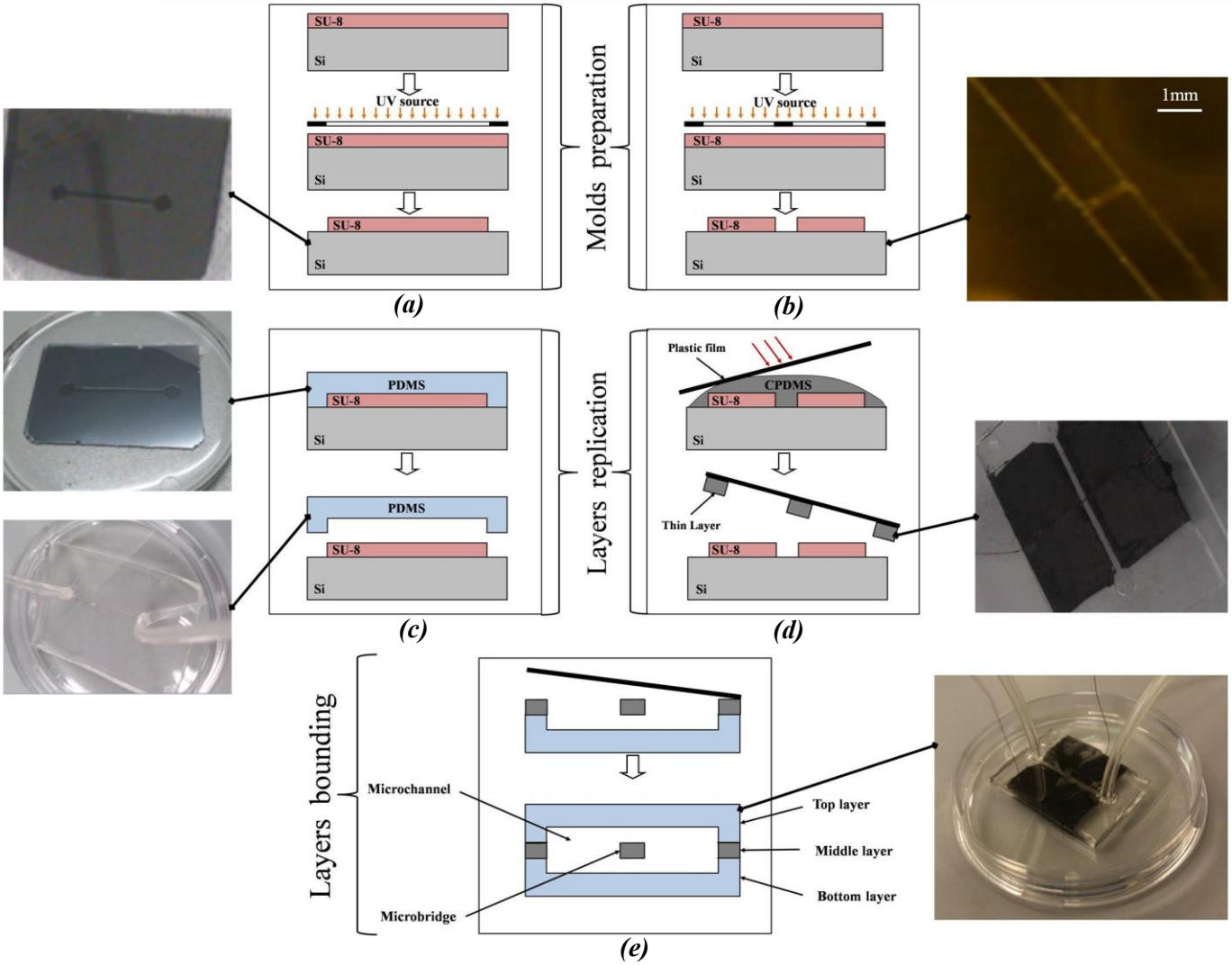

Figure 6: *Flow sensor fabrication process*

The first step of the process flow outlines the molds fabrication (figure 6*a–b*). Two molds are made separately using a SU-8 (Micro Chem Corp.) negative photoresist. This latter is patterned on a silicon wafer to obtain the mold using standard photolithographic technique. The process of mold preparation for the top and the bottom layers is shown in figure 6*a* and the process of mold preparation for the middle layer is shown in figure 6*b*.

The second step consists of the fabrication of PDMS layers (figure 6*c–d*). A liquid mixture of PDMS prepolymer (Sylgard 184 Dow Corning) with a curing agent at a volume ratio of 10:1 is poured onto the SU-8 mold (figure 6*c*) for top and bottom layers replication. The prepared CPDMS composite mixture is also poured onto the SU-8 mold to prepare the middle layer (figure 6*d*). A plastic film is then carefully placed on

it to avoid the introduction of any bubble underneath (figure 6*d*). After the curing procedure is completed, the layers are peeled off from their molds (figure 6*c–d*).

The third step must be started by Corona treatment (BD-20AC, ELECTRO-TECHNIC PRODUCTS INC.) on the layers to oxidize the PDMS surface to facilitate the adhesion between different layers. Then, the bottom and middle layers are bounded. After which, the plastic layer is separated from the package and the top layer is sealed on top (Figure 6*e*).

More importantly, the bounding process of the three PDMS layers needs a microscope alignment. In other words, an accurate alignment must be achieved between bottom, middle and top layers. Otherwise, the design accuracy of the overlaying of the three layers cannot be assured.

Figure 7*a* illustrates the complete fabricated flow sensor system entails a microchannel with two circular tubing holes representing inlet and outlet flow connections. This microchannel has a width of 756µm and height of 410µm. The microchannel is crossed by squared section CPDMS microbridge which is the sensing element with side length of 190µm as shown in figure 7*b*. The image (Figure 7*b*) is obtained using an optic microscope. A 50 µm diameter electrical cupper wire is buried and connected to the microbridge forming electric signal connections.

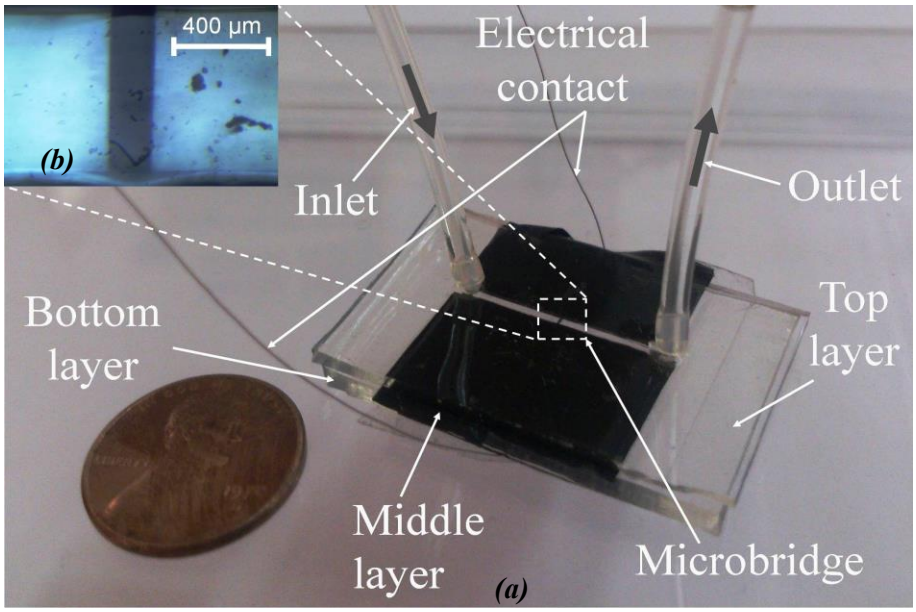

***Figure 7**: (a) Final fabricated flow sensor device, (b) The optic microscope image of microbridge.*

4. Sensing measurement:

4.1. Experimental setup: The performance of the fabricated flow sensor was tested with an experiment setup sketched in figure 8*a*. The testing fluid was pure deionised (DI) water at room temperature. It was injected using a syringe pump (TS-2A Syringe Pump Controller LONGERPUMP) through inlet and exited

toward outlet. The flow rate is controlled by the syringe pump controller ranging from 0.2-1.0ml.min^{-1} which is a typical standard microfluidic range. The flow in the microchannel causes microbridge deflection which is directly transduced to an electrical signal monitored by a digital multi-meter owing piezoresistive behavior. The photograph of the experimental setup is shown in figure 8*b*.

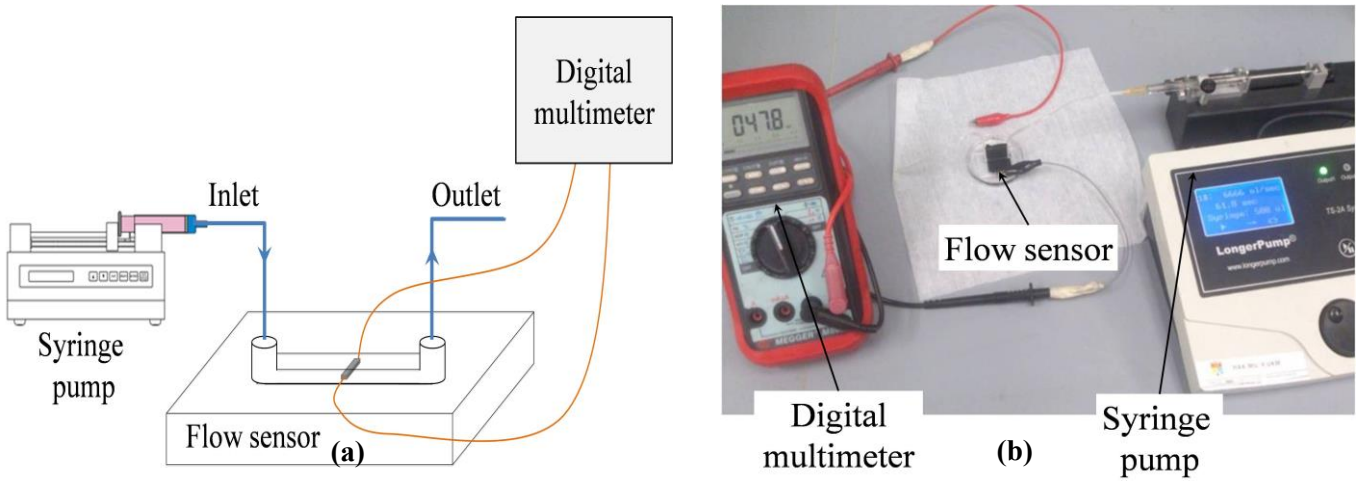

Figure 8: *Testing and characterization device, (a) Schematic of experimental setup for fluid flow test of flow sensors, (b) Experimental setup.*

4.2. Measurement results: Several experimental measurements were performed using the fabricated flow sensor using the experimental set up. The experimental data of the sensor response is given through a relative change in the electrical resistance $\Delta R/R_0$. The measured microbridge electrical initial resistance of the fabricated sensor was 28.45kΩ. Using the actual geometric dimensions, the deduced initial resistivity $\rho(0)_{CB\text{-}PDMS}$ was 1.38Ω.m. Based on these experimental values, new behaviors sensor simulations were carried out. The comparison of simulation results and experimental measurements is shown in figure 9. This comparison gives a reasonable accuracy and linear behavior for relatively weak flow rate range under 0.4ml.min^{-1}. For greater flow rate the nonlinear response of the sensor is really apparent. This shift compared to the experimental results can be explained by the non-linearity in the mechanical behavior. In numerical model a constant Young modulus was used predicting a linear behavior. Finally, the actual sensitivity of the sensor is 0.361%.ml^{-1}.min which is relatively greater than the predicted simulated sensitivity of 0.234%.ml^{-1}.min. This difference can be explained by the nonlinearity behavior not taken into account by the numerical model.

ISSN: 0067-3064

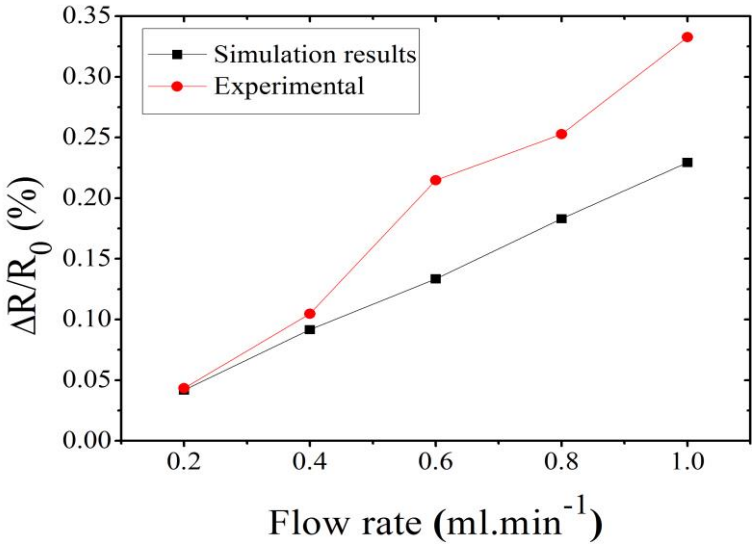

Figure 9: *Simulation and experimental results of piezoresistivity sensor response variation under different flow rates.*

5. Conclusion:

In this letter, a piezoresistive flow sensor adapted for microfluidic systems has been fabricated. Detailed design and fabrication process of this sensor based on the soft-lithography technique is presented. The sensor is a CPDMS microbridge obstacle integrated directly within a PDMS microchannel. The preparation of piezoresistive CPDMS based on the mixture of CB nanoparticles and PDMS polymer matrix, is explained. The design allows the microbridge sensing element to transduce any mechanical stress to an electrical signal owing to the CPDMS piezoresistive property. Simulation results give more efficiency to the sensor design by verifying the fluid structure interaction between the microbridge and the fluid flow in the microchannel. Indeed, to avoid the strangling effect, the design must take into account two key-parameters: the microchannel height and the adapted microbridge dimensions. The fabricated sensor based on PDMS brings several advantages such us low toxicity, thermal stability and low permeability with biocompatibility characteristic [8, 11, 21]. Experimental measurements of the fabricated flow sensor using flow rates ranging from 0.2ml.min^{-1} to 1.0ml.min^{-1} through the microchannel are performed. The measured sensitivity of 0.361%.ml^{-1}.min which is in agreement with the simulated predicted value of 0.234%.ml^{-1}.min. This sensitivity can be increased by optimizing the dimension of the microbridge and microchannel and using softer composite polymer in future studies. Finally, it is important to notice that this adapted design for soft-lithography technique fabrication used in this work is relevant to the rapid-prototyping microfluidic structures technology. In addition, the sensor can typically measure the flow rate of biological fluid that has a

wide range of properties. Also, the electrical response of the sensor can open a new horizon for wide applications in embedded microfluidic systems and BioMEMS.

6. Acknowledgments:

The authors would like to thank Dr. Hakim Tahi and Abderahmane Benhaffaf in the manuscript preparation. Great thanks to IMEN staff, MEMS group, LOC group in UKM Malaysia and MEMS & Sensors Group at CDTA for their assistance and help.

7. References:

[1] Sia S. K., Whitesides G. M.: 'Microfluidic devices fabricated in poly(dimethylsiloxane) for biological studies', Electrophoresis, 2003, 24, pp. 3563–3576

[2] Wbitesides G. M.: 'The origins and the future of microfluidics', Nature, 2008, 442, (27), pp. 368–373

[3] Lim Y. C., Kouzani A. Z., Duan W.: 'Lab-on-a-chip: a component view', Microsyst. Technol., 2010, 16, pp. 1995–2015

[4] Culbertson C. T., Mickleburgh T. G., 'Stewart-James S. A., Sellens K. A., Pressnall M.: 'Micro Total Analysis Systems: Fundamental Advances and Biological Applications', Anal. Chem., 2014, 86, pp. 95−118

[5] Mistry K. K, Mahapatra A.: 'Design and simulation of a thermo transfer type MEMS based micro flow sensor for arterial blood flow measurement', Microsyst. Technol., 2012, 18, pp.683−692

[6] Chen P., Zhao Y., Tian B., Li Y.: 'Design and fluid–structure interaction analysis of a micromachined cantilever-based differential pressure flow sensor', Micro & Nano Letters, 2014, 9 (10), pp. 650–654

[7] Nezhad A. S., Ghanbari M., Agudelo C. G., M. Packirisamy, Bhat R. B., Geitmann A.: 'PDMS Microcantilever-Based Flow Sensor Integration for Lab-on-a-Chip', IEEE Sensors Journal, 2013,13 (2), pp. 601–609

[8] Cheri M. S., Latifi A. H., Sadeghi A. J., Moghaddam A M. S., Shahrakia A. H., Hajghassemc H.: ' Real-time measurement of flow rate in microfluidic devices using a cantilever-based optofluidic sensor', Analyst, 2014, 139, pp. 431–438

[9] Aiyar A. R., Song C., Kim S-H., Allen M. G.: 'An all-polymer airflow sensor using a piezoresistive composite elastomer', Smart Materials and Structures, 2009, 18, pp. 1150021–1150021

[10] Friend J., Yeo L.: 'Fabrication of microfluidic devices using polydimethylsiloxane', Biomicrofluidic, 2010, 4, pp. 0265021–02650215.

[11] Niu X., Peng S., Liu L., Wen W., Sheng P.: 'Characterizing and Patterning of PDMS-Based Conducting Composites', Advanced Materials, 2007, 19,pp. 2682–2686.

[12] Rizvi R., Cochrane B., Biddiss E., Naguib H.: 'Piezoresistance characterization of poly(dimethyl-siloxane) and poly(ethylene) carbon nanotube composites', Smart Mater. Struct., 2011, 20, pp. 0940031–0940039

[13] Luheng W., Tianhuai D., Peng W.: 'Influence of carbon black concentration on piezoresistivity' , Carbon, 2009, 47, pp. 3151–3157

[14] Perdigones F., Luque A., Quero J.M.: 'Integration of polydimethylsiloxane membranes in SU-8 structures', Micro & Nano Letters, 2010, 5 (5), pp. 333–335

[15] Belgroune N., Hassein-Bey A., Hassein-Bey A.S.L., Tahraoui A., Majlis B.Y. , Benamar M. E. A., Serhane R.: 'Design and FEM simulation study of a microflow sensor based on piezoresistive PDMS composite for microfluidic systems', Microsystem Technologies, 2016, DOI :10.1007/s00542-016-2891-6

[16] Belgroune N., Hassein-Bey A., Majlis B.Y. , Benamar M. E. A.: 'Modeling and fem simulation using fluid-structures interaction of flexible micro-bridge bending within pdms micro-channel', IEEE International Conference on Semiconductor Electronics, Kuala Lumpur, Malaysia, 2014, pp. 495–498

[17] Cugat O., Reyne G., Delamare J., Rostaing H.: 'Novel magnetic micro-actuators and systems (MAGMAS) using permanent magnets', Sensors and Actuators A, 2006, 129, pp. 265–269

[18] Liu C. X., Choi J. W.: 'Improved Dispersion of Carbon Nanotubes in Polymers at High Concentrations', Nanomaterials, 2012, 2, pp. 329–347

[19] Kong J. H., Jang N. S., Kim S. H., Kim J. M.: 'Simple and rapid micropatterning of conductive carbon composites and its application to elastic strain sensors', Carbon, 2010, 77, pp. 199–207

[20] Luheng W., Tianhuai D., Peng W.: 'Effects of conductive phase content on critical pressure of carbon black filled silicone rubber composite', Sensors and Actuators A, 2007, 135, pp. 587–592

[21] Camou S., Tixier-Mita A., Fujita H., Fujiiy T.: 'Integration of Microoptics in Bio-Micro-Electro-Mechanical Systems towards Micro-Total-Analysis Systems', Japanese Journal of Applied Physics, 2004, 43 (8B), pp. 5697–5705.

ISSN: 0067-3064

Solar light Induced Degradation of Rhodamine B on TiO_2Thin Films Prepared by Sol Gel Spin Coating

A. Sedik[1], A. M. Ferraria[2,3],R. Outemzabet[1], M.Trari[4]

[1] Laboratory of Semiconductor Material and Metallic Oxides, Faculty of Physics, University USTHB, BP 32, 16111 Algiers (Algeria)

[2]BSIRG, iBB, DEQ, Instituto Superior Técnico, Universidade de Lisboa, Av. RoviscoPais, 1049-001 Lisboa (Portugal)

[3]AssociateLaboratory i4HB—Institute for HealthandBioeconomyat Instituto Superior Técnico, Universidade de Lisboa, Av. Rovisco Pais, 1049-001 Lisboa (Portugal)

[4]Laboratory of Storage and Valorization of Renewable Energies (LSVER), Faculty of Chemistry, USTHB University,BP 32, 16111 Algiers (Algeria)

Abstract

The present workis devoted to the study of the crystalline structure, chemical composition, optical properties and photocatalytic activity of TiO_2 thin films prepared by sol-gel spin coating on glass substrates. The films were characterized by the Raman spectroscopyand X-ray Photoelectron Spectroscopy (XPS). The optical properties have been investigated by UV-Vis absorption spectroscopy in both reflectance and transmittance modes. The XPS and Raman analyses confirm the formation of the anatase polymorph, while the UV-Vis spectroscopy shows the dependence of the energy gap (E_g) on the preparation conditions.The Raman spectra show the characteristic bands of the tetragonal anatasecentered at143 and 396 cm^{-1}, thus confirming the single phase. The intensity of the peaks increases with increasingthe number of layers.The UV Visspectra show a strong absorption in the UV region (λ< 380 nm) corresponding to the edge absorption with a red shift in the UV region. The TiO_2 films were successfully tested for the oxidation of Rh B under solar light.The influence of the number of spin-coated layer (1 – 4 depositions) (annealed for2 h after each deposition)on the photocatalytic properties of the TiO_2 film for the degradation of Rhodamine B (Rh B)is

ISSN: 0067-3064

investigatedan abatement efficiency of 48% is obtained under an average light flux of 780 Wm^{-2}.

Keywords: Sol-Gel; TiO_2 thin films; anatase;Rhodamine B.

I- Introduction

Metal oxides are advantageous in the solar energy conversion due to their facile synthesis, low cost and chemical stability,and thin filmsare attractive from an economical point of view.Among the candidates, TiO_2 remains very popular and possesses a tunable band gap and an adsorption ability in the UVA region. It has been used in many fields, such as gas sensor, photocatalysts, sunscreens, dye-sensitized solar cells, and other applications [1**].**

Currently, many **works** have been **devoted** to the degradation of polluants likethe mineralization of ibuprofen to CO_2ontoTiO_2 irradiated by the UVC light **[2]**, andTiO_2-containing perfluorinated TiO_2**[3].**

TiO_2films were prepared by different methods like reactive thermal vaporization**[4, 5]** electrochemical deposition [6**]**, sol-gel spin coating **[7],** magnetron sputtering **[8]**thermal oxidation**[9, 10]**and sol-gel dip coating **[11].** The latter is relatively inexpensive and permits film coatings with various geometries and controlled thicknesses.

On the other side, thesolar energy continues to attract a growing interest because of its cleanliness and availability and nowadays the photo-electrochemistry is extensively used for environmental protection **[12]**and energy supply [**13].**Indeed, the heterogeneous photocatalysis is a friendly alternative able to replace partially the conventional techniques for the water treatment [**14],** particularly in the third world where the water became a scarce commodity [**15].** Effluents containing Rhodamine B(Rh B), a hazardous compound encountered in the effluent streams of the dyes industry, must be treated at the source before they are spilled into the aquatic medium. The Rh B concentration in water is drastically restricted below 0.5 mg L^{-1} by the water safety standards. Although TiO_2 is widely used, it was synthesized in our case by spin coating, in order to use it for the degradation of Rhodamine B, a toxic and recalcitrant dye **[16]**

In this work, we studyTiO_2 thin layers, prepared by sol-gel spin coating on the photocatalytic activity. The films were characterized physically and applied for the degradation of Rh B under sunlight.TiO_2 (anatase polymorph) has been extensively studied over the last decades owing to

ISSN: 0067-3064

its high efficiency under both sunlight and UV irradiation and continues to attract a great attention. It can be used in the photodegradation of organic compounds unlike the rutile phase which has a poor photoactivity[**17]**. TiO_2 was also used for cleaning water and air [**18**, **19**] and is an ideal photocatalyst for in the environmental protection [**20, 21].**

II- Experimental

The precursor solution (0.5 M) was prepared with analytical reagent grade $TiCl_4$ (Fluka, 99.99%) in absolute ethanol (Spectro-Scientific),stirred for 1 h at room temperature to get a transparent solution.TiO_2 films were grown by the sol-gel spin-coating method onto soda lime glass substrates. The substrates were first degreased in alkali free detergent, washed with distilled water and immersed finally in absolute ethanol. Then, they were cleaned ultrasonically for 15 min in double distilled water and dried at 70 °C for 10 min.

The films were deposited by spin-coating at room temperature with different number of layers(1 to 4), each one was maintained 5000 rpm during 45 s and dried for 10 min under a tungsten lamp (100 W). After each deposition, the film was annealed at 500 °C (for2 h) aiming the crystallization of titania. This process was repeated the several times to obtain multi-layer TiO_2 films.

The Raman spectra were plotted at room temperature with a JobinYvon R600-10S spectrometer with a 633 nm radiation as excitation source. The spectra were collected between 100 and 3600 cm^{-1}, with a resolution of 0.3 cm^{-1} and an exposure time of 10 s; the region of interest was the (50 - 800 cm^{-1}) range.

The films surfaces were characterised by X-ray Photoelectron Spectroscopy (XPS) using a XSAM800 spectrometer from KRATOS with non-monochromatic X radiation Mg Kα (1253.7 eV). The spectra were recorded thanks to the software Vision 2 for Windows, Version 2.2.9 (Kratos). Details on the operation parameters and data treatment are described elsewhere [**22**]; the quantification factors were those of the Vision 2 software library.

The optical properties (transmittance/reflectance) were recorded with a double beam UV-Vis spectrophotometer (3101 PC Shimadzu).

The photocatalytic performance of TiO_2 films was assessed through the degradation of Rh B. The TiO_2 film (1 cm^2) was immersed in 10 mL of aqueous Rh B solution (10 ppm) and exposed

ISSN: 0067-3064

to solar light for 4 h(from 11am to 15 pm) where the light flux fluctuates between 650 and 342 W m^{-2}, measured with a Pyranomètre (KIPP &ZONEN, CMP11). The Rh Bconcentration was determined by UV-Visible spectrophotometry (Specord 200 Plus) by using a linear interpolation on the calibration graph.

III- Results and discussion

1- Structural and chemical characterization

a- Raman spectroscopy

The Raman spectra (Fig. 1) show symmetric modes of vibration of the tetragonal anatase phase identified at: 143 cm^{-1}(E_{gv1}), 197 cm^{-1} (E_{gv5}), 398 cm^{1} (B_{1gv2}), 513 cm^{-1}(B_{1gv5}) and 639 cm^{-1}(E_{gv6}).The broadening of the intense Raman peak (Fig. 1) suggests the presence of a quantum size effect (a decrease in the particles size) attributed to the phonon confinement[**23**],and structural disorder with the presence of strains in the as-grown nanocrystalline phase as reported elsewhere [**24**, **25].**Changes in the Raman spectra produced by the non-stoichiometry and phonon confinement effect are still under discussion[**26**]**.**

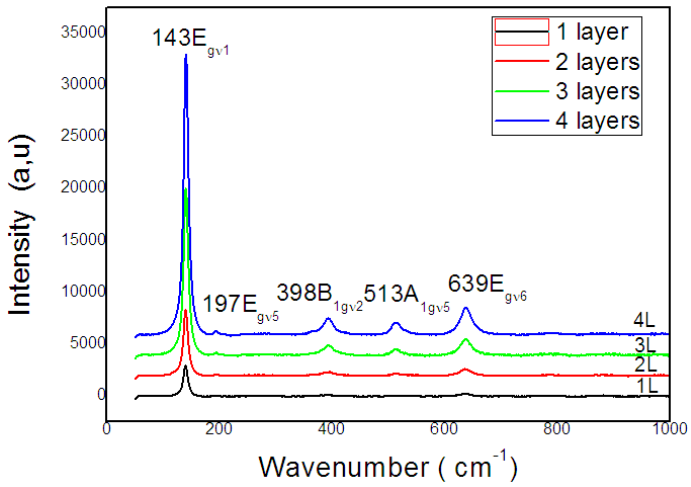

Fig.1: Raman spectra of TiO_2 thin films prepared by sol-gel spin coating as a function of the number of layers

ISSN: 0067-3064

b- XPS

The effect of the number of layers on the TiO_2 film chemical compositionwas investigated. A bare glass substrate, cleaned by using the same protocol as the spin-coated substrates, was also analysed for a comparison purpose.Table1 gathers the corrected binding energies (BE) and corresponding assignments for all samples. Given the qualitative similarities between the prepared films, the BE value of the Glass/TiO_2 samples for different layers are given of four values with the corresponding standard deviation. The error in the glass substrate BE is the experimental error; Fig. 2 shows the XPS regions of Ti *2p* and O *1s*.

Table 1: Corrected binding energies, BE (eV) (Reference BE for charge correction: 285 eV, assigned to C-C and C-H aliphatic carbon atoms) and assignments [**27**]. (*) see text.

	Glass substrat	**Glass/TiO_2 (different number of layers)**	**Assignments**
Ti $2p_{3/2}$	—	458.6 ± 0.1	**Ti**-O
Ti $2p_{1/2}$		464.3 ± 0.1	
O 1s	—	530.1 ± 0.1	***O***-Ti
		531.6 ± 0.1	Mainly**O**-Si, ***O***=C
	532.5± 0.1	532.7 ± 0.1	Mainly ***O***-Si, ***O***-C(can also include O from other substrate oxides)
Cl $2p_{3/2}$	—	198.3 ± 0.1	Cl^-
Cl $2p_{1/2}$		199.9 ± 0.2	
Si $2p_{3/2}$	103.1± 0.1	102.0 ± 0.2	Glass
Si $2p_{1/2}$	103.7± 0.1	102.6 ± 0.2	
C 1s	285.0± 0.1	285.0 ± 0.0	**C**-**C**, **C**-H aliphatic
	286.7± 0.1	286.6 ± 0.5	***C***-O
	288.8± 0.1	288.6 ± 0.1	**C**=O, O-***C***=O
	290.5± 0.1	290.4 ± 0.7	**C**O_3^{2-}
Na 1s	1072.2± 0.1	1071.9 ± 0.1	Na_2O (*)
Ca$2p_{3/2}$	347.6± 0.1	346.9 ± 0.1	CaO (*)
Ca$2p_{1/2}$	351.1± 0.1	350.6 ± 0.1	

ISSN: 0067-3064

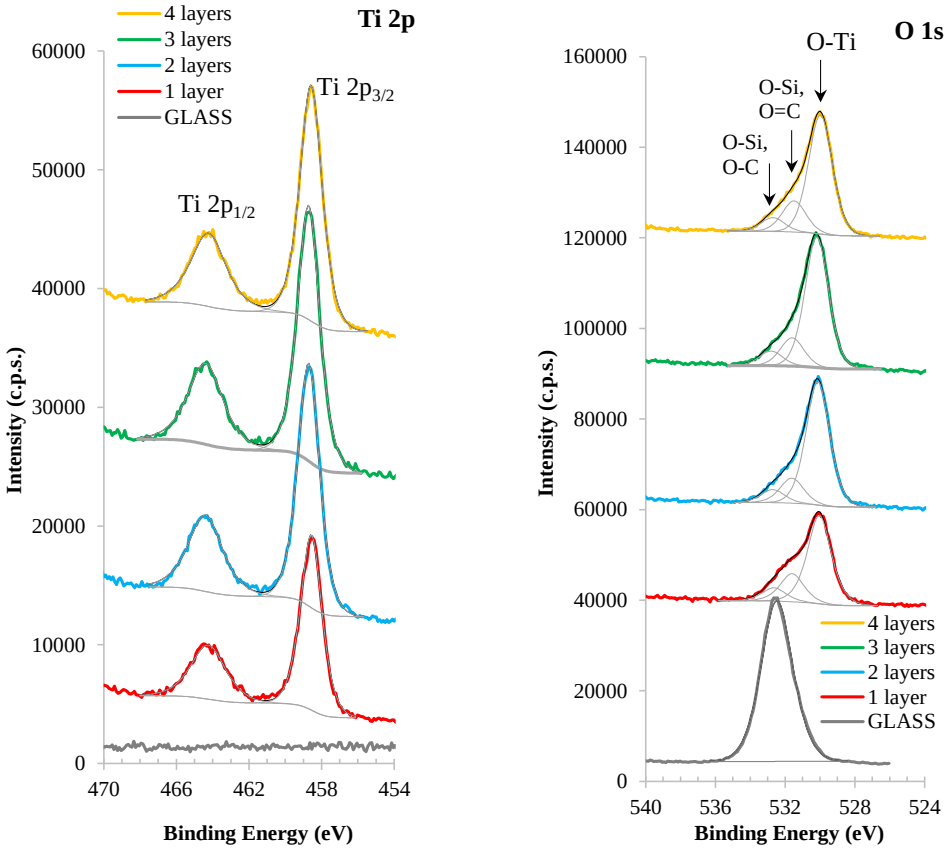

Fig.2: XPS regionsTi*2p* and O *1s* for Glass and Glass/TiO_2 films prepared with different number of layers (from bottom to top: Glass; 1 layer; 2 layers; 3 layers; and 4 layers).

Ti *2p* is a doublet with spin-orbit separation of 5.7 (± 0.1 eV) and the most intense peak Ti $2p_{3/2}$centred at 458.6 eV, typical of Ti^{4+}. To confirm whether titanium is mainly from the crystalline TiO_2 and not from the $TiCl_4$ precursor,both O*1s* and Cl*2p* regions were accurately analyzed. O *1s*, which is a single peak centred at 532.5 eV in the bare glass substrate (mainly SiO_2), is fitted with three peaks in the Glass/TiO_2 spectra: two peaks centred at 531.6 and 532.7 eV, assigned to oxygen bonded to carbon and some residual oxygen from the glass substrate (Table 1) and a third peak, centred at (530.1eV), typical of oxygen bonded to titanium. Chlorine is also detected in a residual amount as shown below (Table 1). Besides Si *2p* ($BE_{(Si\ 2p_{3/2})}$ = 103.1 eV), other features related to the glass substrate are also detected: namely Na *1s* (1072.2

ISSN: 0067-3064

eV) and Ca*2p*($BE_{(Ca\ 2p_{3/2})}$ = 347.6 eV). These regions appear to be slightly deviated to lower BE in the Glass/TiO_2 samples which can be due to the presence of a contact potential between the substrate and the film.

As attested by the quantitative analysis (namely from O/Ti and Cl/Ti atomic ratios presented in Table 2), TiO_2 films with different number of layers are formed after the heat treatment.

Table 2: Global quantification and relevant atomic ratios.

	Glass substrate	**Glass/TiO_2 (different number of layers)**			
Number of layers		1	2	3	4
At. Conc. (%)					
Ti		7.8	11.2	11.5	10.6
O	55.2	33.6	40.4	41.2	39.1
Cl		0.3	0.4	0.5	0.2
Si	14.7	1.4	0.8	0.9	0.8
C	25.8	46.2	34.2	32.4	35.9
Na	3.8	10.1	12.1	12.2	12.5
Ca	0.5	0.6	1.0	1.3	0.9
Atomic ratios					
$O_{530.1\ eV}$/Ti		2.9	2.8	2.7	2.7
Cl/Ti		0.04	0.04	0.04	0.02
Ti/Si		5.6	13.1	12.7	13.3
C/Si	1.8	33.3	40.2	35.8	45.3
Na/Si	0.3	7.3	14.2	13.4	15.8
Ca/Si	0.03	0.4	1.1	1.4	1.1
O/Si (glass)	2.9				

The quantitative analysis (Table 2) complements the above information: the atomic ratio $O_{530.1\ eV}$ /Ti larger than 2, being $O_{530.1\ eV}$ the oxygen peak centred at lower BE in O *1s* (Fig. 2), is quite usual at the extreme surface of TiO_2, indicating, probably, the presence of titanium hydroxyls. Actually, a similar result was obtained for the bare substrate, which presents an atomic ratio O/Si = 2.9. This ratio was computed from the oxygen atomic concentration subtracted from the oxidized carbonaceous species, as well as Na_2O and CaO (composing the

ISSN: 0067-3064

glass substrate); a ratio larger than 2 reveals the presence of hydroxyls at the extreme surface. For the modified substrates, the Cl/Ti<< 4 shows that the precursor $TiCl_4$ has reacted and chlorine was almost completely eliminated.

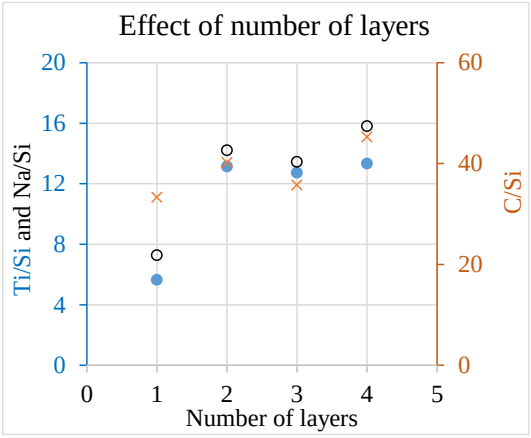

Fig. 3: Ti/Si and Na/Si (left axis, full and empty symbols) and C/Si (right axis, crosses) *vs* number of layers.

Fig.3 shows that the Ti/Si atomic ratio increases significantly from 1 to 2 spin-coatings, indicating that an increasing amount of Ti covers efficiently the glass substrate, attenuating the photoelectron signal coming from the glass. However, Ti/Si remains almost constant as the number of deposits increases. This XPS result is compatible with the aggregation of TiO_2, which crystallizes after each annealing (following each deposition), the substrate being equally detected in spite of the increasing number of spin-coatings. If the Ti/Si ratio increased with the number of deposits, it would mean that the substrate was being coated homogeneously with an increasingly thicker layer of TiO_2; However, looking at the Na/Si (plotted) and the Ca/Si atomic ratios of the Glass/TiO_2samples (Table 2), one can see that these ratios are surprisingly much larger than those found in the uncoated glass. Since no other source of Na and Ca exists (other than glass) .These ratiossuggest that Na and Ca migrate from the substrate to the extreme surface of the film during the heat treatment (500 ºC) to obtain crystalline TiO_2. Therefore, one can anticipate that Si also migrates in the same manner, follows the same trend.Another, more likely, hypothesis must be considered when analysing the evolution of Ti/Si ratios: these ratios remainsalmost constant after 2 spin-coatings due to a possible segregation of Si at the extreme

ISSN: 0067-3064

surface, resulting in Ti/Si ratios lower than expected. Regarding the C/Si ratio, it increases with the number of layers, indicating that the main source of carbon is the organic ligand from $TiCl_x(OCH_2CH_3)_{4-x}$, produced in the presence of ethanol, during the heat treatment.

2- Optical studies

a- *Transmittance and Reflectance*

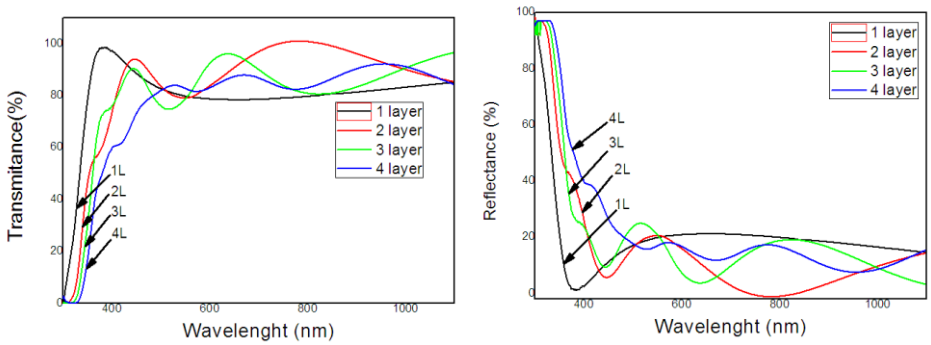

Fig. 4: UV–VIS spectra of thin films with various numbers of layers

The variation in the UV–Vis transmittance and reflectance spectra of TiO_2 (Fig.4) illustrates the influence of the number of layers where the absorption is red shifted from 307 to 340 nm. Sathish et al. explain this effect by the variation of the crystallite size (quantum effect) and/or the formation of electronic energy levels within the energy band gap [**28**]. A high transmittance exceeding 80% is achieved over the whole region up to 950nm and more fringes are depicted with increasing the number of layers, which leads to an thicker, smooth and uniform surface with a high transparency in the visible region is formed [**29**,**30].**

b- Calculation of refractive index and thickness of TiO_2 thin films

To elucidate the optical properties of TiO_2 films with the numbers of layers, the transmittance data were calculated by applying the Swanepoel model **[31].**This model shows that the optical properties of a uniform thin film of thickness (*d*), refractiveindex (*n*) and absorption coefficient (α), deposited on a substrate of index of refraction n_s, can be obtained from the transmittance T

ISSN: 0067-3064

(λ). The refraction index of the film is calculated from the two envelopes namely the upper, T_M (λ), and lower tangent envelopes,T_m(λ),of the transmission spectrum, taking an index n_s = 1.5given by:

$$n= [n + (n^2-n_s^2)^{1/2}]^{1/2},\ n =2\times n_s\times \left[\frac{T_M-T_m}{T_M T_m}\right] +\frac{n_s^2+1}{2} \qquad (1)$$

The thickness can be calculated from the relation (2):

$$d=\frac{\lambda_1-\lambda_2}{2(\lambda_1 n_2-\lambda_2 n_1)} \qquad (2)$$

Where the refraction indexes of the film, corresponding to two maximums (or minimums) adjacent to points 1 and 2, are given by n_1 at λ_1 and n_2 at λ_2.

The band gap (E_g) is obtained from the linear plot $(\alpha h\nu)^{1/2}$ against the photon energy (hν), according to the well-known relation (3):

$$(\alpha h\nu)^{1/2}= \text{Const.} \times (h\nu - E_g) \qquad (3)$$

The absorption coefficient α can be computed from Equ. (4), where T is the measured transmittance:

$$\alpha= (1/d)\ \ln(\ T) \qquad (4)$$

The plot of $(\alpha h\nu)^{1/2}$ versus (hν)andTiO_2films in the UV-Vis region for different number of layers, are shown in Fig.5. A red shift in the absorption region indicates the decrease of the gap. In fact, the E_g value evaluated by extrapolation of the line $(\alpha h\nu)^{1/2}$ versus (hν) (Table 3) confirms this result and agrees with the literature **[32].**

ISSN: 0067-3064

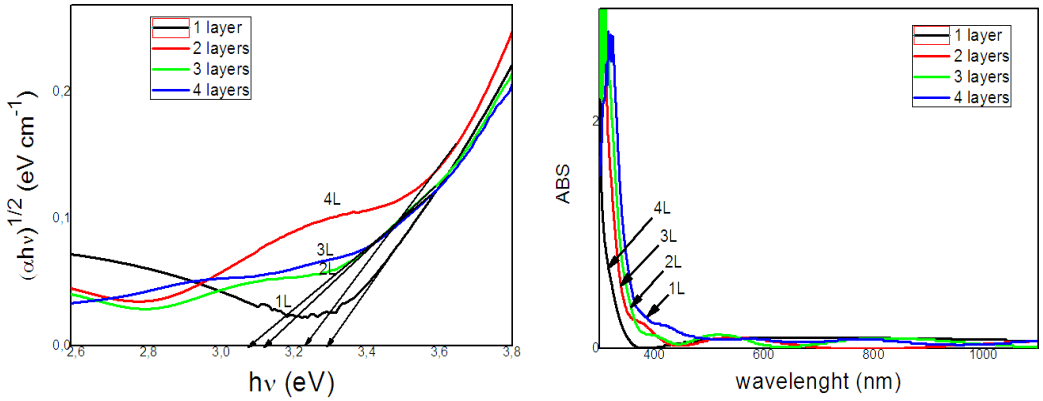

Fig. 5: Plots of $(\alpha h\nu)^{1/2}$ versus $(h\nu)$ of TiO_2 films and absorption UV-Vis spectra for different number of layers

Table3: Different optical constantsofTiO_2films for different number of layers.

Number of layers	1	2	3	4
Thickness ***d*** (nm)	82	185	324	518
Refractive index ***n***	2.08	2.11	1.96	1.82
Band gap $\mathbf{E_g}$ (eV)	3.29	3.23	3.12	3.07

IV- Photocatalysis

Rh B is a hazardous and persistent dye employed as in water; it is suspected of being carcinogenic and its elimination is highly recommended by the environmentalists**[33]**.It exhibits a strong absorption at 553 nm which results in a broad asymmetric band, due to the n $\rightarrow\pi^*$ transition [**34]**, the photo-degradation efficiency is defined as:

$$\eta=\frac{Ai-Af}{Ai} \qquad (5)$$

A_i and A_f are respectively the initial and final absorbances of the Rh B solutions.

ISSN: 0067-3064

The adsorption is the first step of any photocatalytic process; the adsorption / desorption of Rh B onto TiO_2 occurred after 4 h in the dark.Table 4 reports the calculated photodegradation efficiencies of the glass substrate coated with a different number of TiO_2layers. Rh B is not removed neither by photolysisnor by adsorption .The absorption spectra with and without TiO_2 films is shown in Fig.6; it is useful to mention that the dark adsorption is low on thin film (<4%).

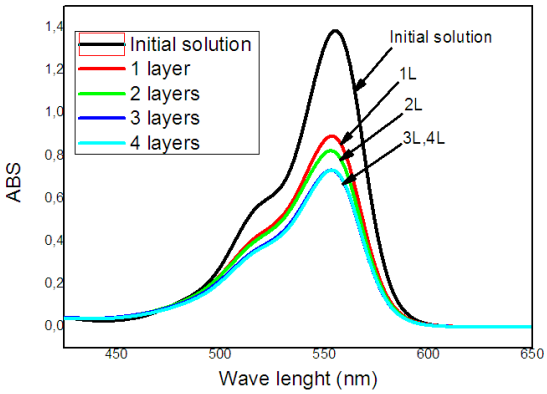

Fig. 6: Absorbance of Rhodamine B after 4 h under sunlight in contact with glass coated with various numbers of TiO_2 layers

High efficiencies upon 4 h of solar irradiation are obtained for 3 and 4 layers films (η = 48%), indicating that over 3 layers, the photoactivity remains nearly constant with a clear saturation.

Table 4: Photocatalytic efficiencies of the Rh B oxidation on TiO_2 thin film for different number of layers

Number of layers	1	2	3	4
η(%)	35%	42%	48%	48%

TiO_2 crystallites behave as nono photo-electrochemical cells. The involved electrochemical reactions occur on the opposite sides of the according the following pathways:

$TiO_2 + h\nu \rightarrow e^-_{CB} + h^+_{VB}$ (6)

$2\ e^- + 2\ H_2O \rightarrow H_2 + 2\ OH^-$ (7)

ISSN: 0067-3064

$e^- + O_2 \rightarrow O_2^{\bullet -}$ (8)

$h^+_{VB} + OH^- \rightarrow {}^{\bullet}OH$ (9)

$h^+_{VB} + H_2O \rightarrow {}^{\bullet}OH + H^+$ (10)

$H_2O^{\bullet} + H^+ \rightarrow H_2O_2$ (11)

${}^{\bullet}OH + Rh\ B \rightarrow CO_2 + H_2O$ (12)

Both the potentials of TiO_2-CB and$O_2/O_2^{\bullet -}$ are pH independent and the activity does not change significantly with pH. It is helpful to outline at this level that the excitation of Rh B with visible light does not result in a photoactivity with no electrons injection to TiO_2-CB.This clearly indicates that the lowest unoccupied energy (LUMO-level) of Rh B is located below the conduction. The TiO_2 layers

IV- Conclusion

In this work, TiO_2 thin films were deposited by sol-gel spin coating on soda-lime-silica glass substrateat room temperature with different number of layers(1 to 4). The crystallization occurred at 500 °C during 2 h for each layer. The Raman spectra showed the formation of the anatase polymorph with a tetragonal structure, identified in various symmetric modes of vibration of the anatase phase. The broadening of the intense peak in the Raman spectra increase with thenumber of layers, indicating their influence and the decrease of the crystallite sizes. The optical spectra showed a good transmittance, exceeding 80%.Ared shift in the absorption front was observedand depends on the number of layers, indicating a decrease in the band gap. The latter was calculated by extrapolating the linear part $(\alpha h\nu)^{1/2}$to the energy axis. The XPS method also attests the successful synthesis of TiO_2 thin films for all samples and the quantitative analysis is also compatible with some migration of the glass substrate elements through the TiO_2 layers, during the annealing treatment.

The photocatalytic degradation of Rhodamine B using TiO_2 was successfully tested and the results confirmed thepositive influence of the number of layers where the degradation efficiency increases from 35 to 48% respectively for 1 and 4 layers. This variation is due to the increased photogenerated(electron–hole) pairs which lead to the oxidation of Rhodamine B under solar light by both the radicals $O_2^{\bullet -}$ and ${}^{\bullet}OH$.

Acknowledgements

The authors thank the University of Science and Technology USTHB (Algeria), Faculty of Physics and Chemistry for the support to obtain A.Sedik Doctorate diploma and continued to research work and **honored BELLAL Bachir for his contribution in the chemical part of** A.Sedik **PhD Thesis.** The authors would also like to thank Fundação para a Ciência e a Tecnologia (FCT), Portugal, for support with iBB projects UIDB/04565/2020 and UIDP/04565/2020 and i4HB project LA/P/0140/2020.

References:

1[A. Sedik et al.] : A. Sedik, A. M. Ferraria, A. P. Carapeto, B. Bellal, M.Trari, R.Outemzabet Characterization of TiO_2 films obtained by a wet chemical process, ***Electrical Engineering***, 68 (**2017**) 31–36

2[G. Cerrato et al.]: G. Cerrato, CL. Bianchi, F.Galli, C.Pirola, S.Morandi, V.Capucci, Micro-TiO_2coatedglasssurfacessafely abate drugs in surfacewater, ***Hazardous Materials***,363(**2019**)328-334

3[M. Sansotera et al.]: M. Sansotera , S. G. M. Kheyli , A. Baggiolia , C. L. Bianchi , M. P. Pedeferria , M. V. Diamantia, W. Navarrinia, Absorption and photocatalytic degradation of VOCs by perfluorinatedionomeric coating with TiO_2nanopowders for air purification, ***Chemical Engineering*** 361 **(2019**) 885_896

4[S. Konstantinidis et al.]:S. Konstantinidis, R. Snyders, Reactive ionized physical vapor deposition of thin fims,***European Physical Journal: Applied Physics, EDP Sciences***, 56 (**2011)**24002-p1_ 24002-p7

5[M. GRODZICKI et al.]: M. GRODZICKI, R. WASIELEWSKI, P. MAZUR, S. ZUBER, A. CISZEWSKI,TiO_2 thin films grown on SiO_2–Si(111) by the reactive evaporation method, ***Optica Applicata,***43**(2013)**99-107

6[S.Karuppuchamy et al.]: S. Karuppuchamy, D. P. Amalnerkar, K. Yamaguchi, T. Yoshida, T. Sugiura, and H. Minoura, CathodicElectrodeposition of TiO_2 Thin Films for Dye-Sensitized Photoelectrochemical Applications, ***Chemistry Letters***,30 (**2001**) 78-79

7[L. P. R. Palaa et al.] :L. P. R. Palaa , V. Udaya , D. Gogoia , N. R.Peela **,** Surface and photocatalytic properties of TiO2 thin films prepared by nonaqueous surfactant assisted sol-gel method, ***Environmental Chemical Engineering***,8 (**2020)** 104267_1 – 104267_13

8[A. Braga et al.]: A. Braga, C. Baratto, P. Colombi, E. Bontempi, G. Salvinelli, G. Drera, L. Sangaletti, An ultrathin TiO_2 blocking layer on Cd stannate as highly efficient front contact for dyesensitized solar cells, ***Physical Chemistry Chemical Physics***, 15 (**2013)** 16812 –16818.

9[N. Huang et al.]:N. Huang, Y.R. Chen, J.M. Luo, J. Yi, R. Lu, J. Xiao, Z.N. Xue, X.H. Liu, In vitro Investigation of Blood Compatibility of Ti with Oxide Layers of Rutile Structure, ***Biomaterials Applications***, 8 (**1994)** 404-412

10[R. Hazemet al.]:R. Hazem, M. Izerrouken ,M.Trari, **A.**Benyagoub, TiO_2 films photocatalytic activity improvements by swift heavy ions irradiation, ***Radiation Physics and Chemistry,***101 **(2014**)1-7

11[A. Velasco-Hernàndez et al.]: A. Velasco-Hernàndez , R.A. Esparza-Munoz , F.J. de Moure-Flores , J. Santos-Cruz , S. A. Mayén-Hernandez, Synthesis and characterization of graphene oxide - TiO_2 thin films by sol-gel for photocatalytic applications, ***Materials Science in Semiconductor Processing***,114 (**2020**) 105082_1 -105082_9

12[J. Singh]:J. Singh, Optical Properties of Condensed Matter and Applications, Copyright © 2006 John Wiley & Sons, Ltd**(2006) [https://onlinelibrary.wiley.com/doi/book/10.1002/0470021942]**

13[A. Abdi et al.]: A. Abdi , R. Bagtache , M. Trari, Physical and photo-electrochemical properties of oxygen-rich delafossite CuYO2.25, ***Solid State Electrochemistry*** 22**(2018**) 1-6

14[J. Schneider et al.]:J. Schneider, M. Matsuoka, M. Takeuchi, J. Zhang, Y. Horiuchi, M. Anpo, D.W. Bahnemann, Understanding TiO_2photocatalysis: mechanisms and materials, ***Chemical Reviews***, 114 (**2014**) 9919–9986.

15[J. Singh et al.]J. Singh, S. A. Khan , J. Shah , R.K. Kotnala , S.Mohapatra,Nanostructured TiO_2 thin films prepared by RF magnetron sputtering for photocatalytic applications, ***Applied Surface Science***,422 (**2017**) 953–961

16[T. Ochiai et al.]: T. Ochiai, A. Fujishima, Photoelectrochemical properties of TiO_2photocatalyst and its applications for environmental purification,***Photochemistry and Photobiology C: Photochemistry Reviews***, 13 **(2012)** 247– 262

17[S. Kment et al.]: S. Kment, I. Gregora, H. Kmentova, Raman spectroscopy of dip-coated and spin-coated sol–gel TiO_2 thin films on different types of glass substrate, ***Sol–Gel Science and Technology,***63 (**2012**) 294–306

18[K. Ediputra et al.]:K. Ediputra, Syukri, Emriadi, H. Aziz,A study of TiO_2 coating structure on surfaces of meranti wood (*shoreasp*) as a photocatalyst in peat water purification,***Critical Reviews***,7(**2020)** 661-665

19[**R. Gherbi et al.]:** R. Gherbi , N. Nasrallah, A. Amrane , R. Maachi , M. Trari , Photocatalytic reduction of Cr(VI) on the new hetero-system CuAl2O4/TiO2,***Hazardous Materials,*** 186 (**2011**) 1124–1130

20[S. R. Meher et al.]:S. R. Meher and L. Balakrishnan, Sol-gel derived nanocrystalline TiO_2 thin films: A promising candidate for self-cleaning smart window applications, ***Materials Science Semiconductor Processing***, 26 (**2014**) 251-258.

ISSN: 0067-3064

21[M. Abbas et al.]:M. Abbas, M. Trari, Removal of Methylene Blue in Aqueous Solution by Economic Adsorbent Derived from Apricot Stone Activated Carbon , ***Fibers and Polymers,***21**(2020)** 810–820.

22[V. Parra et al.]:V. Parra ,M. ReiVilar, N. Battaglini, A. M. Ferraria, A. M. Botelho do Rego, S. Boufi, M. L. Rodríguez-Méndez, E. Fonavs, I. Muzikante, and M. Bouvet, New Hybrid Films Based on Cellulose and HydroxygalliumPhthalocyanine. Synergetic Effects in the Structure and Properties, ***Langmuir***, 23**(2007**) 3712-3722

23[N. R. Mathews et al.]: N.R. Mathews , Erik R. Morales , M.A. Cortés-Jacome, J.A. Toledo Antonio,TiO_2 thin films - Influence of annealing temperature on structural, optical and photocatalyticpropertie,***Solar Energy***,83 (**2009**) 1499–1508

24[R. P. Antony et al.]: R. P. Antony, A. Dasgupta, S.Mahana, D. Topwal, T. Mathews and S.Dhara, Resonance Raman spectroscopic study for radial vibrational modes in ultra-thin walled TiO_2nanotubes,***Raman Spectroscopy***,46 (**2015**) 231–235

25[N. C. Raut et al.]: N.C. Raut , Tom Mathews, P. Chandramohan, M.P. Srinivasan, S. Dash, A.K. Tyagi,Effect of temperature on the growth of TiO_2 thin films synthesized by spray pyrolysis: Structural, compositional and optical properties, ***Materials Research Bulletin***, 46 (**2011**) 2057–2063

26[R. Alcántara et al.]: R. Alcántara, J. Navas, C. Fernández-Lorenzo, J. Martín, E. Guillén, and J. A. Anta, Synthesis and Raman spectroscopy study of TiO_2 nanoparticles, ***Physica. Status Solidi C***, 8(**2011**) 1970–1973

27[**G. Beamson et al.]:** G. Beamson, D. Briggs, High Resolution XPS of Organic Polymers, TheScienta ESCA300 Database, Wiley, NewYork, (**1992)**

28[M. Sathishat et al.]: M. Sathish, B. Viswanathan,R. P. Viswanath, and Chinnakonda S. Gopinath, Synthesis, Characterization, Electronic Structure, and Photocatalytic Activity of Nitrogen-Doped TiO_2Nanocatalyst, ***Chemistry of Materials***, 17(**2005**) 6349-6353

29[**R. Bensaha et al.**]: R. Bensaha and H.Bensouyad , Synthesis, Characterization and Properties of Zirconium Oxide (ZrO_2)-Doped Titanium Oxide (TiO_2) Thin Films Obtained via Sol-Gel Process, ***Heat Treatment – Conventional and Novel Applications*** ,(**2012)** 207-234

30[S. Kim et al.]: S. Kim, J. Yum, Y. Sung , Flexible dye-sensitized solar cells using ZnO coatedTiO_2 nanoparticles, ***Photochemistry and Photobiology A: Chemistry***, 171(**2005)** 269-273

31[**R. Swanepoel]:**R. Swanepoel,Determination of the thickness and optical constants of amorphous silicon,***Physics E Scientific Instruments***,16 (**1983),**1214-1222

32[H. Rasoulnezhad et al.]:H. Rasoulnezhad, G. Hosseinzadeh, J.Yekrang,Preparation and Characterization of Nanostructured S and Fe co-doped TiO_2Thn Film by Ultrasonic-assisted Spray Pyrolysis Method , ***Nanostructures*** ,8 (**2018)** 251-258.

ISSN: 0067-3064

33[S. Rajalakshmi et al.]: S. Rajalakshmi, S .Pitchaimuthu, N. Kannan, and P. Velusamy, Enhanced Photocatalytic Activity of Metal Oxides/β-CyclodextrinNanocomposites for Decoloration of Rhodamine B Dye under Solar Light Irradiation, ***Applied Water Science***, 7 **(2014)** 1-13.

34[R. M. Ahmed et al.]: R. M. Ahmed and M. Saif, Optical Properties of Rhodamine B Dye Doped in Transparent Polymers for Sensor Application,***Chinese of Physics***,3 **(2013)** 511-521

ISSN: 0067-3064

Study of the magnetic properties of Ni-Zn-Cu ferrite materials for energy storage

Zahi Souilah[1*] and Amina Sidi Moussa[2]

1 Centre for Development of Advanced Technologies (CDTA), City 20-08-56, Baba Hassen, Algiers, Algeria.
2 Ecole Nationale Polytechnique, 10 Rue des Frères Oudek, El Harrach, Alegria.
* Corresponding author. E-mail address: souilahzahi@gmail.com

Abstract

Homogeneous Ni-Zn-Cu ferrite particles with well-controlled electromagnetic properties can be obtained by several chemical methods. In this study, uniform Ni-Zn-Cu ferrite particles were prepared and fabricated by sol-gel method at low temperatures. Scanning electron microscope (SEM) image analyzes were used to identify the formation of Ni–Zn–Cu spinel ferrite. The results obtained by X-ray diffraction (XRD) showed that a certain amount of single-phase spinel ferrite components can be formed at temperatures below 1000°C. The microstructure of the sintered ferrite core had fine, uniform grains containing spinel ferrite magnetic domains. The initial magnetic permeability of the sintered ferrite cores at 1200 °C showed that the inductance of the fabricated ferrite cores has a greatest value, and the corresponding losses were small. Therefore, at the end, a new design was reported to improve the efficiency of solar panels for storing electrical energy.

Keywords: Soft ferrite, characteristics, microstructure, magnetic properties, energy storage.

1. Introduction

A magnet is a substance that has a strong property of attracting or repelling another magnet. In general, magnets can be divided into metal alloy magnets such as aluminum-nickel-cobalt magnets, or ceramic magnets such as ferrite. Ferrite [1] is a new type that has been developed recently and is widely used due to its unique properties. Like most other ceramics, ferrite is hard, brittle, does not conduct electricity well, and is polycrystalline. It can have several different types of crystal structure, including spinel, garnet, perovskite, and hexagonal structures. Ferrites exhibit a form of magnetism called ferrimagnetism, which differs from the known ferromagnetic materials such as iron, cobalt, and nickel. Compared to metallic magnetic materials, ferrites have higher resistivity,

ISSN: 0067-3064

high dielectric properties, high magnetic permeability at high frequencies, and low saturation magnetic induction, making them suitable for high frequency and low current applications.

Ferrite can be divided into permanent ferrite, soft ferrite [2] and microwave ferrite. Permanent ferrites are black in color and are composed of iron oxide, barium carbonate, or strontium carbonate. After it is magnetized, it can keep a residual magnetic field for a long time due to its high coercive force, so they are difficult to demagnetize. They are used as refrigerator magnets, loudspeakers, small electric motors, microwave devices, recording media, magneto-optical media, telecommunications, etc. Soft ferrite is obtained by sintering iron oxide and one or more other metal oxides such as nickel oxide, zinc oxide, manganese oxide, magnesium oxide, barium oxide, strontium oxide, etc. The residual magnetic field is small or almost absent due to its low coercivity, so they easily change their magnetization and act as conductors of magnetic fields. They are used as ferrite cores for high frequency inductors, transformers, antennas, electromagnets, etc., which rely on either high magnetic permeability or high electrical resistance. Microwave ferrite refers to ferrite materials with gyromagnetic properties.

Ferrite is an important class of magnetic materials. At present, the main applications of spinel soft ferrite are limited to two ferrite materials. Most of these ferrites are synthesized using the classical method, which is the traditional ceramic process known as solid-state reaction. Most non-traditional powder preparation processes are wet methods. Some of these processes are co-precipitation, organic precursors, spray co-frying, freeze drying and sol-gel method [3]. The most common soft ferrites usually use a mixture of no more than 4 elements: nickel oxide, zinc oxide, manganese oxide and iron oxide. The two applicable ferrites are: NiZn ferrite, due to its high resistivity, used for frequencies above 1 MHz, and MnZn ferrite, due to its high permeability with high saturation inductance, used for applications below 5 MHz. Recently, extensive development of these compounds has been going on very rapidly. Thus, in light of our limited initial work on the introduction of copper into ferrite alloys [4], a new large-scale work has recently been put forward, which is reported in this paper.

2. Experimental Procedures

ISSN: 0067-3064

2.1 Synthesis

The original nickel-zinc-copper-iron acetates were accurately weighed in the molecular mole fraction (Equation 1) and dissolved separately in acetic acid and a small amount of water with continuous stirring. The solutions were mixed together and stirred for six hours at room temperature. The resulting formulation was stirred with the addition of excess distilled water for another six hours to make the solution homogeneous. The solution was then warmed from room temperature and maintained at 70 °C until the solution became viscous and a gel formed. The gel was dried in ambient air in an oven at 115 °C overnight to remove the last traces of acetic acid and water. First, to determine the lowest crystallization temperature, the phase of various samples calcined at different temperatures, subjected to both SEM and XRD was analyzed. Secondly, toroids weighing 9.72 g each (outer diameter 20 mm, inner diameter 12 mm, thickness 11 mm) were made from the gel: the dried powder was preheated to a temperature of 600 °C, kept for 4 hours in the air. Then the heated powder was mixed with polyvinyl alcohol (PVA), dried from 1 to 2 wt. %, crushed and sieved to a particle size of 75 microns. The sieved powder was mixed with 0.3 wt. % zinc stearate. Then, the granular powder was molded and pressed at a pressure of 220 MPa. The toroidal molds were finally sintered at the temperatures of 1200 °C for 4 hours in air.

$$0.3\ Ni(CH_3COO)_2 + 0.6\ Zn(CH_3COO)_2 + 0.1\ Cu(CH_3COO)_2 + 2\ Fe(CH_3COO)_3 \rightarrow Ni_{0.3}Zn_{0.6}Cu_{0.1}Fe_2O_4 + \text{volatilities} \quad (1)$$

2.2 Characterization and testing

The phase was analyzed by XRD using Cu Kα radiation on a D8 Advance-Bruker diffractometer. The photographs of the calcined samples were obtained using a scanning electron microscope (JEOL JSM-6400). Both the initial magnetic permeability (μ_i) and the loss factor (RLF) were calculated by substituting the corresponding values of the inductance *Lp* and the *Q* factor, which were measured on the sintered toroids wound with 10 turns of red copper wire 340 mm long, the ends of which were scratched using SiC and and coated with Tin, and finally connected to the HP model 4195A network spectrum analyzer in the frequency range of 10-500 MHz on a toroidal ferrite to their resonant frequency. The photomicrographs of the sintered shapes were taken on thin specimens. Specimens were mechanically ground using SiC papers and polished with 0.3 micro α-

ISSN: 0067-3064

Al_2O_3. The polished specimens were thermally etched in the furnace at 100°C below the sintering temperature for about one hour, in air. The photomicrographs were taken by the SEM. The grain sizes were measured by the line-intersection method.

3. Results and discussion

Figure 1 shows the histogram of the ferrite powder calcined at 200°C in air. The histogram measures different areas of brightness. This is a graph that shows the distribution of data. The diagram showed that there are two broad phase peaks, as well as many amorphous forms, and that the dark phase has higher intensity. Figure 2 shows additional image characteristics of the ferrite powder. No additional information can be obtained from the images, and the ferrite is still not sufficiently calcined. This firing temperature can only initiate the reaction of the raw materials, since for ferrite; the complete reaction can be obtained at temperatures above a thousand degrees.

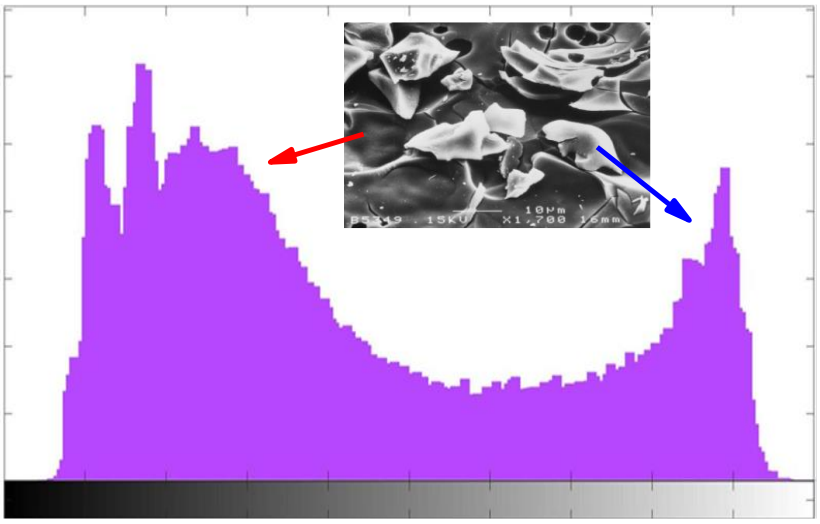

Figure 1. Histogram of the ferrite powder calcined at 200°C in air.

ISSN: 0067-3064

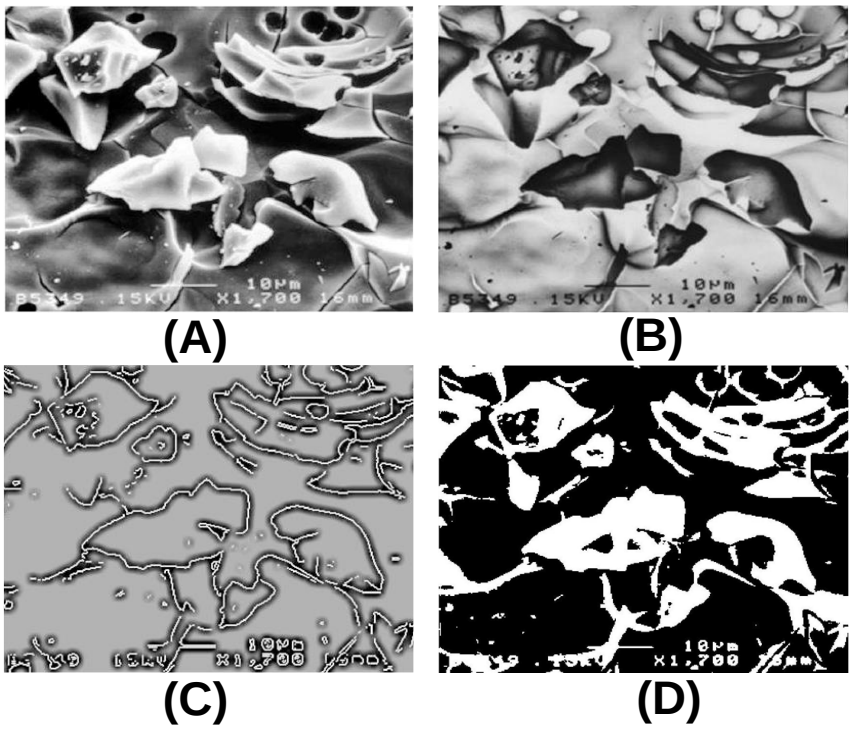

Figure 2. The ferrite powder calcined at 200°C is shown in different images: (A) contrast enhancement, (B) negative, (C) edges, and (D) binary image.

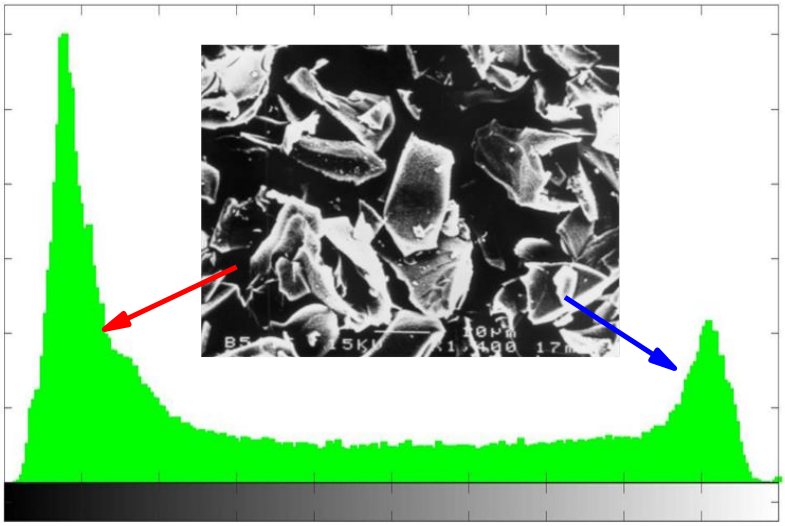

Figure 3. Histogram of the ferrite powder calcined at 600°C in air.

Figure 3 shows the histogram of the ferrite powder calcined at 600°C in air. The diagram showed that there were two narrow phase peaks, as well as many amorphous forms with low intensity, with the dark phase having much higher intensity. Figure 4 shows additional characteristics of the ferrite

ISSN: 0067-3064

powder image. The images showed that each grain was a mixture of crystalline, amorphous and other phases. Thus, one can notice the growth of half-grains. The nearly perfect spherical grains indicated the early formation of nickel-zinc-copper ferrite crystals.

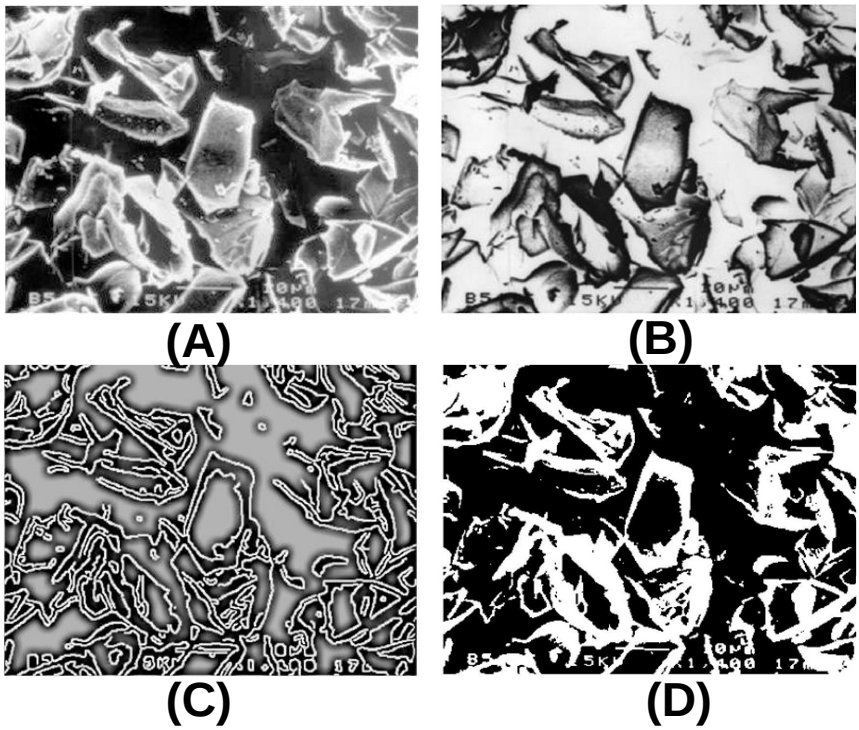

Figure 4. The ferrite powder calcined at 600°C is shown in different images: (A) contrast enhancement, (B) negative, (C) edges, and (D) binary image.

The X-ray diffraction patterns of the ferrite calcined at 900°C for 4 hours are shown in Figure 5. The diffraction spectrum of Ni-Zn-Cu ferrite was mainly calcined or mostly sintered, since the crystal structure of the cubic spinel $Ni_{0.3}Zn_{0.6}Cu_{0.1}Fe_2O_4$ was formed due to the fact that all the reflection planes (220), (311), (222), (400), (422), (511/333) and (440) coincided well with the reflections of nickel-zinc-copper ferrite corresponding to the standard card. In addition, few peaks were recorded for the secondary phase due to the reflection of Fe_2O_3 molecules.

ISSN: 0067-3064

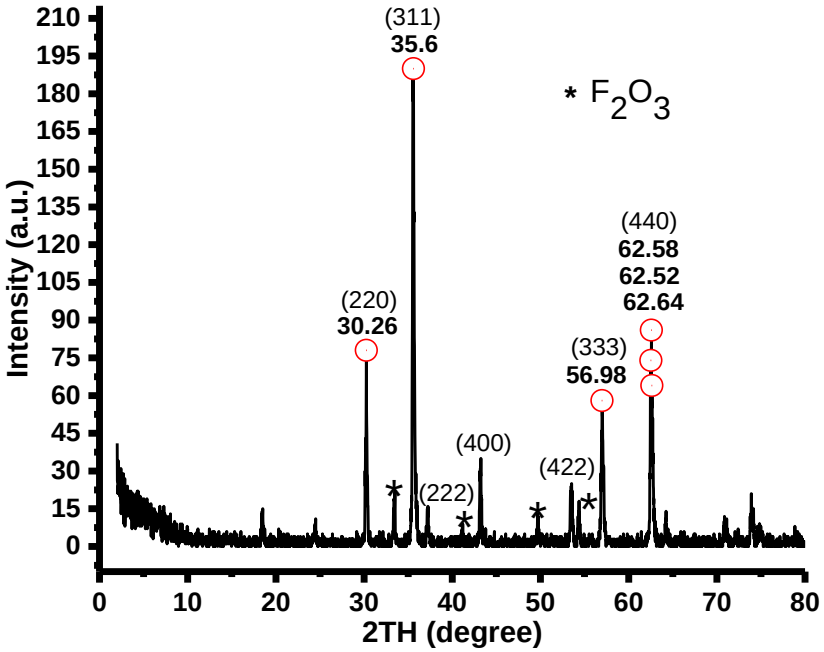

Figure 5. XRD diffraction patterns of the ferrite calcined at 900°C in air.

Figure 6 shows the histogram of the ferrite core sintered at 1200°C in air. The diagram showed that there was only one phase peak. The peak was broad, which may relate to various ferrite components including nickel, copper, zinc and ferrite. Figure 7 indicates the formation of the final ferrite product, but the dark phase may indicate the presence of spots, which are attributed to the voids between the grains because their size was not uniform. This final product had spherical grains, free of defects and an average grain size of less than 1 micrometer. It was observed that the average grain size increased to approximately 10 micrometers when the sintering temperature was increased to 1400 °C [5]. This is due to the fact that the grain size depended on the sintering conditions, i.e. temperature and time. On the other hand, below the Curie temperature, each grain can contain several domains, each of which differs from its neighbor only in the direction of magnetism.

ISSN: 0067-3064

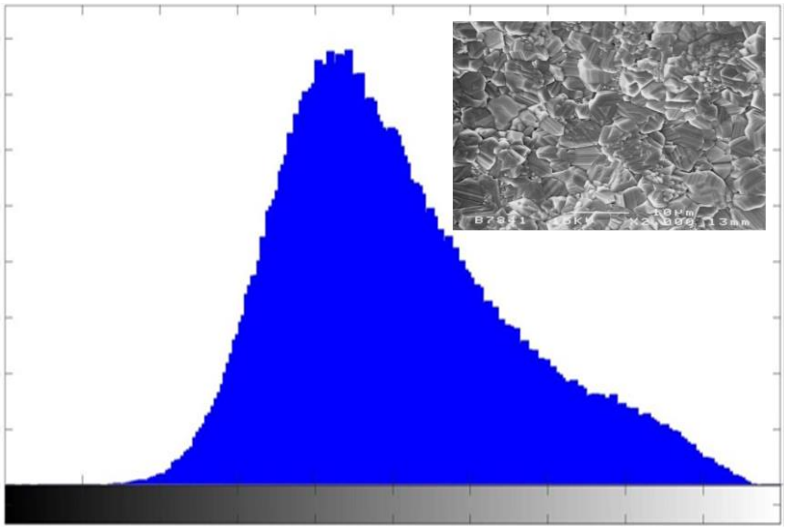

Figure 6. Histogram of the ferrite cores sintered at 1200°C in air.

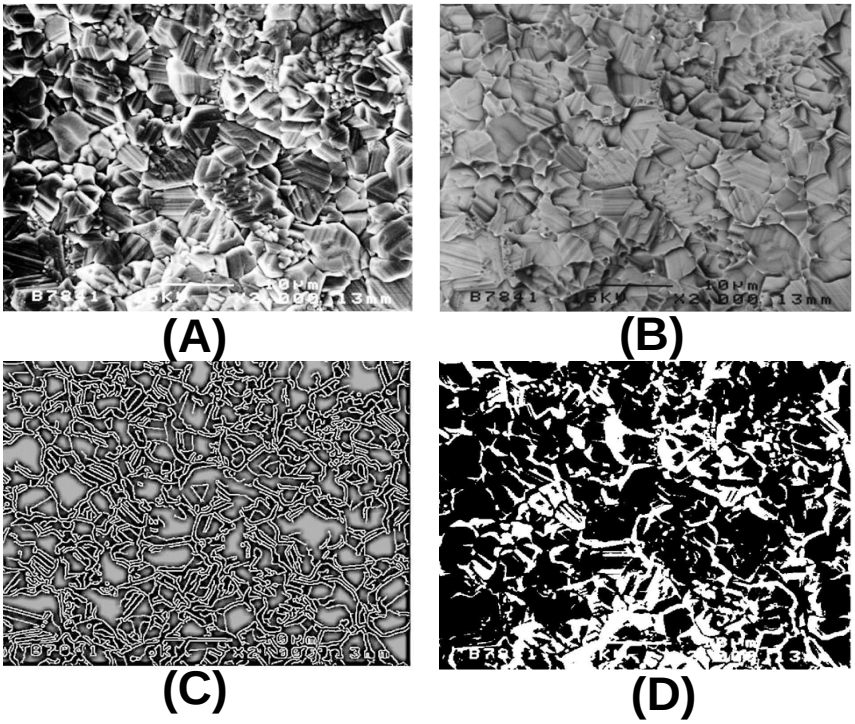

Figure 7. The ferrite core sintered at 1200°C is shown in different images: (A) contrast enhancement, (B) negative, (C) edges, and (D) binary image.

The magnetic induction of ferrite can be measured by its permeability $\mu = \mathbf{B}/\mathbf{H}$, which is generally not constant, but depends on the strength of the **H** field. Permeability (μ) is a physical property that describes the ease of creating magnetic flux in a component. The effective permeability for a small alternating **H** field, the initial permeability (μ_i) depending on frequency, is shown in Figure 8. The

ISSN: 0067-3064

initial permeability is the tangent to the initial magnetization during displacement of the reversible wall, which is the region between two adjacent domains. The frequency band was determined to a value below the resonant frequency. The measured initial permeability at 10 MHz (application point) was about 683, and the calculated relative loss factor (RLF) was 0.0012, which is considered small as compared to the ferrites obtained by the traditional method. This initial permeability is much better compared to Ni-Zn ferrites prepared under the same conditions published elsewhere [6-8]. When a conductor is exposed to a changing magnetic field, such as when it moves across a magnetic field or when the magnetic field itself changes, a voltage is induced in the conductor and the direction of the induced current opposes the change in the magnetic field. These circulating currents are known as eddy currents and are responsible for dissipating energy in the form of heat. Loss of eddy current can have serious consequences for a variety of electrical and magnetic systems. Figure 9 suggests that our domain had very small defects that led to the small eddy current losses.

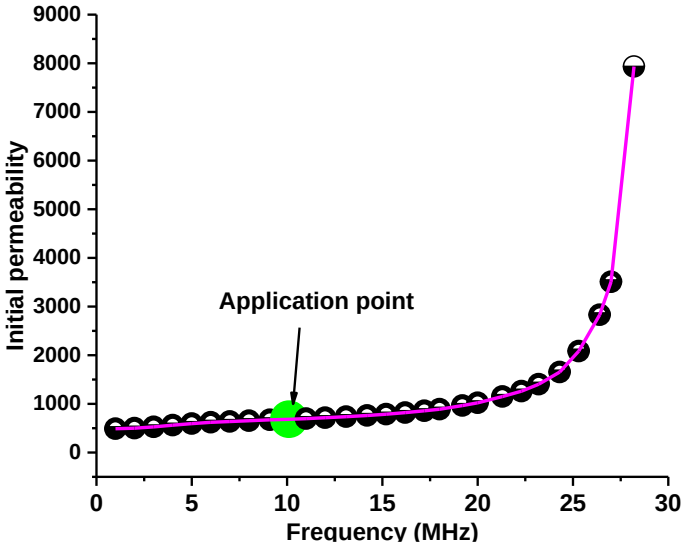

Figure 8. Initial permeability of $NiZnCuFe_2O_4$ cores sintered at 1200°C.

ISSN: 0067-3064

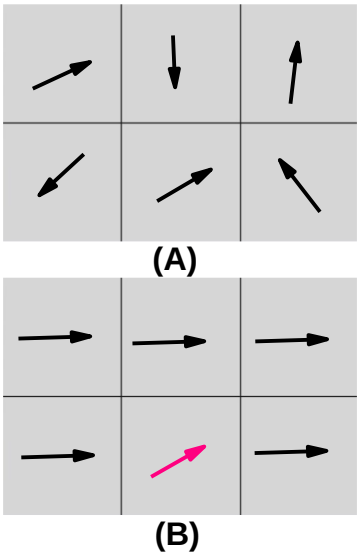

Figure 9. The magnetic domains: (A) before magnetization and (B) after magnetization.

The inductance L is an important parameter for the designs that use ferrite cores. It can be defined as the flux linkage per unit current, i.e. for an alternating current of peak amplitude $\hat{I}$, L can be given as shown in Equation (2). For a uniformly wound magnetic toroid with N turns of length ℓ and cross-sectional area A, having an initial permeability value, L can be written as given in Equation 3.

$$L = \frac{N\hat{B}A}{\hat{I}} \qquad (2)$$

$$L = \frac{\mu_0 \mu_i N^2 A}{\ell} = L_0 \mu_i \qquad (3)$$

where L_0 is the inductance that would be measured if the core had unity permeability, and the flux distribution remaining unaltered.

Toroidal cores typically consist of a donut-shaped ferrite magnetic core around which a wire is coiled, making the coil usable over a wide MHz range due to its high Lp/Q ratios and self-shielding properties. Accordingly, a donut-shaped core was chosen to provide the smallest stray field outside the system. Due to the fact that air cores have low inductance compared to magnetic cores, the inductance found in this study has a high value. Thus, the design shown in Figure 10 used a toroidal core to store electrical energy. Until now, the efficiency of solar cells is still very low, and a unit of solar panel can provide very limited energy. Solar cell efficiency refers to the portion of energy in the form of sunlight that can be converted by photovoltaics into electricity using a solar cell.

ISSN: 0067-3064

There are two ways to produce electricity using magnets: either by moving or rotating a permanent magnet around a coil or by creating a magnetic field that produces electricity through a wire through passing a current through a coil wound on soft magnetic cores to magnetize it. The idea is to improve the efficiency of solar energy by first passing its current through a toroidal core around which wire is wound to produce electricity, and then storing it in lithium-ion batteries.

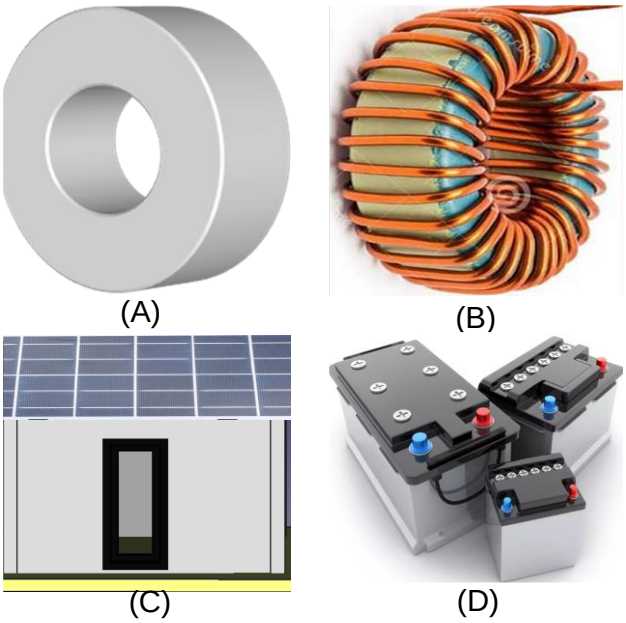

Figure 10. Electrical energy storage system: (A) Toroid, (B) ferrite coiled with copper wire, (C) solar panel and (D) lithium-ion batteries.

4. Conclusions

The sol-gel method was suitable for fabricating small-sized high-inductivity Ni-Zn-Cu ferrite. Low-temperature, defect-free sintered N-Zn-Cu ferrite can possess fine-grained microstructures combined with excellent magnetic properties for high-performance, low-cost electrical applications. The intended application was mainly to improve the efficiency of solar cells to address the current climate change crisis: Some of the potential measures to mitigate the worsening effects of climate change include phasing out oil and gas and replacing them with renewable energy sources, including energy from solar, wind, sea, etc.

Acknowledgments

ISSN: 0067-3064

The authors express deep gratitude to Amina's fellow students who helped with image processing.

References

[1] T. Nakamura, Low-temperature sintering of Ni-Zn-Cu ferrite and its permeability spectra, Journal of Magnetism and Magnetic Materials, 1997, 168: 285-291.
https://doi.org/10.1016/S0304-8853(96)00709-3

[2] O. Dehghani Dastjerdi, H. Shokrollahi, S. Mirshekari, A review of synthesis, characterization, and magnetic properties of soft spinel ferrites, Inorganic Chemistry Communications, 2023, 153: 110797.
https://doi.org/10.1016/j.inoche.2023.110797

[3] Souilah Zahi, Synthesis of Ni-Zn ferrite and Ni-Zn-Cu ferrite via sol-gel route and solid state reaction. Master's thesis, Universiti Putra Malaysia, 2000.
http://psasir.upm.edu.my/id/eprint/7972/

[4] Souilah Zahi, Mansor Hashim and AR Daud, Preparation of Ni-Zn-Cu ferrite Particles by sol-gel technique, Materials Letters, 2006, 60: 2803–2806.
https://doi.org/10.1016/j.matlet.2006.01.093

[5] S. Zahi, AR Daud and M Hashim, A comparative study of nickel-zinc ferrites by sol-gel route and solid state reaction, Materials Chemistry and Physics, 2007, 106: 452-456.
https://doi.org/10.1016/j.matchemphys.2007.06.031

[6] Souilah Zahi, Mansor Hashim and AR Daud, Synthesis, magnetic properties and microstructure of Ni-Zn ferrite by sol-gel technique, Journal of Magnetism and Magnetic Materials, 2007, 308: 177-182.
https://doi.org/10.1016/j.jmmm.2006.05.033

[7] S. Zahi, Synthesis, permeability and microstructure of the optimal nickel zinc ferrites by sol-gel route, Journal of Electromagnetic Analysis and Applications (open access), 2010, 2: 56-62.
https://www.scirp.org/journal/paperinformation.aspx?paperid=1236.

[8] S. Zahi, Nickel-zinc ferrite fabricated by sol-gel route and application in high temperature superconducting magnetic energy storage for voltage sag solving, Materials & Design, 2010, 31: 1848–1853.
https://doi.org/10.1016/j.matdes.2009.11.004

ISSN: 0067-3064

Smart Data-Driven GRU Predictor for SnO2 Thin films Characteristics*

Faiza Bouamra[1], Mohamed Sayah[2,*], Labib Sadek Terrissa[3], and Noureddine Zerhouni[4]

[1] LPCMIA Laboratory, University of Blida1, Sciences Faculty, Physics Department, BP270 route de Soumaa, Algeria
[2] LITIO laboratory, University of Oran1, Department of Computer Science, BP1524, El Mnaouer, Es-senia, Oran, Algeria
[3] LINFI Laboratory, Department of Computer Science, University of Biskra, BP145 RP 07000, Algeria
[4] FEMTO-ST, Franche-Comté Electronique Mécanique Thermique et Optique – ENSMM, France

Abstract. In material physics, characterization techniques are foremost crucial for obtaining the materials data regarding the physical properties as well as structural, electronics, magnetic, optic, dielectric, and spectroscopic characteristics. However, for many materials, ensuring availability and safe accessibility is not always easy and fully warranted. Moreover, the use of modeling and simulation techniques need a lot of theoretical knowledge, in addition of being associated to costly computation time and a great complexity deal. Thus, analyzing materials with different techniques for multiple samples simultaneously, still be very challenging for engineers and researchers. It is worth noting that although of being very risky, X-ray diffraction is the well known and widely used characterization technique which gathers data from structural properties of crystalline 1d, 2d or 3d materials. We propose in this paper, a Smart GRU for Gated Recurrent Unit model to forcast structural characteristics or properties of thin films of tin oxide SnO2(110). Indeed, thin films samples are elaborated and managed experimentally and the collected data dictionary is then used to generate an AI - Artificial Intelligence - GRU model for the thin films of tin oxide SnO2(110) structural property characterization.

Keywords: Crystalline · Characterization · X-ray diffraction · prediction · GRU.

1 Introduction

X-Ray diffraction, discovered by Röntgen in 1895 [1], is a crucial method for understanding and extracting structural properties of crystalline materials, which are usually resumed in lattice parameters a, b, c, grain size D and strains [2]. This diffraction technique plays a pivotal role in characterizing material properties across various fields, from minerals to advanced technological raw materials. The X-Rays diffraction principle consists on the interaction of X-rays with solid materials, resulting in diffraction patterns that provide insights into the periodicity of atomic structures. Unlike this, availability and exponential cost of X-ray diffraction make its use very challenging for researchers and engineers, but mainly because that X-ray diffraction requires significant samples of experimental data due to the high number of parameters. Furthermore, the `ab-initio` calculation methods are emerging nowadays as a promising alternative for characterizing the atomic structure and properties of materials.

Unfortunately and instead of the progress of theoretical and simulation methods, the structural characterization still be too limited because of the current available computing capacity of machines, especially when dealing with complex crystalline structures with high number of atoms [3] [4]. Thus, more new explorations have been done to search for soft and less costly

* LPCMIA, LITIO, LINFI, and FEMTO-ST, *Corresponding Author.

alternatives, particularly around the fields of advanced simulation and artificial intelligence techniques that were enhanced by the evolution in modeling approaches but also technological computing capacities. In fact, new and innovative data-driven methods were considered to estimate or even forecast physical properties of materials. These well known artificial intelligence (AI) techniques are now widely adopted in various domains such as machinery, chemistry, physics, and PHM (Prognostics and Health Management) [5][6][7][8][9].

We notice that when studying materials and dealing with complex crystalline structures in the context of limited access to equipment, artificial intelligence networks such as the GRU - Gated Recurrent Unit models and others are gaining prominence, value and trust and are currently considered as the more favorite techniques to enhance XRD's capabilities and strengthen predictions of materials' structural properties [10]. Indeed, it is worth noting that in our context, thin films samples are elaborated experimentally by the technique Sol-Gel Dip-Coating [11] [12] with some defined conditions such as catalysis, velocity of dip, time of dip, number of dip. The obtained samples are characterized with X-ray diffraction technique and then analyzed with HighScore tool [13], to have the structural parameters a, b and D. Next, using the collected data samples dictionary from the real experiences, our proposed GRU neural network Predictor of the structural properties, is generated after a learning and testing processes. Finally, the designed AI-based GRU model [14] along with the elaborated experiments show the benefits of our approach for material characterization and prove the relevance and insights of implementing data-driven models for material properties prediction. Later in the recent future, the use of more robust and complex AI models should certainly boost the material characterization domain and this will cover a wide range of materials.

2 Data-Driven Material Characterization Framework

In the depicted framework below (see Figure 1), we illustrate the different stages of our data-driven characterization process. When fully developed, the proposed AI GRU model [15] will facilitate the materials characterization by estimating the cristal properties using the experimental dataset.

We notice that there are three different stages or modules interrelated in order to help experts in their final decisions:

1. *Experiment Stage* : At this stage - see Figure 1, the engineers and researchers do real physical experiments, define relevant properties that may fit the physical or chemical situation and collect concrete samples to construct a data dictionary that summarises the experimental specifications. These collected data are then used in modeling, simulation, or even to design data-driven models.
2. *Information Stage* : This stage - Figure 1 - mainly concerns the data-driven model development. The data dictionary is pre-processed and the data are prepared using normalization, regularization and features reduction to respond to a task or goal oriented request. Finally an AI model is designed and tested to get better of its performances.
3. *Decision Stage* : In this stage we integrate the constructed AI driven model in the decision process. Here, the data-driven model will be tested to see its compliance by regards to the client and user requirements.

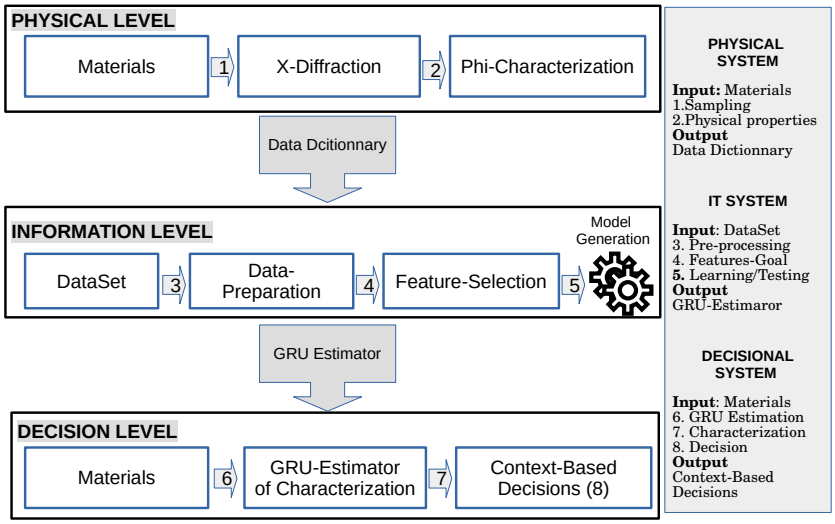

Fig. 1: AI-Based Materials Characterization Framework.

3 X-ray Diffraction for SnO2 Characterization

In this section, we will describe in details the process of structure materials characterization using the non destructive X-ray diffraction technique - see Figure 2. This latter shows a derivation of Bragg's law, where a sample of crystal material is placed at the center of the instrument, and an incident beam of X-ray is directly oriented towards this sample- see details in Figure 2. Then, the outgoing beam, who makes a 2θ with awards one, is obtained as a result of interaction with the atoms of the crystal. Every wavelength λ of the X-ray beam should be proportional to the spacing of the set of crystal planes (hkl), d and the reflection will occur if Bragg's law below is satisfied - See the equation 1, where, n is a positive integer, λ a wavelength and d is gain size.

$$2dsin(\theta) = n\lambda, \quad Where \quad \lambda = 1.540A^{\circ} \tag{1}$$

Next, to compute lattice parameters a and c, we use the equation 2 obtained from lattice spacing formula for a tetragonal crystal system [16], where h,k and l are Miller indices defining an (hkl) plane in the lattice :

$$\frac{1}{d^2} = \frac{h^2 + k^2}{a^2} + \frac{l^2}{c^2} \tag{2}$$

By applying the Bragg law's and considering the constants A = $\lambda^2/(4a^2)$ and C = $\lambda^2/(4c^2)$, we obtain:

$$sin^2(\theta) = A(h^2 + k^2) + Cl^2. \tag{3}$$

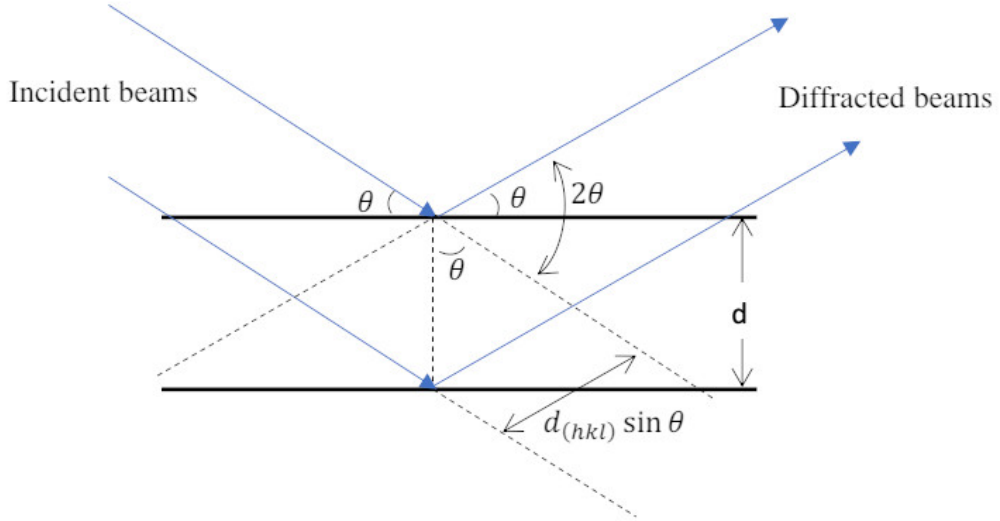

Fig. 2: XRD Diffraction Scheme.

Thus, for $l = 0$, we define $hk0$ as $sin^2(\theta) = A(h^2 + k^2)$, and from the other lines of the patterns, we determine the C value in : $sin^2(\theta) - A(h^2 + k^2) = Cl^2$. Finally, the Grain size D, is calculated using Scherrer relation [17]:

$$D = \frac{K * \lambda}{\beta * cos(\theta)} \tag{4}$$

With K the Scherrer constant, on which depends the crystallites, and is typically in [0.9, 1.0]. β is the full width at the half-maximum (FWHM).

We notice that the obtained patterns has interference maxima (peaks) corresponding to the diffracted X-ray by the regularly planes of the crystal lattice - see Figure 3. It's worth nothing to know that X-ray diffraction techniques involves two main methods resumed in (1) powder or (2) single crystal diffraction.

In our research work, we especially have a focus on the diffraction of X-ray for single crystal of thin oxide SnO2. In addition, samples of SnO2 thin films were elaborated with sol-gel dip coating technique. After getting a reliable thin films, we have optimized some experimental parameters such as solution, speed of dip, number of dip and others and finally we get these parameters that correspond to the final output sample with its proper characteristics.

In the Figure 3, we represent some results patterns from X-ray diffraction technique that were treated with HighScore software [13]. The first pattern represent theoretical sheet obtained from data based on the perfect SnO2 thin films, and the others are the different cases obtained with changing experimental parameters, as mentioned clearly in the Figure 3. These collected data are considered and examined during the development of the GRU model.

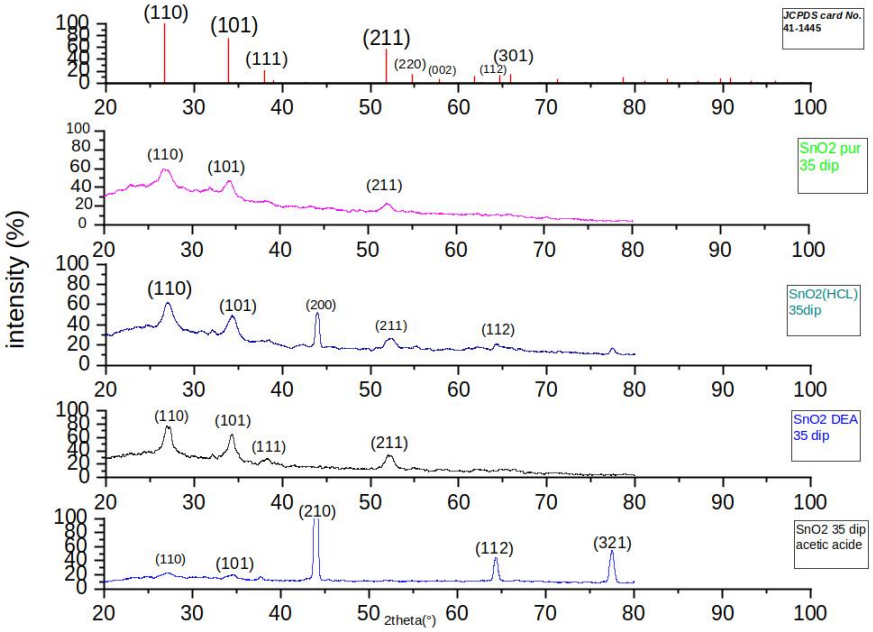

Fig. 3: X-Ray diffraction patterns of SnO2 thin films obtained by Sol-Gel (Dip Coating) technique. a) ideal pattern of Sno2, b) pur SnO2, c) SnO2 with HCI solution, d) SnO2 with DEA solution, e) SnO2 with acetic acide.

4 GRU-Based Predictor

As a streamlined version of complex AI models [18][19][20][21][22] , the gated recurrent unit (GRU) [23] achieves good performance and do faster computing. A GRU model contains a reset gate and an update gate. These gates are composed by sigmoid activations functions σ to force their output values to lie in the interval [0, 1]. The reset gate controls at what extent the previous states should we remembered. In the same way, the update gate tracks how much of the new states are just a copy of the old ones - See Figure 4.

Here are the analytical equations that map the GRU cell's computation states at each time step t. Let consider the notations, where W_*, W'_*, and b_* denote respectively the learned weight matrices and biases for each gate referred to as index $*$. Also, the σ is the logistic sigmoid function. The current input is X_t, and R, Z are the reset and update gates respectively, H_{t-1} denotes the previous iteration's hidden state, whereas H_t corresponds to the current hidden state.

$$\begin{aligned} Z_t &= \sigma(W_Z\, X_t + W'_Z\, H_{t-1} + b_Z) \\ R_t &= \sigma(W_R\, X_t + W'_R\, H_{t-1} + b_R) \\ G_t &= \tanh(W_G\, X_t + W'_G\, (R_t \circledcirc H_{t-1}) + b_G) \\ H_t &= Z_t \circledcirc H_{t-1} + (1 - Z_t) \circledcirc G_t \end{aligned} \tag{5}$$

The flowchart below illustrates the inputs for both the reset and update gates in a GRU, given the input of the current time step X_t and the hidden state H_{t-1} of the previous time step. The outputs of the gates are given by two fully connected layers with a sigmoid activation function.

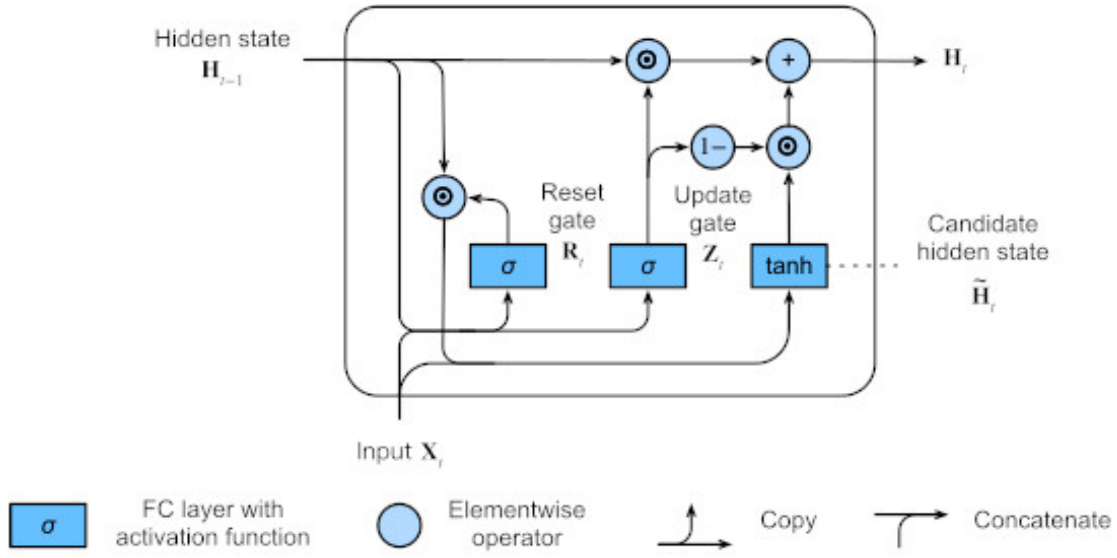

Fig. 4: GRU Cell/Unit Computation[24].

4.1 Performance Measurements

The adopted performance metrics below will be used to depict and to prove the performance of the proposed regression GRU model, and this enables the identification of a good performing parameters that best fits the requirements of our defined problem. In fact, the mean squared error MSE in the equation 6 computes the error between the experimental c ground truth values and the GRU estimated c' values.

$$MSE = \frac{1}{n}\Sigma_{i=1}^{n}\left(c_i' - c_i\right)^2 \tag{6}$$

Again, the R^2 score, the Coefficient of determination, is a regression metric. This metric is a normalized version of the MSE that makes it easier to compare ML models. The closer R^2 is to 1 (ideal), it means the regression was able to capture 100

$$R^2 = 1 - \frac{\Sigma_{i=1}^{n}\left(c_i' - c_i\right)^2}{\Sigma_{i=1}^{n}\left(c_i - \overline{c}\right)^2} \tag{7}$$

With n the total number of samples in testing data set, and c, c' respectively the actual coefficient value and the estimated coefficient.

In addition, the scores S measurement in 8 formula track the sensitivity of the learning and shows its smoothness.

$$S = \begin{cases} \alpha * (\frac{exp^{|ei|}}{10} - 1) & |e_i| >= \epsilon \\ 0 & |e_i| < \epsilon \end{cases} \tag{8}$$

Where, S is the sensitivity score of the learning/generalization functions. α is the amplification factor, and e_i is the deviation between the learning `loss` and the generalization `val-loss` parameters. When, the absolute positive error $|e_i|$ is exactly less than ϵ the sensitivity tends to zero (0) and the learning/generalization process is good. Conversely, In contrast, for every error $|e_i|$ greater or equal to ϵ, the learning is not stable even if the `loss` decreases considerably.

5 GRU Model: Design and Experiments

In this section, we design a GRU-Based Predictor for structural properties of SnO2, and its possible adoption for the characterisation of various other materials. Clearly, we depicted in the following the different steps that are used to construct, tune and test the GRU model, starting by the essential data collection and preparation phase for each AI data-driven modeling.

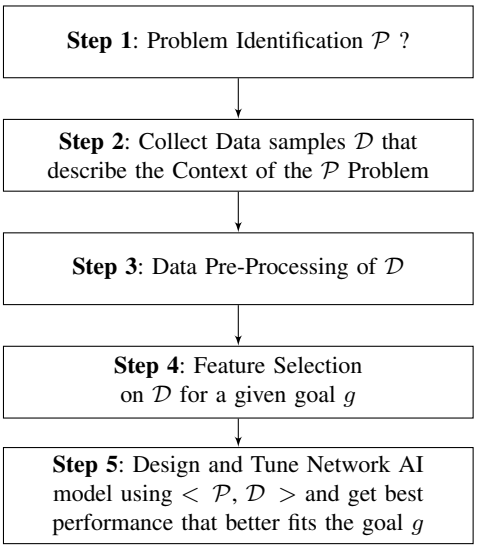

Fig. 5: GRU-Based Model Implementation

1. *Problem Identification:* As mentioned in section 1, the objective of this work consists to analyse the obtained X-Ray diffraction spectra using other programs such as HighScore [13], Origin [25] and to compare them to a specters in the program data base. The spectra properties is resumed in lattice characteristics a, b and grain size D. We notice

that the comparison with previous existing results in the literature, enables us to verify the nature of the structure and proves that it concerns tetragonal phase of Tin Oxide SnO2 thin films.

2. *Data Sample Collection:* To determine a structure for 1d, 2d and 3d materials we must determine stucturals parameters as well as: lattice parameters a, b and c to classified them among the seven systems and fourteen Bravais lattices as mentioned in the crystallography.
3. *Data Pre-processing:* Data pre-processing techniques are applied, including duplicate detection and removal, missing data imputation, outlier detection and treatment. Data transformation techniques such as normalization and standardization are also employed to ensure data consistency.
4. *Feature Selection:* Relevant features are selected, with the assistance of domain expert possessing deep knowledge and expertise in the field. These experts provide valuable insights into the key characteristics that define part quality and prioritize the most important features.
5. *Design and Tuning of Network AI model:* A GRU model is generated after the learning process and its performance are proven using testing.

5.1 Data Preparation

– *Data Description and Collection*
Expert in material physics specify precisely the parameters that should be considered for the characterization of structural materials. Also, all the pipeline tools that is used during the characterization process are identified and configured. After, a data dictionary is constructed as illustrated in the Table 1. Thus, physical symbols and theirs respective designations are specified and validated by material physics experts. We note that this step is crucial and should be done correctly to get an adequate data-driven models that fit precisely the situation of characterization.
After, the task of data collection has to be considered with care, knowing its sensitivity and determination in the learning process. It is important to notice here that inaccurate data with poor quality should lead to catastrophic decisions. Many AI models are ineffective because of the lack of date and/or the quality of data.

– *Data Pre-processing*
Once the data has been specified and then collected, we can analyse statistically their nature, either by visualization or by computing statistical characteristics, such as the mean μ, the standard variation σ, the $Median$ and others. This will enable us to choose the best data preparation technique to use - See Table 2. We have noticed that the parameters $Tsec(\%s)$ and $Time(\%s)$ are constants because theirs standard deviations are null (See Table 1, σ= **0.0**†) and there are multiple scaling in the data set (See Table 1, $\mu(Vdip) = 06.09^{*} << \mu(Trec) = 454.55^{*}$ and $\sigma(\theta) = 03.68^{*} << \sigma(Trec) = 52.22^{*}$) and this is not sane to use the data set without normalization and reduction. Thus, we have applied a normalization on the data to have a single scaling for our data and to avoid the multi scaling bias.

Table 1: Parameters specification including input or system variables and decision variables, with their respective numerical types. .

Symbol	**Definition**	**Type**
θ	Angle between thin films planes and incident beam	float
Ndip	Number of dip	Integer
Vdip	Velocity of dip	Integer
Tsec	Drying temperature	Integer
Trec	Annealing time	Integer
Time	Drying time	Date
P_{sol}	Pure SnO2	Boolean
D_{sol}	Diethanolamine 'DEA' Solution	Boolean
H_{sol}	Hydrochloric acid Solution	Boolean
A_{sol}	Acetic acid solution	Boolean
a	Lattice parameter for tetragonal structure in tow direction x and y	float
b	Lattice parameter for tetragonal structure in z direction	float
D	Grain size	float

Table 2: Description of Data Set distributions of the different features and statistical metrics μ, σ and Median.

	θ	Ndip	Vdip	**Tsec**	Trec	**Time**	P_{sol}	D_{sol}	H_{sol}	A_{sol}	a	b	D
t_0	34.2599	35	7	100	500	120	1	0	0	0	2.62	2.61	99.58
t_1	34.36	7	7	100	500	120	1	0	0	0	2.61	2.60	212.94
t_2	27.0841	35	7	100	500	120	0	1	0	0	4.65	2.61	112.11
t_3	27.08	7	7	100	500	120	0	1	0	0	4.65	2.60	182.07
t_4	26.96	35	7	100	500	120	0	0	1	0	2.60	2.60	602.63
t_5	34.4126	35	7	100	500	120	0	0	0	1	2.60	2.60	602.63
t_6	34.0546	6	7	100	400	120	1	0	0	0	2.63	2.63	1351.28
t_7	26.827	7	7	100	400	120	1	0	0	0	4.69	0	630.41
t_8	26.82	8	7	100	400	120	1	0	0	0	4.69	0	882.48
t_9	27.0714	35	2	100	400	120	1	0	0	0	4.65	2.61	124.65
t_k	...	...	...		...		...	...	...	...	...	...	...
t_n	27.02	35	2	100	400	120	0	1	0	0	4.66	2.60	171.09
μ	29.63	22.27	06.09*	100	454.55*	120	00.55	00.27	00.09	00.09	04.55	02.07	52.22
σ	03.68*	14.63	02.02	**0.0**†	52.22*	**0.0**†	00.52	00.47	00.30	00.30	00.23	00.69	51.46
Median	27.08	35.00	07.00	100	500.00	120	01.00	00.00	00.00	00.00	04.65	02.28	31.50

Sometimes and to overcome the lack of the real experimental data, Gaussian augmentation to the dataset are applied. Each data transaction t is used to generate new mutant

transactions set $\{t'_k\}$ of size k in the neighbor space of some features or attributes in t.

– *Feature Selection and Reduction*
At this stage of data preparation, features are splitted in input and output variables and some parameters may be just dropped. This techniques called features reduction should be done under the advice of experts in materials physics. In our context, the considered system variables are : θ, $Ndip$, $Vdip$, $Trec$, P_{sol}, D_{sol}, H_{sol}, A_{sol}, and the decision variables a, b, D.

5.2 GRU Predictor Models: Learning and Testing

We have generated experimentally the best configuration of the GRU model and the optimal learning parameters are depicted below. In fact, the description of the parameters and their values used along the following experimentation section are introduced right after.

– `Tsteps` (*Time steps refers to the sequence length in the input data.*): `24`
– `IN:#Features + OUT:#Decisions` (*Indicates the number of distinct attributes measurements in input.*): `8 (input parameters) +1 (decision variable features #`a`, #`b`, #`D`).`
– `Loss` (*This function measures the dissimilarity between the predicted values and the ground truth values during training.*):
– `Metrics` (*These custom functions are used to evaluate the model's performance during training and testing.*): `MSE, `R^2`, S`.
– `#Layer` (*It denotes the number of layers in the neural network model.*): `2`
– `#Cells` (*It specifies the number of cells or units per layer of the GRU model.*): `64`
– `#Epochs` (*This parameter represents the number of times the model iterates over the entire training dataset.*): `limit <= 800 + StopEarling (SE)`
– `#Batch` (*It refers to the number of samples or data points processed in each training iteration.*):
– `Act_func` (*It is a mathematical function that controls the outputs of each neuron in the GRU neural network.*): `Relu`
– `%Dropout` (*Dropout is a regularization technique used during training to avoid overfitting and to boost the training.*): `20%`
– `#FCDense` (*Known as fully connected layers.*): `1`
– Adam_{lr}(*They are used to configure the* `lr` *learning rate.*): `lr = 0.0001`

Table 3: Tuning hyper-parameters of the learning process GRU^a_{64}, GRU^b_{64} and GRU^D_{64} Models.

Model	Metrics	Tsteps	#Layers	#Cells	#Epochs (Early Stopping)	#Batch	Act_func	Adam_{lr}
GRU^a_{64}	MSE/S	50	3	(8, 64, 1)	450	25	Relu	0.001
GRU^b_{64}	MSE/S	50	3	(8, 64, 1)	480	25	Relu	0.001
GRU^D_{64}	MSE/S	50	3	(8, 64, 1)	270	25	Relu	0.001

After the tuning of the GRU model training parameters, we will now define an experimental protocol that consists first, in the adoption of the latter fixed learning parameters in Table 4. Second, for each crystal materials characteristics a, b, and D, we have determined respectively the corresponding models as $\text{GRU}^{a}_{(8,64,1)}$,$\text{GRU}^{b}_{(8,64,1)}$, and $\text{GRU}^{D}_{(8,64,1)}$ - see Table 4. These are trained and then tested using the metrics MSE and S included in the section 4.

Table 4: Performance of the GRU models based on Metrics: (a) MSE: Mean Square Error, (b) μ_S: Mean scores S, and (c) Mode_S: Mode Scores

Model	**MSE**	μ_S	**Mode**$_S$	**#Cells**	**Act_func**
GRU^{a}_{64}	7.2901e-14	0.0659	0.5970	(8, 64, 1)	$Relu$
GRU^{b}_{64}	7.7273e-05	0.0675	0.8797	(8, 64, 1)	$Relu$
GRU^{D}_{64}	1.8649e-09	0.0166	0.1749	(8, 64, 1)	$Relu$

At this time, we have depicted the traceability of the training and the testing of our designed models $\text{GRU}^{a}_{(8,64,1)}$,$\text{GRU}^{b}_{(8,64,1)}$, and $\text{GRU}^{D}_{(8,64,1)}$. Three figure are presented to define the dynamics of the GRU predictor models. In green curve, we have the learning loss function (`loss`), and the purple curve represents the generalization or the `val-loss` function. Finally the red sensitivity function determines whether the learning is stable or not - see Figures 6, 7, 8.

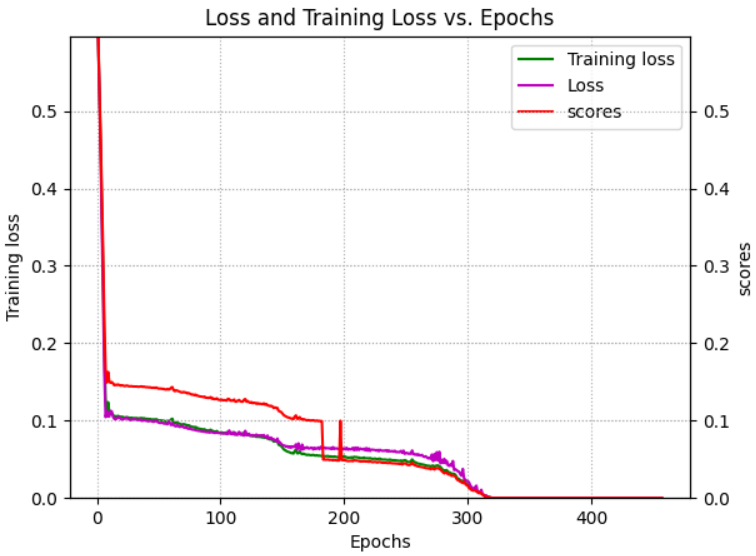

Fig. 6: $\text{GRU}^{a}_{(8,64,1)}$ Model - Learning loss, Generalization val-loss and Sensitivity scores

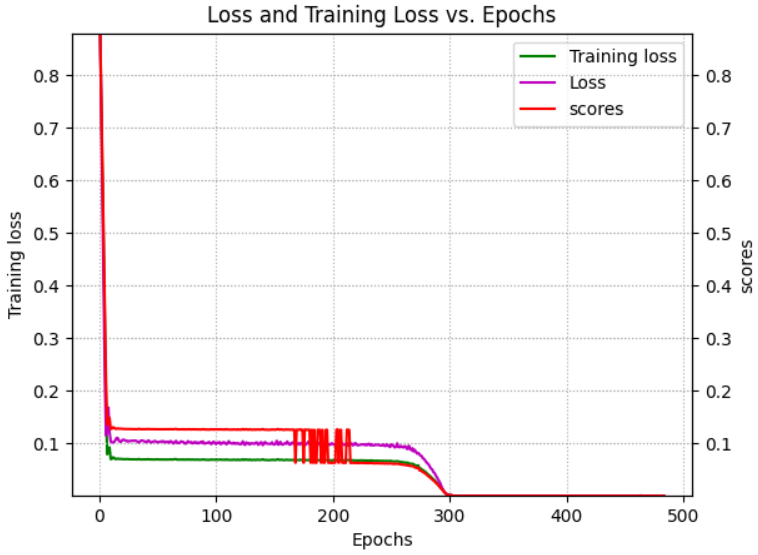

Fig. 7: $GRU^{b}_{(8,64,1)}$ Model - Learning loss, Generalization val-loss and Sensitivity scores

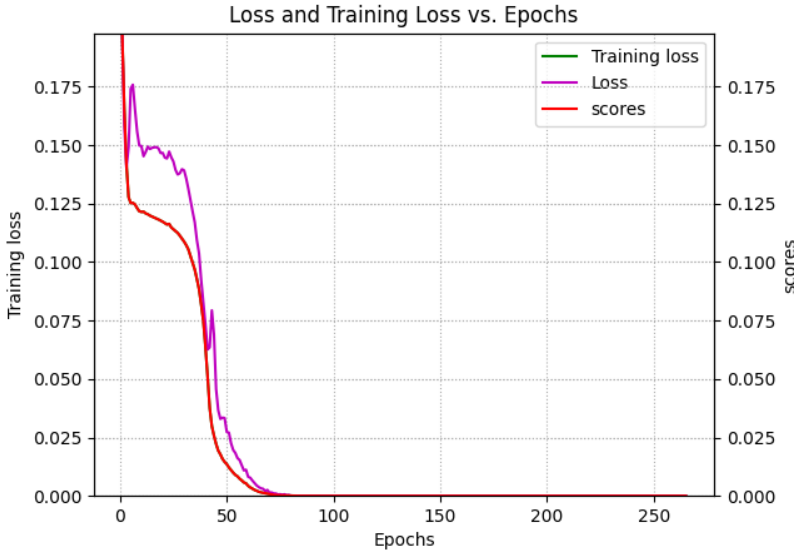

Fig. 8: $GRU^{D}_{(8,64,1)}$ Model - Learning loss, Generalization val-loss and Sensitivity scores

– We notice in the Figure 6, relative to the generation of the $GRU^{a}_{(8,64,1)}$ predictor model for the a crystal geometric feature, that the learning process is unstable until the 200^{em} epochs. Before this stage, the learning and generalization are entangled, which means that the learning ans training processes are not yet separated. After that, at the stage of $epochs$ in the range $[20, 310]$, the learning and the generalization seem to be efficient and go to a convergence point around the 310^{em} epoch, well with less sensitivity. Finally, when the

$epochs$ parameter is greater than 310, the dynamics of the training converges to optimal GRU network weight values.

– In Figure 7, we can clearly see that the learning in very sensitive in around the 200^{em} epoch, but converges around $epoch = 300$ and demonstrates better performances in terms of learning and generalization for the generated model $\text{GRU}^{b}_{(8,64,1)}$.

– For the model $\text{GRU}^{D}_{(8,64,1)}$ generation - see Figure 8 -, we note that the learning converges earlier and gives a steady results in epochs 80 without any sensitivity.

5.3 GRU Model Predictions

After the GRU model construction and the performance evaluations for each GRU model predictor of the different structural parameters #a,#b, and #D, we will now apply the predictor models to predict the crystal properties considering by the way the truth experimental values in the dataset dictionary.

For each structural features, we use the corresponding model named $GRU^{X}_{(8,64,1)}$, where X is in the set $\{a,b,D\}$. Thus, the truth and the estimated properties a, b, and D are depicted in Table 5 using the above predictor models - see the subsection 5.2. We noticed that in the table 5 (a), the estimated lattice parameter a in the transactions t_0, t_2 and t_6 are exactly the same as the truth experimental values. The remaining estimated values in $\{t_1, t_3,t_4,t_5\}$ have an absolute difference at most equal to $3.00e^{-7}$ of the compared to the truth experimental values. This finding can be observed in the case of the lattices b and D. In fact, the largest absolute difference $2.00e^{-2}$ is shown in the transaction t_5.

In addition, the difference between the estimated and truth values for the D lattice is in the range of $[4.0e^{-6}, 5.9e^{-5}]$. The Figures 9, 11, 13 below, shows in details the R^2 metric which demonstrates the statement that test truth estimated values of a, b and D lattices and the predicted computed values are almost equal. In addition, the truth/predicted discrepancies in the Figures 10, 12, 14, are very small and even zero 0.

T_n	θ	$Ndip$	$Vdip$	$Trec$	P_{sol}	D_{sol}	H_{sol}	A_{sol}	Exp^a	Est$^a_{G64}$	$\delta(Exp^a, Est^a_{G64})$
t_0	34.3569	7	7	500	1	0	0	0	4.6509	4.6509**004**	4.00e-07 †
t_1	27.0812	7	7	500	0	1	0	0	4.0830	4.0830	0.00
t_2	26.9573	35	7	500	0	0	1	0	4.6719	4.6719**003**	3.00e-07 †
t_3	34.4126	35	7	500	0	0	0	1	4.7613	4.7613	0.00
t_4	34.0546	6	7	400	1	0	0	0	4.6525	4.6525	0.00
t_5	26.8223	8	7	400	1	0	0	0	4.6620	4.6620	0.00
t_6	27.0714	35	2	400	1	0	0	0	4.6941	4.6941**004**	4e-07 †

(a) prediction of the Lattice parameter a in (x, y) direction using the GRU G^a_{64} Model.

T_n	θ	$Ndip$	$Vdip$	$Trec$	P_{sol}	D_{sol}	H_{sol}	A_{sol}	Exp^b	Est$^b_{G64}$	$\delta(Exp^b, Est^b_{G64})$
t_0	34.3569	7	7	500	1	0	0	0	2.270**9**	2.270**6723**	0.0002277
t_1	27.0812	7	7	500	0	1	0	0	2.19**26**	2.19**11268**	0.0014732
t_2	26.9573	35	7	500	0	0	1	0	2.277**7**	2.277**169**	0.0005310
t_3	34.4126	35	7	500	0	0	0	1	2.2**839**	2.2**905123**	0.0066123
t_4	34.0546	6	7	400	1	0	0	0	2.2**792**	2.2**806101**	0.0014101
t_5	26.827	7	7	400	1	0	0	0	2.2**703**	2.2**977521**	0.0274521
t_6	27.0714	35	2	400	1	0	0	0	0	1.1e-04	0.0001100

(b) prediction of the Lattice parameter b in z direction using the GRU G^b_{64} Model.

.

T_n	θ	$Ndip$	$Vdip$	$Trec$	P_{sol}	D_{sol}	H_{sol}	A_{sol}	Exp^D	Est$^D_{G64}$	$\delta(Exp^D, Est^D_{G64})$
t_0	34.3569	7	7	500	1	0	0	0	18.575	18.575**012**	1.2e-05
t_1	27.0812	7	7	500	0	1	0	0	11.3**8**	11.3**79986**	1.4e-05
t_2	26.9573	35	7	500	0	0	1	0	31.**5**	31.**49995**	5e-05
t_3	34.4126	35	7	500	0	0	0	1	65.32	65.32**002**	2.e-05
t_4	34.0546	6	7	400	1	0	0	0	12.633	12.63**2996**	4e-06
t_5	26.827	7	7	400	1	0	0	0	17.525	17.525**059**	5.9e-05
t_6	27.0714	35	2	400	1	0	0	0	105.1	105.1**0001**	1e-05

(c) prediction of the Gain Size parameter D using the GRU G^D_{64} Model.

Table 5: Experimental parameters Exp^a, Exp^b, Exp^D, versus Estimated Est^a_{G64}, Est^b_{G64}, Est^D_{G64} values.

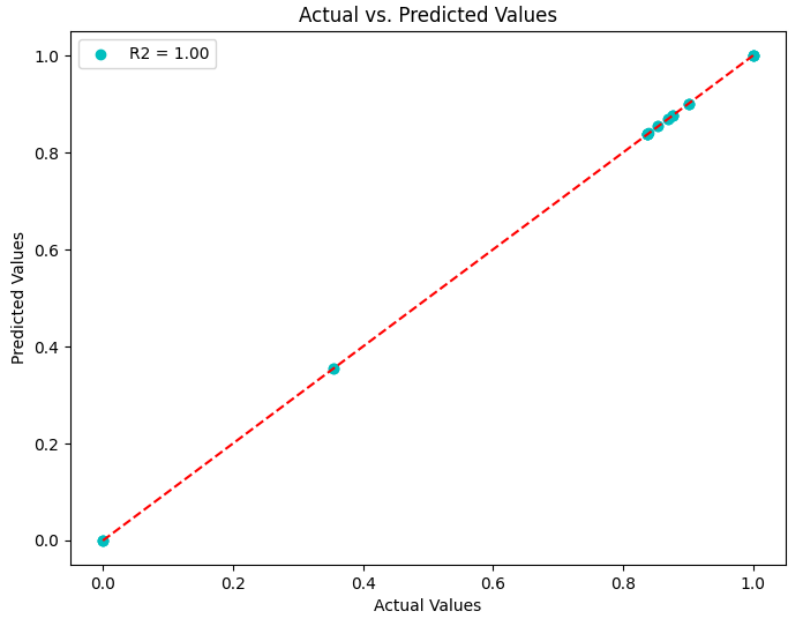

Fig. 9: $GRU^{a}_{(8,64,1)}$ Square R2 Metric.

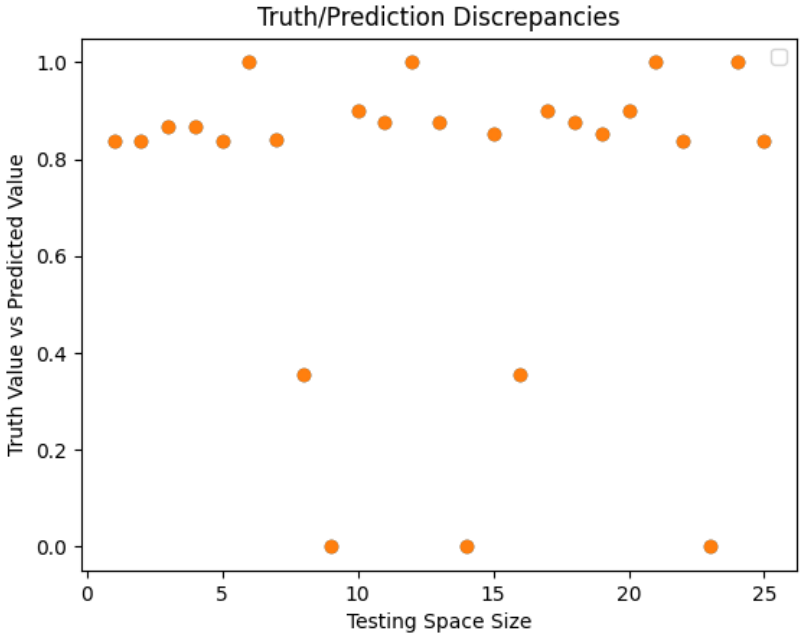

Fig. 10: $GRU^{a}_{(8,64,1)}$ Truth-Prediction Discrepancies.

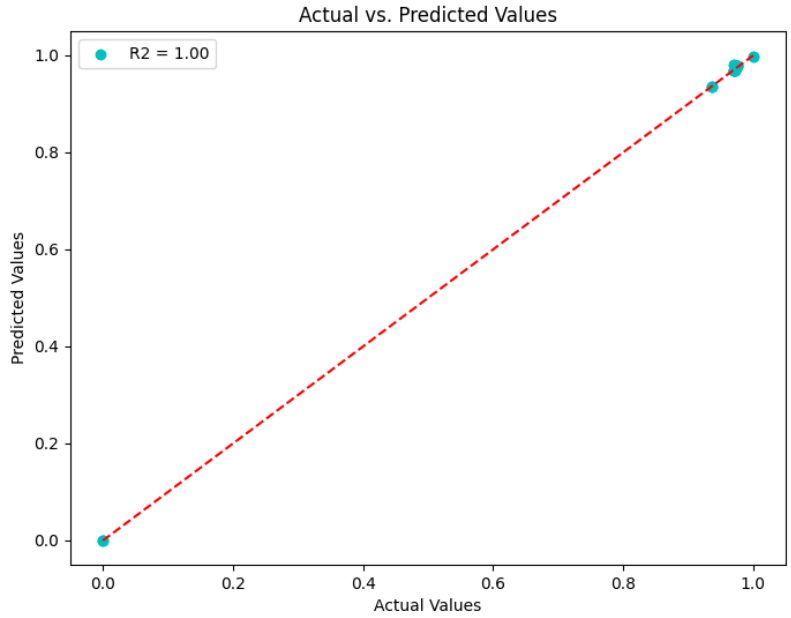

Fig. 11: $GRU^{b}_{(8,64,1)}$ Square R2 Metric.

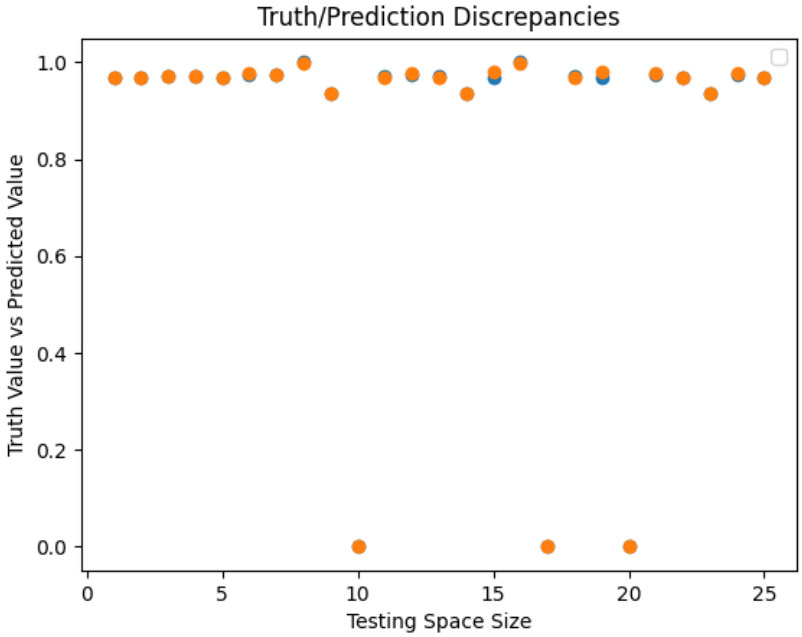

Fig. 12: $GRU^{b}_{(8,64,1)}$ Truth-Prediction Discrepancies.

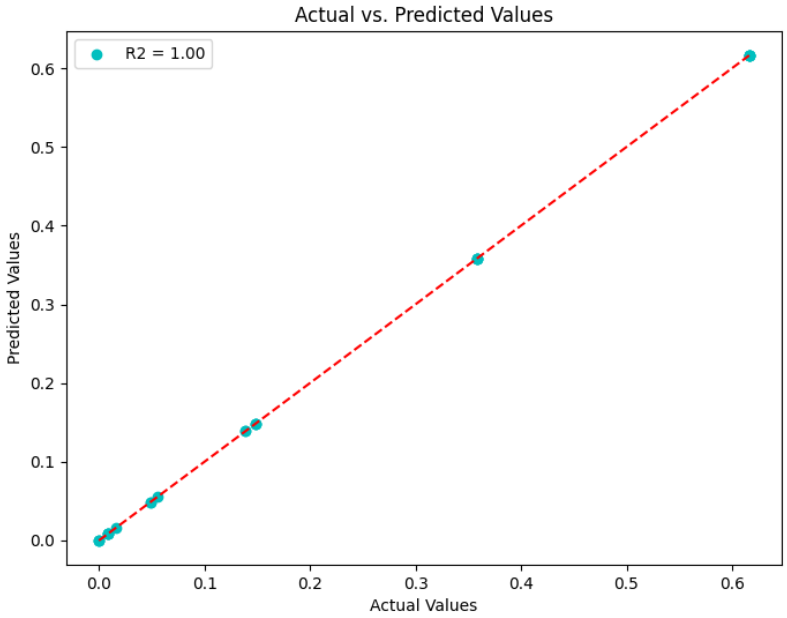

Fig. 13: $GRU^{D}_{(8,64,1)}$ Square R2 Metric.

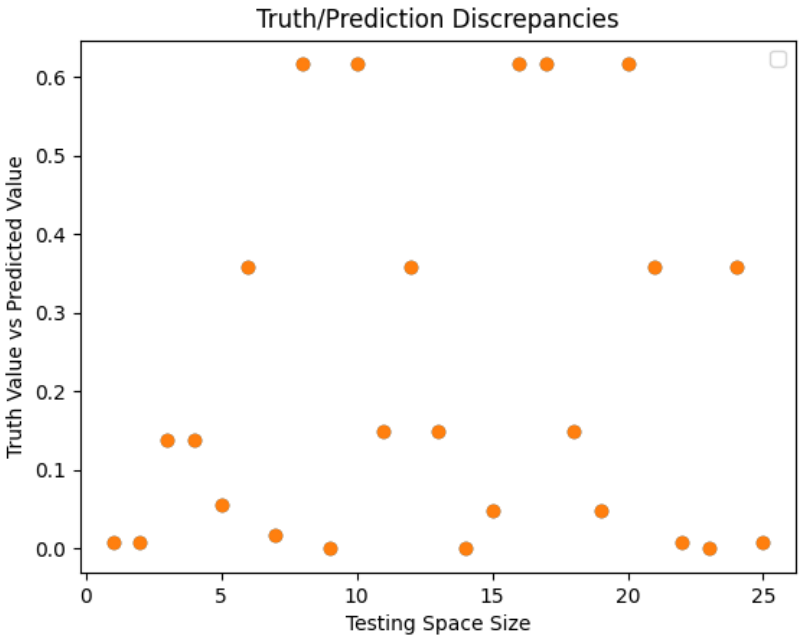

Fig. 14: $GRU^{D}_{(8,64,1)}$ Truth-Prediction Discrepancies.

6 Conclusion

This research work is very beneficial in the sense that it simplifies the hard an complex task of real experiments in materials physics. Indeed, the crucial role of characterization techniques in material physics, particularly emphasizing the significance of gathering data on various physical properties, is not always easy, especially for some methods such as X-ray diffraction that are widely used but still be challenging due to cost, complexity and safety. In brief and to streamline this process, X-ray diffraction outcomes for tin oxide (SnO2) thin films are produced via the Dip-Coating methods deposited onto glass substrates. Then, Various experimental parameters were adjusted to enhance the thin film properties for specific applications. In addition, The structural characteristics, including lattice parameters a and c and the grain size D, are computed, confirming the tetragonal phase of thin films in most cases. Finally, due to the extensive array of experimental parameters to be optimized across multiple samples, the use of artificial intelligence can be highly desirable to be considered. We have adopted the use of artificial intelligence techniques, particularly a Gated Recurrent Unit (GRU) model to predict but also estimate structural characteristics and many physical properties of materials.

The relevance and benefits of the proposed data-driven GRU-Based model Predictor for material properties characterization highlight the importance of AI in material physics and leverage discussion about this new pivotal AI methods for understanding and extracting structural properties of crystalline materials. Again, this may show the emphasizing on AI and its role in characterizing material properties across various fields, when limitations in terms of computation capacity for ab-initio calculation ans simulation methods. Our GRU models have gained prominence in enhancing X-ray diffraction's capabilities and strengthening predictions of materials' structural properties in an easy and safe thin films SnO2 characterization. Furthermore, we proposed a data-driven framework for material characterization, focusing on the proposed AI GRU model among others. In the soon future, we will continue exploit derive crystal properties through experimental data to design specific AI models that can facilitate and revolutionize the field of material science and characterization, offering solutions to the challenges faced by engineers and researchers when using traditional techniques and computational constraints.

References

1. Eric J Mittemeijer. *Fundamentals of materials science*, volume 8. Springer, 2010.
2. Peddavarapu Sivakumar, Harish Sharma Akkera, T Ranjeth Kumar Reddy, Yugandhar Bitla, V Ganesh, P Mohan Kumar, G Srinivas Reddy, and Madhukar Poloju. Effect of ti doping on structural, optical and electrical properties of sno2 transparent conducting thin films deposited by sol-gel spin coating. *Optical Materials*, 113:110845, 2021.
3. Abhinav Saxena, Kai Goebel, Don Simon, and Neil Eklund. Damage propagation modeling for aircraft engine run-to-failure simulation. In *2008 international conference on prognostics and health management*, pages 1–9. IEEE, 2008.
4. Asif Ali, Yi Wai Chiang, and Rafael M Santos. X-ray diffraction techniques for mineral characterization: A review for engineers of the fundamentals, applications, and research directions. *Minerals*, 12(2):205, 2022.
5. Xiao-Sheng Si, Wenbin Wang, Chang-Hua Hu, and Dong-Hua Zhou. Remaining useful life estimation–a review on the statistical data driven approaches. *European journal of operational research*, 213(1):1–14, 2011.
6. A Mosallam, K Medjaher, and N Zerhouni. Component based data-driven prognostics for complex systems: Methodology and applications. In *2015 First International Conference on Reliability Systems Engineering (ICRSE)*, pages 1–7. IEEE, 2015.

7. Xiao-Sheng Si, Zheng-Xin Zhang, Chang-Hua Hu, et al. Data-driven remaining useful life prognosis techniques. *Springer Series in Reliability Engineering*, 2017.
8. Felix O Heimes. Recurrent neural networks for remaining useful life estimation. In *2008 international conference on prognostics and health management*, pages 1–6. IEEE, 2008.
9. Zhigang Tian. An artificial neural network method for remaining useful life prediction of equipment subject to condition monitoring. *Journal of Intelligent Manufacturing*, 23(2):227–237, 2012.
10. Anton Jesche, M Fix, Andreas Kreyssig, William R Meier, and Paul C Canfield. X-ray diffraction on large single crystals using a powder diffractometer. *Philosophical magazine*, 96(20):2115–2124, 2016.
11. Xiaoning Tang and Xiong Yan. Dip-coating for fibrous materials: mechanism, methods and applications. *Journal of Sol-Gel Science and Technology*, 81:378–404, 2017.
12. C Jeffrey Brinker. Dip coating. In *Chemical Solution Deposition of Functional Oxide Thin Films*, pages 233–261. Springer, 2013.
13. Thomas Degen, Mustapha Sadki, Egbert Bron, Uwe König, and Gwilherm Nénert. The highscore suite. *Powder diffraction*, 29(S2):S13–S18, 2014.
14. Farhad Mortezapour Shiri, Thinagaran Perumal, Norwati Mustapha, and Raihani Mohamed. A comprehensive overview and comparative analysis on deep learning models: Cnn, rnn, lstm, gru. *arXiv preprint arXiv:2305.17473*, 2023.
15. Faiza Bouamra, Mohamed Sayah, Sadek Labib Terissa, and Noureddine Zerhouni. A smart gru-based estimator for sno2 thin films characteristics. In *ICCAP 2023: 2nd International Conference on Computational and Applied Physics, University Blida1, Algeria*, pages 1–4. IEEE, 2023.
16. Bernard Dennis Cullity. *Elements of X-ray Diffraction*. Addison-Wesley Publishing, 1956.
17. Victor Drits, Jan Środoń, and DD Eberl. Xrd measurement of mean crystallite thickness of illite and illite/smectite: Reappraisal of the kubler index and the scherrer equation. *Clays and clay minerals*, 45:461–475, 1997.
18. Alex Sherstinsky. Fundamentals of recurrent neural network (rnn) and long short-term memory (lstm) network. *Physica D: Nonlinear Phenomena*, 404:132306, 2020.
19. Mohamed Sayah, Djillali Guebli, Zeina Al Masry, and Noureddine Zerhouni. Robustness testing framework for rul prediction deep lstm networks. *ISA transactions*, 113:28–38, 2021.
20. Mohamed Sayah, Djillali Guebli, Z Noureddine, and Zeina Al Masry. Deep lstm enhancement for rul prediction using gaussian mixture models. *Automatic Control and Computer Sciences*, 55:15–25, 2021.
21. I Remadna, SL Terrissa, M Sayah, S Ayad, and N Zerhouni. Boosting rul prediction using a hybrid deep cnn-blstm architecture. *Automatic Control and Computer Sciences*, 56(4):300–310, 2022.
22. Ikram Remadna, Labib Sadek Terrissa, Zeina Al Masry, and Noureddine Zerhouni. Rul prediction using a fusion of attention-based convolutional variational autoencoder and ensemble learning classifier. *IEEE Transactions on Reliability*, 72(1):106–124, 2022.
23. Kyunghyun Cho, Bart van Merriënboer, Dzmitry Bahdanau, and Yoshua Bengio. On the properties of neural machine translation: Encoder–decoder approaches. In *Proceedings of SSST-8, Eighth Workshop on Syntax, Semantics and Structure in Statistical Translation*, pages 103–111, Doha, Qatar, October 2014. Association for Computational Linguistics.
24. Miao Xu, Hongfei Liu, and Hongbo Yang. A deep learning based multi-block hybrid model for bike-sharing supply-demand prediction. *IEEE Access*, 8:85826–85838, 2020.
25. R Alan May and Keith J Stevenson. Software review of origin 8, 2009.

ISSN: 0067-3064

Analyzing mixing quality in a T-shaped micromixer for moderate Reynolds number flow

O. HADJ RAHMOUN ,T. TAMSAOUT, K. KHELOUFI, E. H. AMARA

Centre de Développement des Technologies Avancées, Laser Material Processing Team, PO. Box 17 Baba-Hassen, 16303 Algiers, Algeria

Abstract:

The micromixers are one of the most important components for microreaction technology in the wide range of industries, especially in chemical and biological fields where mixing is used to facilitate chemical and biological effects. In this work, a numerical study of a T-shaped micromixer channel for laminar regime flow. The continuity and momentum equations, as well as the advection-diffusion equation are so lved to evaluate the mixing performance.

The main objective is to identify the critical values of the transition from the stratified regime to the vortex regime as well as to the engulfment regime for three different dimensions of the T-shaped micromixer and to describe the relationship between the flow characteristics and the values of mixing to suggest possible geometrical modifications to promote mixing. The results show that for the three different dimensions of T-shaped micromixer, the maximum values of mixing index is attended in the beginning of engulfment flow regime**.**

Key words:
T-shaped micromixers; microreactors; microreaction technology, CFD-simulation.

1. Introduction

Microfluidic devices, mainly micro T-mixers, are too important for various processes in microreactor technology, such as: fine chemical, pharmaceutical, medical and food industries [1-3].

Compared by conventional macroscale systems the microreactor ensure the continuity of production, the control of operation with high area-to-volume ratio, efficient heat transfer ability, the avoidance of hot spots by effective temperature control, which ensures the exalt quality of the chemical reaction [4,5].the microfluidic part must be inexpensive and simple to integrate with other parts of the reactor, such characteristics are fulfilled by passive micromixers made by 3d printing where the mixing is favored without the help of any power source external[6] and manufacturing chold be design fast fabrication and modified with low costs[7].

One of the simplest designs of passive micro-mixers is a T shape, in which the inlets join the main channel withT-shaped branches. This type of mixer is also suitable for carrying out fundamental studies, as the T-shaped micro-mixer is often encountered as a junction element in more complex micro-systems. The characteristics of these devices and, in particular, their efficiency in effectively mixing two liquid streams, has been largely studied in previous investigations. [8-10].

The flow in T-shaped mixer can descriped by different flow regimes have been identified, depending on the Reynolds number, Re, namely: the stratified, the vortex, the engulfment and the unsteady flow regimes [4].
the succes of the majority of microchemical processes depends by the efficiency and speed of mixing.
from the 2000s to the present day, the Research is still ongoing where works have been developed and studied according to different mixing principles such as properties of fluids [11-12]and dimension of mixer [13-14] for a well-chosen application.
In this paper, a computation of fluid dynamics in a T-shaped micromixer channel for laminar regime flow. To identify the critical values of the transition from the stratified regime to the vortex regime as well as to the engulfment regime for three different dimensions of the T-shaped micromixer .

2. Mathematical model and numerical simulation

Our work focuses on the evaluation of two different fluids mixing within the T- channel and it shown in figure 1.

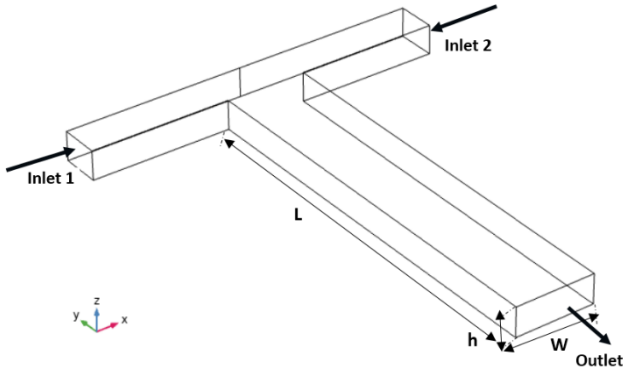

Figure. 1. The adopted geometry.

The microchannel cross-section dimension is h=200µm (height); w=400µm (width); the total length of the channel is 6000µm. The performed numerical simulation is based on solving a three-dimensional incompressible flow using Navier-Stokes and convection-diffusion equations at steady state,implemented in CFD functions of COMSOL Multyphysics .
The performed numerical simulation is based on solving a three-dimensional incompressible flow using Navier-Stokes and convection-diffusion equations at steady state[15,16], implemented in CFD functions of COMSOL Multyphysics [17] .

The two main equations to be solved are:

$\rho(V.\nabla)V$ — $\nabla.\eta(\nabla V + (\nabla V)\,T\,) + \nabla p = 0$ (1)

Where $\nabla.V = 0$

The convection –diffusion equation is:

$\nabla^2 C - V.C = 0$ (2)

Where ρ denotes the fluid density (Kg/m^3),
V is the linear velocity of the fluid (m/s),
denotes the ηfluid viscosity of interest (Pa.s),
p is the pressure (Pa),
D denotes the diffusion coefficient (m^2 /s) and C represents the concentration (mol/m^3).

ISSN: 0067-3064

2.1. **Parameters used in the simulation**

We consider a laminar regime for the inlet flows and the boundary conditions were set as follows:

- Channel Outflow gauge pressure p = 0 Pa,
- Flows Velocity at the channel walls u = 0 m/s,
- Fluid concentrations of the ethanol in the two inlets C01=0.017 mol/m ^{3} and C02=0 mol/m^3 respectively in the left and right inlets.

The considered fluids were composed of ethanol (solute) and water (solvent). The other parameters used in the simulation were:

- Molecular diffusion coefficient for the solute in the solvent.

And D = 21.10-10 m ^{2} /s, Assuming that the fluids are aqueous solutions for which the density ρ= 998 Kg/m ^{3} and the viscosity

η =0.001 N.s.m^{-2} [17, 18].

To achieve the mixing index MI, we start with measuring the relative variance of the concentration profile σ, which is given by:

$$\sigma = \int_{kx}(C - \overline{C})^2 dA / \int_{dx} dA \qquad (3)$$

$$MI = 1 - \sqrt{\frac{\sigma^2}{\sigma^2_{max}}} \qquad (4)$$

kx is the y-z plane intersecting the mixing structure at the x coordinate axis. C is the concentration distribution at the selected cross-section plane, $\overline{C}$ is the averaged value of the concentration field on the plane, A is the area of the plane and σ_{max} is the maximum standard deviation (unmixed at the exit). MI reaches 0 for a complete segregated system and 1 for the homogeneously mixed case [18, 19, 20].

2.2. **Grid optimization**

To minimize the errors and optimize the grid, we have performed a grid-dependence study, 2000µm from the inlet of channel for a Reynolds number Re=225, by the examination of the mixing index dependency on different grid sizes or number of cells.

The grid dependence analysis was carried out and the results are shown in Figure 2.

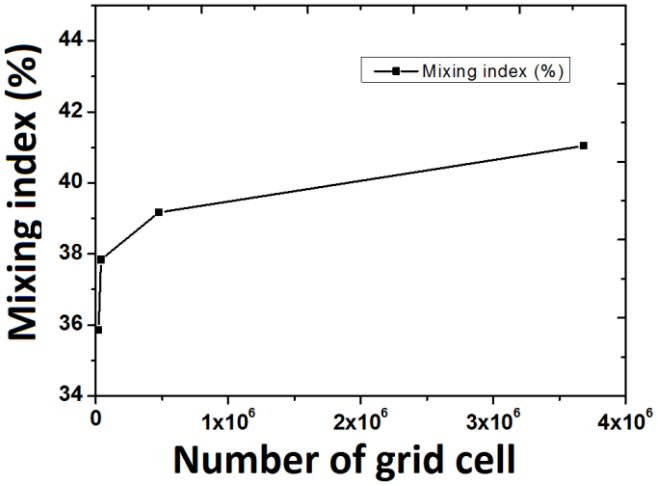

Figure. 2. Dependency of mixing index compared with the number of grid cells (Re=225).

The calculations highlighted that the average mixing index at 2000µm from the inlet of channel. Reaches a steady solution (variation is less than 1% in comparison with the previous iteration). We used in the simulation the tetrahedral grid for the entire channel, with 3682528-grid cell.

ISSN: 0067-3064

3. Results and discussion

The variation of the mixing index MI with Reynolds number at 1000µm from the inlet of channel. for three different dimensions of T-shaped micromixer the variation of the mixing index MI with Reynolds number at 1000µm from the inlet of channel.

3.1. Flow behavior in the micromixer

the figure3 shows the mixing quality for three different dimension of T-shaped mixer of (100x200),(200x400)and(300x600) (notation: (depth of channel in µm x width of mixing channel in µm) with increasing Reynolds number at a channel position of 1 mm from the inlet.

For Re from 5 to 50 : in this range, we observe an increasing rate which can conclude that the diffusion mechanism dominates the mixture.

2. For Re from 50 to 200 : The vortex flow where inertial effects become important and Dean-like rolls appear in the outlet channel,
3. For Re from 200 to 500: the engulfment flow , at a critical Reynolds number the flow breaks the symmetry.

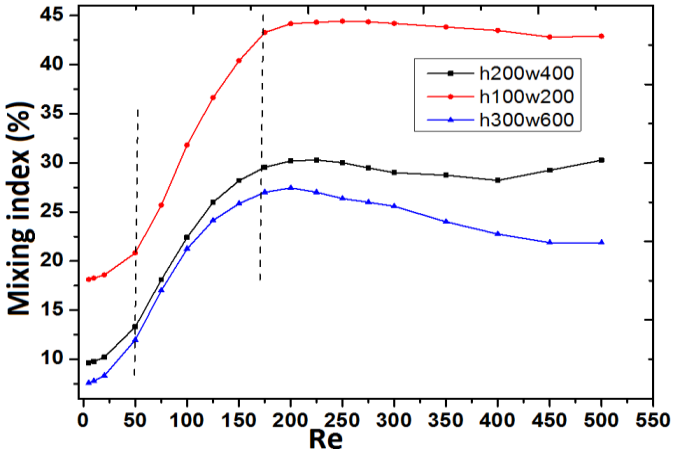

Figure 3. Variation of the mixing index in function of the Reynolds number Re for thrre dimensions of T-shaped micromixer.

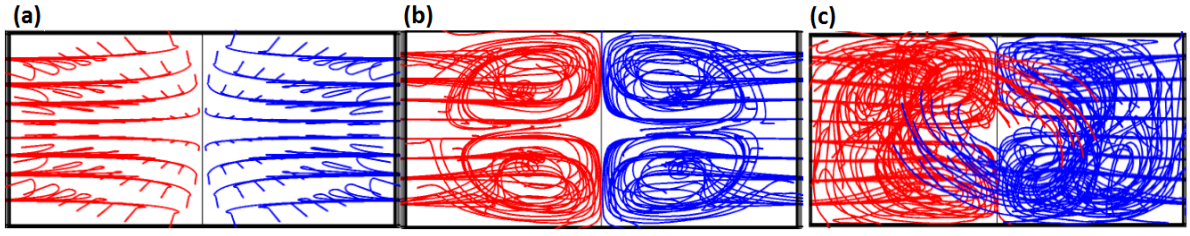

Figure4.. Schematic of the junction of T-channel with dimension (300x300x600) mixer; rear view looking downstream in positive x-direction; (a)symmetric stratified flow at Re=10; (b)symmetric vortex flow at Re=100; and (c)asymmetric engulfed flow regime at Re=275.

The figure4 chows a schematic of the junction of T-channel with dimension (300x300x600) mixer; rear view looking downstream in positive x-direction; (a)symmetric stratified flow at Re=10; (b)symmetric vortex flow at Re=100; and (c)asymmetric engulfed flow regime at Re=275.

ISSN: 0067-3064

L'écoulement résultant dans le canal de sortie peut être caractérisé par trois régimes d'écoulement lors d'un écoulement laminaire : un écoulement dit « stratifié », un écoulement « vortex » et un écoulement « engloutissement ».

3.2.Effect of the geometrical parameter on the anset of engulfment regime .

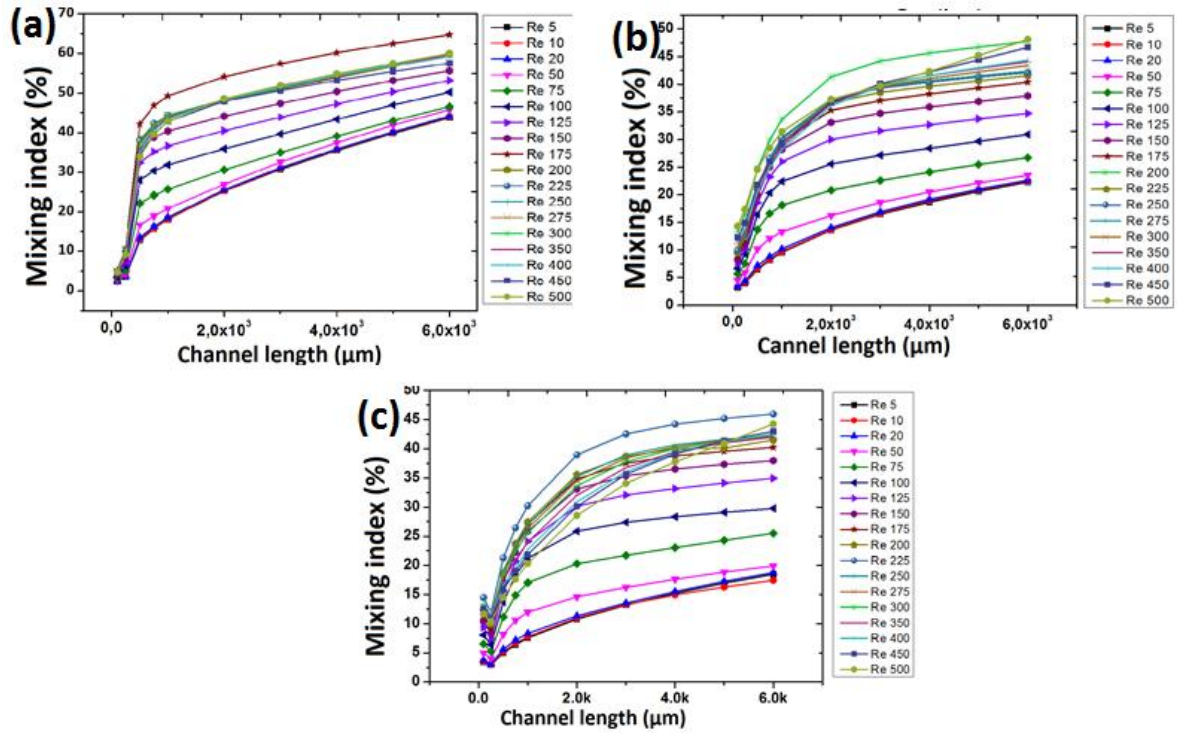

Figure 5. Variation of the mixing index in function of channel length for differends Reynolds number Re of **(a)** 100x100x200 mixer **.(b)** 200x200x400 mixer.**(c)** 300x300x600 mixer.

We observe in figure 5 that all the curves are increasing rapidly with an initial slope between 0 and 200, then increase slowly with a low slope and tend to stabilize from 1500.
in Figure 5a, the best mixing index is obtained for a Reynolds number of Re=175, in Figure 5b, the best mixing index is obtained for a Reynolds number of Re=200 ,in Figure 5b the best mixing index is obtained for a Reynolds number of Re=225.

Conclusion:
Using numerical simulation for three different dimensions of T-shaped mixer, we observe the occurring of three flow laminar flow regimes in the mixing cannel:
1.For Re from 5 to 75 : This flow regime was defined as being where the flow streamlines remain primarily unidirectional and essentially follow the curvature of the Geometry.
2. For Re from 75 to 200 : The vortex flow where inertial effects become important and Dean-like rolls appear in the outlet channel,
3. For Re from 200 to 500: the engulfment flow , at a critical Reynolds number the flow breaks the symmetry.
- At the beginning of engulfment flow in the three dimensions we have the maximum of mixing index,the value of the beginning of engulfment flow is Re=175 for 100x100x200µm, and it's Re=200 for 200x200x400µm and is Re=225 for 300x300x600µm.
- For all dimensions we have to use the value of the beginning of engulfment flow and we must use another mechanism to increase the mixing after 2000µm.

References

[1]Paul watts and Stephen J.haswell,the application of microreactors for small organic synthesis Chem.eng.technol.2005.28,no.3.
[2]Anita Šalić1 , Ana Tušek2 , Bruno Zelić1, Application of microreactors in medicine and biomedicine
J Appl Biomed. 10: 137–153, 2012
[3]Mahito Atobe, Hiroyuki Tateno, and Yoshimasa Matsumura. Applications of Flow Microreactors in Electrosynthetic Processes Chem. Rev. 2018, 118, 4541−4572
[3] Xingjun Yao a,n , Yan Zhang a , Lingyun Du a , Junhai Liu a,n , Jianfeng Yao b,n
Review of the applications of microreactors, Renewable and Sustainable Energy Reviews 47 (2015) 519–539
[4] A. Soleymani a, H. Yousefi b, I. Turunena, Dimensionless number for identification of flow patterns inside a T-micromixer, Chemical Engineering Science 63 (2008) 5291 – 5297.
[5]Simone camarri ,Alessandro mariotti,Chiara gallettti,elisabetta brunazzi,Roberto mauria victtoria salvetti, An Overview of Flow Features and Mixing in Micro T and Arrow Mixers, *nd. Eng. Chem. Res.* 2020, 59, 9, 3669–3686
[6] Oum El Kheir Hadj Rahmoun, Noureddine Tayebi and Mohamed Saighi, Optimization of slanted grooved micromixer with a serpentine channel at a lower Reynolds number, Int. J. Chem. React. Eng. 2021; 19(12): 1363–1373.
[7] Junyao Wang, 1 Yunpeng Li, 1 Huan Liu, 1,a) Gongchen Sun, 1 Xingyu Chen, 1 Tianhong Lang, 1 Rui Wang, 1 Bowen Cui, 1 and Hengyi Yuan2,a) A 3D passive micromixer with particle of stochastic motion through limonene dissolution method, *AIP Advances* 11, 105318 (2021).
[8] Xiangsong Feng,1 Yukun Ren,1,2,a) and Hongyuan Jiang1, An effective splitting-and-recombination micromixer with self-rotated contact surface for wide Reynolds number range applications, BIOMICROFLUIDICS 7, 054121 (2013).
[9] Andrey V. Minakov 1,2,*, Alexander S. Lobasov 1,2, Anna A. Shebeleva 1 and Alexander V. Shebelev 1,2; Analysis of Hydraulic Mixing Efficiency in Widespread Models of Micromixers; Fluids 2020, 5, 211; doi:10.3390/fluids5040211
[10] Jing-Wei Zhanga , Wei-Feng Lia,□ , Xin-Lei Xua , M. El Hassanb,c , Hai-Feng Liua , Fu-Chen Wang; Effect of geometry on engulfment flow regime in T-jet reactors; Chemical Engineering Journal 387 (2020) 124148
[11] Chiara Galletti n , Giacomo Arcolini, Elisabetta Brunazzi, Roberto Mauri, Mixing of binary fluids with composition-dependent viscosity in a T-shaped micro-device; Chemical Engineering Science 123 (2015) 300–310.
[12]A.S. Lobasova,b,□ , A.V. Minakova,b, Analyzing mixing quality in a T-shaped micromixer for different fluids properties through numerical simulation; Chemical Engineering & Processing: Process Intensification 124 (2018) 11–23
[13] Siva Kumar Reddy Cherlo, S. Pushpavanam; Effect of depth on onset of engulfment in rectangular micro-channels; / Chemical Engineering Science 65 (2010) 6486–6490
[14] Simone Camarri; T-shaped micromixers aligned in a row: characterization of the engulfment regime, Acta Mech 233:1987–2077 (2022).
[15] M.Camesasca, I. M. Zloczower, and M. Kaufman, Micromech. Microeng 15, 2038 (2005).
[16] H. A. Stone, A. D. Stroock, and A. Ajdari, annu rev fluid Mechanics 36,381 (2004)

[17]Comsol Multiphysics .availabale online: https://www.comsol.fr/support/download/5.4./
[18]D.Yan , Z. Zhiyi , C. Yim, L. Min , and C. Xudong , Micromachines 1, 19 (2010).
[19]. S .Parez, G. Guevara-carrion, H. Hasse, and J. Vrabec ,Phys chem,chem .Phys 15 ,3985 (2013)
[20]S.Hossain, A.Husain, and K.Y. Kim, Engineering applications of computational fluid mechanics 5, 506 (2011).

First-principles study on the Structural, electronic and optical properties of double perovskites K2AgAsBr6 for solar cell application.

Samir CHAREF [a], Abdenacer ASSALI [b], Abdelkader BOUKORTT [a]

[a] *Elaboration and Characterization Physical Mechanics and Metallurgical of Materials (ECP3M) Laboratory, Abdelhamid Ibn Badis University-Mostaganem, Route Nationale N°11, Kharrouba, 27000 Mostaganem, Algeria.*
[b] *Research Unit in Optics and Photonics- Center for Development of Advanced Technologies (UROP- CDTA), University of Setif, 1, El-Bez, 19000 Setif. Algeria.*

[*]Email : samir.charef.etu@univ-mosta.dz

Abstract

Double Perovskites are among the most promising materials for solar cells application. In this work, we will focus on the structural, electronic and optical properties of the lead-free double perovskite K2AgAsBr6, using the full-potential linearized augmented plane-waves method (FP-LAPW), based on density functional theory (DFT), implemented in the WIEN2K code, the exchange-correlation potential is treated with the approximations nKTP-mBJ-GGA. The structural parameters are calculated through optimization and analytical schemes. The bandgaps of K2AgAsBr6 has been calculated to be 1.34 eV, enabling various optoelectronic and transport applications. Furthermore, the absorption coefficient ranges from infrared to visible and ultraviolet regions, increasing their significance for diverse applications in optoelectronics.

1. Introduction

A novel category of materials, known as perovskites, has recently emerged as highly promising contenders to replace silicon in the production of cost-effective and efficient solar cells. What sets perovskite materials apart is their remarkable capacity to generate more electricity from sunlight. These materials exhibit a distinctive crystalline structure reminiscent of a metal that shares its name with the perovskite family. Interestingly, this metal, originally identified by the German scientist Gustav Rose back in 1839, was named "perovskite" and corresponds to calcium titanate (CaTiO3). In contemporary research, the focus has shifted towards exploring another alternative class of compounds known as double perovskite halides. These compounds, denoted by the general formula A2BB'X6, exhibit semiconductor properties that render them exceptionally well-suited for cutting-edge photovoltaic applications. This research direction is driven by the desire to further advance the capabilities of solar cell technology. In light of the existing literature and these developments, our study has undertaken a comprehensive examination of the structural, electronic, and optical properties of a specific compound, K2AgAsBr6. This choice is motivated by the compound's optimal bandgap values, which hold significant promise for large-scale industrial production of highly efficient solar cells. Our investigation seeks to contribute to the ongoing advancement of photovoltaic technology, leveraging the potential of K2AgAsBr6 as a valuable Material in the pursuit of more efficient and accessible solar energy solutions.

2. Computational methods

The structural, electronic, and optical properties discussed in this study were investigated using the FP-LAPW method, which was implemented in the WIEN2K code within the framework of density

ISSN: 0267-3064

functional theory (DFT). The exchange-correlation functional employed was the generalized gradient approximation (GGA), specifically using the modified exchange approach of Becke-Johnson (mBJ).

The compound under investigation, K2AgAsBr6, is observed to possess a face-centered cubic structure, as illustrated in Figure 1. This crystal structure belongs to the Fm3m (225) space group. The atomic positions within the crystal structure are as follows: K is located at the (8c) site with coordinates (0.25, 0.25, 0.25), Ag is positioned at the (4a) site with coordinates (0.0, 0.0, 0.0), As is found at the (4b) site with coordinates (0.5, 0.5, 0.5), and Br occupies the (24e) site with coordinates (ux, 0, 0).
In our calculations, the RMT parameter Kmax was set to 8. Additionally, a K-mesh of size 10x10x10 was used to sample the Brillouin zone.

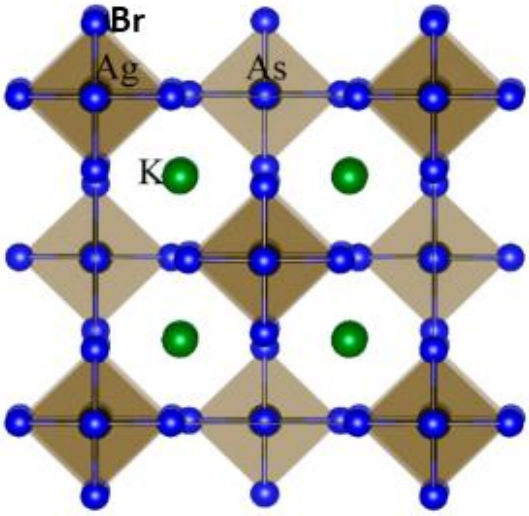

Fig. 1 Crystal structure of K2AgAsBr6 Halide double perovskite compound.

3. Results and discussion

3.1 Structural properties

In order to determine the configuration with the lowest energy, we conducted an analysis of the total energy concerning variations in the unit cell's volume. This analysis was carried out using Birch-Murnaghan's equation of state, and the results are presented in Figure 2.
Birch-Murnaghan's equation of state is commonly employed for investigating the equilibrium properties of materials. It enables us to identify the optimal volume of the unit cell, representing the configuration with the lowest total energy. By systematically adjusting the volume of the elemental cell and calculating the associated total energy at each volume, we can pinpoint the system's equilibrium state.
Figure 2 illustrates the relationship between the total energy and the unit cell's volume. The curve derived from Birch-Murnaghan's equation of state allows us to determine the volume at which the total energy reaches its minimum, thus identifying the most stable configuration of the material.
This analysis of the structural properties yields valuable insights into the optimal arrangement of K2AgAsBr6, shedding light on its stability and potential applications across various fields

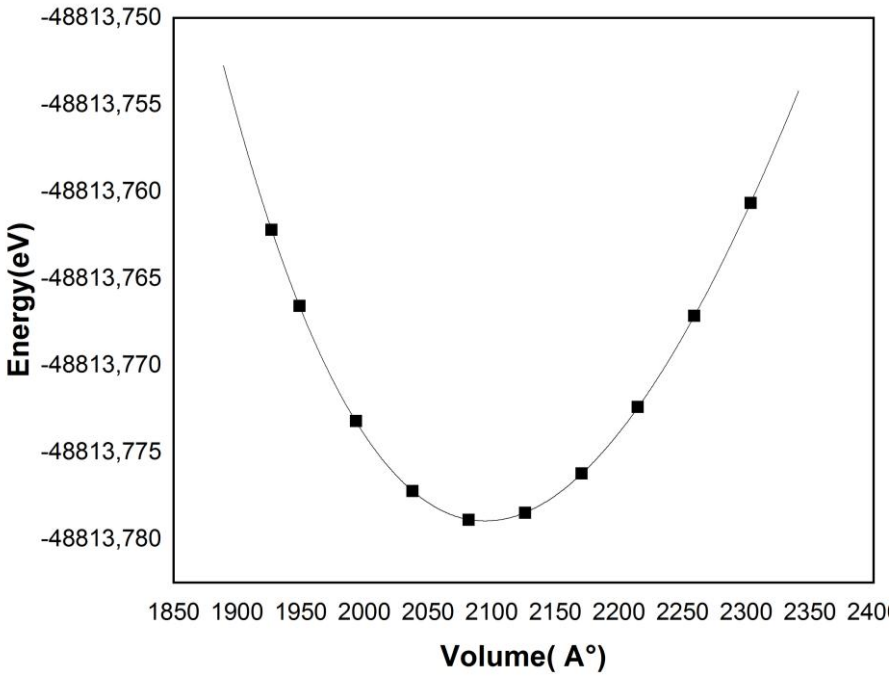

Fig. 2 Variation of the total energy as a function of volume for the K2AgBiBr6 halide double perovskites.

Table 1: Optimized Structural Parameters for Cs2AgBiI6 Cs2AgAsBr6 Double Perovskite.

K2AgAsBr6	a_0(A°)	B’	E	B0(GPa)	Eg(eV
Present work	10.75	4.86	-48813.778962	31.19	1.34
[1]	10.96	-	-	25.92	1.48
[2]	10.42	-	-	39.61	1.6

3.2 Electronic properties

The electronic band structure of the halide double perovskite K2AgAsBr6, calculated using the nKTP-mBJ approximation along high symmetry directions in the Brillouin zone, is presented in Figure 3. It's noteworthy that in K2AgAsBr6, the band gap is indirect and corresponds to the transition from X to L. The calculated energy gap measures 1.34 eV, signifying the semiconductor nature of the material. A summary of these obtained values, along with others, is provided in Table 1.

Figure 4 visually demonstrates the contributions of each atom's orbitals to the materials under investigation in this study. The s-states of K, d-Ag, s-As, p-As, d-As and p-Br play a substantial role in shaping the valence bands, whereas the s-As, p-As, d-As and p-Br are instrumental in forming the conduction bands.

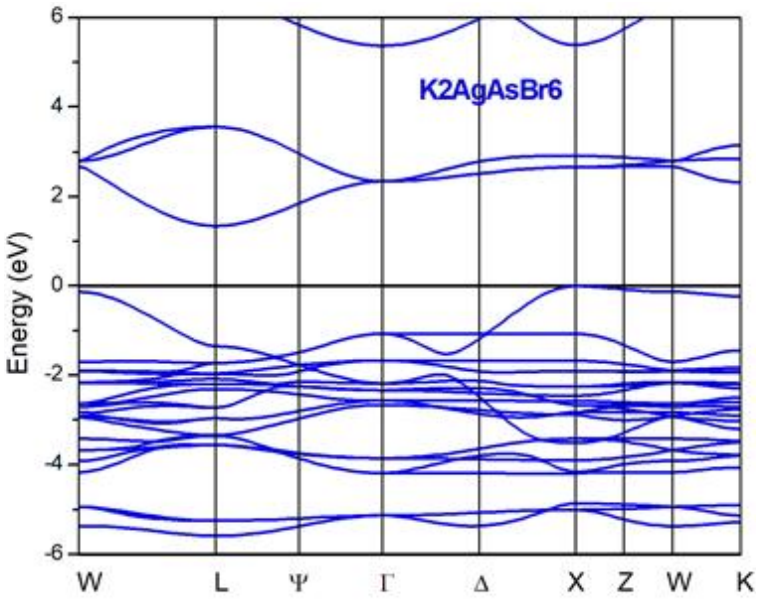

Fig. 3 Band structure of K2AgAsBr6 halide double perovskite.

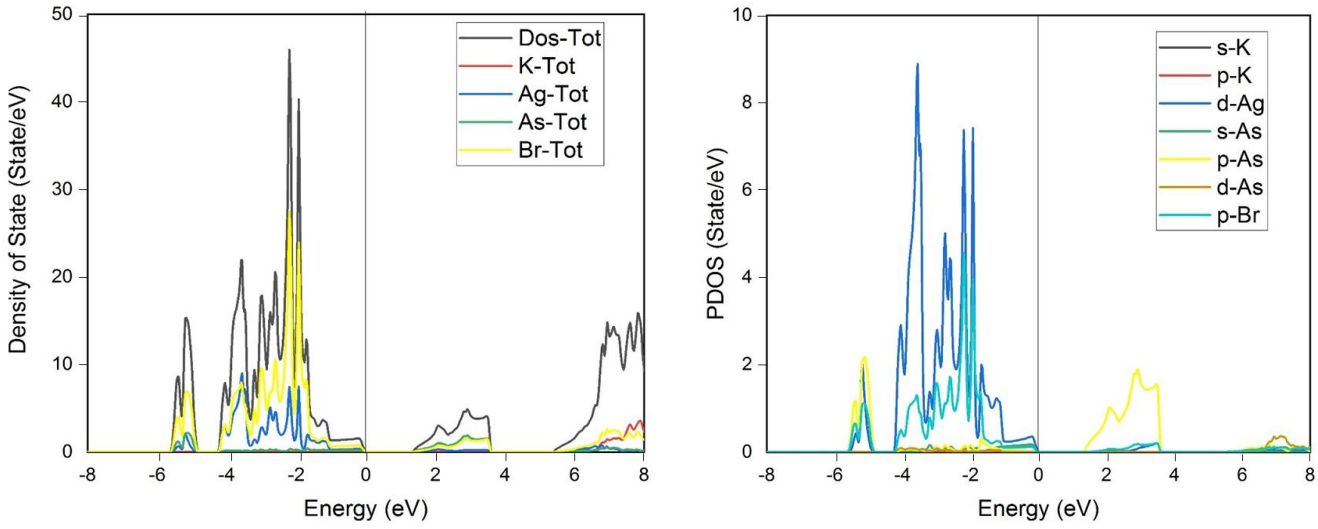

Fig. 4 Total and parietal density of states of K2AgAsBr6 halide double perovskite.

3.3 Optical properties

DFT (Density Functional Theory) is a method that allows for the calculation of a range of optical properties, including the absorption coefficient, refractive index, extinction coefficients, and conductivity. These properties are derived from the dielectric function, which is expressed as:

$\varepsilon = \varepsilon_1 + i\varepsilon_2$,

where ε_1 represents the real part, and ε_2 represents the imaginary part.
In Figure 5, you can see the absorption coefficient, real part ε_1, and imaginary part ε_2 of the dielectric function for K2AgAsBr6 as a function of photon energy. It is notable that the optical absorption of these

compounds occurs in the energy range of 2.59 to 3.69 eV, corresponding to energies within the visible to ultraviolet spectrum. The curves depicting the complex dielectric function ε(ω) display several significant peaks: 2.44 and 2.95 for the real part, and 2.6 and 3.61 for the imaginary part. These peaks in the imaginary part are attributed to inter-band transitions, which are associated with the density of states as presented in Figure 4.

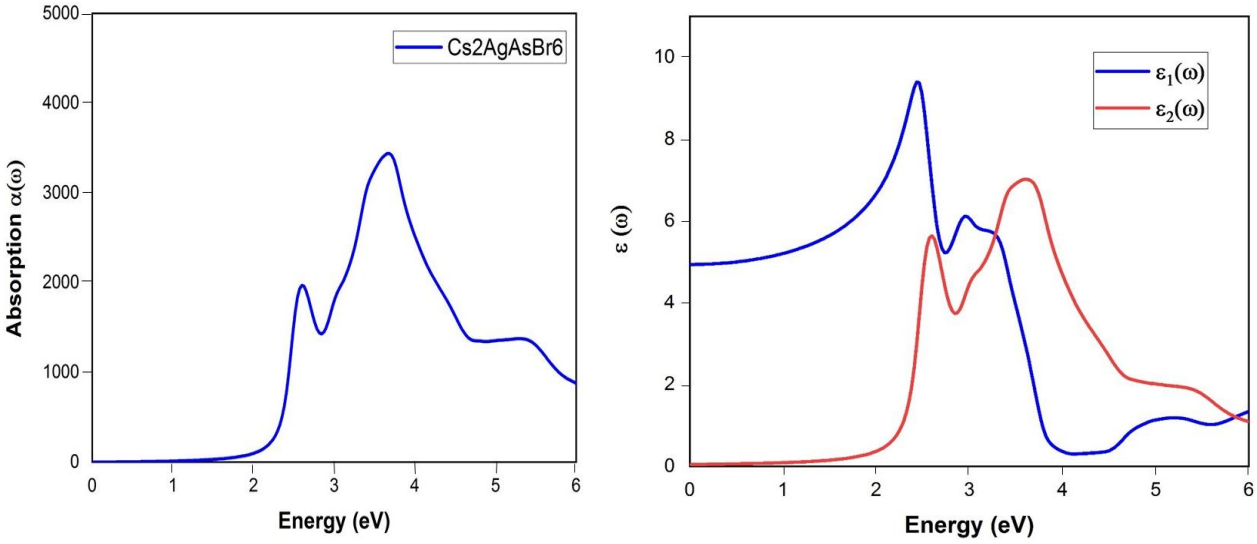

4. Conclusion:

In this study, we employed the Density Functional Theory (DFT) method with the nKTP-mBJ approximation to calculate the electronic and optical properties of halogenated Cs2AgBiI6. The lattice constant we obtained for our compound aligns well with other theoretical values. Electronic analysis revealed that the K2AgAsBr6 double perovskite exhibits semiconductor characteristics with an indirect energy gap. Additionally, these compounds demonstrated a high absorption coefficient within the visible and ultraviolet energy range, signifying significant potential for photovoltaic applications. These findings are noteworthy and underscore the suitability of K2AgAsBr6 for use in photovoltaic applications."

References

[1] Ali, Malak Azmat, et al. "The study of new double perovskites K2AgAsX6 (X= Cl, Br) for energy-based applications." *Journal of Taibah University for Science* 17.1 (2023): 2170680.
[2] Zanib, Maiza, et al. "A DFT investigation of mechanical, optical and thermoelectric properties of double perovskites K2AgAsX6 (X= Cl, Br) halides." Materials Science and Engineering: B 295 (2023): 116604.

ISSN: 0067-3064

Synthesis and elaboration of Polydimethylsiloxane/Titanium Dioxide Nanocomposite Films

Nadir BELGROUNE[1,a *], Assia BESSI[2,b], and Fadia NOUAS[2,c]

[1]Physical Chemical Laboratory of Inorganics Materials and their Applications (LPCMIA), University of Saad Dahlab Blida 1 (USDB 1), Soumâa Road PO Box 270, Blida 09000, Algeria

[2]Laboratory of molecular and macromolecular physical chemistry (LCPMM), University of Saad Dahlab Blida 1 (USDB 1), Soumâa Road PO Box 270, Blida 09000, Algeria

[a]belgroune_nadir@univ-blida.dz, [b]asieadz@yahoo.fr, [c]fadyanouas@gmail.com

Keywords: PDMS/TiO2, Nanocomposite Films, PDMS Polymer, TiO2 Nanoparticles

Abstract. This work describes the synthesis and characterization of Polydimethylsiloxanes/Titanium Dioxide (PDMS/TiO2) biopolymer nanocomposite films using two different synthesis methods: ex-situ and in-situ. The PDMS polymer were filled with titanium dioxide (TiO2) nanoparticles. The effects of varying ratios of TiO2 filler (3%, 5%, 10%, and 15%) on the film properties were investigated. The films were thin, ductile, and varied in transparency depending on the filler ratio. Various techniques scanning electron microscopy and optical microscopy were used to characterize the TiO2 nanoparticles and PDMS/TiO2 nanocomposite films. Results showed that the TiO2 nanoparticles had a perfect crystalline nanostructure. The analyses of the nanocomposite films confirmed the establishment of cross-linking between the matrix and the reinforcement. The bathochromic effect was shown in the filled films due to the presence of TiO2 nanoparticles in the polymer matrix. The addition of TiO2 nanoparticles modified the PDMS matrix properties, such as transparency and antibacterial activity, making it suitable for various applications such as food or biomedical packaging. In-situ synthesis resulted in better roughness and thickness due to medium dispersion of nanoparticles in the polymer lattice, as confirmed by optical microscopy. This comparative study demonstrates that both synthesis approaches can be used for PDMS/TiO2 nanocomposite films and provides insights into the advantages and disadvantages of each method and contributes to the development of new materials with unique properties in various sectors of the market.

Introduction

Nanocomposite materials have gained significant importance in recent years due to their unique properties and potential applications in various fields [1-3]. The combination of a polymer matrix and inorganic Nano-fillers provides enhanced mechanical, thermal, and barrier properties to the resulting nanocomposite films [3-5]. One such material is Polydimethylsiloxane/Titanium Dioxide (PDMS/TiO2) nanocomposite films[6-7]. These films can be tailored to specific applications such as food and biomedical packaging, solar cells, sensors, and energy storage devices[6-10]. Additionally, the incorporation of nanoparticles in the polymer matrix can also result in new functionalities such as antibacterial properties, self-cleaning properties and photocatalytic activity [6-7; 11-15]. The importance of nanocomposite films lies in their ability to provide improved properties over traditional polymer films, making them an attractive option for various industrial applications. With continued

ISSN: 0067-3064

research and development, nanocomposite films have the potential to revolutionize materials science and benefit many industries [1-2, 6, 15].

Polydimethylsiloxane/Titanium dioxide (PDMS/TiO2) nanocomposites are a type of thin films. The combination of both materials, PDMS and TiO2 nanoparticles, creates a synergistic effect, resulting in a material with enhanced properties such as improved transparency, mechanical strength, and antibacterial activity [6-7, 12-15]. The films can be prepared through various methods, including sol-gel, electrospinning, and spin coating [16-18]. The resulting PDMS/TiO2 nanocomposite films have found applications in a range of fields, including biomedical engineering, environmental remediation, and energy production [8, 19]. In biomedical engineering, these films have been used for drug delivery, wound healing, and tissue engineering [8-10]. In environmental remediation, the films have been used for air and water purification [19]. In energy production, the films have been used for solar cell applications due to their high transparency and photocatalytic properties [11, 13, 18-19]. Overall, PDMS/TiO2 nanocomposite films are a promising material with a wide range of potential applications.

While previous studies have explored the synthesis and characterization of PDMS/TiO2 nanocomposite films, there is still a need to investigate and compare different synthesis methods to determine the most effective approach [20]. This study aims to explore ex-situ and in-situ synthesis methods for PDMS/TiO2 nanocomposite films and investigate the effects of varying ratios of TiO2 filler on the film properties. The characterization of PDMS/TiO2 nanocomposite films is crucial to fully understand their properties and potential applications. Therefore, a range of analytical techniques, including, scanning electron microscopy, and optical microscopy, will be used to characterize the TiO2 nanoparticles and PDMS/TiO2 nanocomposite films [21-22].

Synthesis Methods

The synthesis and characterization of PDMS/TiO2 nanocomposite films have opened up new avenues for research and development in the field of advanced materials. In this study, we synthesized PDMS/TiO2 nanocomposite films using two different methods: ex-situ and in-situ. However, The addition of TiO2 nanoparticles modified the properties of the PDMS matrix, resulting in a range of new properties in the resulting nanocomposite films. Here, we discuss some of the key properties of PDMS/TiO2 nanocomposite films Overall, the characterization of the TiO2 nanoparticles and PDMS/TiO2 nanocomposite films provided valuable insights into the structure and properties of the nanocomposite material, which is essential for understanding their potential applications. In the next section, we present the description of the synthesis methods of PDMS/TiO2 nanocomposite films in detail.

Description of the synthesis methods (ex-situ and in-situ). The polymer used for this work is the PDMS SYLCAP 284-S (STANDARD CURE) silicone elastomer kit from MicroLubrol that is widely used in various applications due to its unique properties, such as high flexibility, optical transparency, and good biocompatibility [23]. This PDMS biopolymer were filled with titanium dioxide (TiO2) nanoparticles to obtain PDMS/TiO2 nanocomposite films. Two different synthesis methods were used to prepare the PDMS/TiO2 nanocomposite films: ex-situ and in-situ methods. The experimental process to elaborate film based on PDMS and PDMS filled with TiO2 nanoparticles was detailed.

1. Experimental protocol for Elaboration of PDMS film*:* The PDMS (Polydimethylsiloxane) films can be prepared by mixing the PDMS base polymer with a curing agent, usually in a ratio of

ISSN: 0067-3064

10:1 as shown in figure 1. It is important to use the correct ratio to ensure the proper curing of PDMS and to achieve the desired mechanical properties [23-24]. The curing agent is added to the base polymer and the mixture is stirred until it is well homogenized. Once the PDMS mixture is homogenized, it is typically put in a sonicator to remove any air bubbles that may have formed during mixing. Sonication helps to improve the quality of the final PDMS film by reducing any defects that may have formed during mixing.
The mixture is then poured into a Petri dish and allowed to dry in desiccators for 48 hours. Drying in a desiccators helps to remove any residual solvent and further improve the quality of the PDMS film. After the PDMS film has dried, it can be removed from the petri dish and cut into the desired shape or size. The PDMS film is then ready to be used in various applications, such as microfluidic devices, optical sensors, and biomedical devices [25].

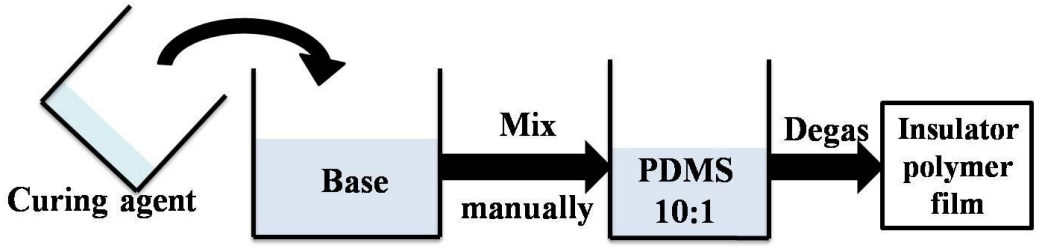

Figure 1. *Preparation PDMS film process.*

Overall, the preparation of PDMS is a simple and straightforward process that can be easily adjusted to meet the specific needs of different applications. It is important to use high-quality PDMS base polymer and curing agent to ensure the best results. Figure 2 show the elaborated PDMS polymer film.

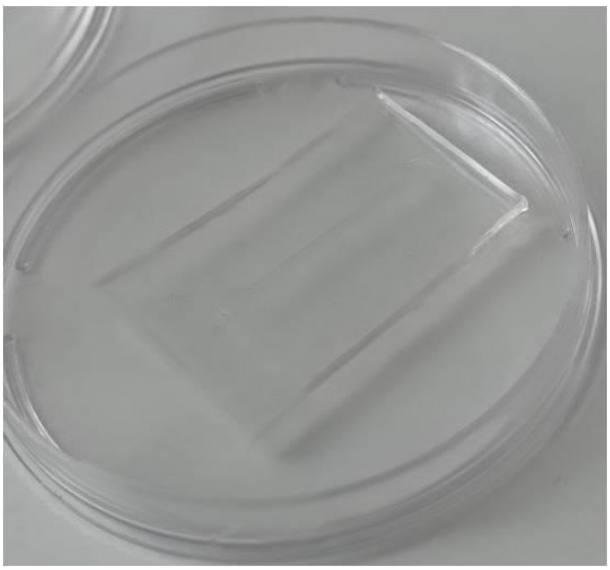

Figure 2. *Picture of elaborated PDMS polymer film.*

2. Experimental protocol of Synthesis of TiO2 by sol-gel Method: In order to synthesize the TiO2 nanoparticles, the detail of experimental protocol for synthesizing nanoparticles using the sol-gel method were presented. The material used for this protocol is: Titanium isopropoxide (TTIP), Ethanol (C2H5OH), Acetic acid (CH3COOH) and Deionized water (DI water). We measure out 50 mL of

ISSN: 0067-3064

ethanol the solvent of the reaction in a clean and dry beaker, then, Stir the ethanol using a magnetic stirrer for about 50 minutes to ensure homogeneity. Slowly, We add to this solution 5ml of acetic acid the catalyst of the reaction with a graduated pipette under stirring for 10min, after that, we add a solution of titanium isopropoxide (TTIP) the precursor of TiO2 drop by drop to the ethanol while stirring. After adding the TTIP, continue stirring the mixture for an additional 15 minutes to ensure thorough mixing. Then the solution is sonicated for 10min and degassed in a desiccators for 24h, after that we heat the solution at 80°C to 100°C until the solution turns opaque white, indicating the formation of powder of TiO2 nanoparticles. Once the solution cools down, it is dried and calcinated the TiO2 nanoparticles in an oven at 500°C for 5 hours until a dry powder is obtained.
Overall, the sol-gel method shown in figure 3 is a widely used method for synthesizing TiO2 nanoparticles due to its simplicity, low cost, and ability to produce highly pure and uniform nanoparticles. The quality and properties of the synthesized nanoparticles can be optimized by adjusting the synthesis parameters such as the precursor concentration, pH, temperature, and reaction time.

Figure 3. *TiO2 preparation procedure.*

PDMS/TiO2 Nanocomposites elaboration. The synthesis of PDMS/TiO2 nanocomposite involves the combination of Polydimethylsiloxane (PDMS) and titanium dioxide (TiO2) nanoparticles to create a new material with unique and improved properties. It can be achieved using various methods such as ex-situ solution mixing process or in situ polymerization process. The resulting PDMS/TiO2 nanocomposite have shown promise in a wide range of applications, including coatings, adhesives, and electronic devices, thanks to their improved mechanical, thermal, and electrical properties.

1. Experimental protocol of ex-situ process: In the ex-situ method, the TiO2 nanoparticles were first synthesized and then added to the PDMS polymer solution to prepare the nanocomposite films. The elaboration of PDMS/TiO2 nanocomposite involves several steps as detailed in figure 4.

ISSN: 0067-3064

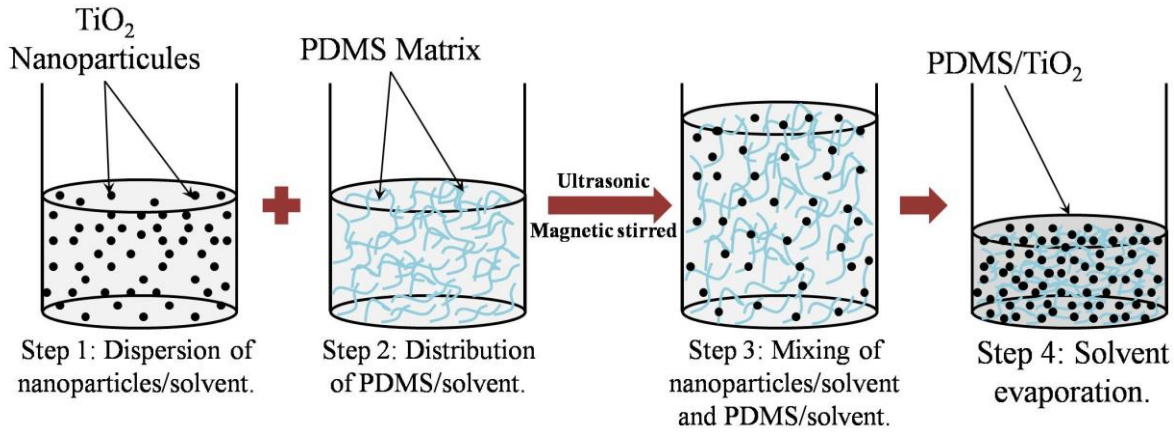

Figure 4. *Elaboration process of PDMS/TiO2 nanocomposite.*

In the first step, the quantity TiO2 nanoparticles are dispersed in a chloroform solvent to form a homogeneous suspension using sonicator for 2 hours then magnetic stirred for 30min. In the second step, the PDMS polymer is dissolved in a chloroform solvent and distributed evenly using the magnetic stirred for 30min then sonicator for 5 min. In the third step, the two suspensions are mixed together, resulting in a homogeneous mixture of TiO2 and PDMS in solution with different ratio of PDMS/TiO2 (3, 5 ,10 and 15%), then sonicate it for 3h then stirred for 30min.
The fourth and final step involves the removal of the solvent through evaporation, which leads to the formation of the solid PDMS/TiO2 nanocomposite material by adding the curing agent and let it cool. The resulting PDMS/TiO2 nanocomposite have shown in figure 5.

Figure 5. *The resulting PDMS/TiO2 nanocomposite.*

2. Experimental protocol of in-situ process: The synthesis of PDMS/TiO2 nanocomposites using an in-situ method involves the simultaneous formation of PDMS and TiO2 nanoparticles within a single reaction mixture. This method is often referred to as the sol-gel process. Figure 6 illustrate the steps involved in the synthesis. In this method, titanium isopropoxide was added drop wise to the PDMS polymer solution under constant stirring, followed by the addition of acetic acid as a catalyst. For the in-situ method, TiO2 nanoparticles were synthesized within the PDMS polymer matrix to form the nanocomposite films. After being desiccated, the resulting mixture was sonicated for 3h, then stirred for 30min, leading to the formation of TiO2 nanoparticles in the polymer matrix.

ISSN: 0067-3064

After that we add the curing agent and mix it manually the we pour it on the petri dish or on a glass slide and let it cool in a desiccators. The PDMS/TiO2 nanocomposite films were then cast and cured to obtain a solid material. This is typically done by heating the mixture at a specific temperature for a specific time. The filling was done for three percentages ratio 3% 5% 10% and 15%.

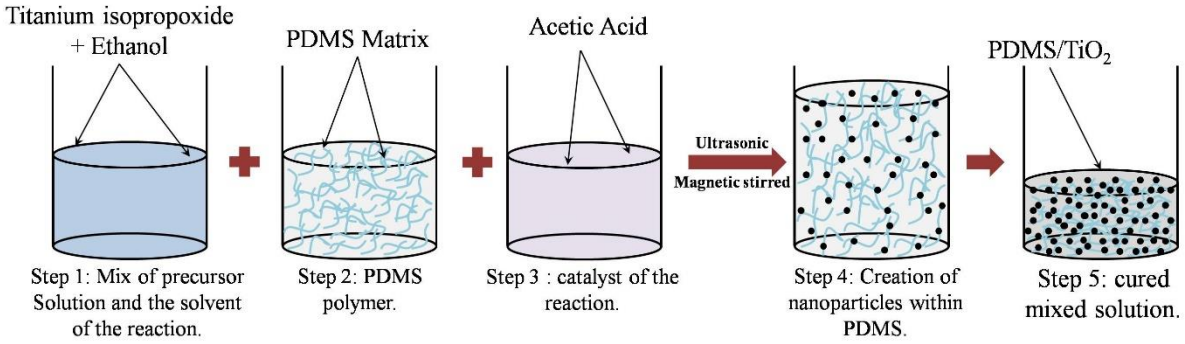

Figure 6. *Steps involved in the synthesis PDMS/TiO2 nanocomposite.*

Comparison of ex-situ and in-situ methods. Both the ex-situ and in-situ methods are two commonly used approaches for preparing nanocomposite films and have their advantages and disadvantages, which can affect the properties and performance of the resulting nanocomposite films. As mentioned, the ex-situ method results in a more uniform dispersion of the nanoparticles in the polymer matrix, leading to improved mechanical properties and better control over the size and shape of the TiO2 nanoparticles content in the films, which can affect their properties, such as their surface area and reactivity. This is because the nanoparticles are well-dispersed before they are mixed with the polymer, which reduces the likelihood of aggregation and improves their distribution within the film. In addition, the nanoparticles can be coated with surfactants or other agents to improve their dispersion in the polymer matrix, which can enhance the mechanical, optical, or electrical properties of the resulting film.

However, the ex-situ method can also have drawbacks. For example, the nanoparticles can settle during mixing, leading to a non-uniform distribution within the film. This can result in weaker mechanical properties or reduced functionality of the nanocomposite. In addition, the additional step of synthesizing the nanoparticles can increase the cost and time required for film preparation.

On the other hand, the in-situ method allows for the synthesis of nanoparticles in the presence of the polymer matrix, which can lead to better interaction between the nanoparticles and the polymer matrix. This can result in improved properties, such as enhanced adhesion and increased stability. Additionally, this method allows for the synthesis of thicker films with a rougher surface, which can be useful for certain applications. However, the control over the TiO2 content in the films is less precise than the ex-situ method, and the synthesis of the nanoparticles in the polymer matrix can lead to aggregation and non-uniform distribution. In addition, the control over the size and shape of the nanoparticles may be limited, which can affect their functionality.

Therefore, the choice of method depends on the specific requirements of the intended application. Factors to consider include the desired properties of the nanocomposite film, the cost and time constraints, and the feasibility of each method. If a uniform dispersion of nanoparticles and precise control over their content in the film are critical, then the ex-situ method may be more suitable. On the other hand, if better interaction between the nanoparticles and the polymer matrix, and the ability to produce thicker films with a rougher surface are more important, then the in-situ method may be

ISSN: 0067-3064

preferred. In some cases, a combination of both methods may be used to achieve the desired properties and functionality of the nanocomposite film.

Results and Discussion.

In the pursuit of enhancing the comprehension of the observed correlations between varying TiO2 nanoparticle concentration and resultant film properties, it is crucial to consider additional details about the experiments. The research methodology entailed methodical incremental adjustment of the TiO2 filler proportion in the PDMS nanocomposites spanning 0-15 wt% using the presented sonication approach described earlier. The resulting thin film were evaluated using several characterization methods by previews works to determine optical transmittance, elastic modulus values, and dielectric constant properties. By monitoring changes in these key parameters across the concentration range, it was possible to uncover the trade-offs between optical transparency, mechanical rigidity, and electrical characteristics, which were dependent on the quantity of TiO2. At lower concentrations (3-5 wt%), transparency and ductility approached pure PDMS while dielectric performance heightened. Higher nanoparticle contents (10-15 wt%) induced sharper declines in transmittance and flexibility but additional augmentations in the dielectric constant emerged. These interconnected dependencies play a critical role in determining the optimal formulations for electroactive device applications. Additional efforts to enrich the experimental dataset through continued testing seek to strengthen mechanistic interpretations and further advance adaptive materials development founded on polymer nanocomposites.
Subsequent to elaborating the procedural steps for synthesizing the PDMS/TiO2 nanocomposite films, an array of techniques was employed to characterize the TiO2 nanoparticles and resulting nanocomposite films. This section delineates the resultant findings derived from said analyses and examines emergent trends.

Effect of varying ratios of TiO2 filler on film properties. The synthesis of PDMS/TiO2 nanocomposite films was accomplished by employing a sonication technique to combine the PDMS polymer with TiO2 nanoparticles. The film properties were examined by investigating the influence of varying ratios of TiO2 filler (3%, 5%, 10%, and 15%). The resulting nanocomposite films exhibited thinness, ductility, and diverse levels of transparency contingent upon the filler ratio. At lower TiO2 filler contents, specifically 3% or 5%, the resulting nanocomposite films maintained transparency and displayed mechanical properties akin to those of the pure PDMS film. Conversely, increasing the filler ratio to 10% or 15% led to reduced transparency, as well as heightened stiffness, hardness and dielectric properties in the films. This shift is attributed to the augmented quantity of TiO2 nanoparticles present in the polymer matrix, which restricts polymer chain movement and intensifies interparticle interactions. Table 1 provides a comprehensive overview of the elastic modulus, transmittance, and dielectric constant of the PDMS-TiO2 nanocomposites at various TiO2 concentrations [26]. In the context of our present study, we acknowledge the importance of these mechanical properties and we are actively carrying out additional studies in order to obtain the required data.

Table 1. Mechanical, Optical and electrical properties of TiO2

TiO2 Concentration	Elastic Modulus	Transmittance	Dielectric Constant
PDMS	860 kPa	100%	2.9
3 wt% PDMS/TiO_2	700 kPa	83%	3.5
5 wt% PDMS/TiO_2	820 kPa	80%	3.8

ISSN: 0067-3064

10 wt% PDMS/TiO_2	880 kPa	56%	3.9
15 wt% PDMS/TiO_2	960 kPa	12%	4.0

The elastic modulus demonstrated a gradual increase as the concentration of nanoparticles rose, reaching a peak value of 960 kPa for TiO2 nanocomposites with a concentration of 15 wt%. This peak value represents a significant enhancement of 11.62% compared to unreinforced PDMS, which has an elastic modulus of 860 kPa. These comprehensive mechanical property data offer a thorough understanding of how the mechanical behavior of PDMS/TiO2 nanocomposite films evolves as the TiO2 filler ratios vary. The impact of nanoparticles on the elastic modulus is presented in table 1. For low particle concentrations below 3 wt%, the elastic modulus of the nanocomposite decreases with increasing nanoparticle concentration. However, once the particle concentration exceeds 3 wt%, the elastic modulus starts to increase. The influence of nanoparticles on the elastic modulus can be attributed to two factors: the softening effects resulting from the interference of cross-linking (which is the major effect for TiO2 concentrations below 3 wt%) and the hardening effects resulting from the intrinsic high elastic modulus of TiO2 (which is the major effect for TiO2 concentrations above 3 wt%). At a particle concentration of 3 wt%, these two effects balance each other out, resulting in an elastic modulus that is more or less the same as that of the pure PDMS elastomer. This change in elastic modulus with respect to particle concentration has been reported by other research groups [26], particularly those using high particle concentrations (above 15 wt%). It has been observed that the elastic modulus increases continuously with increasing TiO2 concentration due to the high intrinsic elastic modulus of TiO2 particles.

Moreover, the fluctuating proportion of TiO2 filler can also influence the optical properties of the nanocomposite films (table 1). The introduction of TiO2 nanoparticles can result in modifications to the refractive index and absorption coefficient of the nanocomposite film, consequently affecting its properties of light transmission. The transmittance diminishes to 80 % when the concentration of TiO2 reaches 5 wt%, and this value decreases to nearly 12 % when the TiO2 concentration reaches 15 wt%. The decrease in transmittance is a consequence of the relatively large size of the particles. Achieving dispersion of TiO2 in a polymer matrix with a diameter below 100 nm, even with the implementation of high-energy ball milling, is exceedingly challenging. Agglomeration is an inevitable outcome due to the high surface energy of the nanoparticles. The scattering of light caused by the particles results in the loss of transmittance when light traverses through the nanocomposite film.

In addition to the transparency and mechanical properties, the varying proportion of TiO2 filler can also influence the electrical properties characteristics of the nanocomposite films. The increase in the TiO2 filler ratio leads to an enhancement in the electrical conductivity of the nanocomposite film due to the conductive nature of the TiO2 nanoparticles. The relationship between the static dielectric constant and particle concentration is illustrated in table 1. A significant surge in the dielectric constant, from 2.9 to 3.8, was observed when the weight fraction of TiO2 nanoparticles increased from 0% to 5%. Subsequently, the dielectric constant gradually increased to 4.0 as the concentration of nanoparticles rose to 15 wt% [26]. The two phases of increasing trends in the dielectric constant may be attributed to particle bridging or flocculation at high particle concentration. A comprehensive

ISSN: 0067-3064

investigation of the mechanism underlying this phenomenon will be conducted in future studies. The heightened dielectric constant provides the advantage of increased electric force exerted on EAPs, thereby reducing the necessity of higher driving voltages.
To summarize, the variation in the proportion of TiO2 filler in PDMS/TiO2 nanocomposite films can influence their properties of transparency, mechanics, electricity, and optics. The optimal proportion of TiO2 filler is contingent upon the specific application of the nanocomposite film and the desired properties. The examination of the effects stemming from varying ratios of TiO2 filler on the film properties is of great significance in order to optimize the synthesis of PDMS/TiO2 nanocomposite films for specific applications.

. **Scanning Electron Microscopy (SEM) Characterization of TiO2 nanoparticles.** The TiO2 nanoparticles were characterized using various analytical techniques to study their properties and structure. The following techniques were used for the characterization. As shows in figure 7, obtained by Scanning Electron Microscope (SEM), the micrograph shows a perfect nanostructure made up of a collection of crystallites. This indicates that the TiO2 nanoparticles are well-formed and have a high degree of crystallinity. The presence of crystallites suggests that the nanoparticles have a regular and ordered atomic arrangement, which is characteristic of crystalline materials.

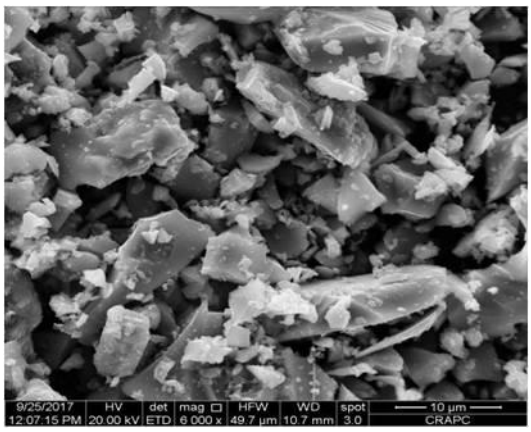

Figure 7. *SEM Micrographs of synthesized TiO2 nanoparticles.*

The micrograph also provides information about the size and shape of the nanoparticles. From the micrograph, it is possible to estimate the size of the nanoparticles and determine their shape. The size and shape of nanoparticles can have a significant impact on their properties, including their catalytic activity, optical properties, and surface area. This information can be used to understand behavior of the nanoparticles in various applications, such as photocatalysis, water purification, and solar energy conversion.

Obtained PDMS/TiO2 nanocomposite films. The initial observation of the synthesized films using two different methods, ex-situ and in-situ, showed that they were easily demoulded and had varying degrees of transparency depending on the presence of different ratios of TiO2 filler (3%, 5%, 10%, and 15%). The virgin films were transparent, while those filled with TiO2 were opaque or white in appearance. Despite this change in appearance, all films remained ductile and thin.

ISSN: 0067-3064

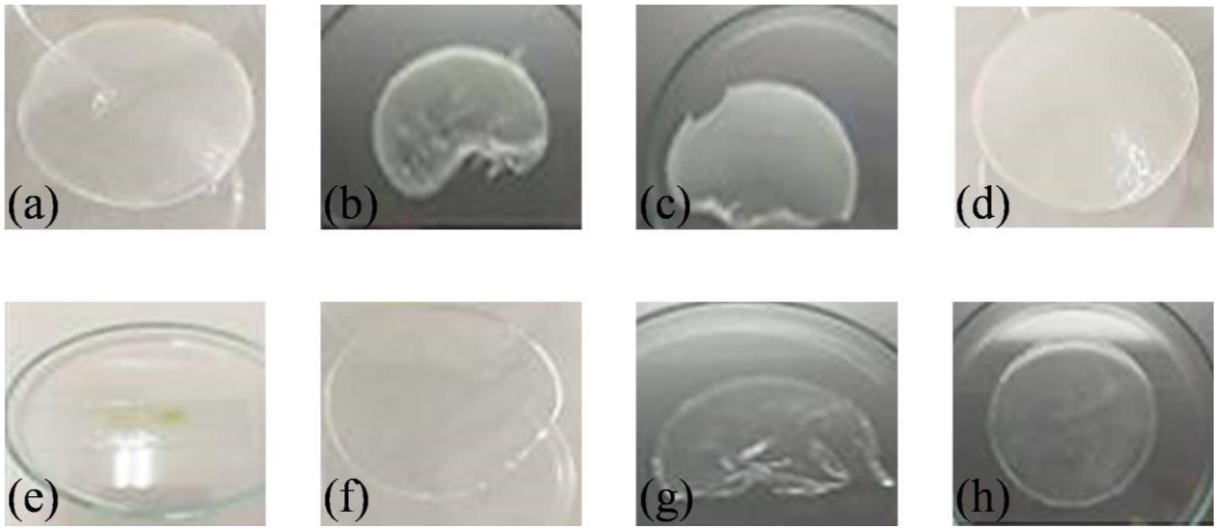

Figure 8. *Different films of synthesis PDMS/TiO2 nanocomposite : (a) ex-situ with ration of 3%, (b) ex-situ with ration of 5%, (c) ex-situ with ration of 10%, (d) ex-situ with ration of 15%, (e) in-situ with ration of 3%, (f) in-situ with ration of 5%, (g) in-situ with ration of 10%, (h) in-situ with ration of 15%*

The different films of synthesis PDMS/TiO2 nanocomposite are shown in the figure 8, for (a), (b), (c) and (d) we have ex-situ method with ration of 3%, 5%, 10% and 15% respectively and for (e), (f), (g) and (h) we have in-situ method with ration of 3%, 5%, 10% and 15% respectively. These initial findings suggest that the addition of TiO2 nanoparticles modifies the optical properties of the films, making them potentially useful in various applications where transparency is not a primary concern.

Optical microscopy. It is noteworthy that as the amount of TiO2 increases, the surface becomes lumpy, with some aggregates of fillers present. This phenomenon is evident in figure 14 and is attributed to the high surface energy of nanoparticles at high loading, which reduces their dispersion in the polymer lattice. This observation highlights the importance of optimizing the nanoparticle loading to achieve a uniform distribution in the polymer matrix, which can impact the mechanical and optical properties of the resulting nanocomposite. Overall, the Optical Microscopy technique proved to be a valuable tool for investigating the surface morphology and particle distribution in these nanocomposite films.

In addition to the detection of white dots on the surface of the PDMS samples, the Optical Microscopy technique also enables the examination of the particle distribution within the polymer lattice. The images suggest that the TiO2 nanoparticles are dispersed in the PDMS matrix, which is a desirable characteristic of nanocomposite films. However, the degree of dispersion can vary based on the fabrication process and nanoparticle loading. For instance, the micrographs of PDMS samples with 3% filler TiO2 indicate a moderate dispersion of nanoparticles, but also show some evidence of agglomeration in the ex-situ process. This means that the nanoparticles tend to cluster together rather than being uniformly dispersed in the polymer matrix.

ISSN: 0067-3064

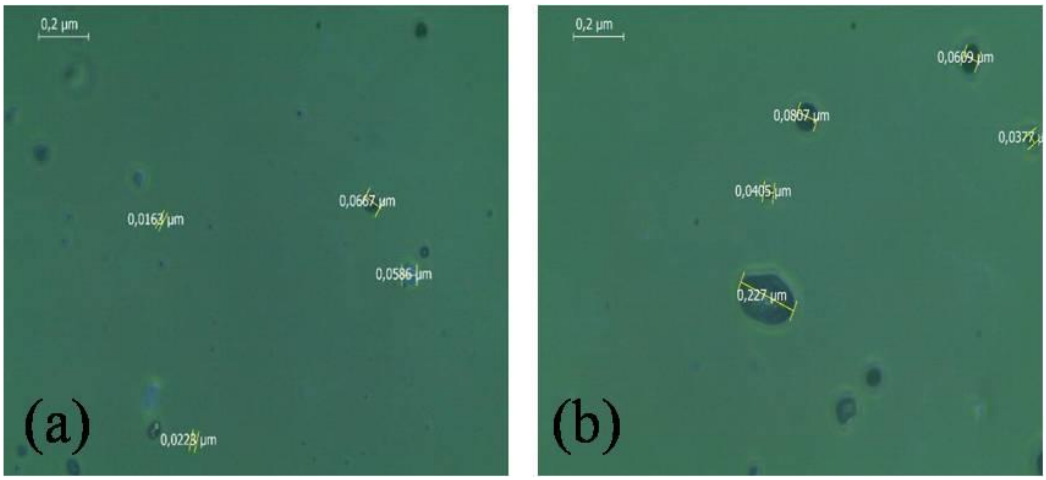

Figure 9. *Optic microscope image of the : (a) 3% ratio in-situ film, (b) 3% ratio ex-situ film.*

Interestingly, the same ratio of 3% filler TiO2 in the in-situ PDM-TiO2 process displays a better dispersion of nanofillers, as shown in figure 9 (a). The in-situ process involves the incorporation of nanoparticles into the polymer matrix during synthesis, which may facilitate a more homogeneous distribution of the nanoparticles. This is likely due to the formation of bonds between the metal and organic films during the synthesis process. However, as the nanoparticle loading increases, the dispersion of nanoparticles becomes more challenging due to the high surface energy of the nanoparticles. The images of PDMS samples containing higher amounts of TiO2 (e.g. 3%) exhibit a lumpy surface with some aggregates of fillers, as depicted in figure 9 (b). This suggests that the nanoparticles tend to form clusters on the surface, leading to reduced dispersion in the polymer matrix. Overall, the Optical Microscopy technique provides valuable insights into the morphology and particle distribution of nanocomposite films, which are critical factors in determining their properties and performance.

Conclusions.

The PDMS/TiO2 nanocomposite films were successfully synthesized using both ex-situ and in-situ methods. The nanocomposite films showed improved properties such as transparency and mechanical properties. The comparative study of the two synthesis methods revealed that each method had its advantages and disadvantages, and the choice of method depends on the specific requirements of the intended application. The characterization results showed that the TiO2 nanoparticles were uniformly dispersed in the PDMS polymer matrix. Overall, the PDMS/TiO2 nanocomposite films have potential applications in various sectors such as food and biomedical packaging. Although PDMS/TiO2 nanocomposite films have shown promising properties and potential applications, there are still some challenges that need to be addressed. One of the major challenges is achieving uniform dispersion of TiO2 nanoparticles in the PDMS matrix. The aggregation of nanoparticles can lead to uneven properties and affect the performance of the films. Another challenge is optimizing the ratio of TiO2 nanoparticles in the PDMS matrix to achieve the desired properties for specific applications. The optimal ratio may vary depending on the application and desired properties such as transparency, mechanical strength, and antibacterial activity. Moreover, the exploration of new applications of PDMS/TiO2 nanocomposite films can lead to the development of innovative and sustainable solutions for various sectors of the market. For example, the use of these films in smart packaging

ISSN: 0067-3064

and wearable devices can revolutionize the way we interact with technology and improve our daily lives.

Acknowledgments.

Authors would like to thank faculty of sciences, LPCMIA Labs and LCPMM Labs in university of Blida 1 for their supports in the present work.

References

[1] H. Fischer, Polymer nanocomposites: From fundamental research to specific applications, Materials Science and Engineering: C, 23 (2003) 763–772.

[2] P.H.C. De Camargo, K.G. Satyanarayana, F. Wypych, Nanocomposites: synthesis, structure, properties and new application opportunities, Materials Research-Ibero-American Journal of Materials, 12 (2009) 1–39.

[3] S. Li, M.-K. Lin, M.S. Toprak, D.K. Kim, M. Muhammed, Nanocomposites of polymer and inorganic nanoparticles for optical and magnetic applications, Nano Reviews, 1 (2010) 5214.

[4] T. Ramanathan, S. Stankovich, D.A. Dikin, H. Liu, H. Shen, S.T. Nguyen, L.C. Brinson, Graphitic nanofillers in PMMA nanocomposites—An investigation of particle size and dispersion and their influence on nanocomposite properties, Journal of Polymer Science Part B, 45 (2007) 2097–2112.

[5] M. Okamoto, Polymer nanocomposites, Eng, 4 (2023) 457–479.

[6] M.T.S. Tavares, A.S.F. Santos, I.M.G. Santos, M.R.S. Silva, M.R.D. Bomio, E. Longo, C.A. Paskocimas, F.V. Motta, TiO2/PDMS nanocomposites for use on self-cleaning surfaces, Surface & Coatings Technology, 239 (2014) 16–19.

[7] N.K. Sethy, Z. Arif, P.K. Mishra, P. Kumar, Nanocomposite film with green synthesized TiO2 nanoparticles and hydrophobic polydimethylsiloxane polymer: synthesis, characterization, and antibacterial test, Journal of Polymer Engineering, 40 (2020) 211–220.

[8] S. Jafari, B. Mahyad, H. Hashemzadeh, S. Janfaza, T. Gholikhani, L. Tayebi, Biomedical Applications of TiO2 Nanostructures: Recent Advances, International Journal of Nanomedicine, Volume 15 (2020) 3447–3470.

[9] M. Taherimehr, H. YousefniaPasha, R. Tabatabaeekoloor, E. Pesaranhajiabbas, Trends and challenges of biopolymer-based nanocomposites in food packaging, Comprehensive Reviews in Food Science and Food Safety, 20 (2021) 5321–5344.

[10] J. Rhim, H.-M. Park, C. Ha, Bio-nanocomposites for food packaging applications, Progress in Polymer Science, 38 (2013) 1629–1652.

[11] C.M. Magdalane, K. Kanimozhi, M.V. Arularasu, G. Ramalingam, K. Kaviyarasu, Self-cleaning mechanism of synthesized SnO2/TiO2 nanostructure for photocatalytic activity application for waste water treatment, Surfaces and Interfaces, 17 (2019) 100346.

[12] D. Ariyanti, A. Afiatin, P.D. Shintawati, A. Purbasari, TiO2-PDMS Super Hydrophilic Coating with Self-Cleaning and Antimicrobial Properties, Jurnal Kimia Sains Dan Aplikasi, 24 (2021) 192–199.

ISSN: 0067-3064

[13] J.H. Kim, S.M. Hossain, H. Kang, H.-J. Park, L.D. Tijing, G.W. Park, N. Suzuki, A. Fujishima, Y. Ju1n, H.K. Shon, G.J. Kim, Hydrophilic/Hydrophobic silane grafting on TIO2 nanoparticles: photocatalytic paint for atmospheric cleaning, Catalysts, 11 (2021) 193.

[14] Z. Yin, X. Chen, T. Zhou, M. Xue, M. Li, K. Liu, D. Zhou, J. Ou, Y. Xie, Z. Ren, Y. Luo, H. Zhang, Mussel-inspired fabrication of superior superhydrophobic cellulose-based composite membrane for efficient oil emulsions separation, excellent anti-microbial property and simultaneous photocatalytic dye degradation, Separation and Purification Technology, 286 (2022) 120504.

[15] X. Xia, J. Liu, Y. Liu, Z. Lei, Y. Han, Z. Zheng, J. Yin, Preparation and Characterization of Biomimetic SiO2-TiO2-PDMS Composite Hydrophobic Coating with Self-Cleaning Properties for Wall Protection Applications, Coatings, 13 (2023) 224.

[16] Q. Lu, Synthesis of PDMS-Metal Oxide Hybrid Nanocomposites Using an in Situ Sol-Gel Route, 2020.

[17] T.R. Nayaki, M.V. Chalam, T.V. Suki, S. Kar, Preparation and Characterization of Nanocrystalline TiO2 Thin Films Prepared By Sol-Gel Spin Coating Method, International Journal of Innovative Research in Science, Engineering and Technology, 03 (2014) 16707–16711.

[18] M. Castellano, R. Cantù, M. Mauri, E. Marsano, S. Vicini, Poly(dimethylsiloxane)/TiO2 Photocatalytic Membranes Obtained by Different Electrospinning Systems, Journal of Nanoscience and Nanotechnology, 16 (2016) 6587–6594.

[19] T.K. Das, M. Jesionek, Y. Çelik, A. Poater, Catalytic polymer nanocomposites for environmental remediation of wastewater, Science of the Total Environment, 901 (2023) 165772.

[20] Q. Guo, R. Ghadiri, T. Weigel, A. Aumann, E.L. Gurevich, C. Esen, O. Medenbach, W. Cheng, B.N. Chichkov, A. Ostendorf, Comparison of in Situ and ex Situ Methods for Synthesis of Two-Photon Polymerization Polymer Nanocomposites, Polymers, 6 (2014) 2037–2050.

[21] A. Saka, J.L. Tesfaye, N. Nagaprasad, R. Shanmugam, L.P. Dwarampudi, R. Krishnaraj, Synthesis and characterization of zinc oxide nanoparticles using moringa leaf extract, Journal of Nanomaterials, 2021 (2021) 1–6.

[22] A. Cordoba, E.M. Rivera-Muñoz, R. Velázquez-Castillo, K. Esquivel, PDMS/TIO2 and PDMS/SIO2 nanocomposites: Mechanical Properties' evaluation for improved insulating coatings, Nanomaterials, 13 (2023) 1699.

[23] MICROLUBROLTM SYLCAPTM 284-S Silicone Elastomer Encapsulant Kit, Transparent, Optically Clear, 10:1 Mix, 500 Gm/ML (0.5 kg). MicroLubrol - Ultra Performance Lubricants. Available from: http://www.microlubrol.com/MICROLUBROLSYLCAP284-SSiliconeElastomerEncapsulantKitTransparent.aspx

[24] N. Belgroune, B.Y. Majlis, A. Hassein-Bey, M.E.A. Benamar, Modeling and FEM simulation using fluid-structures interaction of flexible micro-bridge bending within PDMS micro-channel, IEEE International Conference on Semiconductor Electronics ICSE'14 (2014) 495–498.

[25] N. Belgroune, A. Hassein-Bey, A. Hassein-Bey, A. Tahraoui, B.Y. Majlis, M.E.A. Benamar, R. Serhane, Design and FEM simulation study of a microflow sensor based on piezoresistive PDMS composite for microfluidic systems, Microsystem Technologies, 23 (2016) 1275–1284.

ISSN: 0067-3064

[26] G. M. Ouyang, K. Y. Wang, X. Y. Chen, Enhanced electro-mechanical performance of TiO2 nano-particle modified polydimethylsiloxane (PDMS) as electroactive polymers, 16th International Solid-State Sensors, Actuators and Microsystems Conference, Beijing China (2011). 614-617, doi: 10.1109/TRANSDUCERS.2011.5969778

ISSN: 0067-3064

Determination of the fast neutron flux by activation method

Naima Belouadah[a@], Fatiha Kadem[a], Khelifa Boukeffousa[b], Liela Yettou[a],
Mohamed Belgaid[a] ,Nabila.Taibouni[a] and Zahir Idiri[b]

[a]USTHB, Faculté de Physique, Laboratoire SNIRM, B.P. 32, El-Alia, 16111 Bab Ezzouar, Algeria

[b]Centre de Recherche Nucleaire d'Alger, 02 Bd Frantz Fanon, B.P.399, Alger-Gare, Algeria

Corresponding author: Email: b_belouadah@yahoo.fr

Abstract

Flux measurement of an accelerator based D-T neutron generator was achieved by the activation technique. The neutron generator can produce maximum neutron yield of 1.8 10^8 n/sec at the Tritium-target For the measurement of 14 MeV neutron flux , ^{56}Fe(n, p)^{56}Mn and ^{27}AI(n, p)^{27}Mg reactions are most suitable because of their higher threshold energies.

The fast neutrons were produced, via the ^{3}H(n,d)^{4}He reaction by Neutron Generator at the Research Nuclear Center of Algiers. The Neutron Activation Analysis (NAA) technique was adopted, the γ ray spectra for the Fe and Al were detected for the Germanium Hyper Pure coupled in the Genie 2000 data acquisition software. The measured flux values via the ^{56}Fe(n, p)^{56}Mn and ^{27}AI(n, p)^{27}Mg reactions is (1.32±0.04) 10^7 and (1.12±0.03) 10^7n.cm^{-2}.s^{-1} .

***Keywords*:** D-T neutron generator, neutron activation analysis, fast neutron, neutron flux

1. Introduction

Based on fission or spallation reactions, the activation technique has been widely applied to calculate the time integrated neutron flux from fission reactors and high intensity neutron sources. The fast neutron flux from a neutron generator can be measured indirectly using multi-foil activation analysis. Multiple activation foils are selected to cover a broad energy range of fast neutrons [1]. The half-lives, isotopic branching ratios and resulting intensities of emitted gamma-rays after activation are essential factors in selecting what type of foil to activate. If the half-lives of the activated isotopes are too short, not many activated nuclei survive to the beginning of the counting. Also, intensities (branching ratios)

ISSN: 0067-3064

and energies of characteristic gamma-rays emitted from activated nuclei must be suitable to accumulate enough net counts above background to be detected during gamma-ray spectroscopy [2].

In the present paper, we report on the measurement of the fast neutron flux via at the neutron energy of 14.7 MeV by using the Neutron Generator at Research Center Nuclear Algiers. The principal nuclear reactions of interest in the measurement of neutron flux from neutron generators by activation analysis are (n, p) reaction. Iron and Aluminum have been selected to measure the neutron flux of D-T neutron generator [3]. The nuclear reactions of interest are ^{56}Fe(n,p)^{56}Mn and ^{27}AI(n,p)^{27}Mg. These reactions have high threshold energies, their reaction cross-section is well measured and the half-life of the reaction product is few minutes.

2. Experimental techniques

Irradiation of the samples was carried out at Neutron Generator at Research Center Nuclear Algiers were produced by the T(d, n)^{4}He reaction with an effective deuteron beam energy of 150 keV and beam current of 400 μA. The target it is the type Cu (TiT) in which the tritium is adsorbed in a thin layer of titanium deposited on a 49 mm diameter copper disc, the diameter of the tritiated surface being equal to 30 mm; the activity of the targets used is 0.4 to 0.8 Curies / cm2 [4] . The neutron flux was monitored by an Iodure of the Lithium (Li (I)) detector. The sample are placed at 90◦ angle relative to the beam direction and centered about the T–Ti target at distances of 2 cm. The ^{56}Fe(n,p)^{56}Mn and ^{27}AI(n, p)^{27}Mg reactions were selected for to measure the neutron flux at 14.7 MeV neutron energy.

3. Irradiation and activity measurements

The monitors were irradiated at the Neutron Generator at Research Center Nuclear Algiers. The monitor neutron flux was measured at this outer-end position an irradiation time of 30 mn. After irradiation of the Iron and Aluminum monitors a High purity Germanium (HPGe) detector was used to calculate the activity. The resolution of this detector was of ~1.92 keV for 1332.5 keV (^{60}Co) and 0.9 keV for 122 keV (^{57}Co) with a relative measured efficiency of 46.6%. The collected data were analyzed by using the gamma spectrometry Genie 2000 data acquisition software [5].

ISSN: 0067-3064

To determine the efficiency with gamma ray energy dependence the following expression is used:

$$\varepsilon(E) = A_1 \exp(-E/t_1) + A_2 * \exp(-E/t_2) + y_0 \quad (1)$$

The fitting parameters y_0, A_1 , A_2 , t_1 and t_2 were determined by using the least squares method (Figure 1). The difference between the experimental points and the calculated points is generally less than 1%.

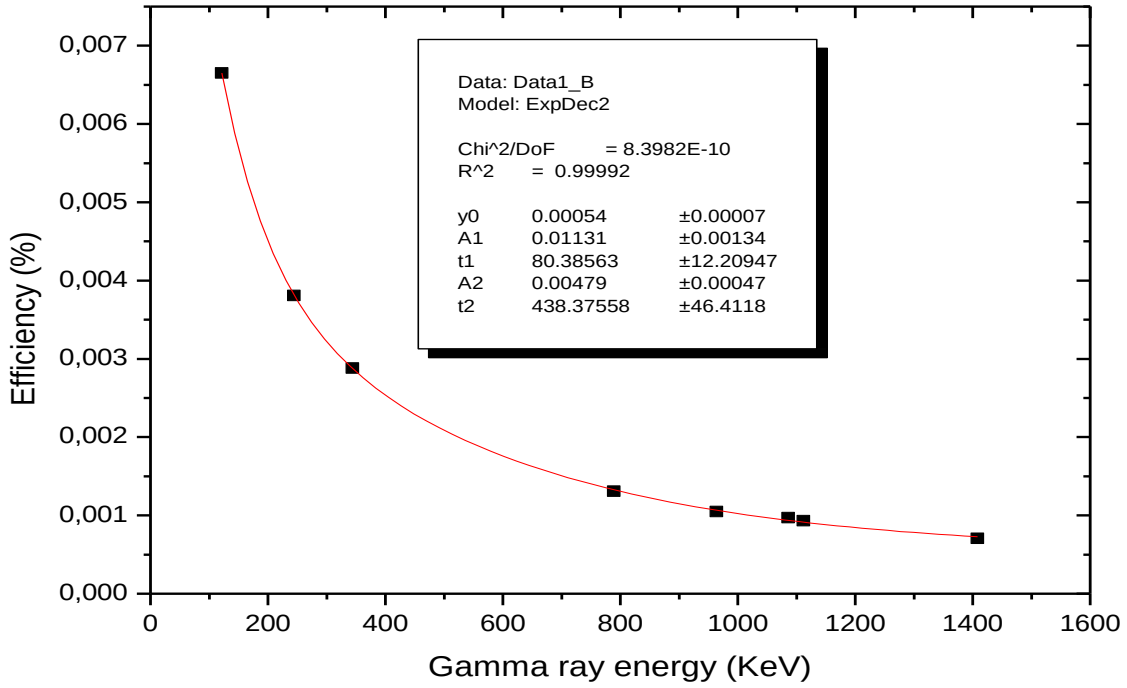

Figure 1: Efficiency curve via gamma ray energy

The decay characteristics of the product radioisotopes and the natural abundances of the monitor foils under investigation are summarized in Table 1.

Table1. Nuclear Data ofy ^{27}Al (n, p)^{27}Mg and ^{56}Fe (n, p)^{56}Mn reactions.

Nuclear reaction	σ(m barn) E_n=14.7 MeV	Half-life	γ-ray energy (keV)	γ emission probability (%)
^{27}Al(n,p)^{27}Mg	77	588s	844	71.80
			1014	21.20
^{56}Fe(n,p)^{56}Mn	108±4	2.58h	846.6	91.72

ISSN: 0067-3064

4. Data analysis

To measure the flux of incident neutrons at 14.7 MeV, we used pure Iron and Aluminum foils because the cross sections has been accurately established and to the appropriate decay parameters [6]. The monitor fast neutron flux is given by the well-known activation formula:

$$\Phi_m = \frac{\lambda N_{et}}{n\varepsilon_\gamma I_\gamma \sigma\, e^{-\lambda t_c}(1-e^{-\lambda t_d})(1-e^{-\lambda t_i})} \qquad (2)$$

Where N_{et} is the total counts of gamma-ray peak area and λ the decay constant; the number of target atoms is defined as:

$$n = N_{Av}\,\frac{W\,\theta}{M} \qquad (3)$$

Where W is the Gold weight, θ the isotopic abundance, M the Atomic weight and N_{Av} the Avogadro number. ε_γ is the gamma peak efficiency, I_γ the branching ratio of gamma ray, σ monitor thermal cross section of at 14.7 MeV, t_c the counting time (s), t_d the decay time (s) and t_i the irradiation time (s) [7].

5. Flux measurement results

The peak counts of the γ-ray line (844 keV) and (847 keV) in the spectrum were used to determine the activity of the ^{27}Mg and ^{56}Mn radionuclide produced through the (n,p) reaction. The selected irradiation and counting times were respectively 30 min and 1 h.

The obtained gamma ray spectrum and the corresponding radionuclide counts are shown in Figure 2 and Figure 3

ISSN: 0067-3064

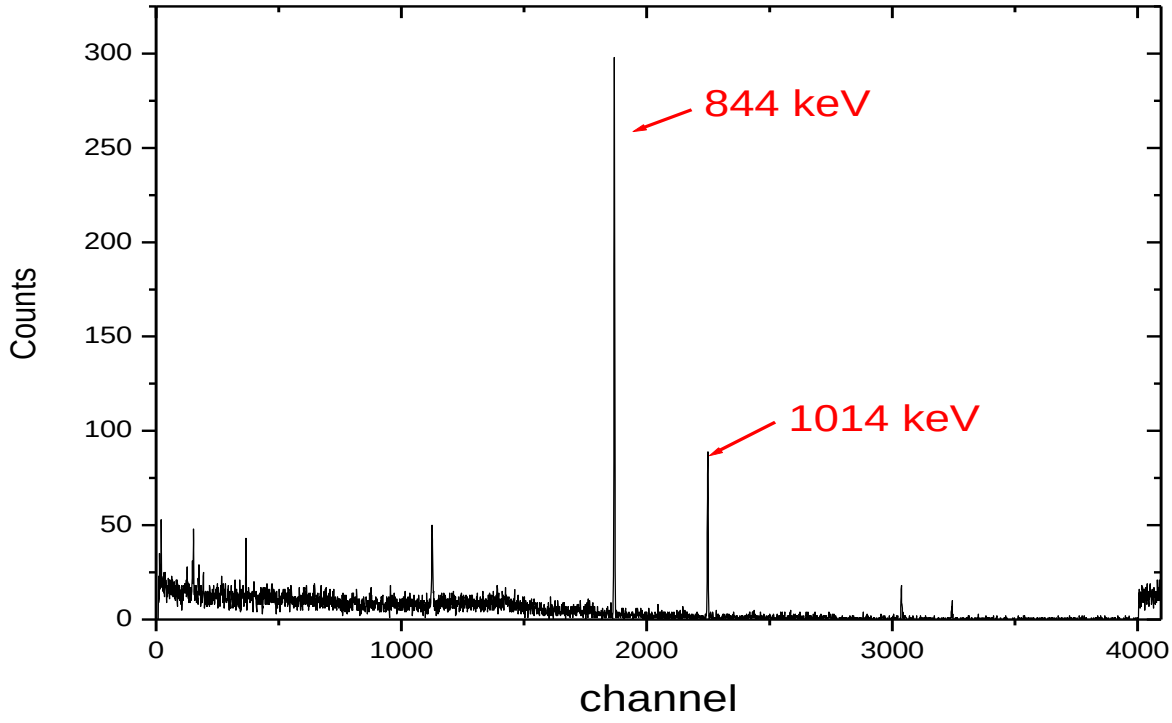

Figure. 2: Gamma-ray spectrum of the radioactive Al-Sample.

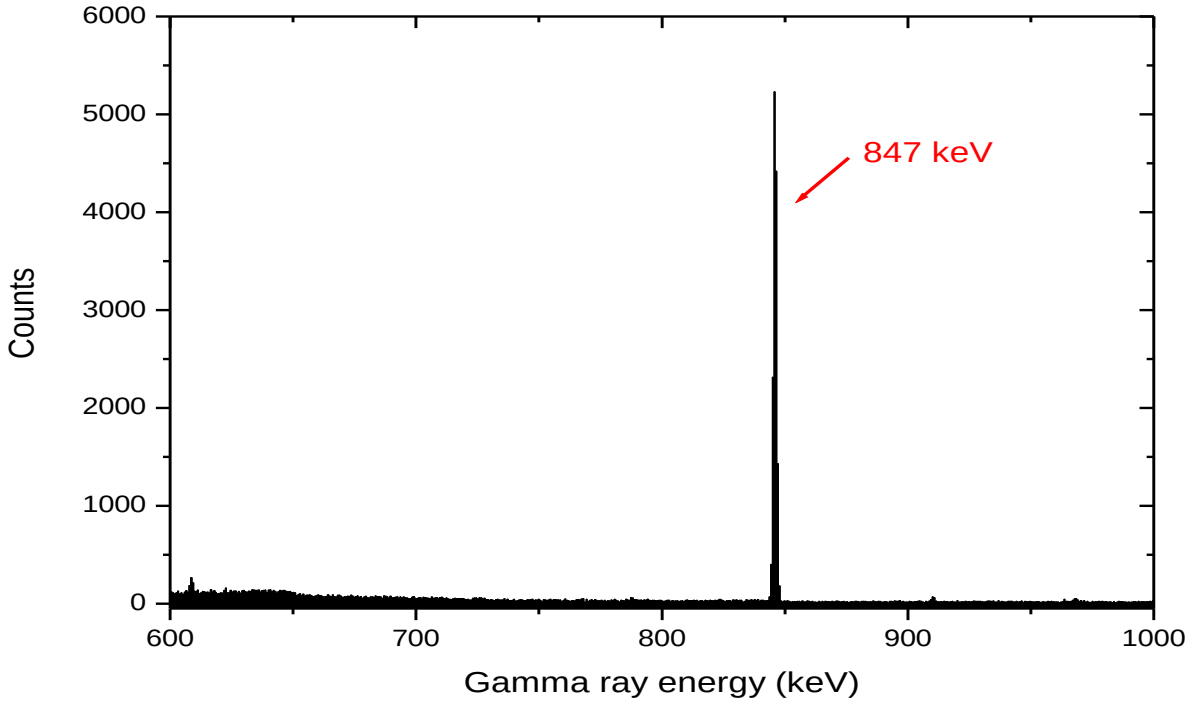

Figure. 3: Gamma-ray spectrum of the radioactive Fe-Sample.

ISSN: 0067-3064

The experimental neutron flux for the $^{27}Al(n,p)^{27}Mg$ and $^{56}Fe(n,p)\ ^{56}Mn$ reactions at an energy of 14.7 MeV is determined from eq. (2) by considering all the measured quantities mentioned, a values via the $^{56}Fe(n,\ p)^{56}Mn$ and $^{27}AI(n,\ p)^{27}Mg$ reactions is (1.32±0.04) 10^7 and (1.12±0.03) $10^7 n.cm^{-2}.s^{-1}$ respectively.

The total uncertainty in the measured neutron flux was determined by combining the estimated individual uncertainties of the nuclear data; the uncertainty for neutron flux amounted to 3% is estimated by considering all uncertainties with parameters related to the flux calculation like foil mass measurements (0.01%), peak area analysis (1%) cross section of monitor reaction (2.5%) and efficiency (2%).

6-Conclusions

For a few tens of minutes, precise time-integrated flux measurements can be obtained using the technique detailed in the paper. The technique can be expanded to measure the cross section for the reactions (n,2n), (n,p), and (n,α) as well as to determine the neutron spectra over any desired energy range by employing the proper stack of metal foils.

References

[1] S.Jakhar, C V S Rao, A Shyam and B Das.Measurement of 14 MeV Neutron Flux from D-T Neutron .IEEE Nuclear Science Symposium Conference Record,2008.
[2] D.Lee and al. Determination of the Deuterium-Tritium (D-T) Generator Neutron Flux using Multi-foil Neutron Activation Analysis Method. Idaho National Laboratory 2018.
[3] M.Belgaid,M.Siad.M, M.Allab, J. Radioanalytical and Nucl. Chem., Letters.166, Issue.6, 493 ,1992
[4] N. Belouadah, F. Kadem, M. Belgaid, Z. Idiri and F. Redjem" Measurernents of activation cross section reaction induced by 14.7 MeV neutrons" ICRA'l7.].International Conference on Radiations and Applications, Algiers, 2017.
[5] Genie 2000, Spectroscopy Software V3.2, Canberra Industries Inc., Meriden, USA. 2008.
[6]Kinsey,R.R.The NuDat Program for Nuclear Data on the Web (http://www.nndc.bnl.gov/nndc/nudat), version 2.5, NNDC, BNL, New York.1996.
[7] N.Belouadah, F.Kadem, H. Slamene, N. Osmani, M.Belgaid, L. Yettou and M. Trari Experimental cross section of the $^{164}Dy(n,\gamma)^{165}Dy$ reaction at the neutron energy of 0.0372 eV using Neutron Diffraction Facility Radiochimica Acta, vol. 110, no. 12, 2022, pp. 947-953

ISSN: 0067-3064

Effects of Level Densities and Those of a-Parameter in the Framework of Preequilibrium Model for ^{58}Ni(n, xp) reaction in neutrons at 8 to 11 MeV

Yettou Leila[a]*, Belgaid Mohamed[a], Belouadah Naima[a], Amrani Naima[b] and Kadem Fatiha[a]

a University of Sciences and Technology of Bab Ezzouar, Faculty of Physics, Laboratory SNIRM, Algiers, Algeria
b University of Sétif, Sétif, Algeria

Abstract: in this study, the calculations of proton emission spectra produced by ^{58}Ni (n, xp) reactions are used in the framework of preequilibrium model with the TALYS code. The two-component exciton model combined with the Kalbach angular distributions systematics were used and some necessary parameters as the level density with the level density a-parameter have been investigated for our calculations. The comparison with experimental data shows clear improvement over the Preequilibrium Exciton Model calculations.

Keywords: Exciton model, level density, level density a-parameter, TALYS code.

1. Introduction:

Nickel is a major component of austenitic steel that is widely employed in the nuclear industry and it is important structural material for nuclear applications [1]. Through an elaborate work [2], cross sections and spectra for (n,xp) and (n,xα) reactions on ^{58}Ni and ^{60}Ni at energies of 9.4 and 11 MeV and for ^{58}Ni at 8 MeV have been based on comparison of Hauser-Feshbach calculations with the measured spectra. The main purpose of this work is to investigate the sensitivity on the input parameters from the level density [3] with the level density a-parameter [4] considered in our calculations affect strongly the results compared to the experimental data.

The cross sections for the emission of proton for incident neutron energy 8, 9.4 and 11MeV on ^{58}Ni are calculated in the framework of pre-equilibrium [5], and equilibrium [6] models by using the TALYS code [7]. The plots are presented with the comparison between the results from the TALYS code [7] calculations and the experimental data which are retrieved from the EXFOR database [8]. The obtained results have been discussed and compared with the available experimental data [8] and found in agreement with each other.

ISSN: 0067-3064

2. Theoretical models formula:

Two versions of the exciton model are implemented in TALYS [7]: the default is the two-component model [5] in which the neutron or proton particles and holes are followed throughout the reaction. The pre-equilibrium differential cross section for the emission of a particle k with emission energy E_k can be expressed in terms of the lifetime of exciton state (p_π, h_π, p_ν, h_ν) τ, the composite nucleus formation cross section σ_{CF}, and an emission rate W_k

$$\frac{d\sigma_k^{PE}}{dE_k} = \frac{\sigma^{CF} \sum_{p_\pi=p_\pi^0}^{p_\pi^{max}} \sum_{p_\nu=p_\nu^0}^{p_\nu^{max}} W_k(p_\pi, h_\pi, p_\nu, h_\nu, E_k)}{\tau\,(p_\pi, h_\pi, p_\nu, h_\nu) \times P\,(p_\pi, h_\pi, p_\nu, h_\nu)} \quad (1)$$

where the factor P represents the part of the pre-equilibrium population that has survived emission from the previous states and passes through the $(p_\pi, h_\pi, p_\nu, h_\nu)$ configurations, averaged over time. There are several models for the level density in TALYS 1.8 code [7]. In the Fermi gas model, Ignatyuk et al. [4] recognized that the correlation between the parameter a and the shell correction term of the liquid-drop component of the mass formula, and the expression which takes into account the presence of shell effects at low energy and their disappearance at high energy can given as:

$$a = a(E_x) = \tilde{a}\left(1 + \delta W \frac{1-exp[-\gamma U]}{U}\right) \quad (2)$$

Here, $\tilde{a}$ is the asymptotic level density and U is the effective excitation energy. The damping parameter γ determines how rapidly $a(E_x)$ approaches $\tilde{a}$. Finally, δW is the shell correction energy. The absolute magnitude of δW determines how different $a(E_x)$is from $\tilde{a}$ at low energies, while the sign of δW determines whether $a(E_x)$ decreases or increases as a function of E_x.The asymptotic value $\tilde{a}$ is given by smooth form

$$\tilde{a} = \alpha A + \beta A^{2/3} \quad (3)$$

where A is the mass number, while the following systematical formula for damping parameter is used,

$$\gamma = \frac{\gamma_1}{A^{\frac{1}{3}}} + \gamma_2. \quad (4)$$

In Eqs.3 and 4, α, β and $\gamma_{1,2}$ are global parameters that have been determined to give the best average level density description over a whole range of nuclides. They are given in Table 4.3 of the TALYS 1.8 code [7], where also the average pairing correction δglobal is given and can be adjusted with the Pshiftconstant keyword.

ISSN: 0067-3064

3. Results and discussions :

By using the two-component exciton model [5] as implemented in TALYS 1.8 code [7], we calculated the double differential cross sections and the angle integrated proton particle emission spectra, and compared with the experimental data [8] as shown in Fig. 1 through 3., (continuous and dotted blue lines) where the principal input parameters are summarized in Table 1 for ^{58}Ni(n, xp) nuclear reaction. As shown in Figs. 1 , 2 and 3 in TALYS 1.8 code [7], the local and global nucleon optical models of Koning and Delaroche [9] have been used for neutrons and protons where the optical model parameters has been adjusted via adjustable parameters through the v1adjust p keyword of equations 4.8 and 4.9 in the TALYS 1.8 code [7]. The Back Shifted Fermi Gas Model [10] level density with the ldmodel 2 keyword and the level density parameter a in $^{59}_{28}Ni$ (compound nucleus) and in $^{58}_{27}Ni$ (residual nucleus), the results are close to the experimental data [8] as shown in Figs. 1 , 2 and 3 (single blue lines).

Table 1: the principal input parameters used in the two-component exciton model calculations at the 8, 9.4 and 11 MeV neutron incident energies for (30◦, 60◦ and 120◦ angles emission).

Optical potential	- Local and global nucleon optical models of Koning and Delaroche
Optical model parameters via adjustable local parameters(at the 8, 9.4 and 11 MeV neutron incident energies for (30°, 60° and 120° angles emission)	- v1adjust p 1.05
Back Shifted Fermi Gas Model level density (at the 8, 9.4 and 11 MeV neutron incident energies for (30°, 60° and 120° angles emission	- Ldmodel2
Level density a- parameter (at the 8, 9.4 and 11 MeV neutron incident energies for (30°, 60° and 120° angles emission	- 40.220 MeV^{-1} in $^{59}_{28}Ni$ (compound nucleus) and 2.9 MeV^{-1} in $^{58}_{27}Ni$; (residual nucleus) at 8 MeV neutron incident energies for (30°, 60° and 120° angles emission); - 23.5 MeV^{-1} in $^{59}_{28}Ni$ (compound nucleus) and 2.9 MeV^{-1} in $^{58}_{27}Ni$ (residual nucleus) at 9.4 MeV neutron incident energies for (30°, 60° and 120° angles emission);

ISSN: 0067-3064

	- 53. MeV^{-1} in $^{59}_{28}Ni$ (compound nucleus) and 4.7 MeV^{-1} in $^{58}_{27}Ni$ (residual nucleus) at 11 MeV neutron incident energies for (30°, 60° and 120° angles emission);

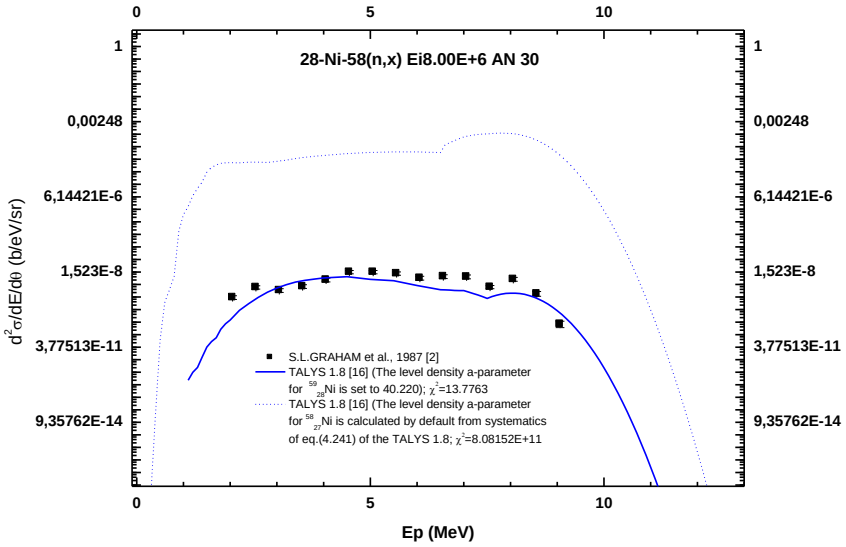

ISSN: 0067-3064

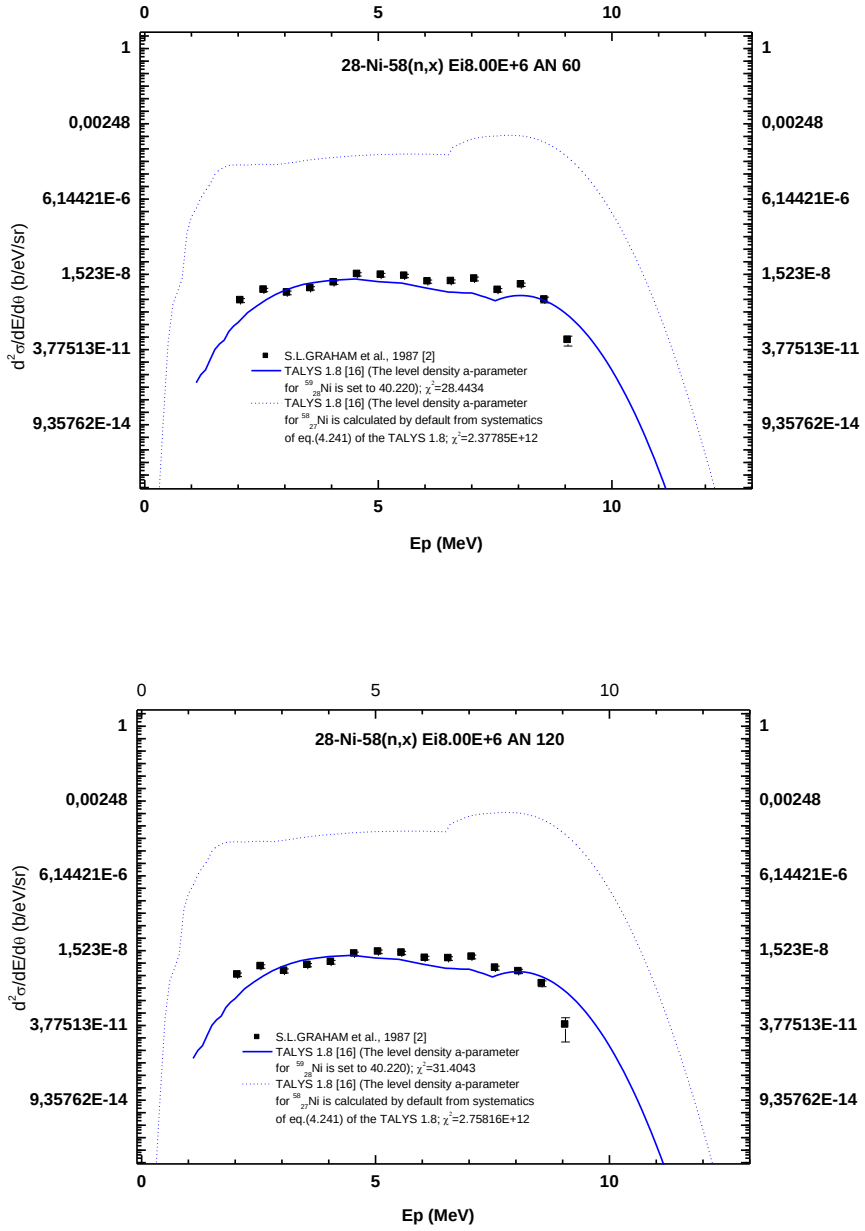

Fig 1.Comparison between double differential cross sections for ^{58}N(n, xp) reaction in neutrons at 8 MeV as calculated with the effect of the level density parameter-a of Back Shifted Fermi Gas Model level density [10] (continuous and dotted blue lines) by using TALYS 1.8 code [7] to the experimental data (solid squares) [8].

ISSN: 0067-3064

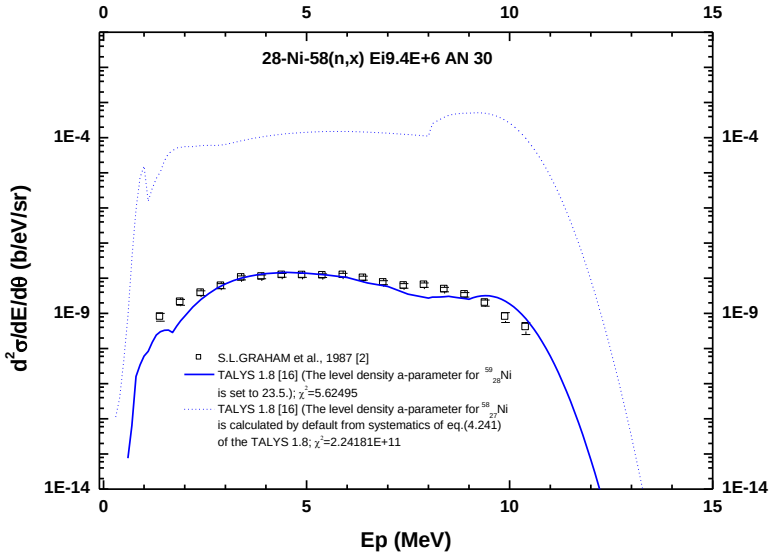

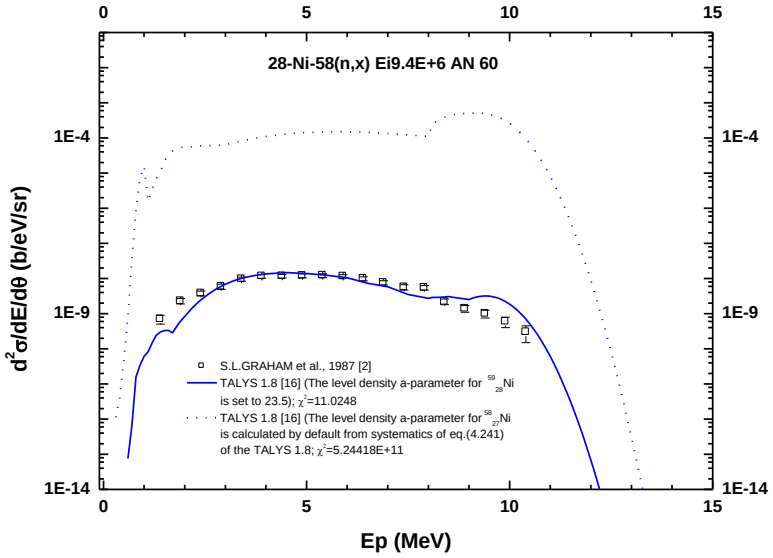

ISSN: 0067-3064

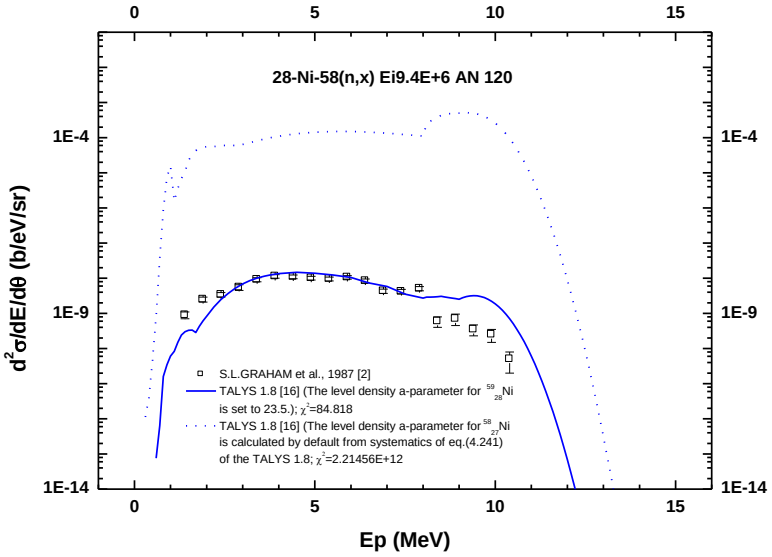

Fig. 2. Comparison between double differential cross sections for ^{58}N(n, xp) reaction in neutrons at 9.4 MeV as calculated with the effect of the level density parameter-a of Back Shifted Fermi Gas Model level density [10] (continuous and dotted blue lines) by using TALYS 1.8 code [7] to the experimental data (open squares) [8].

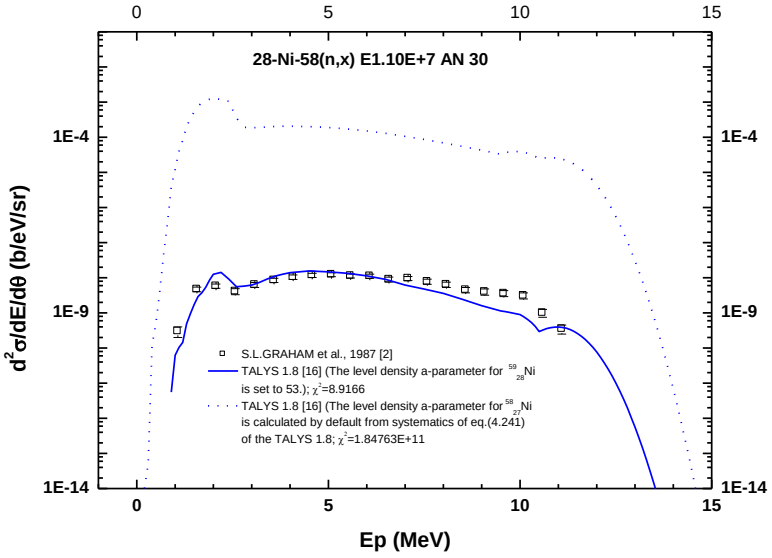

ISSN: 0067-3064

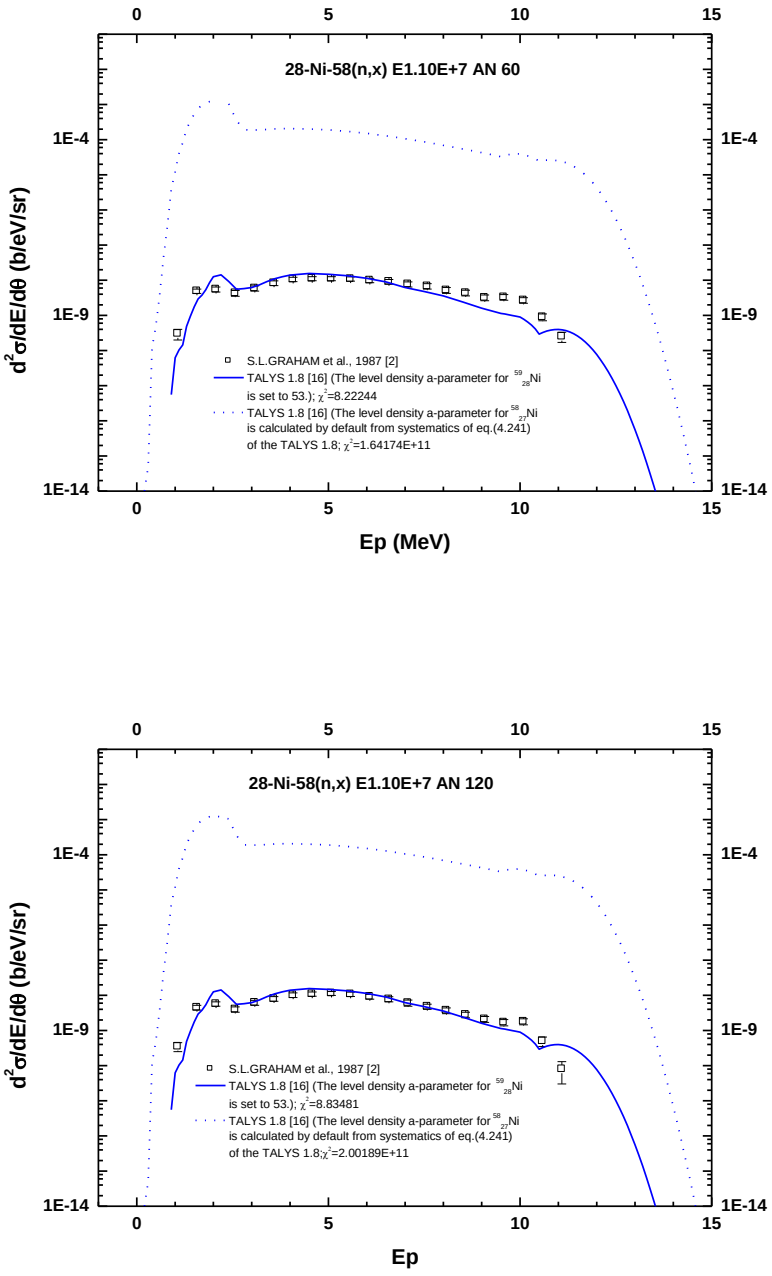

Fig. 3. Comparison between double differential cross sections for ^{58}N(n, xp) reaction in neutrons at 11 MeV as calculated with the effect of the level density parameter-a of Back Shifted Fermi Gas Model level density [10] (continuous and dotted blue lines) by using TALYS 1.8 code [7] to the experimental data (open squares) [8].

ISSN: 0067-3064

4. Conclusion :

We have analyzed the calculated double differential cross sections calculations of (n, xp) reactions on nickel ^{58}Ni target using nuclear reaction model in TALYS 1.8 code [7]. Our results show that the calculations of the pre-equilibrium in terms of exciton model at two components (in TALYS 1.8 code [7]), and the different values of the level density parameter a in residual nucleus and compound nucleus for ^{58}Ni (n, xp) reaction show the similar behavior with the experimental data. For all the figures as shown in this work, the TALYS 1.8 code [7] results are close to the experimental results and the lower χ^2 value give a significantly better fit when compared to the experimental results. We will validate our new nuclear data for neutron induced reaction on isotopes of chromium and iron with criticality and shielding benchmarks.

References

[1] Dispersive coupled-channels optical-model potential with soft-rotator couplings for Cr, Fe, and Ni isotopes. Rui Li et al., *PHYSICAL REVIEW C*87, 054611 (2013).
[2] Graham, S.L., Ahmad, M., Grimes, S.M., Satyanarayana, H., Saraf, S.K., 1987. Cross sections and spectra for (n,xp) and (n,xα) reactions on 58Ni and 60Ni at energies of 9.4 and 11 MeV. Journ.: Nucl. Sci. Eng. 95 (1), 60–69, 1987.
[3] A.J. Koning, S. Hilaire and S. Goriely, "Global and local level density models", *Nucl Phys. A* 810, 13-76 (2008).
[4] A.V. Ignatyuk, G.N. Smirenkin and A.S. Tishin, *Sov. J. Nucl. Phys*. 21, no. 3, 255 (1975).
[5] A.J. Koning and M.C. Duijvestijn, "A global pre-equilibrium analysis from 7 to 200 MeV based on the optical model potential", *Nucl. Phys. A* 744, 15 (2004).
[6] W. HAUSER and H. FESBACH, *Phys. Rev*., 87, 366 (1952),http://dx.doi.org/10.1103/PhysRev.87.366; see also L. WOLFENSTEIN, *Phys. Rev.*, 82, 690 (1951), http://dx. doi.org/10.1103/PhysRev.82.690.
[7] A. J. KONING, S. HILAIRE, and M. C. DUIJVESTIJN, "*Talys-1.0,"Proc. Int. Conf. Nuclear Data for Science and Technology (ND-2007)*, Nice, France, April 22–27, 2007.
[8] Experimental Nuclear Reaction Data (EXFOR) Database Version of March 16, 2015, https://www-nds.iaea.org/exfor/exfor.htm (current as of July 12, 2015).
[9] A. J. KONING and J. P. DELAROCHE, "Local and Global Nucleon Optical Models from 1 keV to 200 MeV,"*Nucl. Phys. A*, 713, 231 (2003); http://dx.doi.org/10.1016/S0375-9474(02)01321-0
[10] W. Dilg, W. Schantl, H. Vonach, and M. Uhl, *Nucl. Phys. A* 217, 269 (1973).